

# **Metal-Organic Frameworks as Crystalline Porous Hosts for Photoactive Molecules**

Inaugural-Dissertation

zur

Erlangung des Doktorgrades

der Mathematisch-Naturwissenschaftlichen Fakultät

der Universität zu Köln

vorgelegt von

Heidi Annemarie Schwartz

aus Bremen

Köln 2018

Berichterstatter:	Prof. Dr. Uwe Ruschewitz
	Prof. Dr. Dominik Schaniel
Vorsitzender:	Prof. Dr. Klaus Meerholz
Schriftführung:	Dr. Selina Olthof

Tag der mündlichen Prüfung: 18. Juli 2018

The experimental investigations of the present thesis were conducted from April 2015 to April 2018 under the supervision of Prof. Dr. Uwe Ruschewitz at the Department of Chemistry of the University of Cologne.



There are two things that are necessary for our work: tireless perseverance and the willingness to throw away something that you put a lot of time and effort into (Albert Einstein).



## Abstract

Molecules, which reversibly transform between two structural configurations upon excitation with electromagnetic radiation, are attractive candidates for the design of smart materials e.g. memory devices. An essential prerequisite for the development of such smart materials is the construction of hybrid systems that contain these photochromic molecules on the one and a porous host matrix, which enables their switching process in solid state, on the other hand. In the present thesis such light responsive materials consisting of switchable guests and crystalline porous hosts were synthesized to form hybrid systems. These systems show photochromic response and host dependent absorption maxima of the incorporated guest molecule, which is known as solvatochromism. Spiropyrans and spirooxazines were selected as guest molecules and different Metal-Organic Frameworks (MOFs) as suitable host matrices.

The starting point of this thesis was the nitro-substituted spiropyran 1,3,3-trimethylindolino-6'-nitro-benzopyrylospiran (SP-Nitro) as photochromic guest molecule. For the first time, the embedment into different MOFs as host matrices allowed the light induced isomerization to convert from its closed SP form to the open MC form in solid state. Moreover, the host scaffolds provide varying chemical environments within their pores, which caused MOF dependent absorption maxima of the incorporated SP-Nitro. This solvatochromic response highly resembles the behavior of SP-Nitro when dissolved in solvents of varying polarity. Thus, the term of solvatochromism is expanded to MOFs, which can be classified as "solid solvents" for spiropyrans. Based on these results, the structurally related spirooxazine 1,3,3-trimethylindolino-naphthospirooxazine (SP-O) was embedded. In contrast to spiropyrans, SP-O exhibits enhanced resistance towards photodegradation. Analogous to SP-Nitro, SP-O converts to its open MC-O form upon UV light exposure inside the MOF pores, but with suppressed photodegradation. Furthermore, solvatochromism was perceived in dependence of the used host scaffold as well. The solvatochromic response of both dyes, spiropyrans and spirooxazines, clearly indicates different polarities of the host lattices, which were finally determined by the embedment of the polarity sensor 4,5-dimethoxy-*N*-butylphthalimide. Here, the light emission also diverged relying on the surrounding host matrix.

Consequently, MOFs behave analogously to solvents as both interact with and influence the electronic structure of the guest molecule. Moreover, MOFs enable switching processes of spiropyrans and spirooxazines in solid state. Therefore, MOFs function as "solid solvents" for

dye molecules. This fundamental knowledge is indispensable for the systematic design and development of functional smart composite materials.

## Kurzzusammenfassung

Substanzen, die sich durch Einstrahlung von Licht reversibel strukturell verändern, sind von großem Interesse als Teil funktioneller Materialien zum Beispiel für die Datenspeicherung. Der Einbau dieser photochromen Moleküle in kristalline poröse Wirtsmatrizen, die die Schaltung auch im Feststoff ermöglichen, stellt dabei eine grundlegende Voraussetzung für die Entwicklung von solchen funktionellen Hybridmaterialien dar. In der vorliegenden Doktorarbeit wurden Hybridmaterialien bestehend aus einer schaltbaren Einheit und einer porösen Wirtsstruktur dargestellt. Die resultierenden Hybridmaterialien zeigen nicht nur Schaltbarkeit des eingelagerten Gastes, sondern auch wirtsabhängige Absorptionsmaxima. Diese Eigenschaft ist als Solvatochromie bekannt und wurde bisher nur für Lösungsmittel beobachtet.

Als Gastmoleküle wurden Spiropyrane und Spirooxazine ausgewählt und in Metall-Organische Gerüstverbindungen (MOFs) als geeignete Wirtsmatrizen eingelagert. Die Kombination von MOF und Schalter ermöglicht zum einen die Schaltbarkeit des Gastes im festen Zustand, aber gleichzeitig auch die Bestimmung der Polarität des Wirtsgitters, was bis zum jetzigen Zeitpunkt noch nicht untersucht worden ist.

Zunächst wurde dazu das sehr gut untersuchte nitro-substituiertes Spiropyran, 1,3,3-Trimethylindolino-6'-nitro-benzopyrylospiran (SP-Nitro), als schaltbares Gastmolekül verwendet. Durch Einlagerung in die MOF-Gerüste konnte der lichtinduzierte Isomerisierungsprozess von der geschlossenen Spiropyran (SP) zu der offenen Merocyanin (MC) Form im Feststoff ausgelöst und damit Schaltbarkeit im festen Zustand erreicht werden. In Abhängigkeit der Wirtsmatrix zeigt SP-Nitro zudem veränderte Absorptionseigenschaften und eine unterschiedliche Stabilisierung der angeregten Form, was dem Verhalten des Farbstoffes in Lösung entspricht. Aufbauend auf diesen Ergebnissen wurde im weiteren Verlauf das strukturell verwandte Spirooxazin 1,3,3-Trimethylindolino-naphthospirooxazin (SP-O) verwendet, welches im Gegensatz zu Spiropyranen eine deutlich erhöhte Photostabilität aufweist. Die lichtinduzierte Schaltung von SP-O kann innerhalb der MOF Poren erfolgen, aber mit vollkommen unterdrückter Photodegradation in MOF-5. Weiterhin zeigt die geschaltete Spezies ebenfalls wirtsabhängige Absorptionsmaxima. Das solvatochrome Verhalten von beiden Farbstoffen, Spiropyran und Spirooxazin, deutet auf unterschiedliche Polaritäten der Wirtsmatrizen hin. Diese wurden mit dem Fluoreszenzfarbstoff 4,5-Dimethoxy-*N*-butylphthalimid (Phth) abschließend bestimmt,

welcher in Abhängigkeit der Polarität des umgebenden Mediums unterschiedliche Emissionsmaxima aufweist und daher als Polaritätssonde verwendet werden kann.

Durch die Einlagerung von Spiropyranen und Spirooxazinen in MOFs wurden so schaltbare Hybridmaterialien dargestellt, die zusätzlich solvatochromes Verhalten aufweisen. Da die Schaltbarkeit innerhalb der MOF Poren und Solvatochromie dem Verhalten der Farbstoffe in Lösung entsprechen, agieren MOFs als „feste Lösungsmittel“ für diese Moleküle. Diese fundamentalen Untersuchungen bilden das Grundgerüst für die zukünftige Darstellung und Entwicklung funktioneller Hybridmaterialien.

## Content

List of Abbreviations.....	III
1 Introduction.....	1
2 Fundamentals.....	3
2.1 Photochromism.....	3
2.1.1 Spiroyrans and Spirooxazines.....	6
2.2 Solvatochromism.....	9
2.3 Hybrid Materials: Incorporation of Dyes in Porous Host Matrices.....	12
2.4 Metal-Organic Frameworks.....	12
2.5 Photoactive Metal-Organic Frameworks.....	14
3 Objective.....	17
4 Results.....	19
4.1 “ICE”-Principle or “How to characterize dye@MOF hybrid materials?”.....	19
4.2 Syntheses and Structure of the Host Materials.....	21
4.2.1 MOF-5.....	21
4.2.2 MIL-68(In) and MIL-68(Ga).....	23
4.2.3 MIL-53(Al).....	27
4.2.4 HKUST-1.....	29
4.2.5 MIL-101(Cr).....	31
4.2.6 MFM-300(Ga <sub>2</sub> ) and fluorinated derivatives.....	32
4.2.7 Zeolite Y.....	33
4.3 Principles of Loading.....	34
4.4 Spiropyran@MOF hybrid materials.....	35
4.4.1 SP-Nitro@MOF hybrid materials.....	36
4.4.2 Other spiropyran@MOF hybrid materials.....	98
4.4.3 Preliminary Conclusions.....	117
4.5 Spirooxazine@MOF hybrid materials.....	119
4.5.1 SP-O@MOF hybrid materials.....	121
4.5.2 Preliminary Conclusions.....	147
4.6 Phthalimide@Porous-Material composites.....	149
4.6.1 Solvent-Dependence of Fluorescence.....	149
4.6.2 4,5-Dimethoxy- <i>N</i> -butylphthalimide.....	151
4.6.3 Phth@Porous-Material composites.....	153

4.6.4	Dilution of Phth in MOF-5 and MIL-68(Ga)	165
4.6.5	Preliminary Conclusions	175
5	Conclusion and Future Perspectives	177
6	Experimental	185
6.1	General Remarks	185
6.2	Syntheses methods	187
6.2.1	Syntheses of Host Materials	187
6.2.2	Syntheses of dye@MOF systems	190
6.3	Characterization	199
6.3.1	Incorporation	199
6.3.2	Composition	201
6.3.3	Effects	202
6.4	Interpretation of Data	205
6.4.1	JANA2006	205
6.4.2	XPS Peak Fit: Determination of Composition	206
6.4.3	Further programs	206
7	References	207
8	Supplement	223
8.1	Host Materials	223
8.2	SP-Nitro@MOF hybrid materials	227
8.3	Further spiropyran@MOF-systems	238
8.3.1	SP@MOF systems	238
8.3.2	SP-N@MOF systems	248
8.3.3	SP-OMe@MOF systems	261
8.4	SP-O@MOF hybrid materials	273
8.5	Phth@MOF/PM systems	279
8.5.1	Dilution of Phth in MOF-5 and MIL-68(Ga)	298

## List of Abbreviations

<i>as</i>	as synthesized
bdc	1,4-benzenedicarboxylate
bptc	biphenyl-3,3',5,5'-tetracarboxylate
btc	1,3,5-benzotricarboxylate
calc.	calculated
C,H,N,S	elemental analysis
D	Debye ( $1 \text{ D} \approx 3.33564 \cdot 10^{-30} \text{ C} \cdot \text{m}$ )
DAE	diarylethene
DTE	dithienylethene
DMF	N,N'-dimethylformamide
EtOH	ethanol
GOF	Goodness of Fit ( <i>Le Bail</i> fit)
h	hour
HKUST	Hong Kong University of Science and Technology
<i>ht</i>	high temperature
IR	infrared
K	Kelvin
<i>lt</i>	low temperature
max	maximum
MC form	merocyanine form
MeOH	methanol
MFM	Manchester Framework Material
MIL	Matériaux de l'Institut Lavoisier
min	minute
MOF	Metal-Organic Framework
NMR	nuclear magnetic resonance
n.s.	not specified
obs.	observed
PDF	pair distribution function
PIZOF	Porous-Interpenetrating Zirconium Organic Framework
Phth	4,5-dimethoxy- <i>N</i> -butylphthalimide

PM	porous material
s	second
SBU	secondary building unit
SP	1,3,3-trimethylindolino-benzopyrylospiran
SP form	spiropyran form
SP-N	1,3,3-trimethylindolino- $\beta$ -naphthopyrylospiran
SP-Nitro	1,3,3- trimethylindolino-6'-nitro-benzopyrylospiran
SP-OMe	1,3,3-trimethylindolino-8'-methoxybenzo-pyrylospiran
SP-O	1,3,3-trimethylindolino-naphthospirooxazine
T	temperature
UV/vis	ultraviolet, visible region of the electromagnetic spectrum
V	volume
$\gamma$	out-of-plane ring bending vibrations or bond bending vibrations
$\delta$	in-plane ring bending vibrations or bond bending vibrations
$\lambda$	wavelength
$\mu$	dipole moment
$\nu$	valence vibration
$\tilde{\nu}$	wavenumber
XPS	X-ray Photoelectron Spectroscopy
XRPD	X-ray Powder Diffraction

# 1 Introduction

There are several natural and synthetic organic molecules featuring reversible transformation upon excitation with electromagnetic radiation - a phenomenon called photochromism.<sup>[1]</sup> These photochromic dyes are attractive candidates for the design of smart materials. The construction of hybrid systems that consist of a switchable unit on the one and a porous matrix, which enables the isomerization processes in solid state, on the other hand, is future directing with respect to potential applications such as data storage devices. Fundamental investigations on such hybrid systems with Metal-Organic Frameworks as the porous host and spiropyrans as well as spirooxazines as the switchable guests are focused on in this work. Moreover, the correlation between the MOF scaffold and the solvents will be shown, since those can be applied as “solid solvents” for photoswitchable molecules concerning two aspects: photochromic and solvatochromic response.

Rhodopsin or visual purple is one example of a natural photoswitchable unit. This compound consists of a protein complex containing the photoactive molecule 11-*Z*-retinal, a vitamin A derivative. Upon absorption of at least one photon of a specific energy 11-*Z*-retinal transforms to all-*E*-retinal.<sup>[2]</sup> The switching process is illustrated in figure 1.1. This photo-transformation triggers a structural change of the whole rhodopsin. Hereby, the process of vision is initiated.

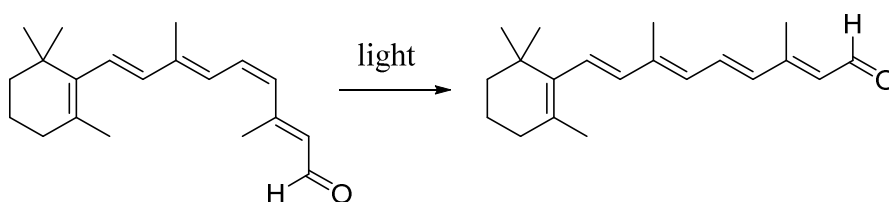


**Figure 1.1** Switching of 11-*Z*-retinal to all-*E*-retinal upon light irradiation.<sup>[2]</sup>

Retinal itself belongs to the class of photochromic compounds and presents one of the organic photoswitches produced by nature. In addition to that, several synthetic switchable dyes exist and are intensively investigated due to their potential applications. The structures and the isomerization processes of important representatives and relevant switches for the present work are illustrated in figure 1.2.<sup>[3]</sup> While the light induced structural changes are comparably small for azobenzenes and diarylethenes as well as dithienylethenes, the reversible transformations of spiropyrans and spirooxazines are profound. They require a certain degree

of sterical freedom, which is not given in the pure solids, but in dissolved state. Therefore, finding ways to achieve photochromic response also in solid state is an obligatory topic to address with regard to possible applications.

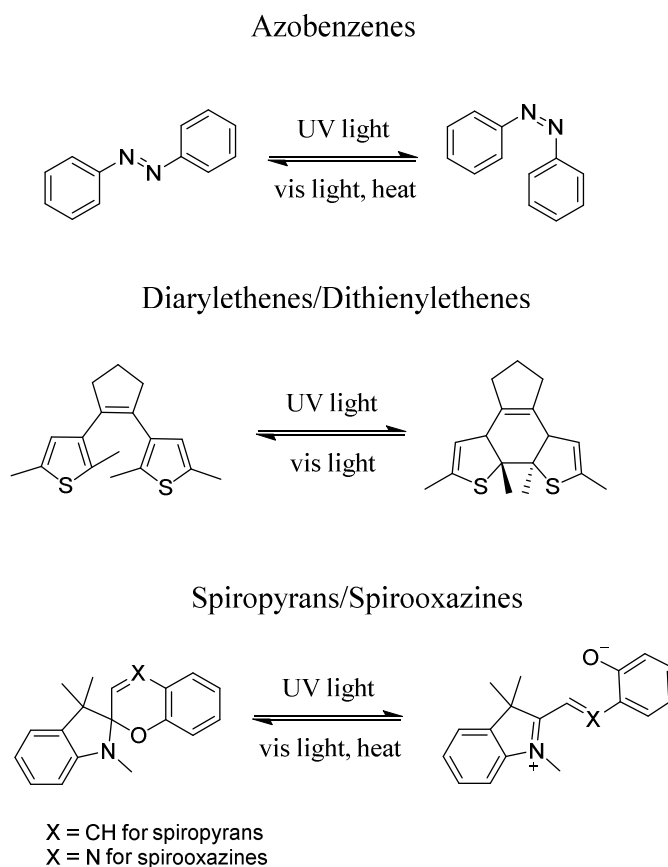


**Figure 1.2** Photoisomerization processes of azobenzene, diarylethenes/dithienylethenes and spiropyran/spirooxazines.

The present work focuses on the two photoswitches spiropyran and spirooxazine and their combination with Metal-Organic Frameworks (MOFs) to form functional hybrid systems with photochromic and solvatochromic response upon UV light irradiation. Bulk materials will be investigated to fundamentally understand occurring host-guest interactions and new properties of the formed dye@MOF materials. The results provide a detailed understanding of such hybrid materials, so that particular properties can be adjusted by specific changes of the host systems and/or guests to systematically design smart functional materials in the future.

## 2 Fundamentals

### 2.1 Photochromism

The phenomenon of photochromism has firstly been discovered by *Fritzsche* in 1867.<sup>[4]</sup> Upon irradiation with sunlight he observed bleaching of an orange colored tetracen solution that retrieved its color overnight. Almost 100 years later in 1950 *Hirshberg* defined photochromism as the reversible transformation of a species between two conformations upon irradiation with electromagnetic radiation of a specific wavelength leading to different absorption properties.<sup>[1]</sup> Reorganization of the ground state is either achieved by light, such molecules are called P-type chromophores, and/or by heat treatment (T-type chromophores).<sup>[3]</sup> If the thermodynamically more stable species A is found to be none or slightly colored, while the irradiated one B is strongly colored, the photochromism is called positive. In this case  $\lambda_{\max}(\text{B})$  of the irradiated moiety is higher than  $\lambda_{\max}(\text{A})$  of the ground state. If  $\lambda_{\max}(\text{A}) > \lambda_{\max}(\text{B})$ , it is called inverse or negative photochromism.<sup>[3]</sup>

Photochromism is found for both organic and inorganic compounds. Since this work focuses on organic switches, only a brief insight is given into photoactive inorganic substances. As an example, the change in coordination of nitrosyl ligands should be mentioned here, which has been intensively studied.<sup>[5-8]</sup> Investigations have been e.g. done by *Schaniel* and co-workers, who observed a change in coordination of NO in  $\text{Na}_2[\text{Fe}(\text{CN})_5\text{NO}] \cdot 2 \text{H}_2\text{O}$  single crystals upon light irradiation.<sup>[9]</sup> These properties were also found when the complex was incorporated in mesoporous silica xerogels.<sup>[10]</sup> The same year, investigations on ruthenium mononitrosyl complexes were presented that showed a structure dependent photochromic response.<sup>[11]</sup>

For organic compounds, the photo response depends on the nature of the photochromic molecule. Different kinds of structural changes occur and vary from simple isomerization processes to transfer reactions and bond breaking. Therefore, these photoswitches are divided into different types, which are listed in the following:

- **E/Z isomerization**

e.g. stilbenes<sup>[12]</sup>, azobenzenes<sup>[13-15]</sup>, photoactive biological molecules, e.g. retinal (see figure 1.1)

- **Ring-opening/-closing (pericyclic reactions)**

e.g. spiropyrans<sup>[16,17]</sup> and spirooxazines<sup>[18]</sup>, diarylethenes<sup>[19]</sup>, fulgides<sup>[20]</sup>

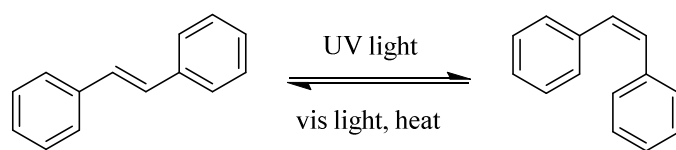
- **Dissociation processes**  
e.g. triphenylmethanes<sup>[21]</sup>
- **Electron-Transfer reactions**  
e.g. viologenes<sup>[22]</sup>
- **Intramolecular hydrogen transfer and group transfer**  
e.g. anilines<sup>[23]</sup>

In figure 2.1.1 the general isomerization processes of the commonly employed photoswitchable compounds stilbenes, azobenzenes, diarylethenes and dithienylethenes, fulgides and spiropyranes as well as spirooxazines are shown.

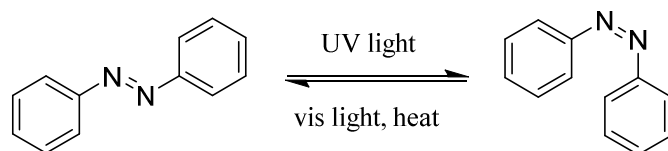
In addition to the different types of photo-induced reactions, the ground and excited state significantly differ in size. For diarylethenes and dithienylethenes these structural changes are rather low, leading to switching properties even in the pure solids (bulk material and single-crystals).<sup>[24]</sup> On the contrary, significant structural changes are observed for e.g. azobenzene and fluorinated derivatives.<sup>[25]</sup> These size differences require a certain degree of sterical freedom for the switching process. The consequences of this are addressed in chapter 2.3.

Photochromic compounds are intensively studied as they are expected to be applied in new functional materials. Since the light induced structural changes cause alterations in absorption properties (color change), dipole moment and/or refractive index<sup>[26]</sup>, photochromic compounds might be used as data storage or memory devices. In 1989 *Rentzepis* and *Parthenopoulos* presented the first spiropyran-based three-dimensional optical data storage device.<sup>[27]</sup> In addition to the employment as data storage memory devices, photochromic compounds are also used as synthetic macromolecular machines: Especially for azobenzene and functionalized derivatives, investigations on the light induced structural changes and movement have been performed. Very recently, *Blegér* and co-workers presented the first fluoro-azobenzene containing hydrogel, whose elasticity is reversibly modulated by green and blue light.<sup>[28]</sup> Further experiments on the contraction and expansion of azobenzene containing moieties have been done.<sup>[29–31]</sup>

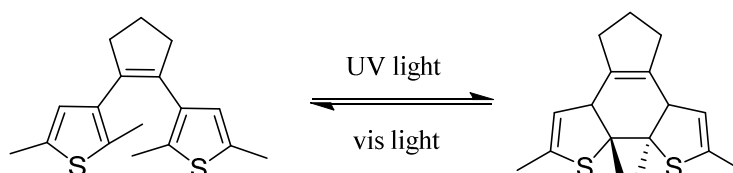
### Stilbenes



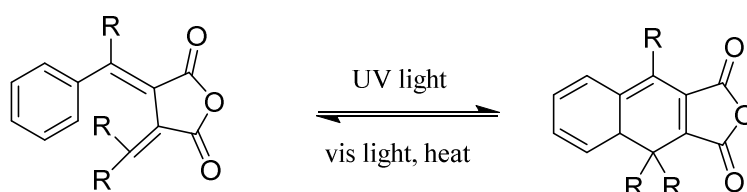
### Azobenzenes



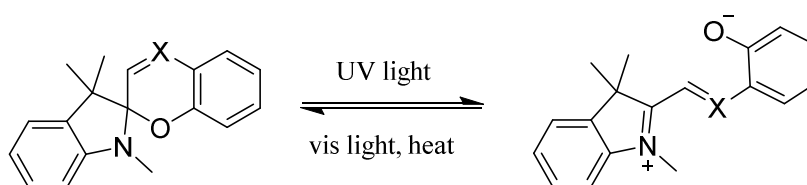
### Diarylethenes/Dithienylethenes



### Fulgides



### Spiropyrans/Spirooxazines



X = CH for spiropyrans  
X = N for spirooxazines

**Figure 2.1.1** Photoisomerization processes of commonly used photochromic compounds. Isomerization is triggered by irradiating the ground state (left) with light of a specific wavelength resulting in the formation of the excited state (right).

The most famous synthetic macromolecular machine has been synthesized by *Feringa* and co-workers in 1999 and was published with the title “Light-driven monodirectional molecular

rotor” in *Nature*.<sup>[32]</sup> For his work on these machines *Feringa* received the Nobel Prize together with *Stoddart* and *Sauvage* (who also worked on molecular machines, but driven by temperature changes) in 2016. The awarding of the Nobel Prize demonstrates the importance of this research area.

Concentrating on the first possible application, data storage or memory devices, the group of spiropyrans and spirooxazines received much attention, since irradiation with light causes significant changes in the absorption spectra of the ground and excited state. In the following chapter these molecules are presented and described in more detail.

### 2.1.1 Spiropyrans and Spirooxazines

Among the many known photochromic molecules, spiropyrans have been intensively investigated since their discovery in 1952 by *Hirshberg* and *Fischer*<sup>[16]</sup> and independently by *Chaudé* and *Rumpf*<sup>[17]</sup>. Spiropyran and spirooxazine dyes consist of two  $\pi$ -electron systems, which are orthogonally oriented with respect to one another. Both, the indoline and the chromene part (for spirooxazines the benzoxazine part) are linked by a tetrahedral spiro-carbon, named  $C_{\text{Spiro}}$ . In figure 2.1.2 the general structure of spiropyrans and spirooxazines is shown.

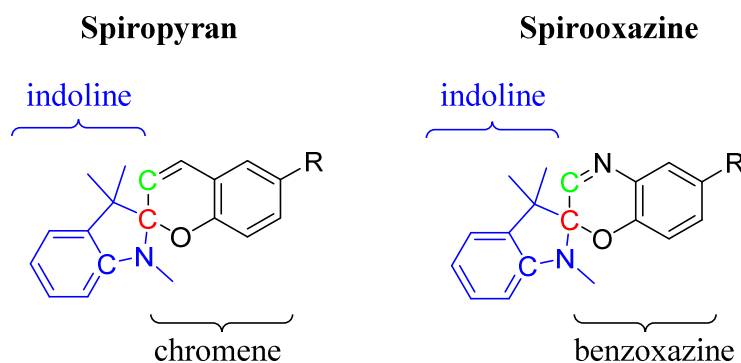


**Figure 2.1.2** Structures of spiropyrans and spirooxazines in their closed SP form. The indoline part is colored in blue, the chromene respectively benzoxazine part is colored in black. The  $C_{\text{Spiro}}$  atom is highlighted in red. The chromene/benzoxazine carbon is highlighted in green, the indoline carbon in blue.

For spiropyrans, the UV/vis spectrum of the closed isomer shows two localized transitions: the first  $\pi-\pi^*$  electronic transition is assigned to the indoline part of the molecule, visible at 272-296 nm. The second one is observed at 323-351 nm and attributed to the chromene

moiety.<sup>[33,34]</sup> By UV light exposure, the spiropyran form (SP form) converts to its merocyanine form (MC form) in a first-order process.<sup>[35]</sup> Initially, the C<sub>Spiro</sub>-O bond is broken, resulting in *Z* merocyanine.<sup>[36–38]</sup> Via rotation around the central C-C bonds<sup>[39,40]</sup> the *E* form of the merocyanine is yielded.<sup>[41,42]</sup> The ring-opening reaction can either be interpreted as a heterolytic C<sub>Spiro</sub>-O bond cleavage or as a 6 $\pi$ -electrocyclization. In both cases, this results in the formation of the zwitterionic or quionidal resonance forms of the merocyanine (see figure 2.1.3). The isomerization of the SP form to its MC form has already been illustrated in figure 2.1.1.

For a better understanding of the isomerization process, the orbitals of the indoline and chromene parts are examined more precisely (since these structural changes are similar in spirooxazines, the following description can also be assigned to spirooxazines). The spiro carbon is covalently bond to the indoline nitrogen and the chromene oxygen. Looking at the nitrogen orbitals, they possess a pyramidal structure with the lone pairs orthogonally to the plane formed by the spiro carbon and the indoline carbon. Furthermore, the nitrogen orbitals are positioned in a dihedral angle of 23-30° with the plane formed by nitrogen, C<sub>Spiro</sub> and the chromene/benzoxazine carbon. Because of this structure, the conjugation between the nitrogen's lone pair and the  $\pi$ -electron system of the benzene ring is reduced. Besides, the oxygen lone pairs occupy an *E* position relative to the one of the nitrogen's lone pair. By this, specific interaction between the lone pair electron orbital of the nitrogen and the antibonding orbital between the spiro carbon and oxygen is caused (anomeric effect). Taking into consideration that the electronegativity of oxygen is greater than the one of nitrogen, the energy level of the lone pairs of nitrogen is higher than the one of oxygen and the antibonding orbital  $\sigma^*_{C-N}$  is higher in energy than  $\sigma^*_{C-O}$ . Hence, the C<sub>Spiro</sub>-N bond is strengthened and the C<sub>Spiro</sub>-O bond is weakened. As a result, photoexcitation by UV light causes cleavage of the already weakened C<sub>Spiro</sub>-O bond.<sup>[43]</sup>

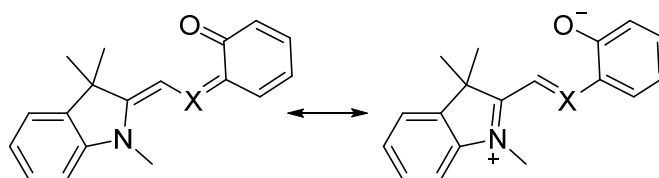


**Figure 2.1.3** Quionidal (left) and zwitterionic (right) form of the merocyanine moiety (X=CH (spiropyrans) and X=N (spirooxazines)).

SP and MC form markedly differ from each other in their physicochemical properties, which makes the spiropyran switch interesting for potential employment in functional materials. The

open MC form shows an extended  $\pi$ -electron conjugation between the indoline and the chromene parts with the ability to absorb photons. Therefore, the merocyanine is strongly colored showing a single delocalized transition in the visible region at  $\lambda_{\text{max}} = 500\text{-}600$  nm in most polar solvents.<sup>[44]</sup> In non-polar solvents, the quionidal form is preferentially stabilized, leading to a bathochromic shift of the MC absorption band.<sup>[38,45]</sup> The exact position of the absorption maximum of MC depends on the polarity of the surrounding environment, which has been intensively studied by *Florea* and co-workers on spiropyran-based microcapillary systems.<sup>[46,47]</sup> Spiroopyrans show negative, spirooxazines both types of solvatochromism. The term of “solvatochromism” will be comprehensively discussed in the following chapter 2.2. Besides the property of solvatochromism, a large difference in dipole moment is observed for SP and MC. The charge separation in MC results in a large electric dipole moment in the range of 14-18 D, whereas SP shows a dipole moment of 4-6 D.<sup>[48,49]</sup> Furthermore, SP and MC significantly differ in their emission properties. While ring-opening results in an intense emission band at  $\lambda_{\text{max}} \approx 650$  nm, the SP form does not exhibit any fluorescence, as the extended  $\pi$ -conjugation is broken by reformation of the pyran-ring.<sup>[50]</sup>

As a fourth difference, the MC form is markedly more basic than SP and can easily be protonated. The protonation results in the protonated merocyanine  $\text{MCH}^+$  with a characteristic absorption band at  $\lambda \approx 420$  nm. This has been studied by *García* and co-workers by photocontrolling the phase portioning of spiropyranes at different pH-values.<sup>[51]</sup>

Due to its molecular structure, merocyanines have a strong tendency to associate into aggregates. This is predominantly driven by dipole-dipole interactions along with the  $\pi$ - $\pi$ -stacking. Arrangement occurs either in a parallel or anti-parallel fashion: “head-to-tail” aggregation (parallel) stacking causes the formation of so-called *J*-aggregates, whereas “side-to-side” aggregation yields *H*-aggregates. Both types can easily be identified in the absorption spectra, since *J*-aggregates show red-shifted (bathochromic) and *H*-aggregates blue-shifted (hypsochromic) absorption. Both types of aggregates are known and studied for MCs.<sup>[52-60]</sup> Merocyanine aggregation stabilizes the open isomer and hence strongly retards or even completely blocks the reversion to the closed SP form.

Even though the isomerization processes and physicochemical properties are almost similar, spiropyranes and spirooxazines differ from each other. Due to their improved performance in comparison to spiropyranes, the synthesis and studies on spirooxazines received much attention in recent years.<sup>[61,62]</sup> Spirooxazines show a high durability with respect to

photoexcitation. For spiropyran, prolonged UV light irradiation results in photodegradation predominantly via a bimolecular process, which involves the triplet excited state of the spiropyran moiety.<sup>[63]</sup> Bimolecular processes are related to the concentration of spiropyran molecules. By immobilization of single dyes on e.g. supports those processes are easily suppressed.<sup>[64]</sup> *Diamond* and co-workers observed an increased fatigue resistance of spiropyran moieties being immobilized in comparison to the ones in dissolved state.<sup>[65]</sup>

In comparison to other photoswitchable compounds, spirooxazines and spiropyran are widely studied, since they can be reversibly activated by several stimuli, such as light, metal-ions<sup>[66-74]</sup>, redox-potential<sup>[75,76]</sup> or pH value<sup>[77-82]</sup>. Due to this widespread response, spiropyran and especially tethered spiropyran have been used for several applications: e.g. photocontrolled enzymatic activity<sup>[83]</sup> and nanoparticle solubility<sup>[84]</sup>, for photocontrolled release of medical compounds<sup>[85]</sup> or smart electrodes<sup>[86]</sup>.

## 2.2 Solvatochromism

Especially for investigations on spiropyran and spirooxazines the term of *solvatochromism* has to be defined more precisely. *Reichardt* has comprehensively dealt with solvent effects in organic chemistry, hence his definitions are used here.<sup>[87]</sup>

The phenomenon of solvatochromism occurs, if a molecule dissolved in solvents of different polarity shows changes in its absorption band with respect to position, shape and intensity. Here, only changes in position are examined. Red-shifted (bathochromic) absorption with increasing polarity of the solvent is referred to as positive, blue-shifted (hypsochromic) as negative solvatochromism.

Alterations in the absorption spectra are a result of solute-solvent interactions, such as dipole-dipole interactions, hydrogen bonding etc. The occurring interaction forces modify the energy gap between the ground and excited state of the chromophore. But how exactly does that happen?

Primarily, the effect on the spectra is dependent on the dye and its type of transition. In this case, the electronic transitions of particular interest are  $\pi \rightarrow \pi^*$  and  $n \rightarrow \pi^*$ , as well as charge-transfer absorptions. As already described in 2.1.1, spiropyran and spirooxazines form the so-called merocyanine form upon irradiation with UV light. Merocyanines belong to the intramolecularly ionic meropolymethine dyes. According to *Dähne*<sup>[88-90]</sup>, organic compounds containing a chromophore with  $\pi \rightarrow \pi^*$  transitions are subdivided into three different groups:

aromatic compounds, polyenes (and polyynes) and polymethines. In contrast to aromatic compounds and polyenes, polymethines are conjugated structures with equal bond lengths and charge distribution along the methine chain. Meropolymethine dyes are located between polyenes and polymethines.<sup>[91,92]</sup> Those compounds, which merocyanines belong to, contain an electron-donating group A (for spiropyrans and spirooxazines this is the N-atom of the indoline part), which is linked by a conjugated system B to the electron accepting group C ( $O_{\text{Spiro}}$  atom of the chromene/benzoxazine part of the spiropyrans and spirooxazines, respectively). This results in two mesomeric electronic states:  $A-B-C \leftrightarrow A^+-B-C^-$ . Obviously, the electronic transition is an intramolecular charge-transfer between the electron donating group A and the electron accepting group C. For this reason, dipole moments of the ground state and excited state differ significantly. Experimental investigations have shown that solvatochromism is mainly found for those substances, whose electronic transitions cause a different charge distribution between the ground and excited state. Concerning spiropyrans and spirooxazines, irradiation with UV light causes a change in electron distribution and thus a formation of a dipolar solute. Hence, two intramolecular electronic transitions can be distinguished: The species being dissolved in either a 1) non-polar or 2) polar solvent.<sup>[93-95]</sup>

### 1) **Non-polar solvent**

A non-polar solvent has no significant dipole moment. Therefore, solvation forces are dipole induced dipoles or dispersion forces. Since the dipole moment of the excited state increases compared to the ground state, the *Franck-Condon* excited state<sup>[96,97]</sup> is more solvated by dipole-solvent polarization, resulting in red-shifted absorption.

### 2) **Polar solvent**

Since both the solute and solvent are dipolar, solvation of the non-irradiated state is caused by dipole-interaction forces and an oriented solvent cage is formed around the solute. For spiropyrans and spirooxazines the electronic transitions increase the dipole moment, resulting in a *Franck-Condon* excited state, which is surrounded by partly oriented solvent molecules. To achieve a better stabilization of the excited state, orientation of the solvent molecules slightly changes, leading to a bathochromic shift in the absorption spectra. For charge-transfer transitions, like in spiropyrans and spirooxazines, the excited state is not sufficiently stabilized by the formed solvent cage. The energy ground state is lowered along with increasing polarity of the solvent, causing a hypsochromic shift in the absorption spectra.

In Figure 2.2.1 the influence of the solvent's polarity on the solute's ground and excited state is illustrated.

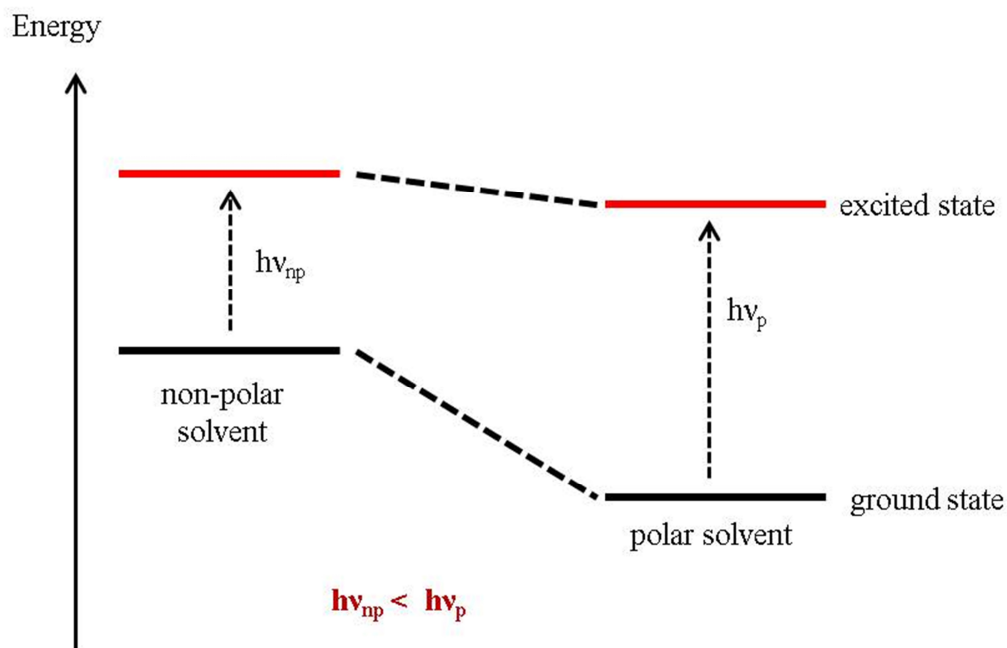


**Figure 2.2.1** Schematic illustration of the electronic transition energy in relation to the solvent polarity for spiropyrans. Non-polar is defined as **np**, whereas polar is abbreviated with **p**. The illustration was adapted from *S. Scarmagnani*.<sup>[98]</sup>

Spiropyrans undergo negative photochromism, since an increase in solvent polarity causes blue-shifted absorption bands: hence, the electronic structure of the excited species shifts from a polymethine-like state to a polyene-like state by increasing the solvent's polarity.<sup>[87,99]</sup> For spirooxazines, both types of solvatochromism have been observed, mainly related to the substitution of the benzoxazine ring.<sup>[100]</sup>

Both, photochromic and solvatochromic, properties are mostly observed in solution, but not in the pure solids. In most cases, the structural reorganization upon light irradiation requires a certain degree of sterical freedom, which is not given in the pure pristine solids. This is a major drawback for possible applications. Therefore, encapsulation of photoswitchable dye molecules into a (porous) host matrix seems to offer a great potential, since the single molecules are separated from each other. Thus, light induced transformations should be enabled. The following chapter 2.3 will deal with those "Hybrid Materials".

### 2.3 Hybrid Materials: Incorporation of Dyes in Porous Host Matrices

Most of the investigations on the photochromic properties of switchable molecules have been performed in solution, rather than in the pristine solid. Especially for spiropyrans with substantial light induced structural changes, investigations have mainly been conducted in solution<sup>[101–104]</sup>, embedded in polymers<sup>[27,33,105–107]</sup> or nanoporous cages<sup>[108,109]</sup>. By the embedment into a crystalline host matrix, especially characterization via powder diffraction methods and analysis of the occurring host-guest interactions would be possible. To meet this requirement, crystalline porous host materials have to be employed. About 20 years ago, *Caro* and co-workers started to implement the photoactive moiety as a guest molecule into a porous host matrix (porous material, PM).<sup>[110]</sup> The authors embedded azobenzene into nanoporous zeolites, forming a photoswitch@PM composite material for the first time. In addition to further synthesized azobenzene@zeolite materials<sup>[111,112]</sup>, spiropyran molecules were also incorporated into different zeolite structures<sup>[113–115]</sup>. In all cases, photochromic properties of the switchable part were observed, making these hybrid compounds promising candidates for the development of functional materials. In comparison to dye@polymer systems, the modification and functionalization of zeolites is rather limited. Hence, porous materials with a high crystallinity combined with the ability to be systematically functionalized are obligatory. Both aspects are realized in Metal-Organic Frameworks (MOFs), which are introduced in the next chapter.

### 2.4 Metal-Organic Frameworks

Since the publication of MOF-5 by *Yaghi* and co-workers in 1999<sup>[116]</sup>, the interest in Metal-Organic Frameworks increased rapidly<sup>[117]</sup>. MOFs are hybrid materials, consisting of inorganic nodes, mostly metal cations or metal-oxo-clusters, which are linked by organic linker molecules with at least two functional groups, forming a two or three dimensional framework with potential voids.<sup>[118]</sup> These compounds were already described before 1999<sup>[119–123]</sup>, but MOF-5 somehow gave the *kick-start* to this research area. The schematic construction of MOFs will be exemplarily described for MOF-5 (see figure 2.4.1):  $Zn_4O^{6+}$  cluster and the carboxylate function of the terephthalate anion form the Secondary Building Unit (SBU). Extended into three dimensions, the framework of MOF-5 with accessible voids is preserved.

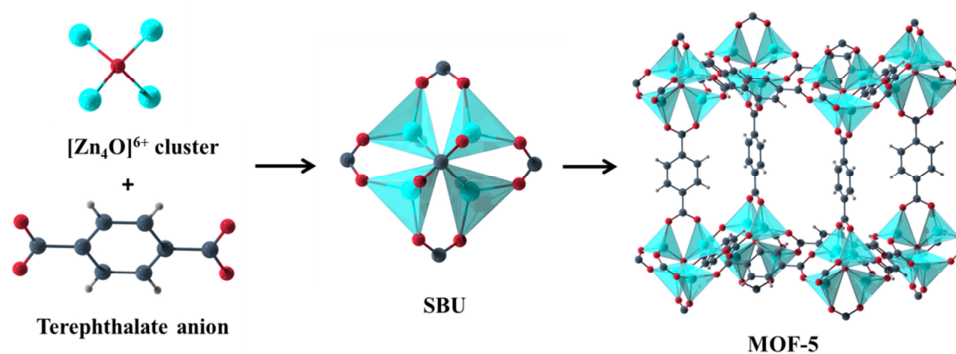


**Figure 2.4.1** Schematic construction of MOF-5 from  $Zn_4O^{6+}$  clusters and terephthalate anions forming a 3 D framework structure with accessible voids. Crystallographic data were taken from *Yaghi* 1999<sup>[116]</sup>. Color code: turquoise: zinc cations, red: oxygen anions, grey: carbon, white: hydrogen.

Especially because of their potential voids, MOFs are extremely promising candidates for both industry and science. If accessible, these voids offer various applications e.g. gas adsorption<sup>[124,125]</sup>, separation of gases<sup>[126,127]</sup> and liquids<sup>[127–129]</sup>, heterogeneous catalysis<sup>[130]</sup>, drug encapsulation and delivery<sup>[131,132]</sup> and electronic devices<sup>[133,134]</sup>. Even structure elucidation of organic substances via embedment into the MOF framework has been shown by *Fujita* and co-workers, who established this as “crystalline sponge method”.<sup>[135–142]</sup>

The diverse applicabilities are the result of the structural design of MOFs. The linker molecules as well as the metal nodes can be variably designed. *Yaghi* and co-workers showed the concept of “crystal engineering” by synthesizing isoreticular MOFs (IR-MOFs), which show similar network-topologies by simultaneous elongation of the linker molecules.<sup>[143]</sup> That way, pore-diameters of up to 98 Å were yielded.<sup>[144]</sup> However, further elongation of the linker molecule does not always lead to larger pores, but to interpenetration, which has been observed e.g. for PIZOFs (porous interpenetrated zirconium-organic frameworks).<sup>[145]</sup>

The systematical design and functionalization of MOF pores is an interesting feature of this class of materials. As a result of modification, the accessible voids possess different physicochemical environments, which make them promising candidates with respect to control guest uptake and host-guest interactions. While most applications focus on gas adsorption and storage, combining MOFs and photoswitches has rarely been addressed. This seems somewhat surprising, since MOFs appear to be ideal host matrices for such molecules. The following section covers these photoactive metal-organic frameworks.

## 2.5 Photoactive Metal-Organic Frameworks

When talking about photoactive Metal-Organic Frameworks, it is obligatory to subdivide the types of the photoactive-part-introduction. Recently, *Gascon* and co-workers presented a review on this topic, assigning the photoactive part either being a part of the framework as *intrinsic* or being a guest molecule as *extrinsic* introduction to the MOF.<sup>[146]</sup> In general, three options can be distinguished in-between and will be shortly described in the following:

### 1) Intrinsic introduction

- a) the photoactive part is part of the linker backbone
- b) the photoactive part is substituent of the linker

### 2) Extrinsic introduction

The photochromic dye is embedded as guest molecule inside the MOF pores

The intrinsic introduction is subdivided into two ways. Firstly, the photoswitchable moiety is part of the linker backbone. As already described in chapter 2.1, light irradiation causes large structural changes, hence e.g. the *E/Z* isomerization is sterically hindered<sup>[147]</sup> or may cause bond breaking and degradation of the framework<sup>[148,149]</sup>. Secondly, the switching molecule is introduced as a substituent of the linker backbone.<sup>[150]</sup> This approach has been realized both for bulk materials and thin films.<sup>[151,152]</sup> It has been demonstrated that the uptake amount of gases could be controlled by light.<sup>[151,153]</sup> Particularly for thin films with azobenzene side groups, the diffusion properties<sup>[154,155]</sup>, permeation and separation factor of membranes<sup>[156]</sup> and even the proton-conduction of guest molecules<sup>[157]</sup> is remote-controlled by light. Unfortunately, isomerization processes are hindered in some cases.<sup>[158]</sup> Besides, the high synthetic effort to prepare such functionalized linker molecules still remains a major drawback and thus limits the broad applications of such photoactive MOFs.

Via extrinsic introduction, the photoactive moieties are embedded as guest molecules inside the MOF pores. This strategy is pioneering, as the mobility triggers a significantly more complex situation than the guest being fixed at the MOF scaffold. For instance, the degree of filling (guest-guest interactions) and the physicochemical environment given by the MOF voids are considered to influence the preferable orientation and configuration of the guest molecule and the photo-stationary state (PSS). Understanding these photoswitch@MOF composite materials is subject of the present work by mainly focusing on spiropyrans and

spirooxazines. Several investigations on such systems have already been done and will be presented shortly.

The first switch@MOF system was synthesized by *Fujita* and co-workers in 2010, who embedded stilbene (see figure 2.1.1) into the porous host  $[\{(ZnI_2)_3(C_{18}H_{12}N_6)_2\} \cdot x(C_6H_5NO_2)]_n$  with the tris(4-pyridyl)triazine ligand by soaking the MOF in a solution of the dye.<sup>[159]</sup> Notably, the resulting *Z*-stilbene@MOF system in cyclohexane showed a nearly 100% photoconversion without the formation of any photo-by-products. Two years later, in 2012, *Kitagawa* and co-workers not only embedded azobenzene as a switching molecule into the flexible host  $[(Zn_2(\text{terephthalate})_2(\text{triethylenediamine}))_n]$  (DMOF-1)<sup>[160]</sup> by gas phase loading, but also observed light induced guest-to-host structural transmissions, which significantly affected gas uptake and release.<sup>[161]</sup> In further studies, *Kitagawa* and co-workers presented a photoresponsive reversible encapsulation-release system with functionalized azobenzene.<sup>[162]</sup> Upon irradiation with UV light, the authors observed guest-release when dissolved in ethanol solution leading to an increased concentration of the *Z* isomer in the supernatant solution. By visible light irradiation this process was reversed. In the workgroup of *Ruschewitz* several azobenzenes as guest moiety were investigated as well, but with respect to non-flexible MOFs.<sup>[163,164]</sup> Particularly, the influence of the different host matrices, namely MOF-5<sup>[116]</sup>, MIL-68(In/Ga)<sup>[165]</sup> and MIL-53(Al<sup>[166]</sup>/Ga<sup>[167]</sup>) on the photochromic properties of azobenzene and fluorinated derivatives was in the focus of their research. Interestingly, switching was found to be more efficient for some of the azobenzene compounds, whereas for MIL-53 as host matrix light triggered changes were not observed. By means of high resolution synchrotron powder diffraction the crystal structure of this composite material was determined pointing to the reason of inhibited photoswitching: because of the dense packing inside the MOF pore the isomerization of azobenzene was sterically hindered. The first insight into structure-property relationships of a guest@MOF system was given here. The authors showed that consequently, size and shape of the host pore as well as the orientation and the amount of the embedded guest molecules within the pores has a marked impact on the resulting optical properties of the photoswitch@MOF system.

Even though azobenzene is an interesting candidate for the formation of such photoswitch@MOF systems, a major drawback is the minor difference in the absorption spectra of the *E* and *Z* isomers. Hence, typically a mixture of both isomers is obtained. Furthermore, azobenzenes belong to the class of T-type chromophores, which are sensitive to temperature changes.

In order to achieve both thermal stability and a significant difference in absorption of the ground and excited state, *Benedict* and co-workers embedded a diarylethene (see figure 2.1.1) into single crystals of DMOF-1<sup>[160]</sup> by melting the dye molecule, forming a photochromic and thermally stable functional material.<sup>[168]</sup>

Investigations of photoswitch@MOF composites were both done in bulk materials and thin films. As photoactive part in those thin films/membranes azobenzenes<sup>[169,170]</sup> were used with only one exception: *Zhu* and co-workers prepared thin MOF films of type JUC-120 loaded with a spiropyran by microwave-assisted synthesis.<sup>[171]</sup> The inclusion of the photoswitch in the MOF material was realized by adding the spiropyran (1-(2-hydroxyethyl)-3,3-dimethylindoline-6'-nitrobenzospiropyran) molecules to the precursor solution prior to the MOF synthesis. Remarkably, the embedded spiropyran showed inverse photochromism and a strong red color, hinting towards a polar environment inside the MOF pore.

The work of *Zhu* and co-workers is the only one so far dealing with the inclusion of spiropyrans to yield a spiropyran@MOF hybrid system. This is somewhat surprising, as the photochromic und solvatochromic properties of spiropyrans could be easily tuned to build smart composite materials, responding towards changing physicochemical environments given by the MOF pores. In addition, spirooxazine@MOF systems were not addressed at all. In the *Staatsexamensarbeit*<sup>[172]</sup> prior to this thesis preliminary experiments on the incorporation of one spiropyran into different MOFs have been conducted. Ongoing studies with further spiropyrans and spirooxazines and a more detailed understanding of the formed composite materials will be part of the presented work.

### 3 Objective

In previous investigations several guest molecules such as azobenzenes or diarylethenes and dithienylethenes were used for the formation of dye@MOF composite materials. This has been comprehensively elucidated before. Nevertheless, embedment of a dye molecule, which exhibits a combined photochromic and solvatochromic response, has not been conducted so far. By using a guest with both properties (photochromism and solvatochromism) two aspects can be focused on: switching of the photoactive molecule inside the host scaffold on the one and determination of the physicochemical properties of the crystalline porous host on the other hand. Investigations on the influence on the electronic structure of the embedded dye molecule by the surrounding medium have mainly been performed with solvents, but not with crystalline porous host materials yet.

Ideal candidates for such investigations are spiropyrans: light-induced transformation is accompanied by a drastic change in the absorption properties, which can be simply followed. Additionally, spiropyrans show negative solvatochromism with increasing polarity of the environment positioned in. Hence, the surrounding medium has a profound impact on the electronic structure of the excited state.

In previous studies in the workgroup by *D. Hermann* on azobenzene and fluorinated derivatives as photoactive guests, Metal-Organic Frameworks (MOFs) were used as host matrices.<sup>[164]</sup> MOFs are preferable porous materials, since they are crystalline and can be systematically functionalized, which is an interesting feature with respect to changing the physicochemical environment of the scaffold. Therefore, MOFs will be used as host materials in the presented studies. Nevertheless, the frameworks have to meet the following requirements:

- the entrance window of the pores has to be big enough for the guest molecule to enter the MOF material
- an adequate pore size is obligatory to ensure the light induced isomerization process of the switchable dye molecule inside the host lattice
- absorption bands of the host und guest must not overlap

Taking these requirements into account, suitable MOFs were chosen for investigations on photochromic and solvatochromic response of different spiropyrans in a first step, which will be introduced in chapter 4.2. In a second step, a structurally related spirooxazine was taken as another photo- and solvatochromic guest molecule, but with an increased resistance towards photodegradation. Last, embedment of a completely different photoactive dye, namely a phthalimide, was applied. These dyes exhibit high fluorescence sensitivity towards polarity alterations, which could be a useful tool for determining the polarity of the MOF matrices.

By the combination of dye and MOF the following fundamental questions are addressed:

- Do spiropyrans/spirooxazines show photochromic properties inside the different host lattices? Which type of photochromism is present?
- Do spiropyrans/spirooxazines exhibit solvatochromic behavior depending on the used MOF host?
- Does the respective host matrix influence the stability of either the ground or excited state?
- Do spiropyrans/spirooxazines associate into aggregates within the respective MOFs matrices?
- Are spiropyrans/spirooxazines photostable inside the MOFs matrices upon repetitive and prolonged UV light exposure?
- Do different MOF matrices exhibit varying physicochemical environments with changing polarity?

In order to answer these questions, a precise and logical pathway for the characterization of such dye@MOF hybrid systems has to be applied. Thereupon, an approach was established to gradually provide a complete picture and understanding of the hybrid dye@MOF functional systems. Before discussing the results on different photoactive-dye@MOF systems following this approach, this so-called “ICE”-principle is introduced.

## 4 Results

### 4.1 “ICE”-Principle or “How to characterize dye@MOF hybrid materials?”

In order to fully understand a dye@MOF hybrid system the characterization has to follow a logical and precise pathway. To meet this requirement, a principle was set up, which addresses the following questions:

- 1) Has the incorporation of the dye been successful?
- 2) What is the composition of the dye@MOF system?
- 3) Does the combination of a MOF and a dye show new properties? What are the occurring effects?

First, successful embedment of the dye molecule can be confirmed by X-ray Powder Diffraction (XRPD). The electron density inside the cages of the porous materials changes upon guest incorporation. This results in intensity alterations of the peaks compared to the pure host material, but not in a change of the peak positions, since the integrity of the frameworks remains. Therefore, a modulation in intensities of the diffraction pattern shows successful incorporation of the dye molecule. Obviously, possible surface adsorption of the guest has to be taken into consideration. However, this would be noticeable as additional peaks in the diffraction pattern. Hence, XRPD represents an adequate method for the confirmation of embedment.

Second, the composition of the hybrid materials can be investigated by means of elemental analysis (CHNS) and X-ray Photoelectron Spectroscopy (XPS). The knowledge of the dye@MOF composition is essential with regard to correctly interpreting possible host-guest and guest-guest interactions. In a previous work of the working group elemental analysis was the method of choice to investigate the amount of embedded guest molecules.<sup>[164]</sup> Here, a second method, XPS, was applied and found to be more sensitive for especially low guest concentrations. For elemental analyses, the values of carbon, nitrogen and hydrogen are experimentally determined. Unfortunately, carbon and hydrogen are both present in the host material and guest molecule. Thus, XPS was mainly used in this work. As nitrogen atoms are only found in the guest, but not in the MOF framework, the nitrogen intensities of typical XPS signals can be compared with the intensities of XPS signals of the respective metal cations of the MOF host. Furthermore, XPS additionally confirms the successful incorporation of the guest, since the influence of a surrounding matrix results in broadening of

the N1s peak. Therefore, determining the composition by means of XPS is considered to be most reliable.

Third, the occurring effects of the guest incorporation have to be investigated. Depending on the guest molecule, different analytical focal points can be set. With respect to photoactive dyes, three methods were applied in this work: UV/vis spectroscopy, IR spectroscopy and fluorescence spectroscopy.

For spiropyrans and spirooxazines the following questions are addressed by UV/vis spectroscopic measurements:

- Is switching of the photochromic compound possible and reversible?
- Does the surrounding host matrix influence the absorption properties of the embedded dye molecule (with respect to solvatochromism and formation of aggregates)?
- Does photodegradation occur?

IR spectroscopy was applied as a second method to follow the switching processes and to assign occurring host-guest and guest-guest interactions more precisely. In addition to spiropyrans and spirooxazines, fluorescent phthalimides were used to form hybrid materials. Investigations of the effects of these materials were done by fluorescence spectroscopy, mainly focusing on the following questions:

- Are the fluorescent properties maintained inside the different host materials?
- Does the phthalimide show shifted emission spectra depending on the used host material?

Other methods, which have not been used in this work, are solid state NMR spectroscopy (nuclear magnetic resonance spectroscopy) and PDF (pair distribution function). Both methods offer the possibility to determine positions of the guest molecule inside the host matrix. Based on these methods, a more detailed understanding of occurring properties is expected.

Overall, the principle was set up to offer a logical pathway for characterization. The questions at the beginning of this chapter refer to the respective points **In**corporation, **C**omposition and **E**ffects, which are eponymous for introducing the **ICE**-Principle as a methodical approach for guest@MOF hybrid material characterization.

## 4.2 Syntheses and Structure of the Host Materials

For the formation of dye@MOF/PM composite materials, all used porous compounds have to meet the following requirements: the guest molecules have to fit into the pores and light induced isomerization must be possible inside these pores. Additionally, the absorption maxima of the respective guest molecule should not overlap with the ones of the used host materials. Therefore, ten host matrices were chosen, which are presented with regard to structure and synthesis procedures in the following.

### 4.2.1 MOF-5

MOF-5 has been presented in 1999 by *Yaghi* and co-workers<sup>[116]</sup> with the sum formula  $\text{Zn}_4\text{O}(\text{bdc})_3$ . When looking at the exact structure of the SBU, a central oxygen anion is surrounded by four  $\text{Zn}^{2+}$  cations in a tetrahedral coordination. The resulting tetrahedron itself possesses six edges, which are capped by carboxylate function of the terephthalate linker molecule. This leads to an octahedral coordination and a  $4^6$  network is formed, which is shown in figure 4.2.1. By capping of the  $[\text{Zn}_4\text{O}]^{6+}$  tetrahedrons and the planar structure of the linker molecule, two pores of a different size are formed. The bigger one reveals a pore diameter of  $\sim 18 \text{ \AA}$  (distance between two  $\text{Zn}^{2+}$  cations facing each other, taking the *van-der-Waals* radius into account, distances were estimated with *Diamond 4.4*<sup>[173]</sup>) and an entrance window of  $\sim 11 \text{ \AA}$  respectively  $\sim 16 \text{ \AA}$  (distance between two  $\text{Zn}^{2+}$  cations/ hydrogen-atoms of two terephthalate linker molecules facing each other, minus *van-der-Waals* radii).

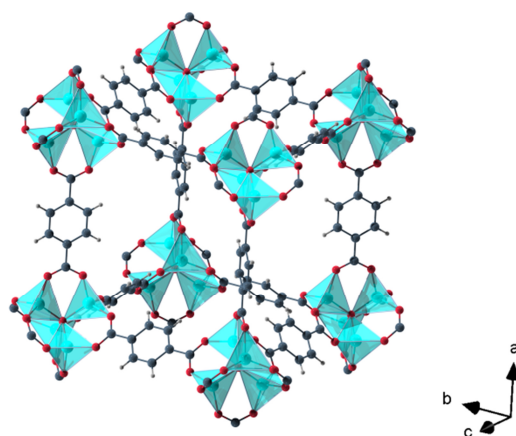


**Figure 4.2.1** Part of the crystal structure of MOF-5.<sup>[116]</sup> The twisting of the linker molecule results in two pores with different sizes; the smaller one is illustrated here. Color code: turquoise: zinc cations, red: oxygen anions, grey: carbon, white: hydrogen.

MOF-5 crystallizes in the cubic space group  $Fm\bar{3}m$  (No. 225). MOF-5 is either synthesized by solvothermal treatment<sup>[116]</sup> ( $Zn(NO_3)_2$  and terephthalic acid in DEF) or by a simple stirring method<sup>[174]</sup>. In the present thesis, MOF-5 was synthesized by the second method: Terephthalic acid and trimethylamine were dissolved in DMF and zinc acetate was dissolved in DMF. While stirring, the zinc salt solution was added dropwise to the organic solution. The mixture was stirred for a few hours. The precipitate was filtered and immersed in DMF overnight. It was then filtered again and immersed in  $CHCl_3$  which was changed several times during the synthesis procedure. Before the product was stored under argon atmosphere to prevent adsorption of moisture and decomposition, the white precipitate was heated at 120 °C and a reduced pressure overnight to remove all solvent molecules. The phase purity was checked by XRPD and compared with the pattern calculated from the literature known crystal structure of MOF-5<sup>[116]</sup>, which is in good agreement with that of the synthesized product. The powder pattern of MOF-5 with the theoretical diffraction pattern is shown in figure 4.2.2. Furthermore, technical MOF-5 was used, which was provided by *BASF* as *BASOLITE™ Z*. The diffraction pattern is found in figure 8.1.1 in the supplement.

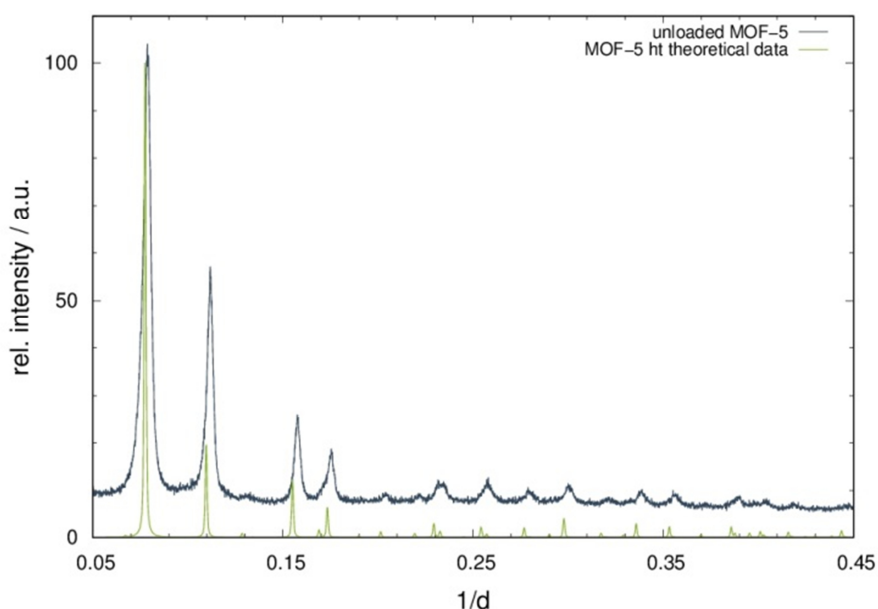


**Figure 4.2.2** XRPD pattern of MOF-5 (blue-grey), measured at 298 K (*Stoe StadiP*:  $\lambda = 1.54 \text{ \AA}$ ) in comparison to theoretical data of MOF-5 (green). A small offset along y (+4%) was applied in order to enhance readability.

## 4.2.2 MIL-68(In) and MIL-68(Ga)

MIL-68(In) and MIL-68(Ga) have been presented by Férey and co-workers in 2008.<sup>[165]</sup> Both compounds feature the general molecular formula  $M^{III}(OH)(bdc)$  with  $M = \text{In}, \text{Ga}$ . The formed network is comparable to a *Kagomé*-like lattice with chains of octahedral units, which are connected by the terephthalate linker molecules. This linkage provides channels with trigonal and hexagonal shape. The exact structure is described subsequently:

Metal-centered octahedra with the composition  $\text{MO}_4(\text{OH})_2$  are linked to each other through the terephthalate ligands. The octahedral units are *E*-connected by hydroxyl groups generating infinite chains, which are illustrated in figure 4.2.3.

In addition, adjacent octahedra are linked through the carboxylate functions, which results in tilted chains, a motif also encountered for e.g. MIL-53<sup>[166]</sup>. Considering the octahedra as nodes, a *Kagomé*-topology is provided composed of hexagonal rings surrounded by six trigonal rings. In figure 4.2.4 the extended unit cell of MIL-68(Ga) with the typical linking pattern is shown. Both MIL-68(Ga) and MIL-68(In) crystallize isotypically in the orthorhombic space group *Cmcm* (No. 63).

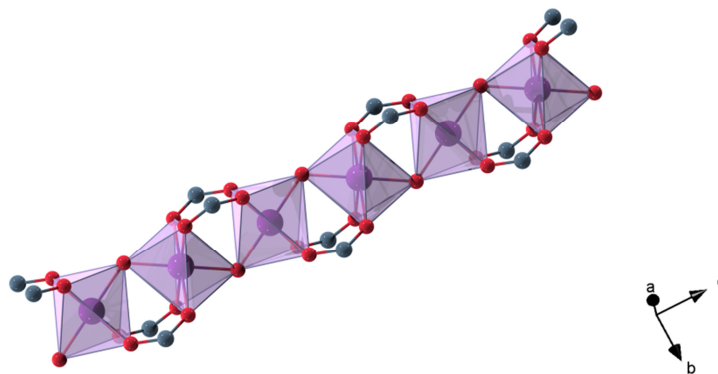


**Figure 4.2.3** Metal-centered octahedra linked to each other by terephthalic acid forming an infinite chain. Crystallographic data were taken from Férey and co-workers.<sup>[165]</sup> Color code: purple: gallium cations; red: oxygen anions; grey: carbon. For clarity, hydrogen cations are omitted.

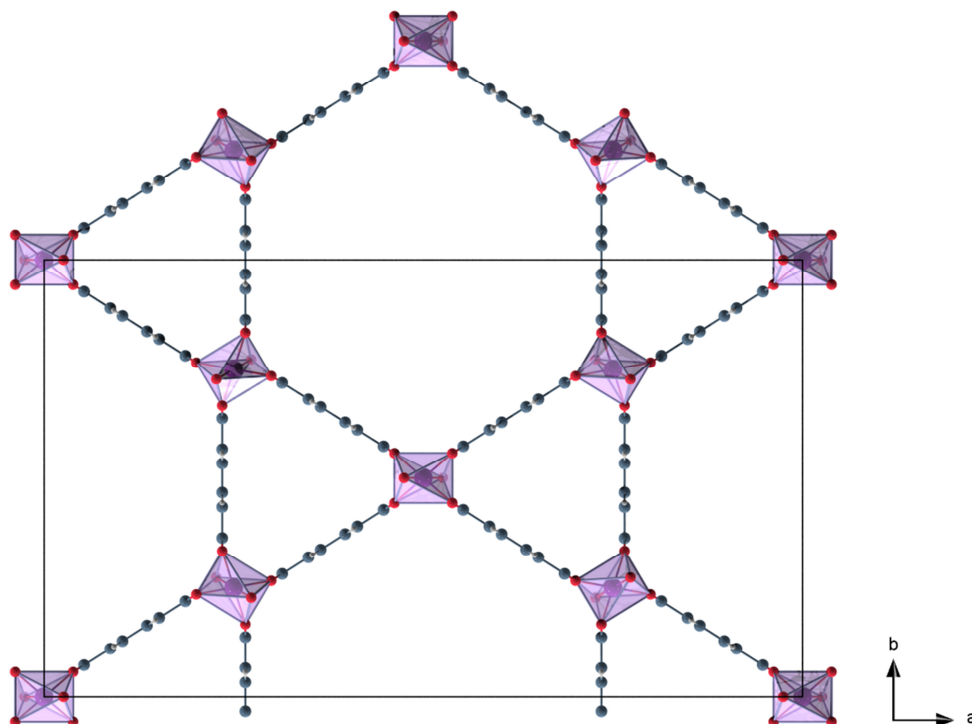


**Figure 4.2.4** Extended unit cell of MIL-68(Ga) with view along the [001]-axis. The trigonal and hexagonal pores are oriented parallel to this axis. Crystallographic data were taken from Férey and co-workers.<sup>[165]</sup> Color code: purple: gallium cations; red: oxygen anions; grey: carbon. For clarity, hydrogen cations are omitted.

For a typical synthesis, the metal nitrate and terephthalic acid were converted solvothermally in DMF.<sup>[165]</sup> The obtained precipitate is referred to as the *as* form, with “*as*” defined as *as synthesized*. For MIL-68 *as* DMF is apparent inside the MOF pores, which is removed by heating the MOF in air, resulting in the irreversible expulsion of the inserted DMF molecules. In spite of the hydrophobic properties of the resulting DMF free MOF, water molecules are reversibly absorbed forming the *lt* form, with “*lt*” defined as *low temperature*. When MIL-68 *lt* is heated at 100 °C and reduced pressure, before being stored under argon atmosphere, the *ht* form is obtained, with “*ht*” defined as *high temperature*. MIL-68 *ht* represents the solvent-free version of MIL-68 and is used in the embedment experiments, since the influence of any solvent molecule should be excluded from all considerations concerning the investigations on the switching behavior of the respective dye moiety.

Due to the rigid structure of MIL-68, the presence of DMF and water within the pores does not affect the peak positions in the diffraction pattern, but causes rather an alteration in intensities, mainly those in the anterior angular range. The modulation in intensities upon guest incorporation will be an indication for the successful embedment of the photoactive molecules and further, new peaks can be identified as a second phase, pointing to free dye

molecules. In figure 4.2.5 the diffraction patterns of MIL-68(In) *ht* and MIL-68(Ga) *ht* with the respective theoretical pattern<sup>[165]</sup> are shown. They are in good agreement with the theoretical data and point to high crystallinity of the MOFs.

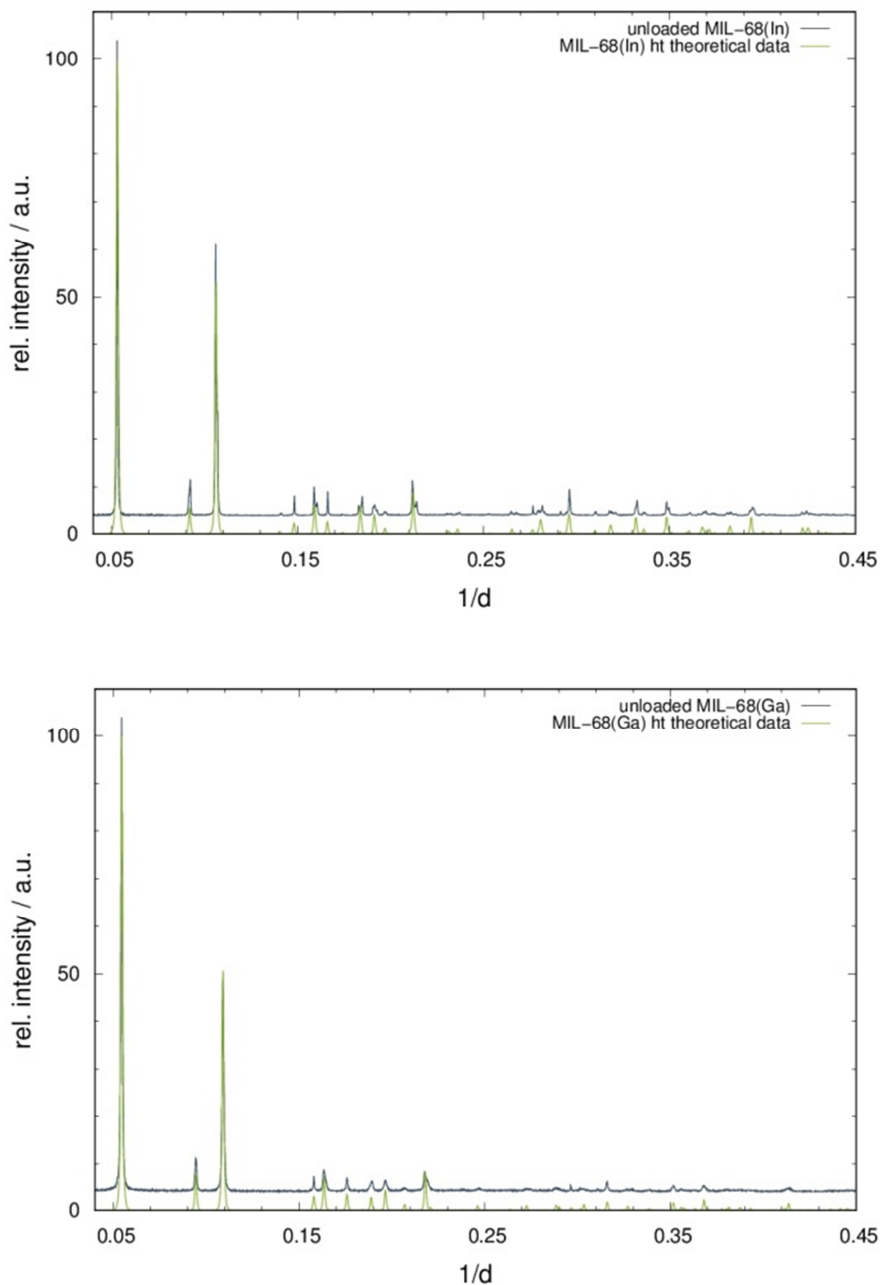


**Figure 4.2.5** XRPD pattern of MIL-68(In) *ht* (on top) and MIL-68(Ga) *ht* (at the bottom) (blue-grey); measured at 298 K (BM01B/ESRF:  $\lambda = 0.504477 \text{ \AA}$ ) in comparison to theoretical data of MIL-68(In) and MIL-68(Ga) (green), respectively. A small offset along  $y$  (+4%) was applied in order to enhance readability.

The hexagonal channels of MIL-68(In) measure  $\sim 18 \text{ \AA}$  in diameter (two opposing  $\text{In}^{3+}$  cations minus their *van-der-Waals* radii, distances were estimated with *Diamond 4.4*<sup>[173]</sup>), the

trigonal ones measure  $\sim 7.5 \text{ \AA}$  between one indium cation and the opposing terephthalate linker molecule. For MIL-68(Ga) diameters of  $\sim 17 \text{ \AA}$  and  $\sim 6.5 \text{ \AA}$  were determined. Hence, only the hexagonal pores are accessible for the different spiropyrans and the spirooxazine, which show a size of  $\sim 14.5 \text{ \AA} \times 7.5 \text{ \AA} \times 7 \text{ \AA}$  in their closed form (the size was estimated from the nitro-substituted spiropyran (SP-Nitro)<sup>[175]</sup> by taking the *van-der-Waals* radii into account; size was estimated with *Diamond 4.4*<sup>[173]</sup>).

### 4.2.3 MIL-53(Al)

In 2004 *Férey* and co-workers introduced MIL-53(Al) as a highly flexible Metal-Organic Framework with a high thermal stability.<sup>[166]</sup> MIL-53(Al) follows the general chemical molecular formula  $M^{III}(\text{OH})(\text{bdc})$  with  $M = \text{Al}$ . Isotypical structures are also known for  $M = \text{Ga}$ <sup>[167]</sup>,  $\text{Fe}$ <sup>[176,177]</sup>,  $\text{Sc}$ <sup>[178]</sup> and  $\text{Cr}$ <sup>[179]</sup>. In all cases, the lattice is composed of infinite chains of octahedral units connected by the linker molecules, generating one dimensional channels. A more detailed description of the structure is given in the following.

The octahedral units with the composition  $\text{MO}_4(\text{OH})_2$  are *E* interconnected by hydroxyl groups leading to a tilted chain (this connection mode has already been described for MIL-68; see figure 4.2.3). Further, the two carboxyl groups of one bdc linker are linked to two distinct adjacent octahedra. This linking pattern results in the formation of one dimensional channels with a rhomboid shape. These channels exhibit different sizes in relation to the nature of inserted guest molecules, which will be described below and is shown in figure 4.2.6.

As a result of their linkage mode, all representatives of the MIL-53 series show reversible shrinking and expanding of their structure upon the presence of guest molecules<sup>[180]</sup>, a phenomenon called “breathing effect”. The high temperature modification MIL-53 *ht* has a volume of  $1412.0(4) \text{ \AA}^3$ . As a result of hydrogen bonding between the hydroxyl functions of the lattice and inserted water molecules, MIL-53 *lt* shows a volume of  $946.7(2) \text{ \AA}^3$ , a shrinkage of nearly 33% in comparison to the solvent-free MOF.<sup>[166]</sup> Since the terephthalate linker is rigid, the coordination of the carboxylate function of the ligand to the metal cations is flexible and comparable to a hinge.

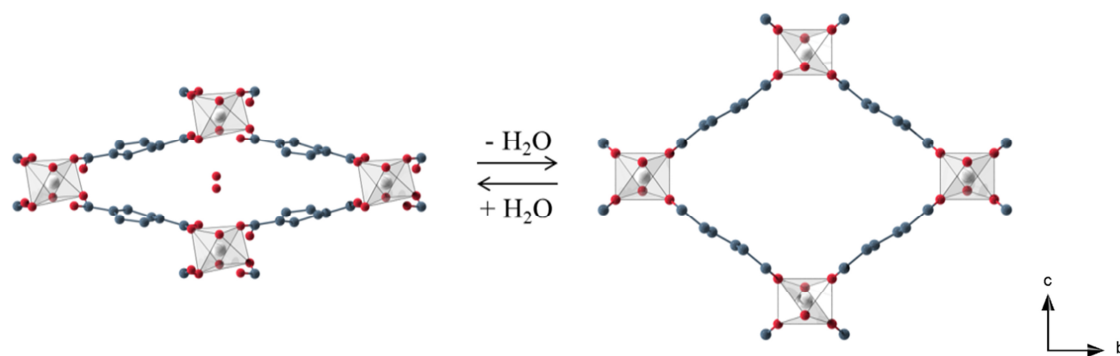


**Figure 4.2.6** Demonstration of the reversible water uptake and release of MIL-53(Al) with MIL-53(Al) *lt* (left) and MIL-53(Al) *ht* (right), respectively.<sup>[166]</sup> Color code: white: aluminum cations; red: oxygen anions; grey: carbon. Hydrogen cations are omitted.

The channel dimensions for the solvent-free *ht* form are  $\sim 12.3 \text{ \AA} \times 7.8 \text{ \AA}$ , and for the water containing *lt* form  $15.1 \text{ \AA} \times 3.2 \text{ \AA}$ . Distances were measured between opposing  $\text{Al}^{3+}$  cations minus the *van-der-Waals* radii, distances were estimated with *Diamond 4.4*<sup>[173]</sup>. MIL-53(Al) *ht* crystallizes in the orthorhombic space group *Imma* (No. 74), MIL-53(Al) *lt* in the monoclinic space group *Cc* (No. 9).

Right after the synthesis, the *as synthesized* form is obtained. For MIL-53(Al) *as* terephthalic acid was found being present in the pores. Upon heating at high temperatures, this is irreversibly removed leading to either *lt* or *ht* form. MIL-53(Al) *as* crystallizes in the orthorhombic space group *Pnma* (No. 62).

For a typical synthesis, aluminum nitrate and terephthalic acid were hydrothermally converted.<sup>[166]</sup> The obtained MIL-53(Al) *as* was heated in air to remove all terephthalic acid molecules generating MIL-53(Al) *lt*. By heating the *lt* modification at  $100 \text{ }^\circ\text{C}$  and a reduced pressure, the solvent-free *ht* modification was obtained, which was constantly kept under an argon atmosphere to prevent adsorption of humidity. In figure 4.2.7 the diffraction pattern of the *ht* form is shown and compared to the theoretical pattern obtained from the structural data published by *Férey* and co-workers.<sup>[166]</sup> The pattern is in good agreement with the theoretical data in positions and intensities of the peaks.

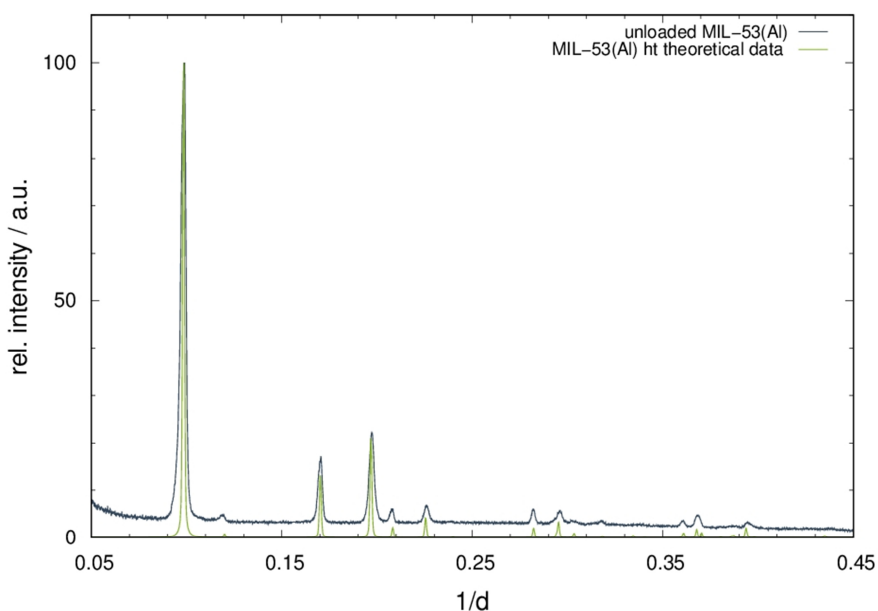


**Figure 4.2.7** XRPD pattern of MIL-53(Al) *ht* (blue-grey), measured at 298 K (*Stoe Stadi P*:  $\lambda = 1.54 \text{ \AA}$ ) in comparison to theoretical data of MIL-53(Al) *ht* (green).

#### 4.2.4 HKUST-1

*Williams* and co-workers presented HKUST-1 in the same year as investigations on MOF-5 were published.<sup>[181]</sup> HKUST-1 with the chemical sum formula  $\text{Cu}_3(\text{btc})_2(\text{H}_2\text{O})_3$  consists of dimeric cupric tetra-carboxylate units interconnected by trimesate linker molecules. This linkage pattern generates channels with square symmetry along [100]. Further, hexagonal windows (with approx. 16 Å in diameter by taking the *van-der-Waals* radii into account, distances were estimated with *Diamond 4.4*<sup>[173]</sup>) along [111] in a honeycomb arrangement are formed, which connect three orthogonal channels.

In detail, the six carboxylate functions of the two trimesate anions bind four coordination sites of the three copper(II) cations. Since copper dimers are present, a square pyramidal coordination is achieved. By further coordination of an axial aqua ligand opposite to the copper dimer, each copper(II) cation is pseudooctahedrally coordinated. The structure of this “paddle wheel” motif is depicted in figure 4.2.8, left. The aqua ligand can be reversibly removed by heating HKUST-1 at 100 °C. The previously turquoise powder turns dark blue, since the coordination sphere of copper changes from an pseudooctahedral to a square pyramidal one.<sup>[181]</sup>

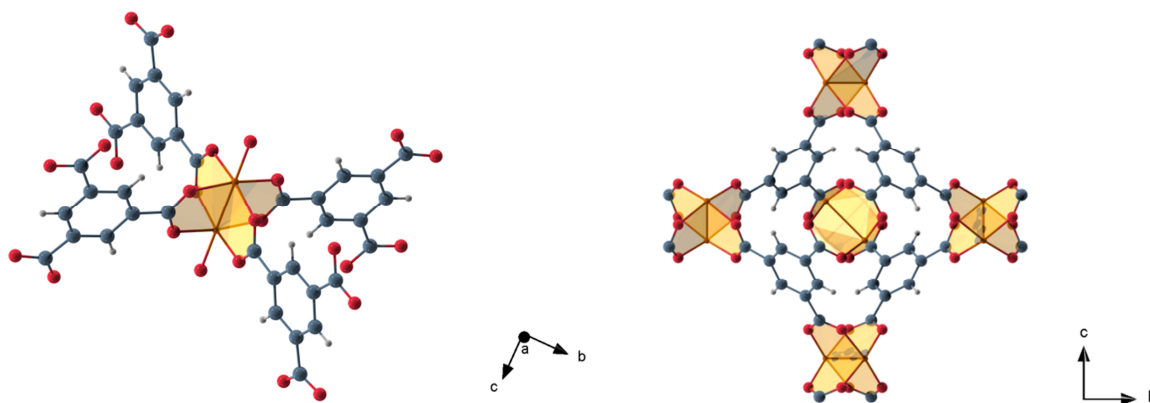


**Figure 4.2.8** Left: “Paddle-Wheel” motif of HKUST-1. Four trimesate linker molecules bind to both copper(II) cations. Axial water molecules (illustrated without the protons) complete the pseudooctahedral coordination sphere; Right: SBU of HKUST-1.<sup>[181]</sup> Crystallographic data were taken from *Williams* and co-workers.<sup>[181]</sup> Color code: orange: copper cations; red: oxygen anions; grey: carbon; white: hydrogen cations.

Completing the “paddle wheel” motif with six further dimeric copper structures leads to the formation of the SBU of HKUST-1, an octahedral unit. By corner-sharing with other such octahedrons, the network of HKUST-1 is delimited. In figure 4.2.9 the structure of one pore

of HKUST-1 is shown. The accessible space is symbolized with a grey sphere. HKUST-1 crystallizes in the cubic space group  $Fm\bar{3}m$  (No. 225).

HKUST-1 is either produced solvothermally<sup>[181]</sup> or by means of a stirring synthesis<sup>[182]</sup>. In the present thesis the MOF was synthesized via the second method. Copper(II) hydroxide and trimesic acid were dissolved in water and ethanol, respectively. Both suspensions were combined and stirred at room temperature. The resulting precipitate was filtered, dried in air and heated at 100 °C and a reduced pressure. HKUST-1 was obtained as a dark-blue powder. The diffraction pattern is shown in figure 8.1.2 in the supplement and compared to the theoretical pattern of *Williams* and co-workers.<sup>[181]</sup> The experimental and theoretical data are in good agreement with respect to positions and intensities of the peaks.

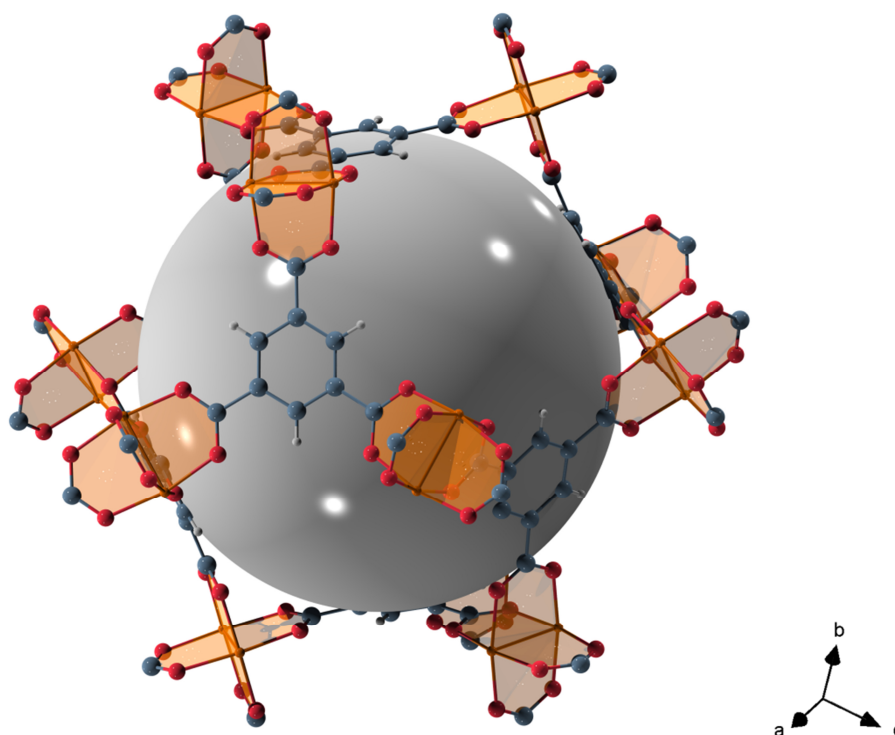


**Figure 4.2.9** Accessible void of HKUST-1 symbolized by a grey sphere. Crystallographic data were taken from *Williams* and co-workers.<sup>[181]</sup> Color code: orange: copper cations; red: oxygen anions; grey: carbon; white: hydrogen cations.

#### 4.2.5 MIL-101(Cr)

MIL-101(Cr) was presented by Férey and co-workers in 2005 as a MOF with pores of an extraordinary large volume.<sup>[183]</sup> MIL-101(Cr) features the general chemical sum formula  $\text{Cr}_3(\text{O})\text{X}(\text{bdc})_3(\text{H}_2\text{O})_2$  with  $\text{X} = \text{F}, \text{OH}$ . The MOF consists of trimeric chromium(III) centered octahedrons. The chromium(III) cation is coordinated by four oxygens of the bidentate dicarboxylate, one oxygen from the terminal water or a fluorine group and one  $\mu_3$ -oxygen. Via the  $\mu_3$ -oxygen the single octahedra are connected to each other forming the trimeric unit, which is also referred to as *tertiary building unit* (TBU). The TBU is illustrated in figure 4.2.10, left. The terephthalate linker connects the TBUs forming a super tetrahedron, which is shown in figure 4.2.10, right. Corner-sharing of these super tetrahedrons results in the formation of a 3D network. This linkage pattern generates two different cages. The smaller one possesses a pentagonal entrance window with a size of 12 Å, the larger one provides a hexagonal entrance window with a free-opening of 16 Å x 14.7 Å, respectively. MIL-101(Cr) crystallizes in the space group  $Fd\bar{3}m$  (No. 227).

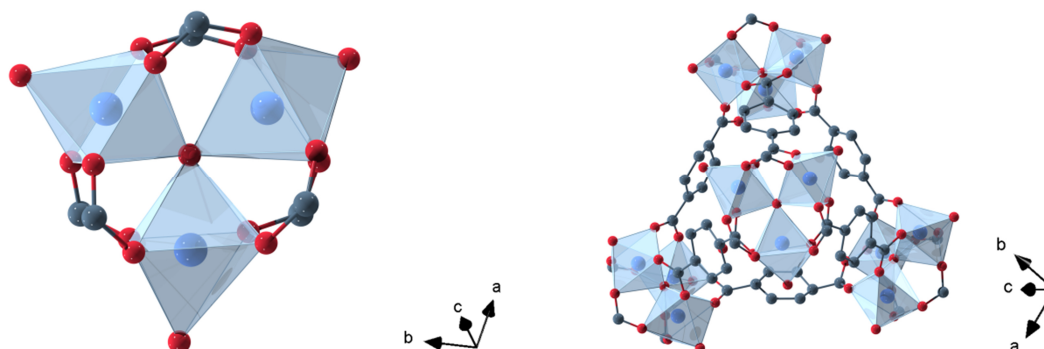


**Figure 4.2.10** Left: Trimeric unit with chromium(III) octahedrons; right: Super tetrahedron consisting of linked TBUs.<sup>[183]</sup> Color code: blue: chromium cations; red: oxygen anions; grey: carbon. For clarity, hydrogen atoms are omitted.

For a typical synthesis, chromium(III) nitrate, terephthalic acid and fluorhydric acid are hydrothermally converted.<sup>[183]</sup> In the present work, a fluorhydric acid free route was applied, following the synthesis procedure of Janiak and co-workers.<sup>[184]</sup> Chromium(III) nitrate, terephthalic acid and nitric acid were reacted under hydrothermal conditions, the precipitate was sonicated and stirred at different temperatures afterwards. MIL-101(Cr) was obtained as a dark green powder. The diffraction pattern of the solvent-free MOF is shown in figure 8.1.3 in the supplement. The experimental data are in good agreement with the diffraction pattern generated from theoretical data.<sup>[183]</sup>

#### 4.2.6 MFM-300(Ga<sub>2</sub>) and fluorinated derivatives

The structure of MFM-300(Ga<sub>2</sub>) has been published by *Schröder* and co-workers in 2016.<sup>[185]</sup> The general chemical molecular formula of this compound is [M<sub>2</sub>(OH)<sub>2</sub>(bptc)] with M = Ga. The MOF consists of metal-centered octahedral units connected by the tetracarboxylate ligands. The Ga(III) cation is coordinated by four oxygen anions from the carboxylate functions of the linker molecule, and two *Z* bridging hydroxyl groups in an octahedral fashion. By this linkage pattern, infinite octahedral chains are generated, which form a square-shaped one dimensional channel along the [001] axis. The diameter of this channel is 6.7 Å x 6.7 Å (by taking the *van-der-Waals* radii of the surface atoms into account). In figure 4.2.11 the channel along the [001] axis is illustrated. MFM-300(Ga<sub>2</sub>) crystallizes in the tetragonal space group *I*4<sub>1</sub>22 (No. 98).

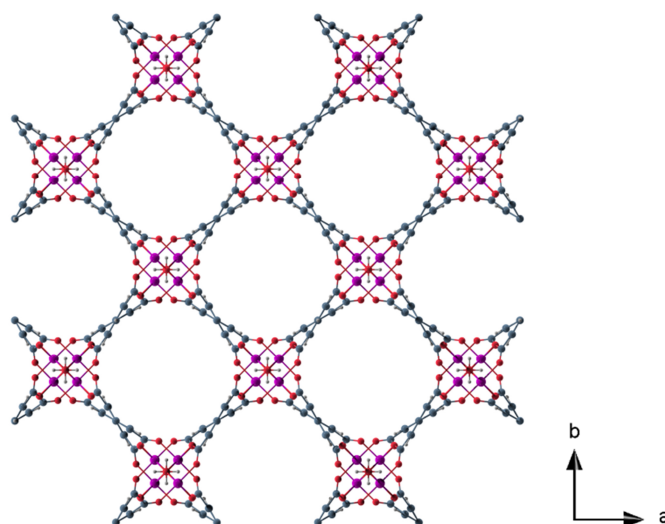


**Figure 4.2.11** Square-shaped channel of MFM-300(Ga<sub>2</sub>) along the [001] axis. Crystallographic data were taken from *Schröder* and co-workers.<sup>[185]</sup> Color code: purple: gallium cations; red: oxygen anions; grey: carbon; white: hydrogen cations.

For a typical synthesis biphenyl-3,3',5,5'-tetracarboxylic acid and gallium(III) nitrate were solvothermally converted in a mixture of DMF, THF and water.<sup>[185]</sup> The exact protocol for the fluorinated derivatives can be found at *C. Stastny*.<sup>[186]</sup> The diffraction patterns are shown in figure 8.1.4 to 8.1.6 in the supplement. The three compounds MFM-300(Ga<sub>2</sub>) and its fluorinated derivatives F-MFM-300(Ga<sub>2</sub>) and F<sub>2</sub>-MFM-300(Ga<sub>2</sub>) were only used for investigations on inner surface polarity of the MOF matrices, since the channels are too small for the incorporation and especially isomerization processes of spiropyrans and spirooxazines.

#### 4.2.7 Zeolite Y

In contrast to MOFs zeolites represent inorganic porous materials, consisting of  $\text{SiO}_4$ - and  $\text{AlO}_4$ -tetrahedrons, which generate a framework with accessible voids. Since every tetrahedrally coordinated aluminum cation carries a negative charge, cations like  $\text{Ca}^{2+}$  or  $\text{Na}^+$  are embedded in the voids to compensate the negative charge.<sup>[187]</sup>

One representative of those materials is Zeolite Y. This compound was firstly synthesized by *Breck* in 1954<sup>[188]</sup> and corresponds to Faujasite found in nature. The exact composition of Zeolite Y depends on the Si:Al ratio. In the present work Zeolite Y  $\text{SiO}_2$ : $\text{Al}_2\text{O}_3$  with a molar ratio of 5.1:1 (Si:Al) was used.

The framework consists of sodalith cages (see figure 4.2.12, left), which are linked to each other via hexagonal prisms (figure 4.2.12, right). This linkage pattern results in the formation of a porous framework. The entrance window of the largest one is 7.4 Å; the cavity measures 12 Å in diameter. Zeolite Y crystallizes in the cubic space group  $Fd\bar{3}m$  (No. 227).<sup>[189]</sup>

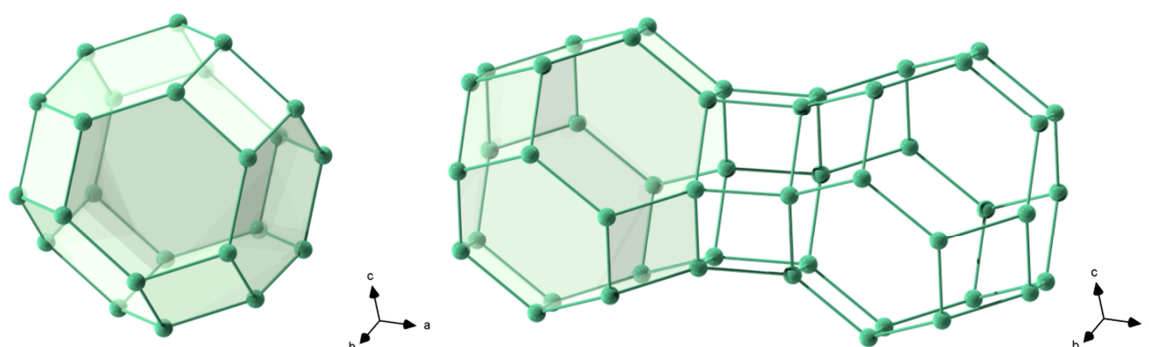


**Figure 4.2.12** Left: Sodalith cage of Zeolite Y; right: two sodalith cages connected via one hexagonal prism. Si/Al cations are colored in green. For a better overview oxygen atoms are omitted.

Zeolite Y is either synthesized by thermal or hydrothermal dealumination, chemical dealumination or the combination of thermal and chemical dealumination.<sup>[190]</sup> In the present work, Zeolite Y from *Alfa Aesar* was used as purchased and without further purification. The XRPD pattern is shown in figure 8.1.7 in the supplement.

### 4.3 Principles of Loading

Embedment of the dye molecules was achieved either by gas phase loading or by mechanochemical synthesis. Both methods were performed with the dye and MOF materials in order to exclude any solvent molecules from all later investigations.

All used dyes are sublimable at moderate temperatures under a reduced pressure. For the syntheses of the hybrid materials, only solvent-free MOFs were used. For this, the host materials were activated at 100 °C and a reduced pressure before stored under an argon atmosphere. For the gas phase loading, the respective MOF and dye were thoroughly ground, transferred into a glass vessel, which was placed in a *Schlenk* tube and heated at a specific temperature and a reduced pressure for several hours. Depending on the system different temperatures were chosen. The successful embedment is obvious by the change in color of the colorless MOF to e.g. slightly pink color in case of MIL-68 as host material and SP-Nitro as guest molecule, which is depicted in figure 4.3.1. Excess dye recrystallized at the top of the *Schlenk* tube. To prevent absorption of humidity, all systems were constantly handled under argon atmosphere.



**Figure 4.3.1** F.l.t.r. 1) Mixture of SP-Nitro and MIL-68 before gas phase loading, 2) after gas phase loading obtaining a slightly colored powder, 3) after irradiation with UV light ( $\lambda = 365$  nm) and 4) after heat supply.

For the spiropyrans SP-N and SP-OMe mechanochemical loading was applied as a second method of incorporation. The respective spiropyran and the MOF materials were thoroughly ground at different molar ratios under an argon atmosphere. Successful embedment became visible by the change in color of the previously colorless mixture of MOF and dye. The color intensified with increasing time of grinding. It should be emphasized that the used spiropyrans are not mechanochromic. Hence, the change in color is only induced by incorporation.

#### 4.4 Spiropyran@MOF hybrid materials

For investigations on spiropyran@MOF systems, different spiropyrans were chosen, mainly focusing on one with an electron-withdrawing nitro group at the 6'-position. Generally, a differing photochromic behavior is observed with respect to the nature of the substituent. In their theoretical study *Leszczynski* and co-workers investigated the substituent effects on the photochromic activity of spiropyrans by introducing electron donating and accepting groups to both the nitrogen of the indoline moiety and to the 6'-position of the chromene ring.<sup>[191]</sup> The authors found that indoline<sub>donor</sub>-chromene<sub>acceptor</sub> pairs elongate the C<sub>Spiro</sub>-O bond. This causes the decrease of the activation energy for bond cleavage and *Z* merocyanine is formed. However, donor-acceptor groups increase the activation energy for the *Z* to *E* isomerization of the merocyanine dye.

Reconversion of *E* merocyanine to its *Z* form is associated with a high activation energy leading to a stabilization of the open MC form for spiropyrans with indoline<sub>donor</sub>-chromene<sub>acceptor</sub> pairs.<sup>[191]</sup>

Furthermore, the nature of the surrounding media has a substantial impact on the isomerization process. While polar media decrease the activation energy for the C<sub>Spiro</sub>-O bond cleavage, the activation energy for the *Z* to *E* isomerization increases. This has been studied for the 6'-nitro substituted spiropyran.<sup>[192]</sup> For retransformation to the closed SP form a high activation energy is required in polar media, since the *E* merocyanine is stabilized, causing a high  $\Delta E_{E \rightarrow Z}$ .<sup>[191]</sup>

By increasing the strength of the indoline<sub>donor</sub>-chromene<sub>acceptor</sub> pairs and the polarity of the surrounding media, the C<sub>Spiro</sub>-O bond is weakened, resulting in the formation of the open merocyanine. At the same time the activation energy for the retransformation to the ground state increases and therefore, the open merocyanine is stabilized.<sup>[191]</sup> In the present work these results will be considered especially for switching properties and stabilization of the open merocyanine form in relation to the used host material.

In the following, the systems composed of several spiropyrans (mainly focusing on 1,3,3-trimethylindolino-6'-nitro-benzopyrylospiran) and different MOF host materials and their properties are presented. For a better understanding, the used dye molecule will be shortly described with respect to structure and photochromic behavior in solution at the beginning of the chapter, before the spiropyran@MOF hybrid systems are discussed following the ICE-principle.

#### 4.4.1 SP-Nitro@MOF hybrid materials

1,3,3-Trimethylindolino-6'-nitro-benzopyrylospiran (abbreviated with SP-Nitro in the following), is probably the most investigated one among spiropyrans. It shows rapid switching and a significant change in color upon UV light irradiation due to the presence of its electron withdrawing nitro group on the chromene ring.<sup>[191]</sup> The structure of SP-Nitro is shown in figure 4.4.1.

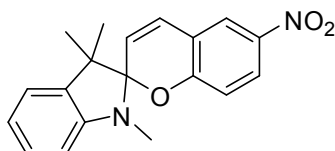


**Figure 4.4.1** Structure of 1,3,3-trimethylindolino-6'-nitro-benzopyrylospiran (SP-Nitro) with a nitro-group substituent at the 6'-position of the chromene ring.

As previously described in chapter 2.2, spiropyrans undergo the phenomenon of solvatochromism. Solvatochromism refers to the strong dependence of the absorption properties of a dye molecule on the polarity of the surrounding medium. In most cases, this is visible by a change in the position of the absorption bands, which is caused by solute-solvent interactions that modify the energy gap between ground and excited state of the absorbing dye. On that occasion, spectroscopic measurements were carried out on irradiated SP-Nitro dissolved in solvents of varying polarity. Figure 4.4.2 shows the strong dependence of the absorption properties of MC-Nitro on the polarity of the solvent.

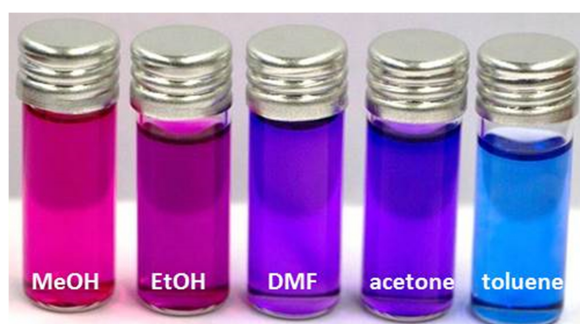


**Figure 4.4.2** Change in color of MC-Nitro dissolved in solvents of varying polarity (decreasing polarity from methanol to toluene).

Depending on the solvent,  $\lambda_{\max}$  of MC-Nitro is red or blue-shifted. For methanol, the lowest  $\lambda_{\max}$ -value is found (527 nm), which increases to 540 nm in ethanol, 558 nm in acetonitrile,

566 nm in acetone and finally 601 nm in toluene (see figure 4.4.3). Furthermore, a shoulder at approx. 560 nm is found for toluene, which can be clearly assigned to the presence of *H*-aggregates.

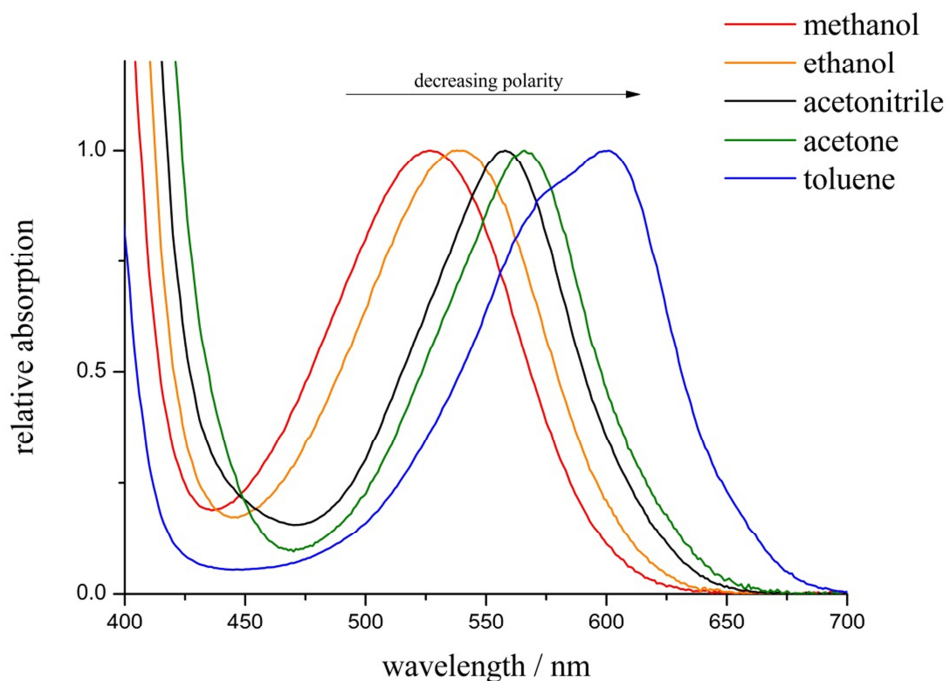


**Figure 4.4.3** Absorption spectra of MC-Nitro dissolved in solvents with varying polarity.

The polarity of a solvent can be determined by its elution power  $\epsilon^0$  on alumina. According to the elutrope series of *Snyder*<sup>[193]</sup>, methanol is the most polar solvent, followed by ethanol, acetonitrile, acetone and finally toluene. For a better overview, the solvents with their respective elution power  $\epsilon^0$  and the absorption maximum of MC-Nitro are listed in table 4.4.1.

**Table 4.4.1** List of the used solvents with their elution power and  $\lambda_{\max}$  of MC-Nitro.

solvent	$\lambda_{\max}$ of MC-Nitro / nm	elution power $\epsilon^{0[193]}$
methanol	527	0.95
ethanol	540	0.88
acetonitrile	558	0.65
acetone	566	0.56
toluene	601	0.29

Obviously, the absorption maximum  $\lambda_{\max}$  of MC-Nitro hypsochromically shifts with increasing solvent polarity. Hence, SP-Nitro undergoes negative solvatochromism. This knowledge is essential for further understanding and characterizing SP-Nitro@MOF systems. SP-Nitro was embedded into the four different MOFs MOF-5, MIL-68(In), MIL-68(Ga) and MIL-53(Al) via a gas phase loading process. Four SP-Nitro@MOF composite materials were obtained:

- (1) SP-Nitro@MOF-5
- (2) SP-Nitro@MIL-68(In)
- (3) SP-Nitro@MIL-68(Ga)
- (4) SP-Nitro@MIL-53(Al)

Preliminary experiments on the resulting hybrid compounds have already been done in the previous *Staatsexamensarbeit*<sup>[172]</sup>. In the present work, these composite materials were investigated and fully characterized by means of the ICE-principle. The results are presented in the following.

#### 4.4.1.1 Incorporation

The successful embedment of SP-Nitro was confirmed by X-ray Powder Diffraction measurements. First, the incorporation of the compounds **1** to **3** will be discussed, since MOF-5 and MIL-68(In/Ga) present non-flexible MOFs.

The unaltered diffraction patterns of **1** to **3** compared to the respective unloaded MOF indicate the integrity of the host lattice upon guest incorporation. However, marked alterations in the

peak intensities are observed, pointing to a changed electron density inside the MOF pores, as expected upon guest loading. Furthermore, the presence of free dye molecules can be excluded, since no additional peaks are present. The diffraction patterns of **1** and **3** in comparison to the respective pristine MOF are exemplarily shown in figure 4.4.4 and figure 4.4.5. The diffraction pattern of **2** is found in the supplement (figure 8.2.1).

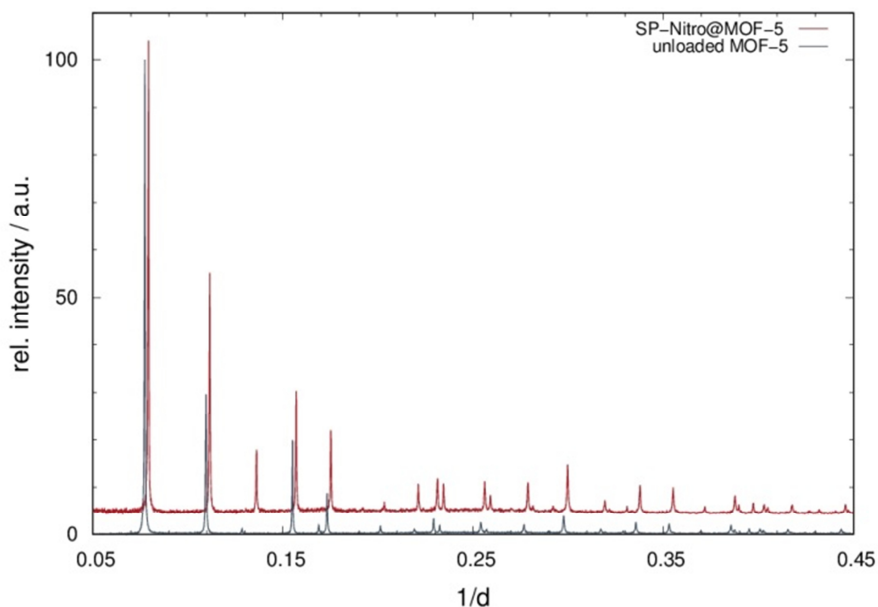


**Figure 4.4.4** XRPD patterns of (**1**) (red) and unloaded MOF-5 (blue-grey), measured at 298 K (BM01B/ESRF:  $\lambda = 0.50561 \text{ \AA}$  (**1**) and  $\lambda = 0.504477 \text{ \AA}$  (unloaded MOF-5)). As both patterns were recorded with different wavelengths  $1/d$  was chosen as  $x$  axis and a small offset along  $y$  (+4%) was applied in order to enhance readability.

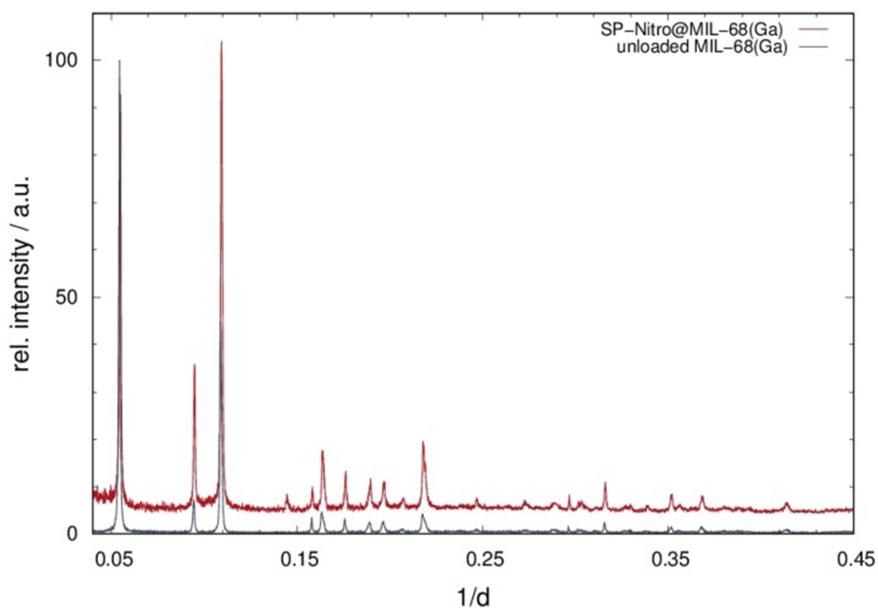


**Figure 4.4.5** XRPD patterns of **(3)** (red) and unloaded MIL-68(Ga) (blue-grey), measured at 298 K (BM01B/ESRF:  $\lambda = 0.50561 \text{ \AA}$  (**3**) and  $\lambda = 0.504477 \text{ \AA}$  (unloaded MIL-68(Ga))). As both patterns were recorded with different wavelengths  $1/d$  was chosen as  $x$  axis and a small offset along  $y$  (+4%) was applied in order to enhance readability.

For **1** and **3** alterations of the peak intensities are obvious. Especially for composite **3** the height of the first and third peak differs significantly compared to the unloaded MIL-68(Ga). Here, the intensity of the first peak markedly decreased, while the intensity of the third one increased. Notably, the *Bragg* peaks of **1** are shifted to higher angles, indicating a contraction of the MOF-5 framework upon guest loading. To validate this fact, *Le Bail* fits in *JANA2006*<sup>[194]</sup> were performed for the composite materials **1** to **3**. The results are listed in table 4.4.2. For MOF-5, guest loading results in a contraction of the framework, pointing to attractive interactions between the guest molecule and the host lattice. Contrary to this finding, guest incorporation into MOFs of the MIL-68 family causes expansion of the framework. This might be a result of repulsive host-guest interactions. Since these alterations are not significant, additional methods (e.g. solid state NMR, quantum chemical calculations) to confirm the suggestion of attractive and repulsive host-guest interactions are obligatory. *Le Bail* fits of **1** to **3** and the respective unloaded MOFs are shown in figures 8.2.2 to 8.2.7, details for the *Le Bail* fits on unloaded MOFs are listed in table 8.2.1 in the supplement.

**Table 4.4.2** Results of *Le Bail* fits of high-resolution synchrotron powder diffraction data of compounds **1** to **3** compared with the unit cell volumes of the respective unloaded MOF.

	(1)	(2)	(3)
T/K	298	298	298
Space Group / No.	$Fm\bar{3}m$ / 225	$Cmcm$ / 63	$Cmcm$ / 63
GOF	0.80	0.97	0.91
$R_p$	0.186	0.167	0.205
$wR_p$	0.291	0.248	0.325
$V/\text{\AA}^3$	17111.3(3)	5911.5(2)	5217(1)
a	25.7688(5)	21.85(0)	21.08(3)
b	-	37.4227(8)	36.707(4)
c	-	7.23(0)	6.7422(5)
$V/\text{\AA}^3$ (unloaded MOF)	17156.0(4)	5901.5(2)	5197.0(7)

For the flexible MOF MIL-53(Al) a different behavior is expected upon guest loading. Dependent on the embedded guest molecule, a change in the diffraction pattern occurs as a result of the “breathing effect”. This has already been shown for azobenzene and fluorinated derivatives.<sup>[163,164]</sup> Even though a change in color was observed during the synthesis of SP-Nitro@MIL-53(Al) (**4**), the diffraction pattern remains unaltered with respect to intensity and position in comparison to the unloaded host material (see figure 4.4.6). This either means that only a small amount was embedded into the MOF pores or SP-Nitro was adsorbed as an amorphous film on the MOF surface. Nevertheless, SP-Nitro@MIL-53(Al) (**4**) was further investigated to understand and clarify the type of host-guest interactions.

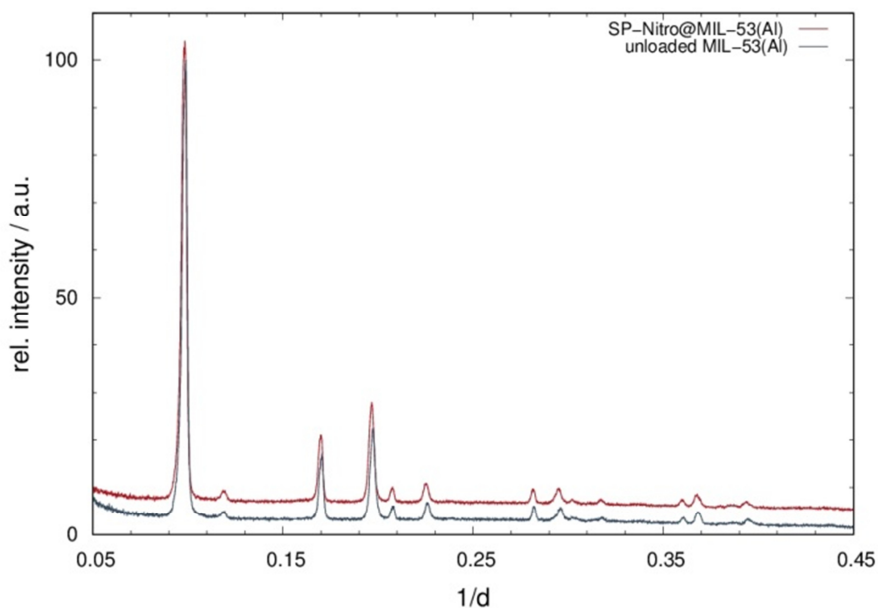


**Figure 4.4.6** XRPD patterns of **(4)** (red) and unloaded MIL-53(Al) *ht* (blue-grey), measured at 298 K (*Stoe Stadi P*:  $\lambda = 1.54 \text{ \AA}$ ). A small offset along *y* (+ 4%) was applied in order to enhance readability.

#### 4.4.1.2 Composition

The knowledge of the approximate dye@MOF composition is essential with regard to correctly interpreting possible host-guest and guest-guest interactions. The composition is approximate, because an exact determination is not possible due to defects in the crystal structure of the MOF material. Furthermore, an even filling of the MOF pores is assumed. The ratio guest molecule per formula unit MOF of **1** to **4** was determined by means of both elemental analysis and XPS. In previous research on photoswitch@MOF composite materials by *D. Hermann*<sup>[164]</sup> elemental analysis was the method of choice. However, for spiropyran@MOF systems, XPS was found to be a more powerful tool, even though XPS is a surface method: Since nitrogen is only present in the guest, but not in the MOF framework, the areas of typical nitrogen XPS signals and the areas of the typical metal cation XPS signals were compared. In table 4.4.3 the results of XPS measurements and elemental analyses are listed. Peak fits of the XPS data and details of the elemental analyses are found in figures 8.2.8 to 8.2.11 and tables 8.2.2 to 8.2.6 in the supplement.

**Table 4.4.3** Ratio of SP-Nitro per formula unit of the respective MOF for **1** to **4** calculated from XPS measurements and elemental analysis.

		XPS	Elemental analysis
SP-Nitro <sub>x</sub> @MOF-5 ( <b>1</b> )	SP-Nitro : (Zn <sub>4</sub> O(bdc) <sub>3</sub> )	2.26 : 1	2.4 : 1
SP-Nitro <sub>x</sub> @MIL-68(In) ( <b>2</b> )	SP-Nitro : (In(OH)(bdc))	0.30 : 1	0.45 : 1
SP-Nitro <sub>x</sub> @MIL-68(Ga) ( <b>3</b> )	SP-Nitro : (Ga(OH)(bdc))	0.24 : 1	0.25 : 1
SP-Nitro <sub>x</sub> @MIL-53(Al) ( <b>4</b> )	SP-Nitro : (Al(OH)(bdc))	0.10 : 1	0.06 : 1

The results of both methods are in the same range, but larger differences are found for MIL-68(In) (**2**) and MIL-53(Al) (**3**) samples. Unfortunately, single measurements of the same compound in the elemental analyses already differ significantly from each other. Hence, XPS seems to be the more accurate method to determine the composition of such guest@MOF systems. In spite of this, the degree of loading for all further systems (chapter 4.4.2 to 4.6) was investigated by means of XPS only.

Notably, the host lattice influences the electronic structure of the embedded guest molecule, which should be obvious in the XPS spectra as well. When looking at the structure of SP-Nitro in figure 4.4.1, two nitrogen peaks are expected: one for the nitro-nitrogen in the chromene part and one for the indoline-nitrogen. For all composite materials **1** to **4** both peaks were found (see figure 4.4.7 and 4.4.8 and figure 8.2.8 to 8.2.9 in the supplement). On top of that, a marked peak broadening was observed for compounds **1** to **3**, but not for **4**. In figures 4.4.7 and 4.4.8 the nitrogen N1s peaks of SP-Nitro@MIL-53(Al) (**4**) and SP-Nitro@MIL-68(Ga) (**3**) are shown, respectively. While both XPS peaks of the N1s of **4** are clearly defined, a significant peak broadening appears for **3** pointing to a successful incorporation of SP-Nitro into MIL-68(Ga), because an interaction of the guest molecule with the MOF framework leads to such broadening. Hence, this is another confirmation that SP-Nitro was successfully incorporated in MOF-5, MIL-68(In) and MIL-68(Ga), but not in MIL-53(Al).

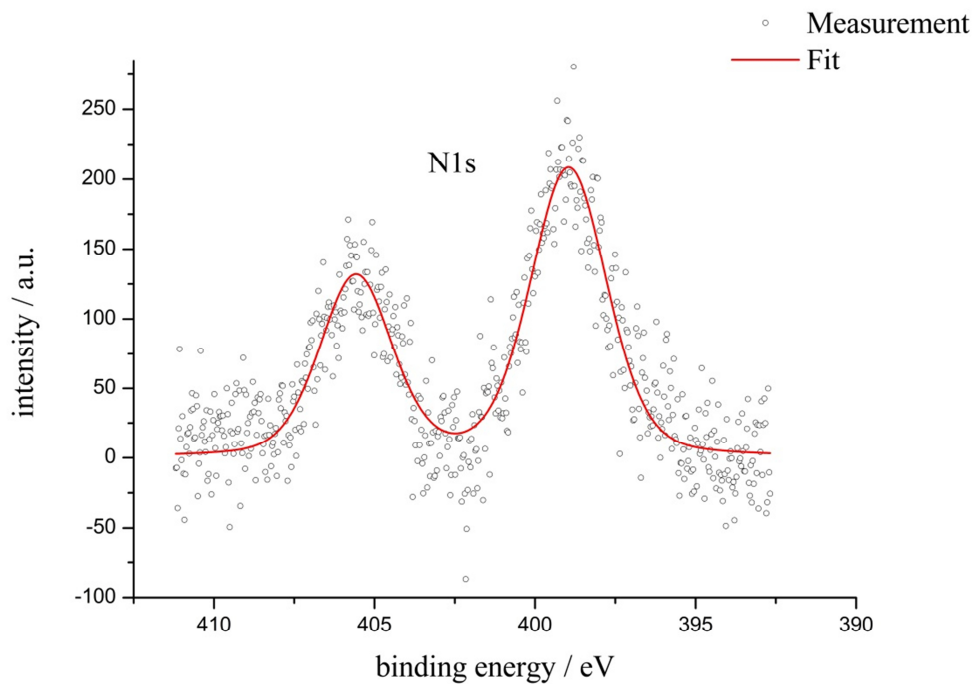


**Figure 4.4.7** XPS spectrum of the N1s peak of SP-Nitro@MIL-53(Al) (**4**) with experimental data (dots) and fit (red).

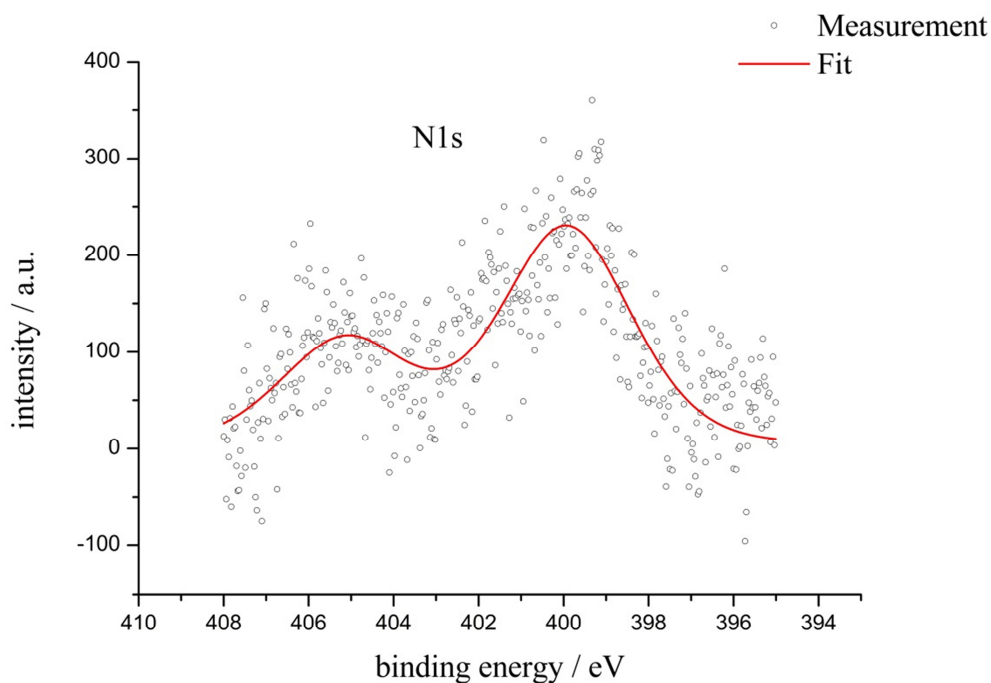


**Figure 4.4.8** XPS spectrum of the N1s peak of SP-Nitro@MIL-68(Ga) (**3**) with experimental data (dots) and fit (red).

#### 4.4.1.3 Effects

In solution, light irradiation of SP-Nitro causes the conversion to its MC-Nitro form, which is strongly colored due to its planar structure and extended  $\pi$ -conjugation between the indoline and chromene part. This has been comprehensively discussed in chapter 2.1.1. For spiropyran@MOF systems, only one system is known up to now: *Zhu* and co-workers prepared thin MOF films of type JUC-120 loaded with a spiropyran by microwave-assisted synthesis.<sup>[171]</sup> This composite material exhibits inverse photochromism upon irradiation with UV light. Spiropyran@MOF hybrid materials with positive photochromism were not published yet. In order to investigate (a) the type of photochromism and if the resulting systems show photoswitching properties, (b) the influence of the host matrices and (c) the reversibility as well as the photostability of the obtained systems **1** to **4**, spectroscopic methods, namely UV/vis, IR and fluorescence spectroscopy, were applied. The results of the investigations are presented in the following, starting with point (a).

##### 4.4.1.3.1 Photoswitching and Type of Photochromism

UV/vis spectra of all compounds **1** to **4** were recorded before and after irradiation with UV light ( $\lambda = 365$  nm, 1 min). It has to be stated that additional adsorption of SP-Nitro on the surface of MIL-53(Al) for compound **4** would result in another interaction between the guest and host material and, hence, cause different optical properties visible as a shoulder in the reflection spectra. In figures 4.4.9 to 4.4.11 the reflection spectra of the non-irradiated and irradiated compounds **1** to **4** are shown, which were recorded in air. Hence, a possible uptake of moisture cannot be excluded. Obviously, no shoulder in the spectra is observed for all composite materials. Therefore, all SP-Nitro molecules are assumed to be present in a similar environment, either incorporated in or adsorbed on the surface of the MOF.

For **1**, a deep pink color is observed immediately after loading and without UV light irradiation. The local minimum in the reflection spectrum of non-irradiated **1** at  $\sim 520$  nm can be clearly assigned to the presence of the open merocyanine form of SP-Nitro (see figure 4.4.9). Irradiation of **1** causes further decrease of the reflection minimum, pointing to a proceeding formation of the merocyanine moiety. The switching process is reversed by simply heating the sample. However, a complete isomerization to the SP form was not achieved. *Zhu* and co-workers observed a similar behavior for 1-(2-hydroxyethyl)-3,3-

dimethylindolino-6'-nitrobenzopyrylospiran embedded in the pores of JUC-120.<sup>[171]</sup> Here, the open MC form is also stabilized inside the MOF host material. Both, the results of *Zhu* and co-workers and for SP-Nitro@MOF-5 (**1**), indicate an environment established by the host material, which is preferred by molecules with a high dipole moment such as merocyanines.

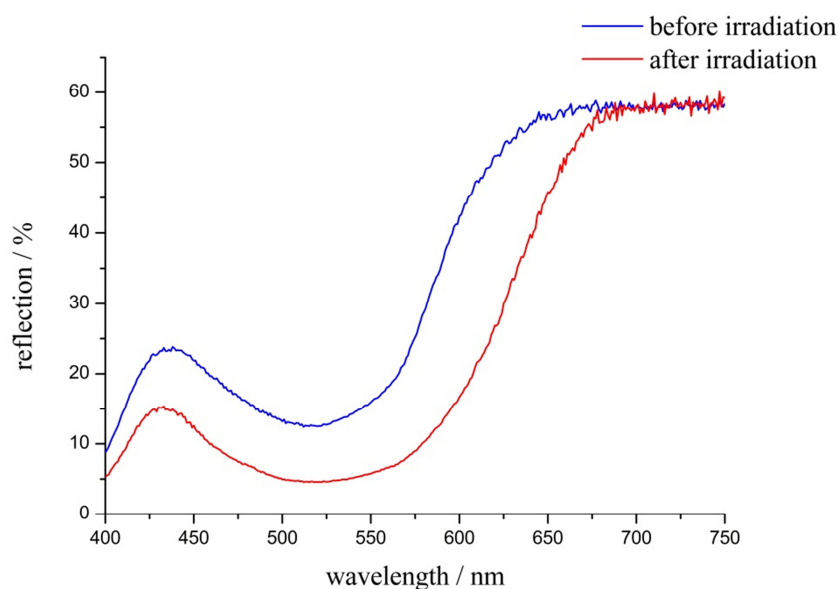


**Figure 4.4.9** Reflection spectra (298 K) of SP-Nitro@MOF-5 (**1**) before (blue) and after (red) irradiation with UV light ( $\lambda = 365$  nm, 1 min).

SP-Nitro@MIL-68(In) (**2**) and SP-Nitro@MIL-68(Ga) (**3**) exhibit a somewhat different behavior upon UV light irradiation. Both compounds are only slightly colored when non-irradiated. Exposure to UV light induces a change in color to deep purple. The reflection minima for **2** at  $\lambda \approx 560$  nm and for **3** at  $\lambda \approx 566$  nm (figure 4.4.10 and figure 4.4.11, respectively) are attributed to the open merocyanine form. Besides, the reflection minima of **2** and **3** are shifted to longer wavelengths in comparison to **1**, leading to a more blueish color. For **2** and **3** switching of the embedded guest is not sterically hindered inside the MOF pores. This finding is similar to **1**. Furthermore, SP-Nitro undergoes positive photochromism inside MIL-68(In) and MIL-68(Ga), thus these systems represent the first hybrid spiropyran@MOF materials exhibiting this type of photochromic behavior.

Reconversion of MC-Nitro to the closed spiropyran form is reversible inside MIL-68(In) and MIL-68Ga) upon heat supply to a certain extent. This will be discussed in chapter 4.4.1.3.2.

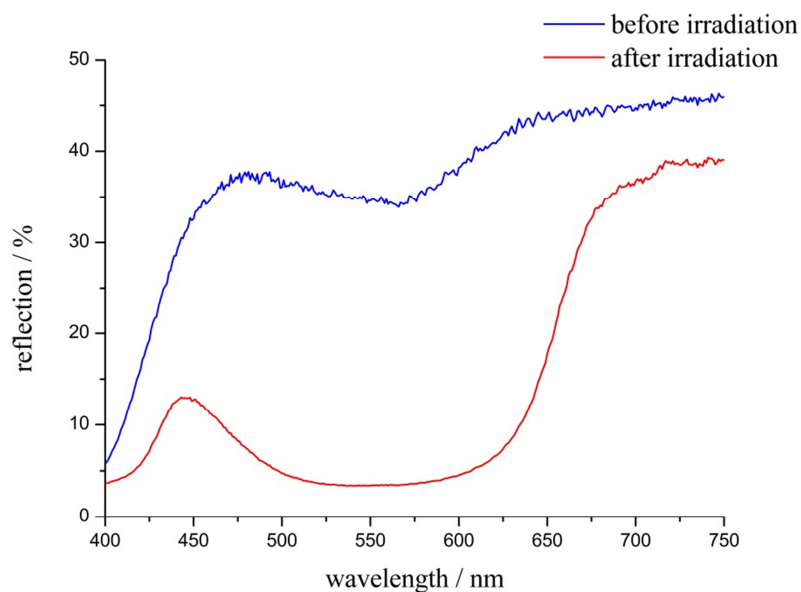


**Figure 4.4.10** Reflection spectra (298 K) of SP-Nitro@MIL-68(In) (**2**) before (blue) and after (red) irradiation with UV light ( $\lambda = 365$  nm, 1 min).

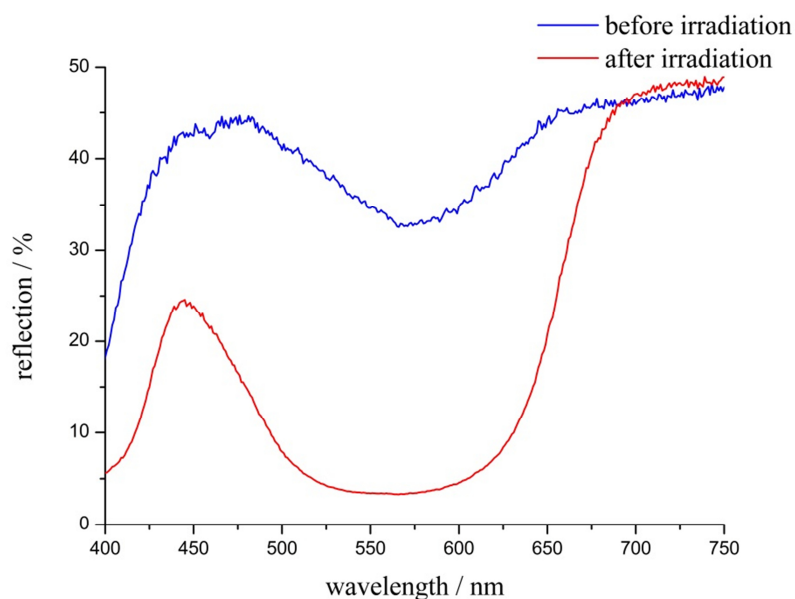


**Figure 4.4.11** Reflection spectra (298 K) of SP-Nitro@MIL-68(Ga) (**3**) before (blue) and after (red) irradiation with UV light ( $\lambda = 365$  nm, 1 min).

Figure 4.4.12 shows the reflection spectra of non-irradiated and irradiated SP-Nitro@MIL-53(Al) (**4**). Although a successful embedment of the guest molecule was not confirmed by means of XRPD and XPS, the combination of SP-Nitro and MIL-53(Al)

exhibits photochromic behavior. Similar to compounds **2** and **3**, **4** features positive photochromism with a reflection minimum at  $\lambda \approx 599$  nm, which is markedly red-shifted in comparison to **1** to **3**.

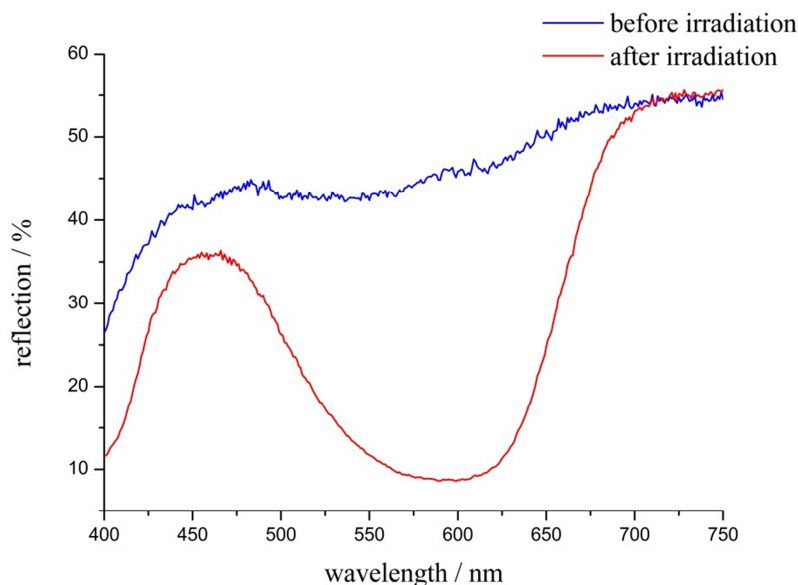


**Figure 4.4.12** Reflection spectra (298 K) of SP-Nitro@MIL-53(Al) (**4**) before (blue) and after (red) irradiation with UV light ( $\lambda = 365$  nm, 1 min).

For all compounds, the resulting reflection minima are very broad. Hence, the centers of these minima were taken.

In order to further understand and track the isomerization processes, IR spectroscopic measurements were performed before and after irradiation with UV light. Irradiation times varied and are given for the respective system. Since the conversion of SP-Nitro to its MC form results in the cleavage of the  $C_{\text{Spiro}}\text{-O}$  bond, the decrease of this band at approx.  $\tilde{\nu} = 950$   $\text{cm}^{-1}$  is used to follow the formation of MC-Nitro.<sup>[195]</sup> The spectra of this fingerprint region are shown in figures 4.4.12 to 4.4.15. For all systems, a significant decrease for the  $C_{\text{Spiro}}\text{-O}$  band was observed with varying UV light exposure times. Notably, long irradiation times are required, since MC-Nitro formed at the surface of the pellet strongly absorbs UV light in a way that SP-Nitro molecules in the bulk receive a markedly lower dose. By irradiating the pellet from the other side (marked with “\*”, turquoise lines), this assumption is validated.

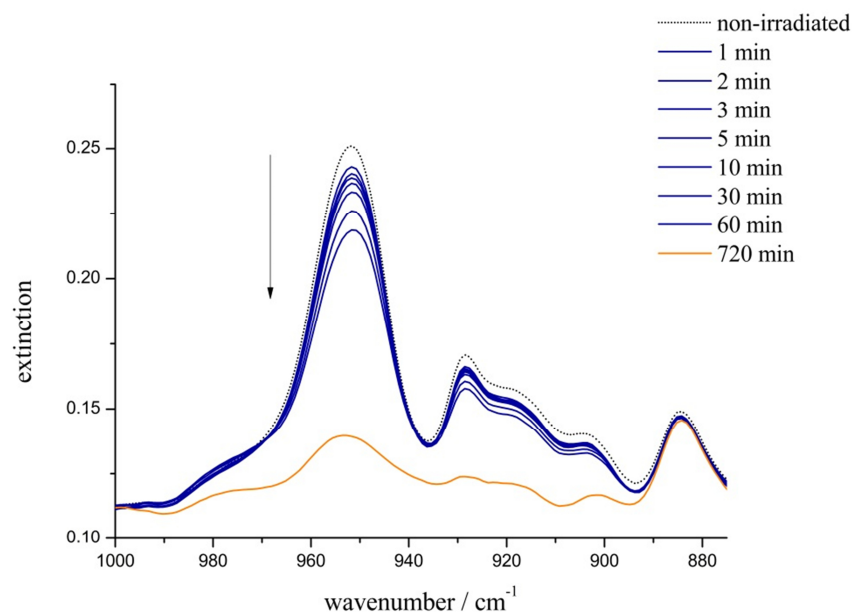


**Figure 4.4.12** IR spectra of **1** during irradiation with UV light ( $\lambda = 365$  nm) focusing on the decrease (the direction of the decrease is marked with an arrow) of the  $C_{\text{Spiro-O}}$  band at approx.  $\tilde{\nu} = 950$   $\text{cm}^{-1}$ .

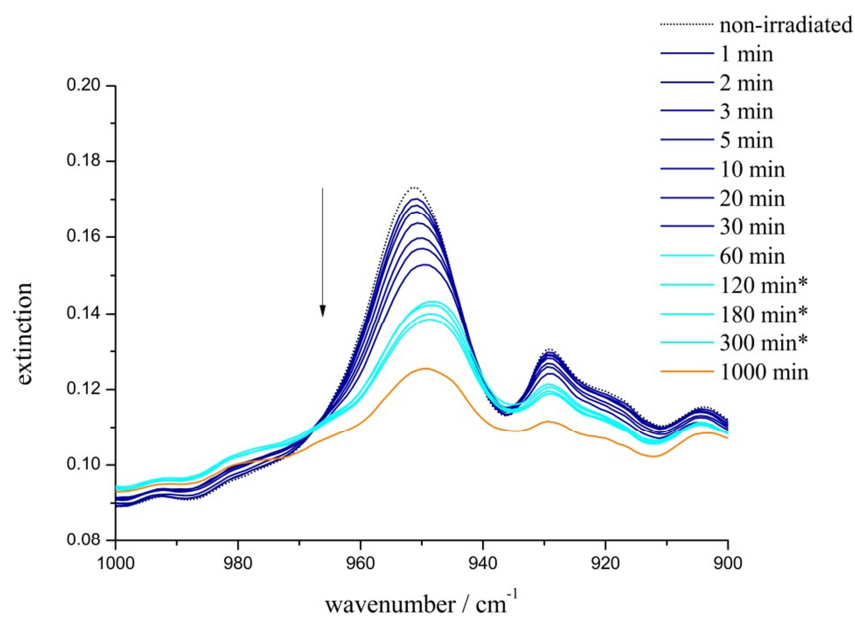


**Figure 4.4.13** IR spectra of **2** during irradiation with UV light ( $\lambda = 365$  nm) focusing on the decrease (the direction of the decrease is marked with an arrow) of the  $C_{\text{Spiro-O}}$  band at approx.  $\tilde{\nu} = 950$   $\text{cm}^{-1}$ .

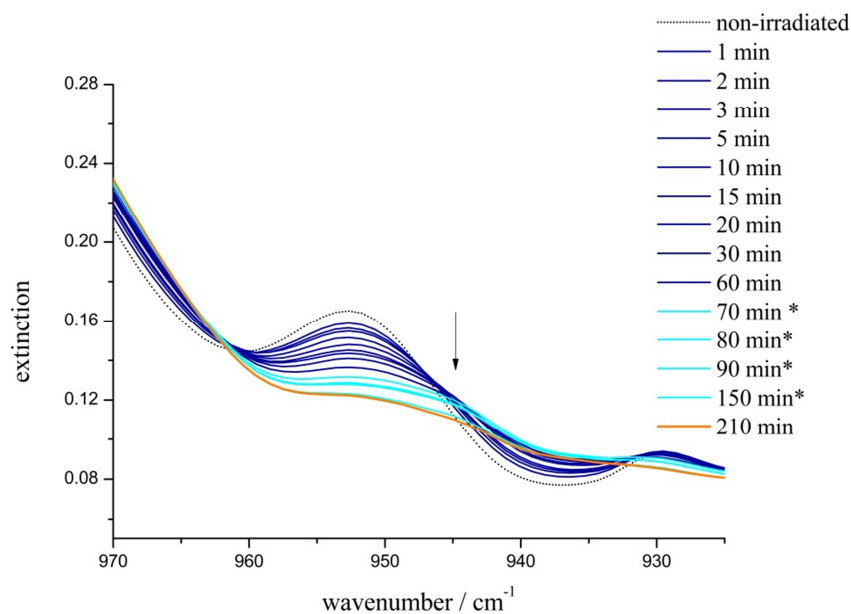


**Figure 4.4.14** IR spectra of **3** during irradiation with UV light ( $\lambda = 365$  nm) focusing on the decrease (the direction of the decrease is marked with an arrow) of the C<sub>Spiro</sub>-O band at approx.  $\tilde{\nu} = 950$  cm<sup>-1</sup>.

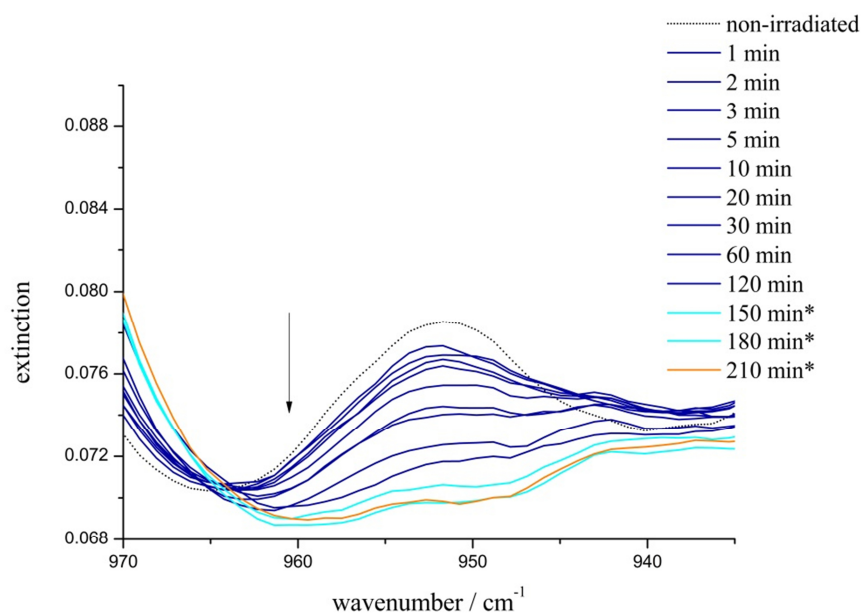


**Figure 4.4.15** IR spectra of **4** during irradiation with UV light ( $\lambda = 365$  nm) focusing on the decrease (the direction of the decrease is marked with an arrow) of the C<sub>Spiro</sub>-O band at approx.  $\tilde{\nu} = 950$  cm<sup>-1</sup>.

Cleavage of the C<sub>Spiro</sub>-O bond is a hint to the successful formation of the merocyanine moiety. However, simple photodegradation of SP-Nitro might directly occur upon irradiation with UV light. Hence, a clear assignment of all IR bands is obligatory.

Interestingly, MC-Nitro occurs in four different isomers, which are shown in figure 4.4.16 (with T for “*trans*” and C for “*cis*”). Among those isomers, the TTC form is most preferably produced upon photoirradiation followed by TTT, CTC and CTT.<sup>[196]</sup>

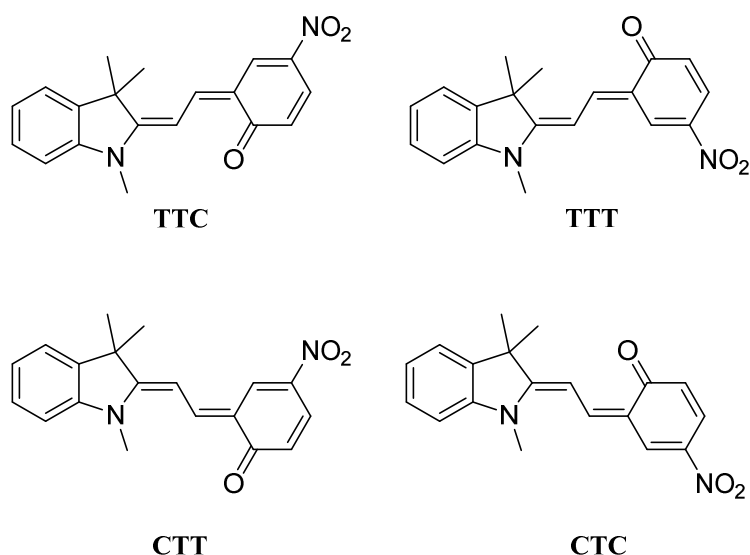


**Figure 4.4.16** Different isomers of the open merocyanine form of MC-Nitro.

*Nakata* and co-workers experimentally determined (in an argon matrix at 8 K) and calculated the vibrational numbers of the SP-Nitro and the TTC form of the corresponding merocyanine moiety. The authors found bands with the highest relative intensities (> 30%) for the following wavenumbers (tables 4.4.4 and 4.4.5):

**Table 4.4.4** Observed and calculated vibrational wavenumbers  $\tilde{\nu}$  (in  $\text{cm}^{-1}$ ) and relative intensities (in %) for SP-Nitro. Data were taken from *Nakata* and co-workers.<sup>[196]</sup>

obs.	rel. intensity / %	calc.	rel. intensity / %
1487	36		
1482	36		
1472	30		
<b>1348</b>	<b>100</b>	<b>1334</b>	<b>100</b>
1275	57	1264	54
		1072	33
959	40		
		934	47

**Table 4.4.5** Observed and calculated vibrational wavenumbers  $\tilde{\nu}$  (in  $\text{cm}^{-1}$ ) and relative intensities (in %) for the TTC isomer of the merocyanine moiety. Data were taken from *Nakata* and co-workers.<sup>[196]</sup>

obs.	rel. intensity / %	calc.	rel. intensity / %
1628	33	1627	33
		1551	88
		1490	68
1469	75		
<b>1324</b>	<b>100</b>	<b>1316</b>	<b>100</b>
1252	44	1247	42
1229	48		
1209	46	1210	31
1086	38		

The authors observed two intensive bands for each isomer at  $1348 \text{ cm}^{-1}$  (experimentally determined) for the closed SP form and at  $1324 \text{ cm}^{-1}$  (experimentally determined) for the open MC form (highlighted in both tables). Upon irradiation with UV light, the band for SP decreases and the band for MC increases; this can be easily followed in the IR spectra. In the present work, an exact assignment of the IR bands to the respective isomer (SP and TTC of MC, respectively) was performed for SP-Nitro incorporated in or combined with the four different MOF matrices. According to the experimental and calculated data of *Nakata* and co-workers on SP-Nitro<sup>[196]</sup>, decreasing and increasing IR bands were analyzed. Thereupon, the data of the non-irradiated species were subtracted from the irradiated ones to obtain  $\text{ext}_{\text{irrad}} - \text{ext}_{\text{ground state}}$ . The resulting spectra (figure 4.4.31 to 4.4.34) are found in chapter 4.4.1.3.3.

That way, the alterations upon UV light irradiation were detected. In the following tables 4.4.6 to 4.4.13 the changes upon UV light irradiation and assumed assignments are listed. Values marked with an “\*” were taken from the theoretical, without “\*” from the experimental data of *Nakata* and co-workers. Highlighted data represent the strongest bands with regard to intensity of *Nakata* et al. (fat: relative intensity > 30%; fat and underlined: intensity 100%). Types of vibrations were attributed according to *Lyubimov* and co-workers<sup>[197]</sup>, *Paal* and *Arnold*<sup>[198]</sup> and *Hesse, Meyer & Zeeh*<sup>[199]</sup>.

For an adequate assignment, the TTC mesomeric form of the merocyanine moiety of the spiropyran has to be examined more precisely with respect to changing bonds in comparison to the closed SP-Nitro. The structure is shown in figure 4.4.17 and compared to the closed SP-Nitro form.

Obviously, the rings I and II remain unaffected by the light induced cleavage of the  $C_{\text{Spiro}}\text{-O}$  bond, whereas ring I' is completely destroyed and II' changes structurally. Therefore, all vibrational modes related to the rings I and II remain.

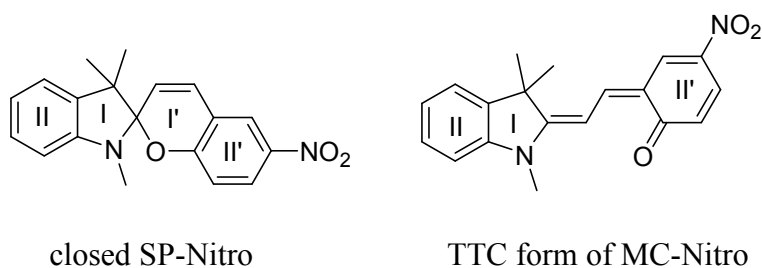


**Figure 4.4.17** Comparison of SP-Nitro in its closed form and the TTC form of the respective merocyanine.

**Table 4.4.6** Assignment of decreasing IR bands of SP-Nitro@MOF-5 (**1**) to experimental and calculated (“\*”) data of Nakata and co-workers<sup>[196]</sup>. Types of vibrations were attributed according to Lyubimov and co-workers<sup>[197]</sup>, Paal and Arnold<sup>[198]</sup> and Hesse, Meyer & Zeeh<sup>[199]</sup>.

decreasing bands / cm <sup>-1</sup>	assignment / cm <sup>-1</sup>	vibration mode
1652	SP(1654)	$\nu(\text{C}=\text{C}), \nu(\text{C}=\text{N})$ <sup>[198]</sup>
1610	SP(1615)	$\nu(\text{C}=\text{C}), \nu(\text{C}=\text{N})$ <sup>[198]</sup>
1589/1578	SP(1583)	ring-valence vibration $\nu(\text{C}=\text{C})$ <sup>[198]</sup>
1517	1508	ring-valence vibration $\nu(\text{C}=\text{C})$ <sup>[198]</sup>
<b>1479</b>	<b>SP(1482/1472)</b>	ring-valence vibration $\nu(\text{C}=\text{C})$ <sup>[198]</sup>
1398	1388 11398	<u>theoretical</u> <sup>[197]</sup> : $\nu(\text{C}-\text{C})$ (II) $\nu(\text{C}-\text{C})$ (II’) $\nu(\text{C}-\text{N})$ (I) $\nu(\text{H}-\text{C}_{\text{Methyl}}-\text{H})$ on N atom
1361	SP(1363)	$\nu(\text{C}-\text{N})$ <sup>[198]</sup>
<b>1334</b>	<b>SP(1334)*</b>	<u>theoretical</u> <sup>[197]</sup> : $\nu(\text{C}-\text{C})$ (I’-II’) $\nu(\text{C}-\text{C}-\text{H})$ (I)
1299	SP(1300)	<u>theoretical</u> <sup>[197]</sup> : $\nu(\text{C}-\text{N})$ (I) $\nu(\text{N}-\text{C}_{\text{Methyl}})$ (I) $\nu(\text{C}-\text{C}-\text{H})$ (II) $\nu(\text{C}-\text{N}-\text{C})$ (I)
<b>1275</b>	<b>SP(1275)</b>	<u>theoretical</u> <sup>[197]</sup> : $\nu(\text{C}-\text{O})$ $\nu(\text{C}-\text{C}-\text{H})$ (II) $\nu(\text{N}-\text{C}_{\text{Methyl}})$ (I) $\nu(\text{C}-\text{C}-\text{N})$ (I)
1220	SP(1221)	<u>theoretical</u> <sup>[197]</sup> : $\nu(\text{C}-\text{C})$ (II’)
1184	SP(1187)	<u>theoretical</u> <sup>[197]</sup> : $\nu(\text{C}_{\text{Spiro}}-\text{O})$ $\nu(\text{C}-\text{C}_{\text{Methyl}})$ (I) $\nu(\text{C}-\text{C})$ (I)

		$\nu(\text{C}-\text{C}_{\text{Methyl}}-\text{H})$ (I) $\nu(\text{C}_{\text{Spiro}}-\text{N})$ $\nu(\text{C}-\text{N})$ (I) $\nu(\text{C}-\text{C})$ (I) $\nu(\text{N}-\text{C}_{\text{Methyl}})$ (I) $\nu(\text{H}-\text{C}_{\text{Methyl}}-\text{H})$
1126	SP(1125)	<u>theoretical</u> <sup>[197]</sup> : $\nu(\text{N}-\text{C}_{\text{Methyl}})$ $\nu(\text{C}-\text{C})$ (I)
1089	SP(1101)	$\delta(\text{C}-\text{H})_{\text{arom.}}$ <sup>[198]</sup>
1023	SP(1025)	<u>theoretical</u> <sup>[197]</sup> : $\nu(\text{O}-\text{C}_{\text{Spiro}}-\text{C})$ (I') $\nu(\text{C}_{\text{Spiro}}-\text{O})$ $\nu(\text{N}-\text{C}-\text{C})$ (I')
1013	SP(1013)	<u>theoretical</u> <sup>[197]</sup> : $\nu(\text{C}-\text{C})$ (II) $\nu(\text{C}-\text{N})$ (I)
951	SP(959)	$\nu(\text{O}-\text{C}_{\text{Spiro}}-\text{N})$ <sup>[198]</sup>
927	SP(929)	<u>theoretical</u> <sup>[197]</sup> : $\nu(\text{C}-\text{C}_{\text{Methyl}}-\text{H})$
835	SP(838)	<u>theoretical</u> <sup>[197]</sup> : deviation of H atoms from the plane (I') out-of-plane vibrations (I'-II') $\nu(\text{C}_{\text{Spiro}}-\text{O})$
806	SP(810)	<u>theoretical</u> <sup>[197]</sup> : deviation of H atoms from the plane (II) out-of-plane vibrations (II)
777	SP(777)	<u>theoretical</u> <sup>[197]</sup> : deviation of H atoms from the plane (II) out-of-plane vibrations (II) $\nu(\text{C}-\text{C})$ (I) $\delta$ (II)
743	SP(743)	$\gamma(\text{C}-\text{H})$ benzene ring <sup>[198]</sup>
681	SP(685)	<u>theoretical</u> <sup>[197]</sup> : out-of-plane vibrations (I', II')

628

635

theoretical<sup>[197]</sup>:  
in-plane-ring bending  
vibrations/bond bending  
vibrations of (I', II') and (II)

**Table 4.4.7** Assignment of increasing IR bands of SP-Nitro@MOF-5 (**1**) to experimental and calculated (“\*”) data of *Nakata* and co-workers<sup>[196]</sup>. Types of vibrations were attributed according to *Lyubimov* and co-workers<sup>[197]</sup>, *Paal* and *Arnold*<sup>[198]</sup> and *Hesse, Meyer & Zeeh*<sup>[199]</sup>.

increasing bands / cm <sup>-1</sup>	assignment / cm <sup>-1</sup>	vibration mode
1686	1642	$\nu(\text{C}=\text{C}), \nu(\text{C}=\text{N})$ <sup>[198]</sup>
<b>1633</b>	<b>MC(1628)</b>	$\nu(\text{C}=\text{C}), \nu(\text{C}=\text{N})$ <sup>[198]</sup>
1617	1617	ring-valence vibration $\nu(\text{C}=\text{C})$ <sup>[198]</sup>
1596	MC(1595)*	<u>theoretical</u> <sup>[197]</sup> $\nu(\text{C}-\text{C})$ (II) $\nu(\text{C}-\text{C})$ (II)
1561	MC(1560)*	<u>theoretical</u> <sup>[197]</sup> $\nu(\text{C}-\text{C})$ (II')
1536	1600-1500	ring-valence vibration $\nu(\text{C}=\text{C})$ <sup>[198,199]</sup>
<b>1500</b>	<b>MC(1490)*</b>	ring-valence vibration $\nu(\text{C}=\text{C})$ <sup>[198,199]</sup>
1459	MC(1459)	<u>theoretical</u> <sup>[197]</sup> $\nu(\text{C}-\text{C})$ (II) $\nu(\text{C}-\text{N})$ (I) $\nu(\text{C}-\text{C}-\text{H})$ (II)
1436	MC(1430)*	<u>theoretical</u> <sup>[197]</sup> $\nu(\text{H}-\text{C}_{\text{Methyl}}-\text{H})$ on N atom $\nu(\text{H}-\text{C}_{\text{Methyl}}-\text{H})$ on C atom
1410	MC(1407)*	$\delta(\text{C}-\text{H})$ neighboring $\text{C}=\text{O}$ <sup>[199]</sup>
1385	MC(1388)	$\delta(\text{C}-\text{H})$ methyl-group of I <sup>[199]</sup>
<b>1317</b>	<b>MC(1316)*</b>	$\delta(\text{C}-\text{H})$ methyl-group of I <sup>[199]</sup>
1288	MC(1281)	<u>theoretical</u> <sup>[197]</sup> $\nu(\text{C}-\text{O})$ $\nu(\text{N}-\text{C}_{\text{Methyl}})$ (I) $\nu(\text{C}-\text{C}-\text{N})$ (I) $\nu(\text{C}-\text{C}-\text{H})$ (II)
<b>1241</b>	<b>MC(1247)*</b>	<u>theoretical</u> <sup>[197]</sup> $\nu(\text{C}-\text{C}-\text{O})$

<b>1210</b>	<b>MC(1210)*</b>	<u>theoretical</u> <sup>[197]</sup> $\nu(\text{C-C})$ (II')
1159	MC(1159)*	<u>theoretical</u> <sup>[197]</sup> $\nu(\text{C-C})$ (I) $\nu(\text{C-C}_{\text{Methyl-H}})$ (I) $\nu(\text{C-C}-\text{C}_{\text{Methyl}})$ (I)
1117	MC(1118)*	$\delta(\text{C-H})_{\text{arom.}}$ <sup>[198]</sup>
1097	MC(1090)	$\delta(\text{C-H})_{\text{arom.}}$ <sup>[198]</sup>
1078	MC(1073)*	<u>theoretical</u> <sup>[197]</sup> $\nu(\text{C-O})$
1052	MC(1048)	<u>theoretical</u> <sup>[197]</sup> $\delta(\text{II})$ $\nu(\text{N-C}_{\text{Methyl}})$
750	MC(745)	$\gamma(\text{C-H})$ (II) <sup>[199]</sup>

**Table 4.4.8** Assignment of decreasing IR bands of SP-Nitro@MIL-68(In) (2) to experimental and calculated (“\*”) data of Nakata and co-workers<sup>[196]</sup>. Types of vibrations were attributed according to Lyubimov and co-workers<sup>[197]</sup>, Paal and Arnold<sup>[198]</sup> and Hesse, Meyer & Zeeh<sup>[199]</sup>.

decreasing bands / cm <sup>-1</sup>	assignment / cm <sup>-1</sup>	vibration mode
1652	SP(1654)	$\nu(\text{C}=\text{C}), \nu(\text{C}=\text{N})$ <sup>[198]</sup>
1612	SP(1615)	$\nu(\text{C}=\text{C}), \nu(\text{C}=\text{N})$ <sup>[198]</sup>
1517	1508	ring-valence vibration $\nu(\text{C}=\text{C})$ <sup>[198]</sup>
<b>1479</b>	<b>SP(1482/1472)</b>	ring-valence vibration $\nu(\text{C}=\text{C})$ <sup>[198]</sup>
<b>1332</b>	<b>SP(1334)*</b>	<u>theoretical</u> <sup>[197]</sup> : $\nu(\text{C}-\text{C})$ (I <sup>2</sup> -II <sup>1</sup> ) $\nu(\text{C}-\text{C}-\text{H})$ (I)
<b>1272</b>	<b>SP(1275)</b>	<u>theoretical</u> <sup>[197]</sup> : $\nu(\text{C}-\text{O})$ $\nu(\text{C}-\text{C}-\text{H})$ (II) $\nu(\text{N}-\text{C}_{\text{Methyl}})$ (I) $\nu(\text{C}-\text{C}-\text{N})$ (I)
1090	SP(1101)	$\delta(\text{C}-\text{H})_{\text{arom.}}$ <sup>[198]</sup>
1023	SP(1025)	<u>theoretical</u> <sup>[197]</sup> : $\nu(\text{O}-\text{C}_{\text{Spiro}}-\text{C})$ (I <sup>1</sup> ) $\nu(\text{C}_{\text{Spiro}}-\text{O})$ $\nu(\text{N}-\text{C}-\text{C})$ (I <sup>1</sup> )
1013	SP(1013)	<u>theoretical</u> <sup>[197]</sup> : $\nu(\text{C}-\text{C})$ (II) $\nu(\text{C}-\text{N})$ (I)
952	SP(959)	$\nu(\text{O}-\text{C}_{\text{Spiro}}-\text{N})$ <sup>[198]</sup>
929	SP(929)	<u>theoretical</u> <sup>[197]</sup> : $\nu(\text{C}-\text{C}_{\text{Methyl}}-\text{H})$
806	SP(810)	<u>theoretical</u> <sup>[197]</sup> : deviation of H atoms from the plane (II) out-of-plane vibrations (II)
741	SP(743)	$\gamma(\text{C}-\text{H})$ benzene ring <sup>[198]</sup>

681

| SP(685)

| theoretical<sup>[197]</sup>:  
| out-of-plane vibrations (I', II')

**Table 4.4.9** Assignment of increasing IR bands of SP-Nitro@MIL-68(In) (**2**) to experimental and calculated (“\*”) data of Nakata and co-workers<sup>[196]</sup>. Types of vibrations were attributed according to Lyubimov and co-workers<sup>[197]</sup>, Paal and Arnold<sup>[198]</sup> and Hesse, Meyer & Zeeh<sup>[199]</sup>.

increasing bands / cm <sup>-1</sup>	assignment / cm <sup>-1</sup>	vibration mode
1675	1642	$\nu(\text{C}=\text{C}), \nu(\text{C}=\text{N})$ <sup>[198]</sup>
<b>1622</b>	<b>MC(1628)</b>	$\nu(\text{C}=\text{C}), \nu(\text{C}=\text{N})$ <sup>[198]</sup>
1603/1592	MC(1595)*	<u>theoretical</u> <sup>[197]</sup> $\nu(\text{C}-\text{C})$ (II) $\nu(\text{C}-\text{C})$ (II)
1565	MC(1560)*	<u>theoretical</u> <sup>[197]</sup> $\nu(\text{C}-\text{C})$ (II') $\nu(\text{C}=\text{N})$ (I')
1532	1600-1500	ring-valence vibration $\nu(\text{C}=\text{C})$ <sup>[198,199]</sup>
<b>1498</b>	<b>MC(1490)*</b>	ring-valence vibration $\nu(\text{C}=\text{C})$ <sup>[198,199]</sup>
1458	MC(1459)	<u>theoretical</u> <sup>[197]</sup> $\nu(\text{C}-\text{C})$ (II) $\nu(\text{C}-\text{N})$ (I) $\nu(\text{C}-\text{C}-\text{H})$ (II)
1438	MC(1430)*	<u>theoretical</u> <sup>[197]</sup> $\nu(\text{H}-\text{C}_{\text{Methyl}}-\text{H})$ on N atom $\nu(\text{H}-\text{C}_{\text{Methyl}}-\text{H})$ on C atom
1412	MC(1407)*	$\delta(\text{C}-\text{H})$ neighboring C=O <sup>[199]</sup>
1387	MC(1388)	$\delta(\text{C}-\text{H})$ methyl-group of I <sup>[199]</sup>
1369	MC(1365)	$\delta(\text{C}-\text{H})$ methyl-group of I <sup>[199]</sup>
<b>1308</b>	<b>MC(1314)*</b>	$\delta(\text{C}-\text{H})$ methyl-group of I <sup>[199]</sup>
1286	MC(1281)	<u>theoretical</u> <sup>[197]</sup> $\nu(\text{C}-\text{O})$ $\nu(\text{N}-\text{C}_{\text{Methyl}})$ (I) $\nu(\text{C}-\text{C}-\text{N})$ (I) $\nu(\text{C}-\text{C}-\text{H})$ (II)

1255	MC(1252)*	<u>theoretical</u> <sup>[197]</sup> v(C–C) (I) v(C–C–C <sub>Methyl</sub> ) v(C–C <sub>Methyl</sub> –H)
1212	MC(1210)*	<u>theoretical</u> <sup>[197]</sup> v(C–C) (II')
1157	MC(1159)*	<u>theoretical</u> <sup>[197]</sup> v(C–C) (I) v(C–C <sub>Methyl</sub> –H) (I) v(C–C–C <sub>Methyl</sub> ) (I)
1134	MC(1126)	<u>theoretical</u> <sup>[197]</sup> v(C–C) (II') v(C–C–H) (II')
1115	MC(1119)*	$\delta(\text{C–H})_{\text{arom.}}$ <sup>[198]</sup>
1080	MC(1086)*	<u>theoretical</u> <sup>[197]</sup> v(C–O)
1043	MC(1048)	<u>theoretical</u> <sup>[197]</sup> $\delta(\text{II})$ v(N–C <sub>Methyl</sub> )
1018	MC(1220)	<u>theoretical</u> <sup>[197]</sup> v(C–C) (II) v(C–N) (I)
1007	MC(1005)*	<u>theoretical</u> <sup>[197]</sup> v(C–C) (II) v(C–N) (I)
981	945 988	<u>theoretical</u> <sup>[197]</sup> $\delta(\text{C}_{\text{Methyl}}\text{–H})$ v(C–N) (I)
938	MC(933)	<u>theoretical</u> <sup>[197]</sup> v(C–C <sub>Methyl</sub> –H)
866	865 868	<u>theoretical</u> <sup>[197]</sup> v(C–N) (I) v(C–C <sub>Methyl</sub> –H) $\delta(\text{II}')$
717	MC(719)	<u>theoretical</u> <sup>[197]</sup> deviation of H atoms from the plane (II)
623	MC(625)	$\delta(\text{II})$ out-of-plane vibrations (II')

**Table 4.4.10** Assignment of decreasing IR bands of SP-Nitro@MIL-68(Ga) (**3**) to experimental and calculated (“\*”) data of Nakata and co-workers<sup>[196]</sup>. Types of vibrations were attributed according to Lyubimov and co-workers<sup>[197]</sup>, Paal and Arnold<sup>[198]</sup> and Hesse, Meyer & Zeeh<sup>[199]</sup>.

decreasing bands / cm <sup>-1</sup>	assignment / cm <sup>-1</sup>	vibration mode
1650	SP(1654)	$\nu(\text{C}=\text{C}), \nu(\text{C}=\text{N})$ <sup>[198]</sup>
1580	SP(1583)	ring-valence vibration $\nu(\text{C}=\text{C})$ <sup>[198]</sup>
<b>1478</b>	<b>SP(1482/1472)</b>	ring-valence vibration $\nu(\text{C}=\text{C})$ <sup>[198]</sup>
<b>1334</b>	<b>SP(1334)*</b>	<u>theoretical</u> <sup>[197]</sup> : $\nu(\text{C}-\text{C})$ (I’-II’) $\nu(\text{C}-\text{C}-\text{H})$ (I)
<b>1274</b>	<b>SP(1275)</b>	<u>theoretical</u> <sup>[197]</sup> : $\nu(\text{C}-\text{O})$ $\nu(\text{C}-\text{C}-\text{H})$ (II) $\nu(\text{N}-\text{C}_{\text{Methyl}})$ (I) $\nu(\text{C}-\text{C}-\text{N})$ (I)
1224	SP(1221)	<u>theoretical</u> <sup>[197]</sup> : $\nu(\text{C}-\text{C})$ (II’)
952	SP(959)	$\nu(\text{O}-\text{C}_{\text{Spiro}}-\text{N})$ <sup>[198]</sup>
929	SP(929)	<u>theoretical</u> <sup>[197]</sup> : $\nu(\text{C}-\text{C}_{\text{Methyl}}-\text{H})$
917	912	<u>theoretical</u> <sup>[197]</sup> : deviation of H atoms from the plane (II’)
904	903	<u>theoretical</u> <sup>[197]</sup> : deviation of H atoms from the plane (II) deviation of H atoms from the plane (II’) deviation of H atoms from the plane (I’) $\nu(\text{C}-\text{C}_{\text{Methyl}})$ (I)

807	SP(810)	<u>theoretical</u> <sup>[197]</sup> : deviation of H atoms from the plane (II) out-of-plane vibrations (II)
743	SP(743)	$\gamma$ (C–H) benzene ring <sup>[198]</sup>
681	SP(685)	<u>theoretical</u> <sup>[197]</sup> : out-of-plane vibrations (I', II')

**Table 4.4.11** Assignment of increasing IR bands of SP-Nitro@MIL-68(Ga) (**3**) to experimental and calculated (“\*”) data of Nakata and co-workers<sup>[196]</sup>. Types of vibrations were attributed according to Lyubimov and co-workers<sup>[197]</sup>, Paal and Arnold<sup>[198]</sup> and Hesse, Meyer & Zeeh<sup>[199]</sup>.

increasing bands / cm <sup>-1</sup>	assignment / cm <sup>-1</sup>	vibration mode
1676	1642	$\nu(\text{C}=\text{C}), \nu(\text{C}=\text{N})$ <sup>[198]</sup>
<b>1620</b>	<b>MC(1628)</b>	$\nu(\text{C}=\text{C}), \nu(\text{C}=\text{N})$ <sup>[198]</sup>
1603/1593	MC(1595)*	<u>theoretical</u> <sup>[197]</sup> $\nu(\text{C}-\text{C})$ (II) $\nu(\text{C}-\text{C})$ (II)
1573	1587 1591	<u>theoretical</u> <sup>[197]</sup> $\nu(\text{C}-\text{C})$ (II') $\nu(\text{C}-\text{C})$ (II) $\nu(\text{C}-\text{C}-\text{H})$ (II) $\nu(\text{C}-\text{C}-\text{H})$ (II')
1531	1600-1500	ring-valence vibration $\nu(\text{C}=\text{C})$ <sup>[198,199]</sup>
<b>1504</b>	<b>MC(1490)*</b>	ring-valence vibration $\nu(\text{C}=\text{C})$ <sup>[198,199]</sup>
1459	MC(1459)	<u>theoretical</u> <sup>[197]</sup> $\nu(\text{C}-\text{C})$ (II) $\nu(\text{C}-\text{N})$ (I) $\nu(\text{C}-\text{C}-\text{H})$ (II)
1438	MC(1430)*	<u>theoretical</u> <sup>[197]</sup> $\nu(\text{H}-\text{C}_{\text{Methyl}}-\text{H})$ on N atom $\nu(\text{H}-\text{C}_{\text{Methyl}}-\text{H})$ on C atom
1415	MC(1407)*	$\delta(\text{C}-\text{H})$ neighboring C=O <sup>[199]</sup>
1396	MC(1399)	$\delta(\text{C}-\text{H})$ methyl-group of I <sup>[199]</sup>
1368	MC(1365)*	$\delta(\text{C}-\text{H})$ methyl-group of I <sup>[199]</sup>
<b>1309</b>	<b>MC(1314)*</b>	$\delta(\text{C}-\text{H})$ methyl-group of I <sup>[199]</sup>
1287	MC(1281)	<u>theoretical</u> <sup>[197]</sup> $\nu(\text{C}-\text{O})$ $\nu(\text{N}-\text{C}_{\text{Methyl}})$ (I) $\nu(\text{C}-\text{C}-\text{N})$ (I) $\nu(\text{C}-\text{C}-\text{H})$ (II)

1256	MC(1252)*	<u>theoretical</u> <sup>[197]</sup> v(C–C) (I) v(C–C–C <sub>Methyl</sub> ) v(C–C <sub>Methyl</sub> –H)
1213	MC(1210)*	<u>theoretical</u> <sup>[197]</sup> v(C–C) (II')
1158	MC(1159)*	<u>theoretical</u> <sup>[197]</sup> v(C–C) (I) v(C–C <sub>Methyl</sub> –H) (I) v(C–C–C <sub>Methyl</sub> ) (I)
1133	MC(1126)	<u>theoretical</u> <sup>[197]</sup> v(C–C) (II') v(C–C–H) (II')
1116	MC(1119)*	$\delta(\text{C–H})_{\text{arom.}}$ <sup>[198]</sup>
1082	MC(1086)*	<u>theoretical</u> <sup>[197]</sup> v(C–O)
1042	MC(1048)	<u>theoretical</u> <sup>[197]</sup> $\delta(\text{II})$ v(N–C <sub>Methyl</sub> )
970	MC(965)*	<u>theoretical</u> <sup>[197]</sup> $\delta(\text{C}_{\text{Methyl}}\text{–H})$ v(C–N) (I)
940	MC(943)	<u>theoretical</u> <sup>[197]</sup> v(C–C <sub>Methyl</sub> –H)
890	MC(898)*	<u>theoretical</u> <sup>[197]</sup> deviation of H atoms from the plane (II, II') v(C–C <sub>Methyl</sub> ) (I)
872	MC(878)*	<u>theoretical</u> <sup>[197]</sup> v(C–N) (I) $\delta(\text{II}')$
859	853	<u>theoretical</u> <sup>[197]</sup> $\delta(\text{I})$
838	MC(831)	<u>theoretical</u> <sup>[197]</sup> out-of-plane vibrations (II')
717	MC(719)	<u>theoretical</u> <sup>[197]</sup> deviation of H atoms from the plane (II)

620

MC(617)

theoretical<sup>[197]</sup>  
 $\delta(\Pi)$   
out-of-plane vibrations ( $\Pi'$ )

**Table 4.4.12** Assignment of decreasing IR bands of SP-Nitro@MIL-53(Al) (**4**) to experimental and calculated (“\*”) data of Nakata and co-workers<sup>[196]</sup>. Types of vibrations were attributed according to Lyubimov and co-workers<sup>[197]</sup>, Paal and Arnold<sup>[198]</sup> and Hesse, Meyer & Zeeh<sup>[199]</sup>.

decreasing bands / cm <sup>-1</sup>	assignment / cm <sup>-1</sup>	vibration mode
1633	1642	$\nu(\text{C}=\text{C}), \nu(\text{C}=\text{N})$ <sup>[198]</sup>
1576	SP(1583)	ring-valence vibration $\nu(\text{C}=\text{C})$ <sup>[198]</sup>
1523	SP(1535)	ring-valence vibration $\nu(\text{C}=\text{C})$ <sup>[198]</sup>
<b>1488</b>	<b>SP(1487)</b>	<u>theoretical</u> <sup>[197]</sup> : $\nu(\text{C}-\text{C})$ (II’) $\nu(\text{C}-\text{C}-\text{H})$ (II’)
<b>1479</b>	<b>SP(1482/1472)</b>	ring-valence vibration $\nu(\text{C}=\text{C})$ <sup>[198]</sup>
1422	SP(1421)	<u>theoretical</u> <sup>[197]</sup> : $\nu(\text{C}-\text{C})$ (II’) $\nu(\text{H}-\text{C}_{\text{Methyl}}-\text{H})$
1397	1388 11398	<u>theoretical</u> <sup>[197]</sup> : $\nu(\text{C}-\text{C})$ (II) $\nu(\text{C}-\text{C})$ (II’) $\nu(\text{C}-\text{N})$ (I) $\nu(\text{H}-\text{C}_{\text{Methyl}}-\text{H})$ on N atom
1364	SP(1363)	$\nu(\text{C}-\text{N})$ <sup>[198]</sup>
<b>1334</b>	<b>SP(1334)*</b>	<u>theoretical</u> <sup>[197]</sup> : $\nu(\text{C}-\text{C})$ (I’-II’) $\nu(\text{C}-\text{C}-\text{H})$ (I)
1300	SP(1300)	<u>theoretical</u> <sup>[197]</sup> : $\nu(\text{C}-\text{N})$ (I) $\nu(\text{N}-\text{C}_{\text{Methyl}})$ (I) $\nu(\text{C}-\text{C}-\text{H})$ (II) $\nu(\text{C}-\text{N}-\text{C})$ (I)
<b>1271</b>	<b>SP(1275)</b>	<u>theoretical</u> <sup>[197]</sup> : $\nu(\text{C}-\text{O})$ $\nu(\text{C}-\text{C}-\text{H})$ (II) $\nu(\text{N}-\text{C}_{\text{Methyl}})$ (I) $\nu(\text{C}-\text{C}-\text{N})$ (I)

1184	SP(1187)	<u>theoretical</u> <sup>[197]</sup> : $\nu(\text{C}_{\text{Spiro}}-\text{O})$ $\nu(\text{C}-\text{C}_{\text{Methyl}})$ (I) $\nu(\text{C}-\text{C})$ (I) $\nu(\text{C}-\text{C}_{\text{Methyl}}-\text{H})$ (I) $\nu(\text{C}_{\text{Spiro}}-\text{N})$ $\nu(\text{C}-\text{N})$ (I) $\nu(\text{C}-\text{C})$ (I) $\nu(\text{N}-\text{C}_{\text{Methyl}})$ (I) $\nu(\text{H}-\text{C}_{\text{Methyl}}-\text{H})$
1124	SP(1125)	<u>theoretical</u> <sup>[197]</sup> : $\nu(\text{N}-\text{C}_{\text{Methyl}})$ $\nu(\text{C}-\text{C})$ (I)
1105	SP(1109)	$\delta(\text{C}-\text{H})_{\text{arom.}}$ <sup>[198]</sup>
1090	SP(1084)	<u>theoretical</u> <sup>[197]</sup> : $\nu(\text{C}-\text{C})$ (I') $\nu(\text{C}-\text{N})$ (I') $\nu(\text{C}_{\text{Spiro}}-\text{O})$ $\nu(\text{C}_{\text{Spiro}}-\text{O}-\text{C})$ (I')
1024	SP(1025)	<u>theoretical</u> <sup>[197]</sup> : $\nu(\text{O}-\text{C}_{\text{Spiro}}-\text{C})$ (I') $\nu(\text{C}_{\text{Spiro}}-\text{O})$ $\nu(\text{N}-\text{C}-\text{C})$ (I')
<b>951</b>	<b>SP(959)</b>	$\nu(\text{O}-\text{C}_{\text{Spiro}}-\text{N})$ <sup>[198]</sup>
929	SP(929)	<u>theoretical</u> <sup>[197]</sup> : $\nu(\text{C}-\text{C}_{\text{Methyl}}-\text{H})$
807	SP(810)	<u>theoretical</u> <sup>[197]</sup> : deviation of H atoms from the plane (II) out-of-plane vibrations (II)
766	SP(762)*	<u>theoretical</u> <sup>[197]</sup> : $\delta$ (II) out-of-plane vibrations (II') $\nu(\text{C}-\text{C})$ (I)
741	SP(743)	$\gamma(\text{C}-\text{H})$ benzene ring <sup>[198]</sup>
698	719	<u>theoretical</u> <sup>[197]</sup> : deviation of H atoms from the plane (II)

679	SP(685)	<u>theoretical</u> <sup>[197]</sup> . out-of-plane vibrations (I', II')
633	635	<u>theoretical</u> <sup>[197]</sup> . in-plane-ring bending vibrations/bond bending vibrations of (I', II') and (II)

**Table 4.4.13** Assignment of increasing IR bands of SP-Nitro@MIL-53(Al) (**4**) to experimental and calculated (“\*”) data of Nakata and co-workers<sup>[196]</sup>. Types of vibrations were attributed according to Lyubimov and co-workers<sup>[197]</sup>, Paal and Arnold<sup>[198]</sup> and Hesse, Meyer & Zeeh<sup>[199]</sup>.

increasing bands / cm <sup>-1</sup>	assignment / cm <sup>-1</sup>	vibration mode
1723/1700	1642	$\nu(\text{C}=\text{C}), \nu(\text{C}=\text{N})$ <sup>[198]</sup>
1593	MC(1595)*	<u>theoretical</u> <sup>[197]</sup> $\nu(\text{C}-\text{C})$ (II) $\nu(\text{C}-\text{C})$ (II)
1531	1600-1500	ring-valence vibration $\nu(\text{C}=\text{C})$ <sup>[198,199]</sup>
1512	MC(1513)*	ring-valence vibration $\nu(\text{C}=\text{C})$ <sup>[198,199]</sup>
<b>1504</b>	<b>MC(1490)*</b>	ring-valence vibration $\nu(\text{C}=\text{C})$ <sup>[198,199]</sup>
1440	MC(1448)*	<u>theoretical</u> <sup>[197]</sup> $\nu(\text{H}-\text{C}_{\text{Methyl}}-\text{H})$ on N atom $\nu(\text{H}-\text{C}_{\text{Methyl}}-\text{H})$ on C atom
1415	MC(1420)	$\delta(\text{C}-\text{H})$ neighboring C=O <sup>[199]</sup>
<b>1310</b>	<b>MC(1314)*</b>	$\delta(\text{C}-\text{H})$ methyl-group of I <sup>[199]</sup>
1289	MC(1281)	<u>theoretical</u> <sup>[197]</sup> $\nu(\text{C}-\text{O})$ $\nu(\text{N}-\text{C}_{\text{Methyl}})$ (I) $\nu(\text{C}-\text{C}-\text{N})$ (I) $\nu(\text{C}-\text{C}-\text{H})$ (II)
<b>1257</b>	<b>MC(1252)*</b>	<u>theoretical</u> <sup>[197]</sup> $\nu(\text{C}-\text{C})$ (I) $\nu(\text{C}-\text{C}-\text{C}_{\text{Methyl}})$ $\nu(\text{C}-\text{C}_{\text{Methyl}}-\text{H})$
1234	MC(1229)	<u>theoretical</u> <sup>[197]</sup> $\nu(\text{C}-\text{C})$ (II') $\nu(\text{C}-\text{C}-\text{O})$
<b>1211</b>	<b>MC(1210)*</b>	<u>theoretical</u> <sup>[197]</sup> $\nu(\text{C}-\text{C})$ (II')
1167/1157	MC(1159)*	<u>theoretical</u> <sup>[197]</sup> $\nu(\text{C}-\text{C})$ (I)

		$\nu(\text{C}-\text{C}_{\text{Methyl}}-\text{H})$ (I) $\nu(\text{C}-\text{C}-\text{C}_{\text{Methyl}})$ (I)
<b>1080</b>	<b>MC(1086)*</b>	<u>theoretical</u> <sup>[197]</sup> $\nu(\text{C}-\text{O})$
987	945 988	<u>theoretical</u> <sup>[197]</sup> $\delta(\text{C}_{\text{Methyl}}-\text{H})$ $\nu(\text{C}-\text{N})$ (I)
942	MC(943)	<u>theoretical</u> <sup>[197]</sup> $\nu(\text{C}-\text{C}_{\text{Methyl}}-\text{H})$
756	765 771	<u>theoretical</u> <sup>[197]</sup> $\delta(\text{II})$ $\nu(\text{C}-\text{C})$ (I) out-of-plane vibrations (II')

For all compounds **1** to **4** the IR bands of increasing and decreasing intensity were completely attributed to SP-Nitro and MC-Nitro. The light induced changes are followed by the formation of the merocyanine moiety, which is clearly seen in the position of the increasing IR bands, whereas the positions of the decreasing bands show the isomerization of SP-Nitro to MC-Nitro. Besides, the TTC isomer of MC-Nitro is present inside the different MOF matrices, which is not surprising, since this isomer is preferably produced. Therefore, this classification leads to the conclusion that exposure to UV light causes the formation of merocyanine in a first step. Response of embedded SP-Nitro to prolonged UV light exposure is discussed in chapter 4.4.1.3.3.

#### 4.4.1.3.2 Influence of the Host Matrices on the Absorption Properties

The influence of the surrounding media on the electronic structure of the merocyanine has previously been elucidated in chapter 2.2 and is referred to as solvatochromism. For compounds **1** to **4** different absorption behaviors are observed. When embedded in MOF-5, MC-Nitro exhibits a blue-shifted reflection minimum in comparison to the other hybrid materials **2** to **4**. In MIL-53(Al) a red-shifted reflection minimum is observed for MC-Nitro. In figure 4.4.18 the reflection minima of irradiated **1** to **4** are shown and compared. All data were recorded in air.

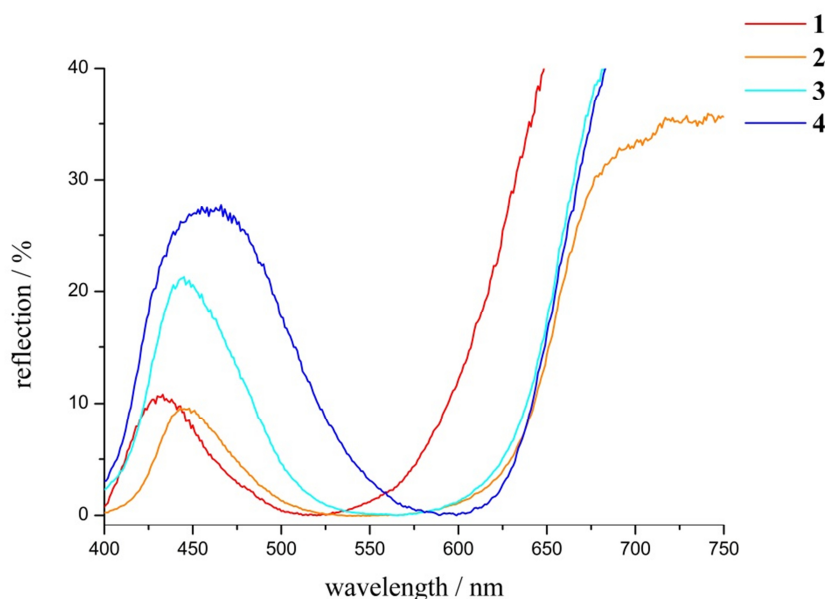


**Figure 4.4.18** Reflection spectra (298 K) of irradiated **1** to **4** ( $\lambda = 365$  nm, 1 min).

Apparently, MC-Nitro exhibits varying absorption properties depending on the used MOF host. While incorporation into MOF-5 already causes a stabilization of MC-Nitro in the absence of UV light and shows a reflection minimum at lower wavelengths, the reflection minima of **2** to **4** are increasingly red-shifted. Taking SP-Nitro's property of negative solvatochromism into account, MOF-5 represents the most polar and MIL-53(Al) the least polar MOF in this study. For understanding this response of MC-Nitro, the structure of the used host materials has to be examined more closely: The same  $bdc^{2-}$  linker molecule is used in all MOFs. Consequently, alterations in the absorption behavior must be related to the inorganic nodes, which are  $[Zn_4O]^{6+}$  for MOF-5 and  $[InOH]^{2+}$  and  $[GaOH]^{2+}$  for MIL-68(In) and MIL-68(Ga), respectively. By contrasting the differences in charge, MOF-5 is more polar than the representatives of the MIL-68 family. The higher polarity of MOF-5 is manifested in

the blue-shifted reflection minimum of **1** and the stabilization of MC-Nitro without UV light irradiation. For MIL-68(In) and MIL-68(Ga) the increasing charge / radius ratio from  $\text{In}^{3+}$  and  $\text{Ga}^{3+}$  is apparently too small to result in a marked alteration in the reflection spectra of **2** and **3**. The inorganic nodes of MIL-53(Al) are  $[\text{AlOH}]^{2+}$  units, which should exhibit a polarity between that of MOF-5 and the MIL-68 family. Nevertheless, there is a strong bathochromic shift associated with the lack of embedment. Hence, the assumption of SP-Nitro being mainly adsorbed on the MOF surface is strengthened. Consequently, the surface of MIL-53(Al) is less polar than the chemical environment given by the MOF pore. Hence, adsorption of SP-Nitro on the surface of MIL-53(Al) causes a red-shifted reflection minimum and, therefore, the blueish color of MC-Nitro.

By comparing the colors of MC-Nitro combined with the different MOFs (figure 4.4.19, left) with the colors when dissolved in solvents of varying polarity (figure 4.4.19, right), MC-Nitro@MOF-5 (**1**) corresponds to the absorption properties of MC-Nitro dissolved in methanol or ethanol, MC-Nitro@MIL-68(In) and MC-Nitro@MIL-68(Ga) to acetone and MC-Nitro@MIL-53(Al) to toluene. Thus, the environment of the MOF pores clearly influences the electronic structure of the embedded SP-Nitro such as solvents of different polarity do.



**Figure 4.4.19** Left: photography of compounds **1** to **4** after irradiation with UV light ( $\lambda = 365$  nm, 1 min); right: photography of MC-Nitro dissolved in solvents of varying polarity.

The ability to successfully isomerize from SP-Nitro to MC-Nitro upon UV light irradiation and dependence of the absorption properties on the used host material are similar to the dissolved state. On top of that, MOF-5 already stabilizes MC-Nitro in non-irradiated **1**, which is an indication of a high polarity of the chemical environment given by the MOF pore. Taking all of this into account, MOFs can be understood as “solid solvents” for spiropyran. To illustrate the correlation between MOF and solvent, the absorption maxima of MC-Nitro

dissolved in different solvents were plotted as a function of the elution power  $\epsilon^0$  of the respective solvent on alumina according to *Snyder*<sup>[193]</sup> (see figure 4.4.20). The values (blue dots) were linearly fitted (blue broken line) and the reflection minima of **1** to **4** were added (red squares). Thus, the polarity of the used MOF hosts was estimated. It has to be stated that the centers of the reflection minima were taken (since the minima are very broad). Hence, the presented results are only of qualitative but not quantitative value.

According to the plot in figure 4.4.20 MOF-5 is even more polar than methanol. Both, MIL-68(In) and MIL-68(Ga) feature a polarity in the region of acetonitrile and acetone, whereas the polarity of MIL-53(Al) (the surface) is in the region of toluene. These results demonstrate that the assumption “MOF equals a solvent” is admissible and strengthens the concept of MOFs as “solid solvents”. However, further proof with other photoactive guest molecules has to be given, which will be part of chapters 4.5 and 4.6.

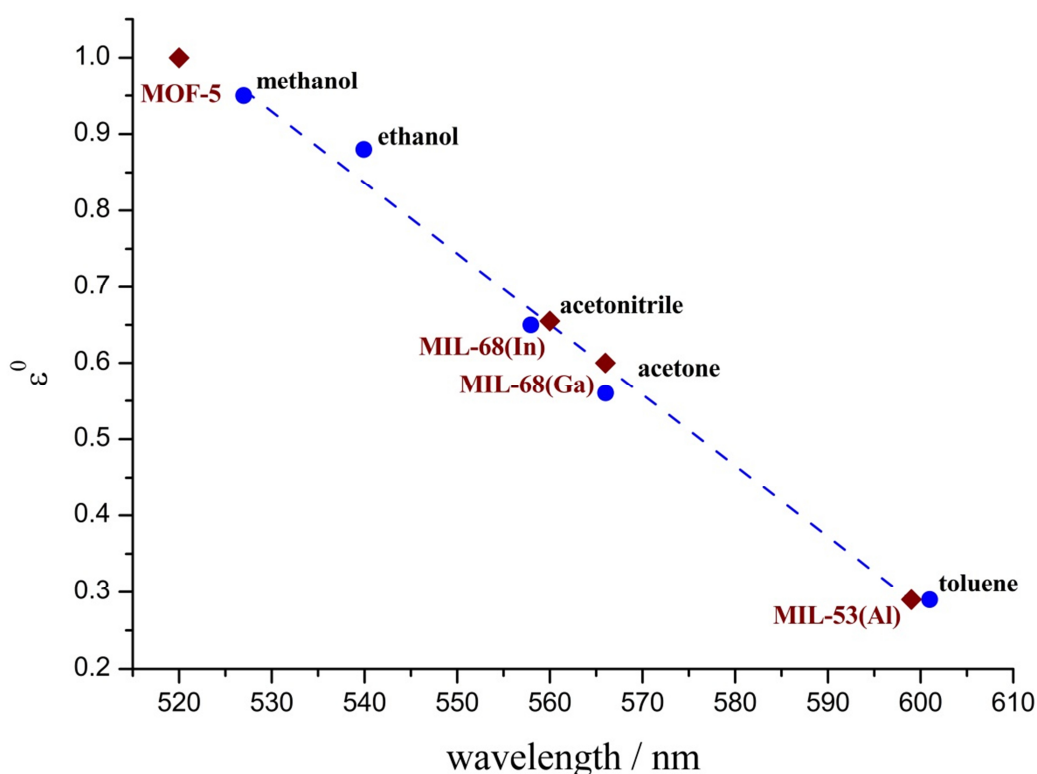


**Figure 4.4.20** Plot of the wavelength of the absorption maxima of MC-Nitro dissolved in different solvents (blue dots) versus the elution power  $\epsilon^0$  on alumina taken from *Snyder*<sup>[193]</sup>, classifying the polarity of the respective MOFs (red squares).

#### 4.4.1.3.3 Reversibility of Switching and Photostability

With regard to possible applications the reversibility of switching and photostability are obligatory to address. Hence, experiments with repetitive and prolonged UV light irradiation were done and investigated by means of UV/vis, IR and fluorescence spectroscopy.

Reversibility of switching was exemplarily investigated for SP-Nitro@MIL-68(Ga). On that occasion, the compound was measured in a KBr pellet under inert conditions. For thermal treatment, the pellet was placed in a simple laboratory oven at different temperatures and for varying heating times. The resulting absorption spectra are shown in figure 4.4.21.

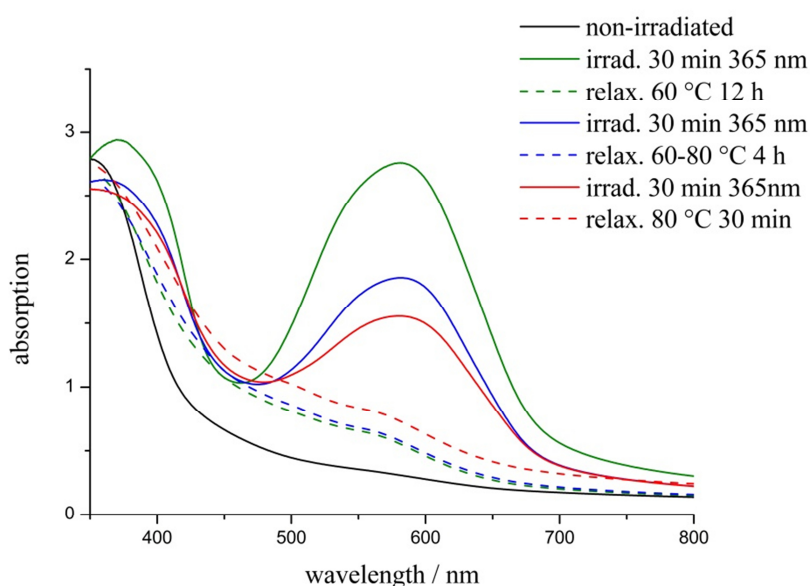


**Figure 4.4.21** Absorption spectra of **3** after irradiation with UV light ( $\lambda = 365$  nm) and heat treatment.

For non-irradiated SP-Nitro@MIL-68(Ga) no local absorption maximum is found (black solid line). After irradiation with UV light the MC-Nitro band becomes visible (green solid line). When thermally treated at 60 °C for 12 h (green broken line), the MC band vanishes. However, reconversion to the ground state is not completely achieved. Further, UV light exposure results in the formation of MC-Nitro, but the intensity of the MC-Nitro band decreases (blue and red solid line). Moreover, the absorption of the heated sample increases (blue and red broken line).

By plotting switching and thermal treatment cycles as a function of the maximal absorption of the relaxed (green squares) and irradiated (red dots) species, a trend towards a limit value for

repetitive UV light exposure is obvious, which is depicted in figure 4.4.22. These findings are pointing to a low fatigue resistance and gradual photodegradation with increasing numbers of switching cycles.

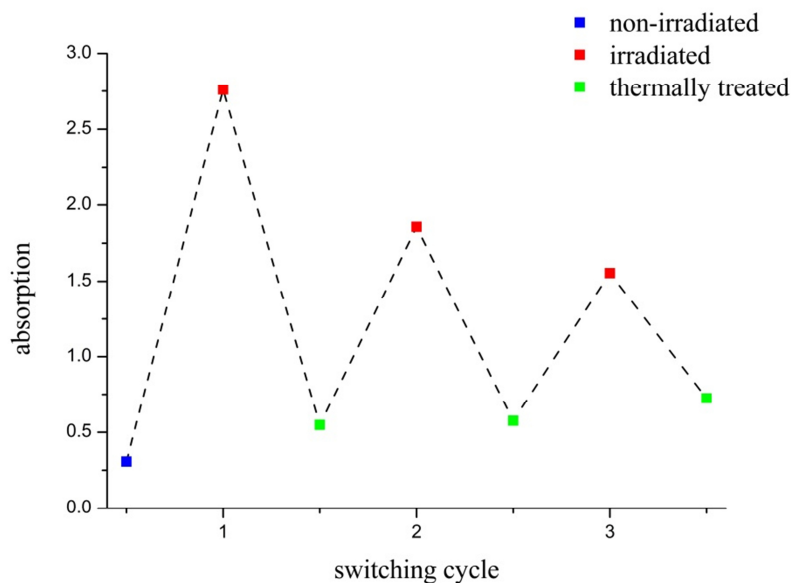


**Figure 4.4.22** Switching cycles for SP-Nitro@MIL-68(Ga) (**3**) as a function of the maximal absorption of the thermally treated (green squares) and irradiated (red squares) species. Non-irradiated **3** is colored in blue.

Reconversion to the SP form was further investigated by means of IR spectroscopy. Thereupon, all compounds were excited with UV light for an extended time to achieve a full conversion from SP-Nitro to MC-Nitro. Afterwards, the samples were first exposed to light of different wavelengths (450 nm, 530 nm, 590 nm and 660 nm) to induce back transformation of the excited species. Additionally, all compounds were thermally treated at 50 °C in a laboratory oven. Since spiropyrans belong to the T-type chromophores, both ways (thermal and photochemical) were tried to achieve reconversion to the ground state.

After an irradiation time of 720 min, a profound decrease of the  $C_{\text{Spiro-O}}$  band at approx.  $\tilde{\nu} = 950 \text{ cm}^{-1}$  in comparison to the non-irradiated SP-Nitro@MOF-5 (**1**) was observed pointing to a successful isomerization of SP-Nitro to MC-Nitro. This has been comprehensively described and analyzed in chapter 4.4.1.3.1. By excitation with electromagnetic radiation of the wavelength  $\lambda = 450, 530, 590$  and 660 nm (colored broken lines) no increase in intensity for the characteristic spiropyran band is found (see figure 4.4.23). Upon light exposure, the IR band of the excited species (orange solid line) remains unaffected for two possible reasons: SP-Nitro becomes a pure T-type chromophore inside

MOF-5 or photodegradation takes place. Further, the MOF host matrix might fully stabilize the dipolar merocyanine as either isolated molecules or associated in aggregates.

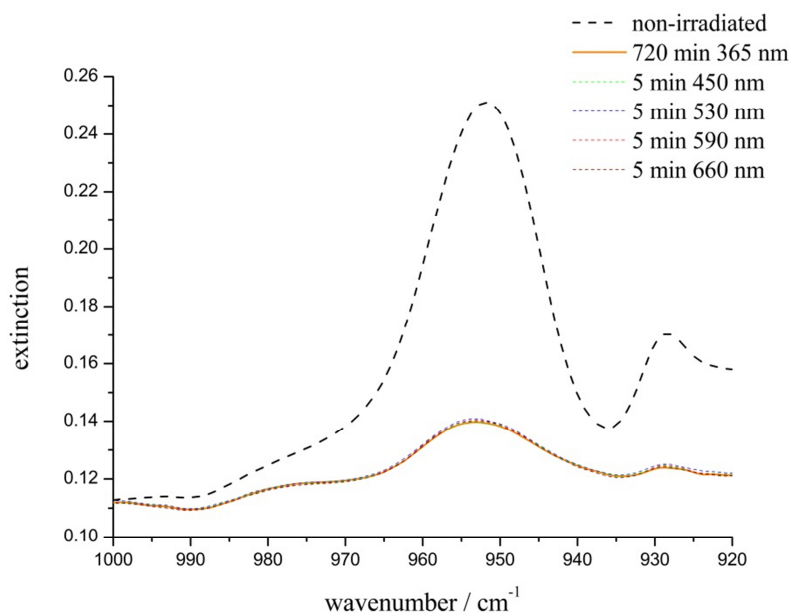


**Figure 4.4.23** Light excitation of SP-Nitro@MOF-5 (**1**) with different wavelengths.

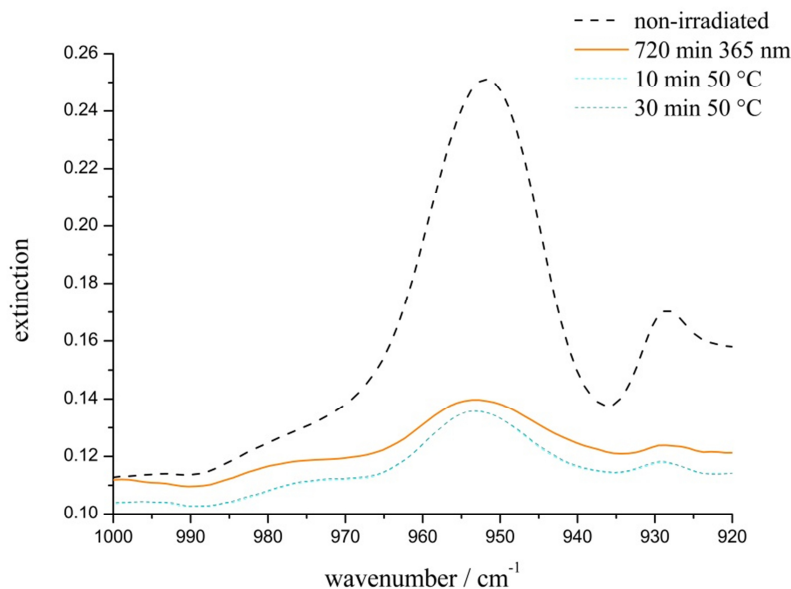


**Figure 4.4.24** Thermal treatment of SP-Nitro@MOF-5 (**1**) at 50 °C.

If being a pure T-type chromophore, heat treatment would cause intensity increase of the  $C_{\text{Spiro-O}}$  band. However, the formation of a small band (cyan and dark cyan broken lines), but with lower intensity than the irradiated species (orange solid line) occurs (see figure 4.4.24).

Thus, stabilization of MC-Nitro and/or photodegradation present the only possibilities to this response on light and heat treatment. Elucidation of this problem will be discussed in a later part of this chapter.

For compounds **2** and **3** an almost similar behavior to **1** is reported for illumination with electromagnetic radiation of different wavelengths: Upon irradiation of the excited species (orange solid line, figure 4.4.25 and figure 4.4.27) the intensity value of the  $C_{\text{Spiro-O}}$  band remains unaffected (colored broken lines, respectively). However, heat treatment causes a slight increase in comparison to the excited state in both cases (figure 4.4.26 and figure 4.4.28, respectively). For compound **2** this is only found for heating times of 20 min duration. Prolonged heating again results in a decrease of the characteristic IR band. Since heat treatment was conducted in air, moisture might have been absorbed causing a loss in intensity. The differences in intensity were found to be rather small for compound **3**.

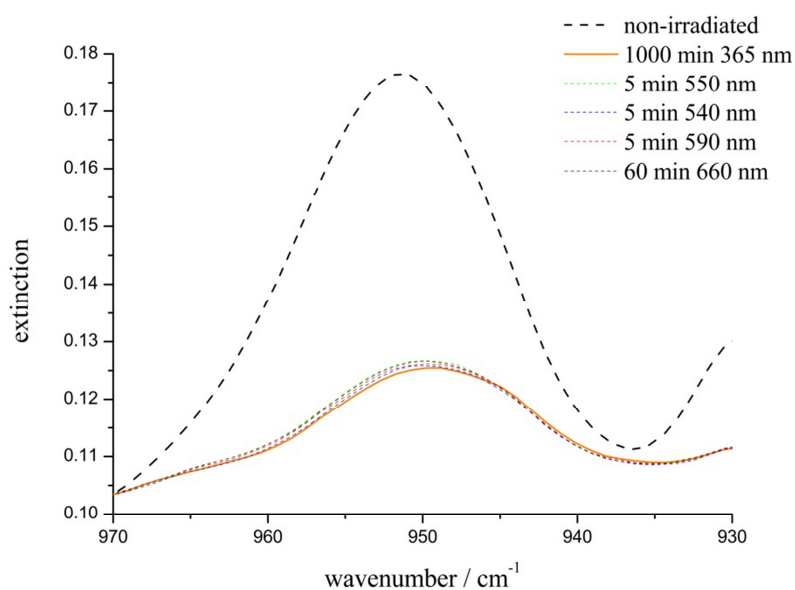


**Figure 4.4.25** Light excitation of SP-Nitro@MIL-68(In) (**2**) with different wavelengths.

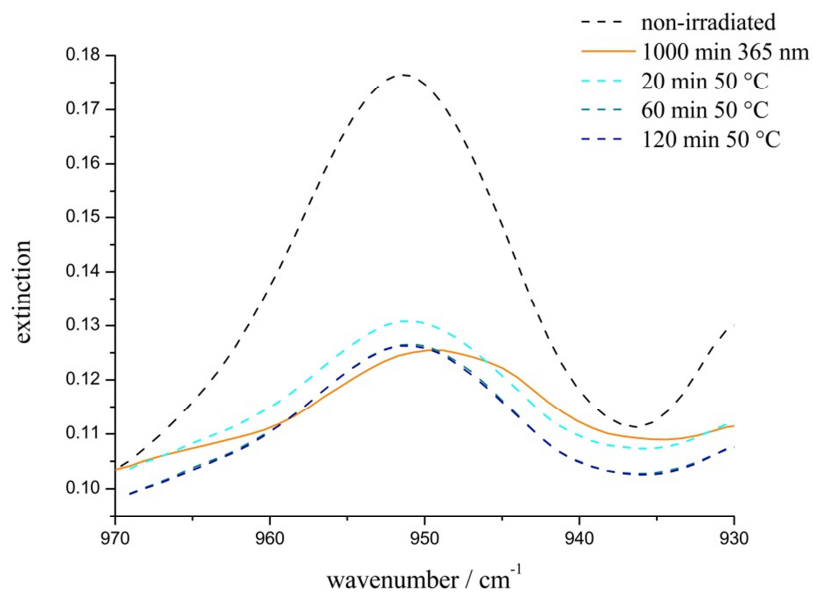


**Figure 4.4.26** Thermal treatment of SP-Nitro@MIL-68(In) (2) at 50 °C.

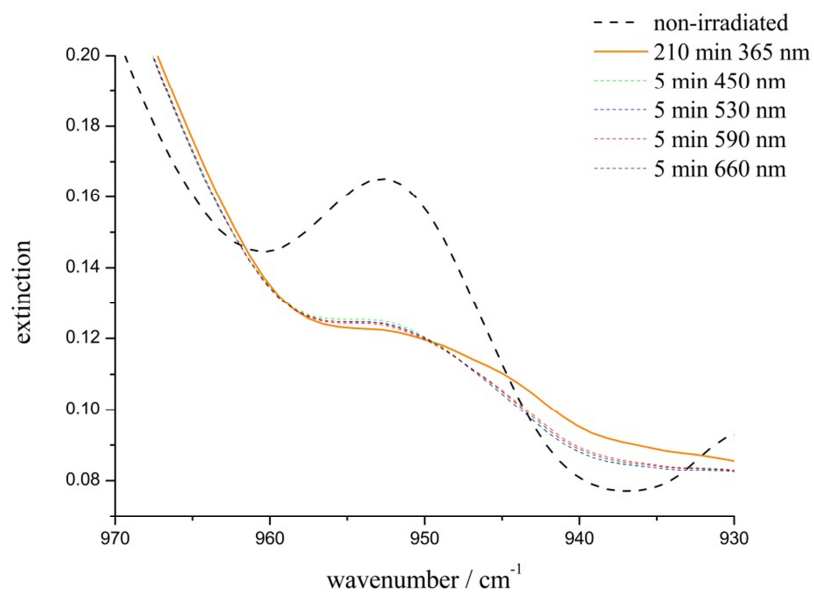


**Figure 4.4.27** Light excitation of SP-Nitro@MIL-68(Ga) (3) with different wavelengths.

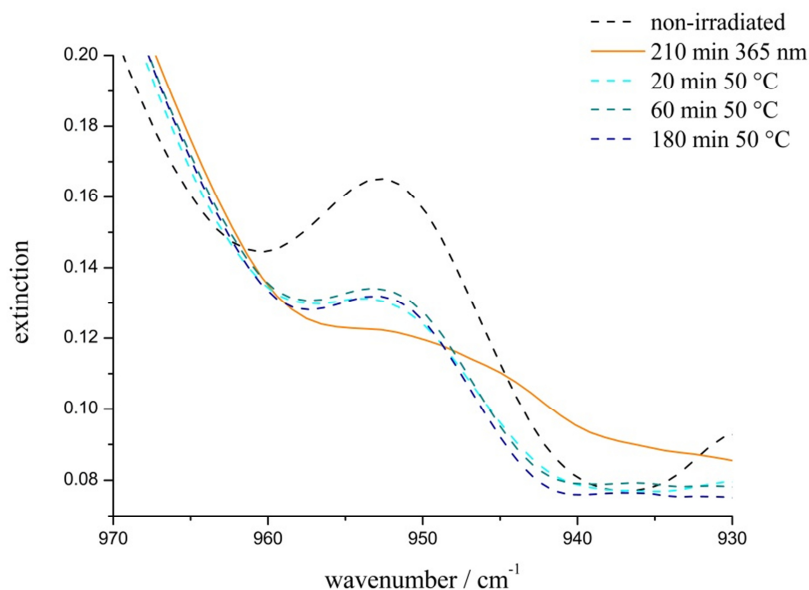


**Figure 4.4.28** Thermal treatment of SP-Nitro@MIL-68(Ga) (**3**) at 50 °C.

In contrast to MC-Nitro@MOF-5 (**1**) MC-Nitro embedded in MIL-68(In) (**2**) and MIL-68(Ga) (**3**) is reconverted to its spiropyran form, but only small amounts. A large amount either remains stabilized or photodegradation takes place, which has already been assumed. Further experiments (differential IR spectra and UV/vis spectroscopy) in this chapter will solve this problem.

Analogue to the findings for compounds **1** to **3** MC-Nitro adsorbed on the surface of MIL-53(Al) exhibits photochemical and thermal resistance towards reversion to the closed SP form. Taking a closer look at figure 4.4.29, response to electromagnetic radiation of different wavelengths is not markedly occurring. Upon heat supply an increase in absorption but without formation of a band is obvious (figure 4.4.30). Higher absorption might be due to interactions between the KBr and MC-Nitro on the surface of MIL-53(Al) when heated and absorption of water.

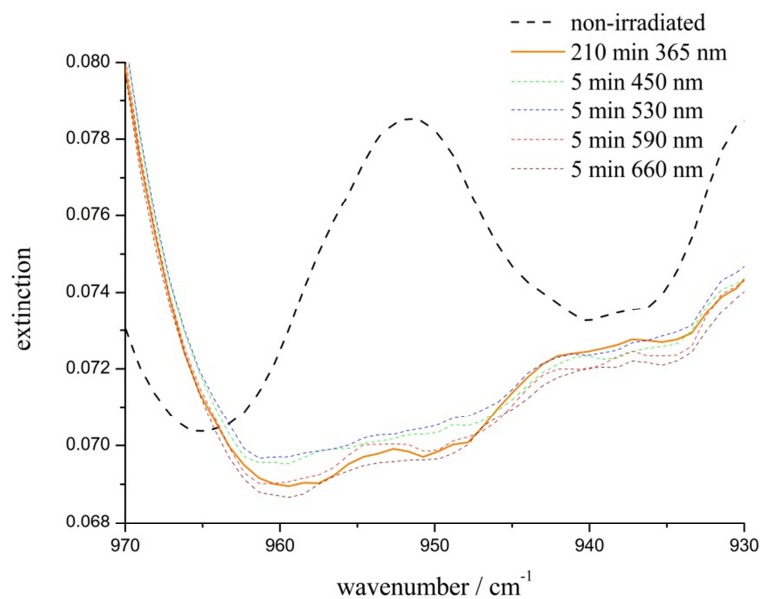


**Figure 4.4.29** Light excitation of SP-Nitro@MIL-53(Al) (**4**) with different wavelengths.

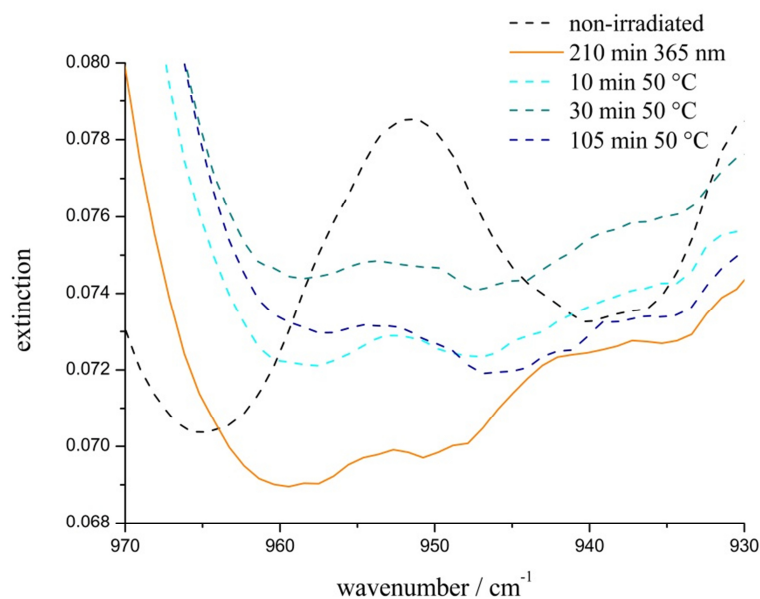


**Figure 4.4.30** Thermal treatment of SP-Nitro@MIL-53(Al) (**4**) at 50 °C.

To exactly understand and determine changes upon heat supply for compounds **2** to **4**, further experiments under inert conditions and without KBr have to be conducted.

The results of “reconverting MC-Nitro to its spiropyran form” clearly point to either stabilization or photodegradation of the dye molecule upon prolonged UV light irradiation.

Up to now, mainly the decrease of the  $C_{\text{Spiro-O}}$  band was followed for long excitation times. Furthermore, assignment of growing bands has been done to prove the formation of MC-Nitro. This has been successfully done for all compounds **1** to **4**. However, detailed analysis of the IR data has to be performed to confirm either stabilization of the excited state or photodegradation. When stabilized, the IR bands of the MC form are expected to remain unaffected upon prolonged UV light irradiation. On the other hand the process of photodegradation will become obvious by decreasing IR bands of the spiropyran as well as the merocyanine bands. Thereupon, the extinction of the non-irradiated species was subtracted from the extinction of the irradiated one, yielding  $\text{ext}_{\text{irrad}} - \text{ext}_{\text{ground state}}$ . That way, alterations in intensity are easier to classify. In all figures 4.4.31 to 4.4.34 the differential spectrum for maximal MC bands (green lines) is compared to the respective maximal irradiation time (orange line; for the respective maximal irradiation time compare figures 4.4.12 to 4.4.15).

In the following, the results of the differential IR spectroscopic measurements will be discussed for every compound in detail, starting with SP-Nitro@MOF-5 (**1**).

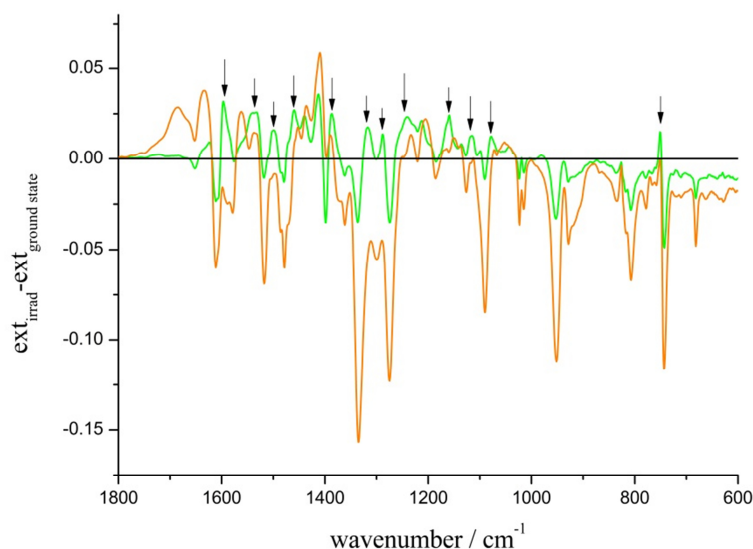


**Figure 4.4.31** Differential IR spectra of SP-Nitro@MOF-5 (**1**) under irradiation with UV light ( $\lambda = 365$  nm). The green line shows the irradiation time (60 min) for maximal MC bands is colored in green, the orange line shows irradiation for 720 min. Decreasing bands are marked with arrows.

In figure 4.4.31 the increasing and decreasing IR bands of **1** upon UV light irradiation are shown. A maximum intensity of the MC bands for 60 min UV light exposure (green line) is observed. UV light exposure for > 60 min results in a significant decrease of several IR bands (orange solid line), which are characteristic for the merocyanine moiety:

**Table 4.4.14** List of decreasing IR bands (in  $\text{cm}^{-1}$ ) for MC-Nitro embedded in MOF-5.

decreasing IR bands in $\text{cm}^{-1}$
1596
<b>1317</b>
1288
1241
1159
1117
1078

Especially the band at  $\tilde{\nu} = 1317 \text{ cm}^{-1}$  is usually the strongest one according to the experimental and calculated data of *Nakata* and co-workers.<sup>[196]</sup> Upon UV light irradiation for longer than 60 min, a significant loss in intensity of this band was detected. Therefore, MC-Nitro is formed upon irradiation with UV light, but only to a certain extent. For prolonged irradiation photodegradation appears, since both the spiropyran and the merocyanine bands decrease.

A similar behavior was discovered for SP-Nitro@MIL-68(In) (**2**) and SP-Nitro@MIL-68(Ga) (**3**). In figures 4.4.32 and 4.4.33 the differential IR spectra of **2** and **3** are shown, respectively, with the maximal MC bands colored in green compared to the bands for maximal UV light irradiation in orange.

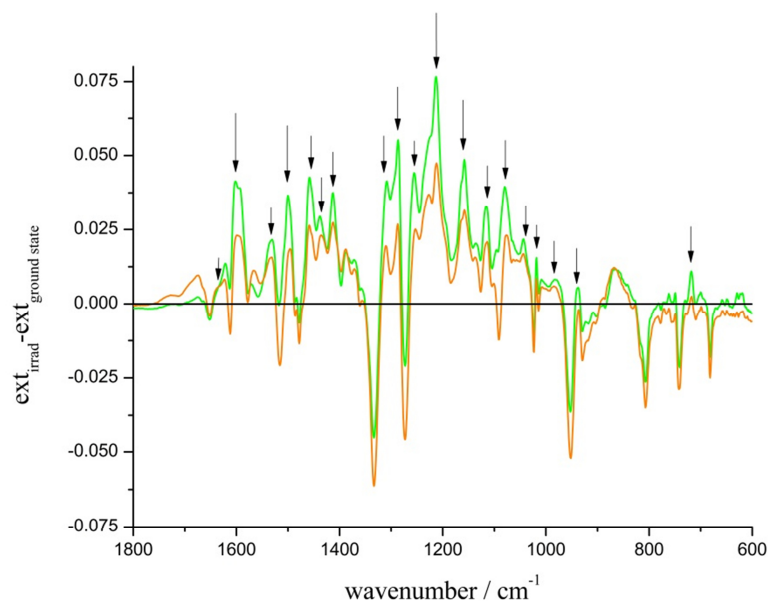


**Figure 4.4.32** Differential IR spectra of SP-Nitro@MIL-68(In) (**2**) under irradiation with UV light ( $\lambda = 365$  nm). The green line shows the irradiation time (60 min) for maximal MC bands, the orange line shows irradiation for 1000 min. Decreasing bands are marked with arrows.

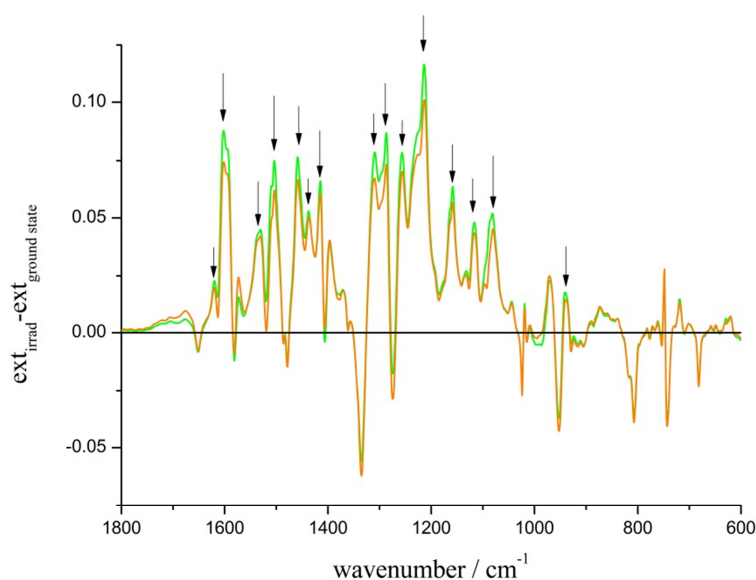


**Figure 4.4.33** Differential IR spectra of SP-Nitro@MIL-68(Ga) (**3**) under irradiation with UV light ( $\lambda = 365$  nm). The green line shows the irradiation time (90 min) for maximal MC bands, the orange line shows irradiation for 210 min. Decreasing bands are marked with arrows.

In a comparable manner to the UV light response of compound **1**, the intensity of typical merocyanine bands diminishes with extended irradiation for both **2** and **3**. These bands are

listed in table 4.4.15. Interestingly, decreasing bands are the same for both compounds, pointing to an analogue behavior of the embedded MC-Nitro inside these MIL-68 matrices. Since MIL-68(In) and MIL-68(Ga) are constructed similar except their metal nodes, this result is not surprising. The most intensive band at  $\tilde{\nu} = 1309 \text{ cm}^{-1}$  according to *Nakata* and co-workers<sup>[196]</sup> significantly loses in intensity for **2** and **3** as well, which has also been observed for compound **1**.

**Table 4.4.15** List of decreasing IR bands (in  $\text{cm}^{-1}$ ) for MC-Nitro embedded in MIL-68(In) (left) and MIL-68(Ga) (right).

decreasing IR bands in $\text{cm}^{-1}$	
MC-Nitro@MIL-68(In) ( <b>2</b> )	MC-Nitro@MIL-68(Ga) ( <b>3</b> )
1603	1603
1532	1531
1498	1504
1458	1459
1438	1438
1412	1415
<b>1309</b>	<b>1309</b>
1286	1287
1255	1256
1212	1213
1157	1158
1134	1133
1115	1116
1080	1082
1043	1042
938	940

For SP-Nitro@MIL-53(Al) (**4**) a different response was expected, since SP-Nitro was found to be mainly absorbed on the surface of the MIL-53(Al) particles. Upon UV light irradiation the formation of MC-Nitro is obvious (see figure 4.4.34). Further, UV light irradiation leads to an increase of the MC-Nitro bands until a maximal intensity of the characteristic bands occurs at 20 min light exposure (green line). Afterwards, only a slight loss in intensity is

observed (210 min, orange line), but again for the most intensive band at  $\tilde{\nu} = 1310 \text{ cm}^{-1}$ . It is assumed that prolonged UV light irradiation not only leads to photodegradation, but also to the formation of aggregates, which might feature a higher photostability than isolated MC-Nitro molecules. Since the absorption properties of MC-Nitro combined with MIL-53(Al) resemble very much the behavior when dissolved in toluene, this suggestion seems to be logical. Further proof has to be made via UV/vis spectroscopy, which will be presented in the following.

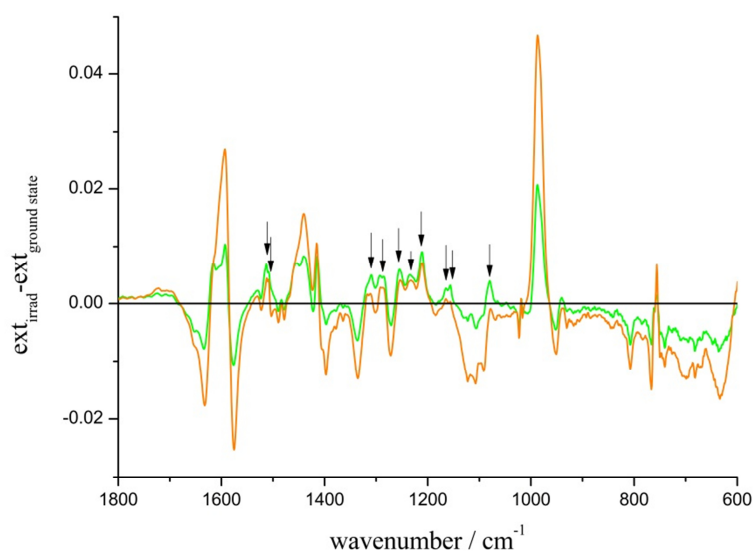


**Figure 4.4.34** Differential IR spectra of SP-Nitro@MIL-53(Al) (**4**) under irradiation with UV light ( $\lambda = 365 \text{ nm}$ ). The green line shows the irradiation time (20 min) for maximal MC bands, the orange line shows irradiation for 720 min. Decreasing bands are marked with arrows.

The increasing IR bands at  $\sim 1600 \text{ cm}^{-1}$ ,  $\sim 1450 \text{ cm}^{-1}$  and  $\sim 1000 \text{ cm}^{-1}$  might be attributed to the formed *H*-aggregates but further proof still has to be done.

**Table 4.4.16** List of decreasing IR bands (in  $\text{cm}^{-1}$ ) for MC-Nitro adsorbed on MIL-53(Al).

<u>decreasing IR bands in <math>\text{cm}^{-1}</math></u>
1512
<b>1310</b>
1289
1257
1234
1211
1167
1157
1080
942

The results of IR spectroscopic measurements on compounds **1** to **4** for prolonged UV light irradiation strongly lead to one conclusion: SP-Nitro does not exhibit photostability on long exposure times. Furthermore, the slight decrease in the characteristic bands for MC-Nitro when combined with MIL-53(Al) indicates the formation of aggregates. Thereupon, additional UV/vis spectra were recorded for all compounds to follow the process of photodegradation and, in case of **4**, possible aggregation. The absorption of the non-irradiated species was subtracted from the irradiated ones for a better overview on decreasing and increasing absorption bands, which was also done for the IR spectra. The resulting differential UV/vis spectra are discussed in the following.

Starting with SP-Nitro@MOF-5 (**1**) loss of intensity of the MC-Nitro band between 500 nm and 600 nm occurs right after 1 min of UV light irradiation (see figure 4.4.35). Extended exposure causes further and increasingly red-shifted decrease of the MC-Nitro absorption. Besides, a local absorption maximum at around 430 nm with an increasing red-shift upon prolonged UV light illumination is formed.

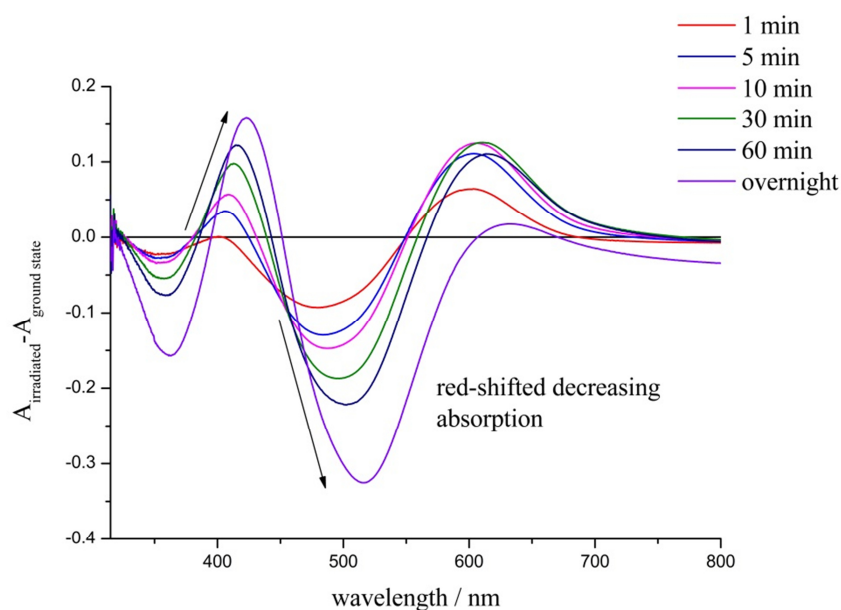


**Figure 4.4.35** Differential UV/vis spectra of SP-Nitro@MOF-5 (**1**) for prolonged UV light irradiation ( $\lambda = 365$  nm).

To understand the absorption behavior, the products of photodegradation have to be known. Already in the 1970s, *Gautron* reported on decomposition of SP-Nitro and other spiropyran derivatives.<sup>[200]</sup> In the solid state the author mainly found three compounds to be generated upon prolonged UV light excitation: 3,3-dimethyloxindole, 1,3,3-trimethyloxindole and 5-nitrosalicylaldehyde. The structures of these compounds are found in figure 4.4.36.

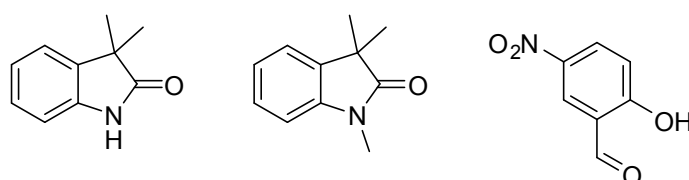


**Figure 4.4.36** Structures of the products mainly formed upon prolonged UV light irradiation: 3,3-dimethyloxindole (left); 1,3,3-trimethyloxindole (middle) and 5-nitrosalicylaldehyde (right).

For 3,3-dimethyloxindole absorption maxima at approx. 200 nm and 250 nm were determined.<sup>[201]</sup> 1,3,3-trimethyloxindole features an absorption maximum in the same range at approx. 250 nm.<sup>[202]</sup> 5-nitrosalicylaldehyde shows an absorption maximum in the range of 330 nm.<sup>[115]</sup> The occurring absorption band at 430 nm might be attributed to the last mentioned product of photodegradation. However, further investigations to finally determine the occurring photo-product have to be conducted. Although a valid assignment of the

increasing absorption band has still to be done, photodegradation of SP-Nitro is proved to occur because of the significant decrease of the merocyanine absorption band.

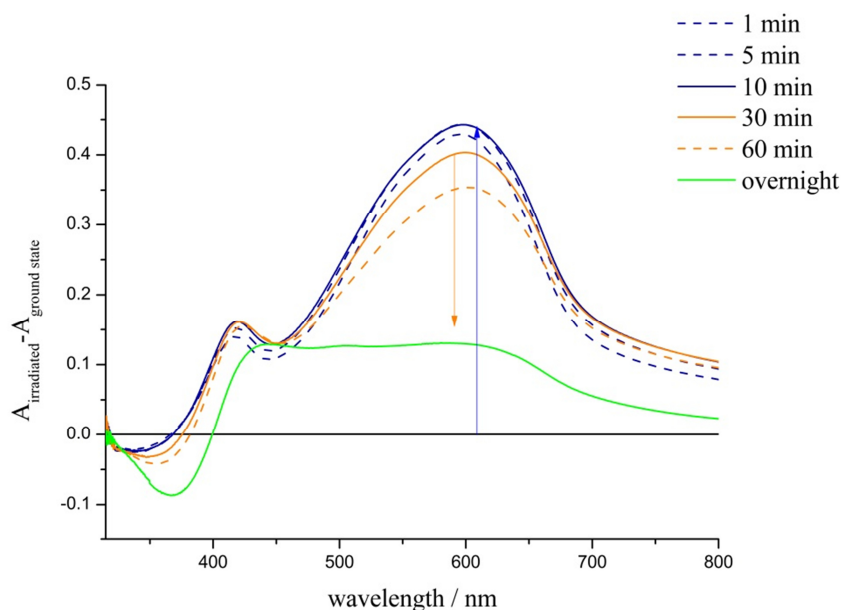


**Figure 4.4.37** Differential UV/vis spectra of SP-Nitro@MIL-68(In) (2) for prolonged UV light irradiation ( $\lambda = 365$  nm). Increasing and decreasing absorption is marked with an arrow.

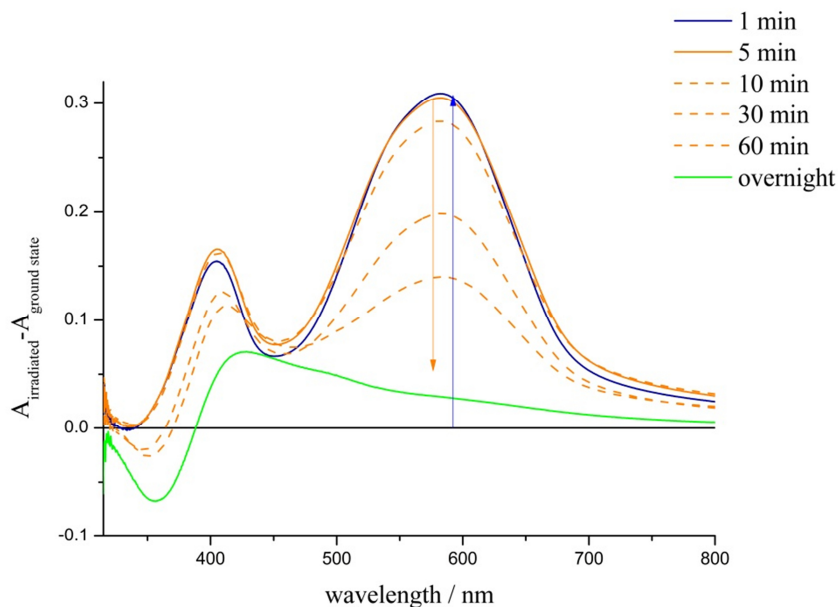


**Figure 4.4.38** Differential UV/vis spectra of SP-Nitro@MIL-68(Ga) (3) for prolonged UV light irradiation ( $\lambda = 365$  nm). Increasing and decreasing absorption is marked with an arrow.

In comparison to 1, compounds 2 and 3 exhibit a different response upon prolonged UV light excitation. When irradiated, SP-Nitro converts into its merocyanine form. When embedded in

MIL-68(In), strengthening of the absorption maxima occurs until a total irradiation time of 10 min (see figure 4.4.37, blue lines). Longer irradiation results in loss of intensity (orange lines) and, finally, a complete disappearance after exposure overnight (green line). Furthermore, broadening of the local absorption maximum is observed.

A similar behavior is found for SP-Nitro being incorporated into MIL-68(Ga) (figure 4.4.38). Excitation up to 5 min leads to the formation of MC-Nitro and an increasing intensity of the characteristic absorption band (blue line). Once more, extended UV light irradiation causes band broadening, loss in intensity and disappearance of the absorption band. For both **2** and **3** complete photodegradation of SP-Nitro is assumed, which corresponds to the results of the IR spectroscopic measurements.

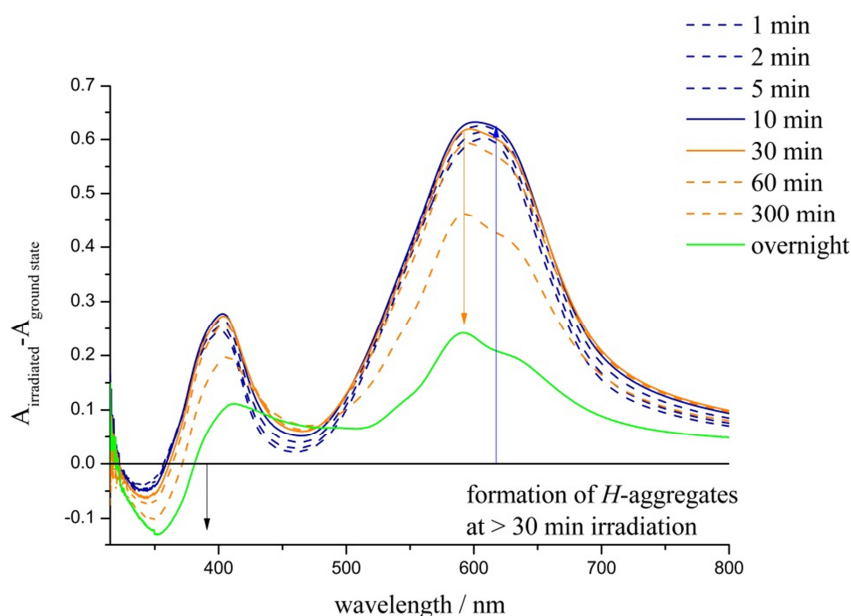


**Figure 4.4.39** Differential UV/vis spectra of SP-Nitro@MIL-53(Al) (**4**) for prolonged UV light irradiation ( $\lambda = 365$  nm). Increasing and decreasing absorption is marked with an arrow.

As expected from the IR spectroscopic measurements, SP-Nitro adsorbed on the surface of MIL-53(Al) exhibits different absorption properties and response to prolonged UV light exposure. In figure 4.4.39 the differential UV/vis spectra of **4** are presented. When irradiated for up to 10 min, formation of MC-Nitro occurs resulting in a local absorption maximum close to 600 nm (blue lines). Furthermore, UV light treatment causes the appearance of a blue-shifted shoulder (orange lines). This shoulder is clearly attributed to the formation of *H*-aggregates. Being exposed to UV light for more than 30 min causes loss in intensity of the

absorption maximum and photodegradation. In contrast to **1** to **3**, the local absorption maximum does not disappear completely, which strengthens the assumption of MC-Nitro associated in aggregates being more resistant towards photodegradation than being present in isolated molecules.

As a third method of tracing photodegradation, fluorescence spectroscopic measurements were only carried out for compound **1**. For a typical measurement, the compound was filled into a small glass vial and closed airtight. Emission spectra were recorded with an excitation wavelength of  $\lambda_{\text{ex}} = 520$  nm. Further, 20 cycles were recorded to follow alterations in emission intensities.

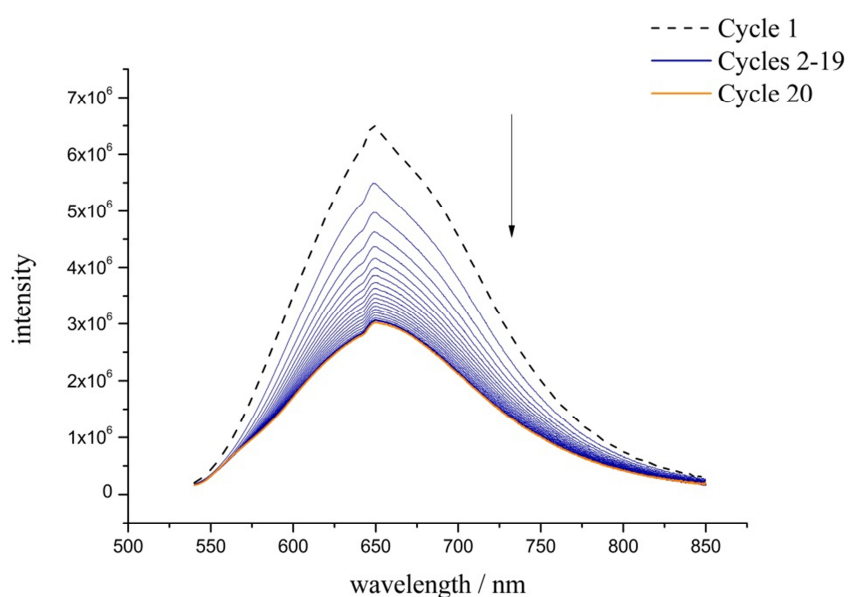


**Figure 4.4.40** Emission spectra of SP-Nitro@MOF-5 (**1**) with  $\lambda_{\text{ex}} = 520$  nm, 20 cycles. Decreasing emission is marked with an arrow.

In figure 4.4.40 the emission spectra of SP-Nitro@MOF-5 (**1**) are presented. At the beginning of the measurement (black broken line, cycle 1) an emission intensity of approx.  $6.50 \times 10^6$  is found. Further excitation results in a significant decrease (blue lines) with a minimum after 20 cycles (orange line). The formation of *H*-aggregates, which exhibit slight or no fluorescence, can be excluded from the results of the UV/vis measurements. Therefore, loss in intensity is caused by photodegradation. For compounds **2** to **3** similar results are expected, whereas compound **4** should exhibit a different response due to the surface adsorption. Measurements on these materials still have to be done.

For all compounds **1** to **4** low photostability was shown upon prolonged UV light irradiation by means of IR, UV/vis and fluorescence spectroscopic measurements. Furthermore, adsorption of SP-Nitro on the surface of MIL-53(Al) causes association into *H*-aggregates upon prolonged UV light exposure, but only to a certain extent. Interesting points to investigate are comparative studies on the photostability of SP-Nitro in different host matrices and different solvents.

#### 4.4.1.4 Further investigations

In addition to the investigations on photochromism and solvatochromism, influence of the host matrix and reversibility of switching as well as photostability, measurements concerning attractive and repulsive interactions and the influence of moisture uptake on the absorption properties were conducted. Additionally, the thermal stability of SP-Nitro@MOF-5 (**1**) was investigated.

##### 4.4.1.4.1 Investigations on attractive and repulsive interactions

For determining the strength of host-guest interactions between SP-Nitro and the respective MOF, all systems were dispersed in DMF and alterations in the absorption spectra were followed over 100 cycles (one cycle every 10 min) via UV/vis spectroscopy. In figure 4.4.41 the results are exemplarily shown for SP-Nitro@MOF-5 (**1**). However, all other compounds show similar behavior (see figures 8.2.12 to 8.2.14 in the supplement).

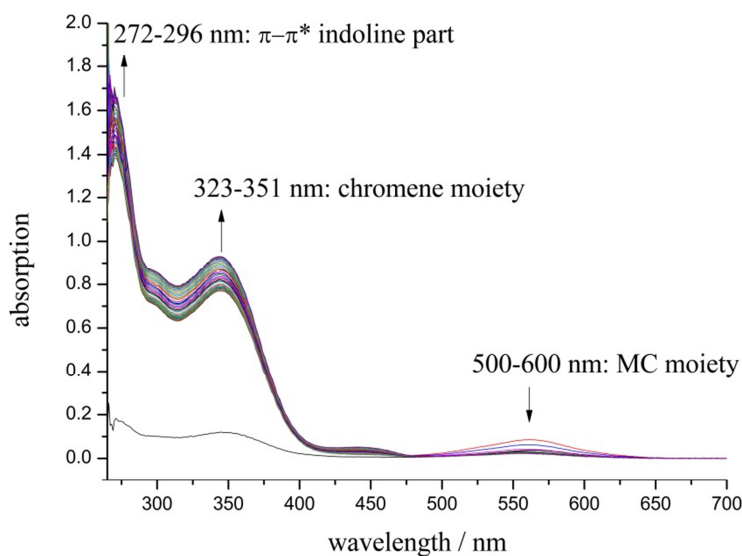


**Figure 4.4.41** Long-time UV/vis measurements on SP-Nitro@MOF-5 (**1**) dispersed in DMF.

Right after the dispersion in DMF three local absorption maxima are observed, which can be easily assigned to the indoline and chromene part of SP-Nitro. A small band is also found at approx. 550 nm for the open MC-Nitro form. Throughout the entire duration of the measurement, the two bands of the indoline and chromene part increase significantly, while the MC band decreases. This finding points to a slow release of SP-Nitro from MOF-5 making the solvent being more attractive for SP-Nitro than the MOF host matrix.

#### 4.4.1.4.2 Influence of moisture on the absorption properties

Due to the hydrophilic character of the porous host materials, absorption of moisture has to be considered at measurements in air. According to *Snyder*, water possesses an elution power of  $\epsilon^0 > 1$ .<sup>[193]</sup> Hence, shifts of the absorption maxima are expected upon moisture uptake. This assumption is supported by drastic shifts when comparing the data of measurements in air and under inert conditions, which are listed in table 4.4.17.

**Table 4.4.17** Comparison of the absorption properties of compounds **1** to **4** when measured in air and under inert conditions.

compound	reflection minimum (nm) / measurements conducted in air	absorption maximum (nm) / measurements conducted under inert conditions
SP-Nitro@MOF-5 ( <b>1</b> )	520	500
SP-Nitro@MIL-68(In) ( <b>2</b> )	560	578
SP-Nitro@MIL-68(Ga) ( <b>3</b> )	566	582
SP-Nitro@MIL-53(Al) ( <b>4</b> )	599	594

Apparently, the values for **2** and **3** are red-shifted under inert conditions with a change of 16 - 18 nm. For **1**, a blue-shift is observed. This contrary finding allows two conclusions to be drawn: Firstly, the chemical environment given by the pores of MIL-68 is less polar than water. Upon water uptake, a change in polarity causes a bathochromic shift, according to the solvatochromic behavior of MC-Nitro. Secondly, the pores of MOF-5 are more polar than water, since water uptake results in a red-shift.

While the absorption properties of **1** to **3** significantly differ when measured in air and under inert conditions, moisture uptake does not have a marked impact on **4** (see table 4.4.17). This finding strengthens the hypothesis of SP-Nitro being mainly adsorbed on the surface of MIL-53(Al), which was already considered because of the results of the XRPD and XPS measurements.

It has to be stated, that trends are the same for measurements in air, but exact values differ significantly due to varying polarity upon moisture absorption of the MOFs. This finding

demonstrates the sensitivity of the embedded dye against small amounts of solvent molecules. Hence, loading MOFs with dye molecules via a diffusion process is not adequate, since smallest amounts of solvent molecules might remain. Because of that, a definite explanation of the absorption properties of the embedded dye molecule being a result of host-guest interactions only cannot be done. Thus, dye incorporation via a solvent-free process, such as gas-phase loading, is recommended to purely investigate the influence of the surrounding host matrix on the photoresponse of the embedded dye.

#### 4.4.1.4.3 Thermal Stability

Investigations on thermal stability of spiropyran@MOF systems were exemplarily conducted for compound **1**. Thereupon, DSC/TGA measurements were performed under an argon atmosphere. The results are shown in figure 4.4.42.

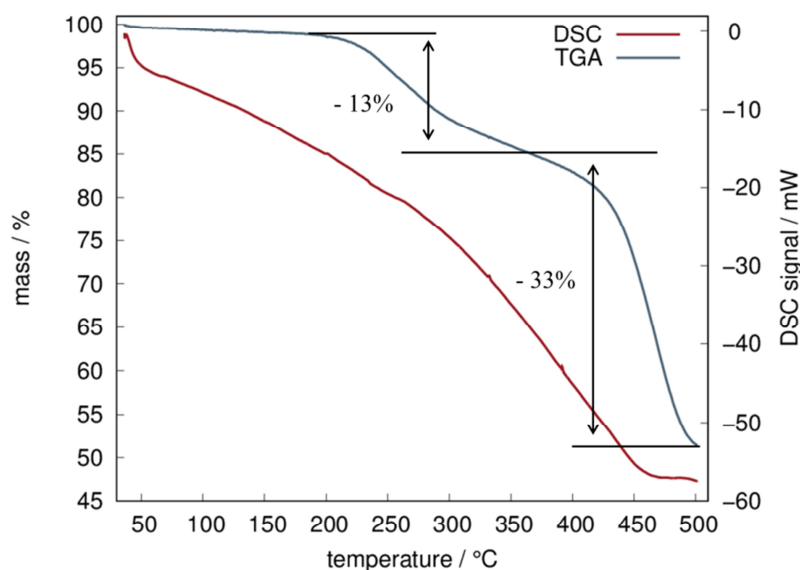


**Figure 4.4.42** DSC/TGA measurements of SP-Nitro@MOF-5 (**1**) under an argon atmosphere in the range of 30 °C to 500 °C.

No profound endo- or exothermal signals are present in the DSC curve during the whole measurement (red line) between 30 °C and 500 °C. Nevertheless, two mass loss steps are found (blue line): one is starting around 190 °C and ends at approx. 355 °C with a loss of ~ 13% in mass. The second step starts at 355 °C until 500 °C with a mass loss of ~ 33%. Both

steps merge seamlessly, making accurate determination of the percentage loss in mass for a single step difficult. However, the mass loss of 13% in the first step corresponds to the release of  $\sim 0.4$  SP-Nitro molecules; the second one is in accordance with  $\sim 1.5$  SP-Nitro molecules. From XPS and elemental analysis a composition of  $n(\text{SP-Nitro}) : n(\text{MOF-5})$  of  $2.4 (\text{XPS}) / 2.26 (\text{elemental analysis}) : 1$  was calculated. A total loss of approx. 1.9 SP-Nitro can be estimated from the DSC/TGA measurement, which is in the range of these results. It has to be stated that MOF-5 is known to be stable up to  $\sim 480$  °C before decomposition.<sup>[203]</sup> Hence loss in mass can be attributed to the release of spiropyran molecules until that temperature. Afterwards, decomposition of the organic linker occurs. Nevertheless, the presence of two steps of loss in mass can be explained as follows:

Probably, two different positions are occupied by the SP-Nitro inside the MOFs pore: one directly at the highly charged  $[\text{Zn}_4\text{O}]^{6+}$  cluster and one directed to the linker molecules and/or mobile inside the MOF pores. This assumption seems plausible, since from the UV/vis measurements partly stabilized MC-Nitro was found to be present even without UV light exposure. Presumably these molecules are oriented at the node and are stabilized in the open MC form at the same time, while the part that can still be switched is freely present in the pore and is therefore less firmly bound. Hence, the “free” SP-Nitro is released before the SP-Nitro located at the inorganic nodes detaches.

Here it becomes clear again that the knowledge of the exact location of the guest molecule inside the MOFs pore becomes important and indispensable for understanding these systems completely.

#### 4.4.2 Other spiropyran@MOF hybrid materials

In addition to the nitro-substituted spiropyran three further spiropyrans were used as guest molecules for the incorporation into the four different host matrices plus HKUST-1 (for SP-N and SP-OMe only) as another, but colored, porous host. The structures of these dye molecules are illustrated in figure 4.4.43.

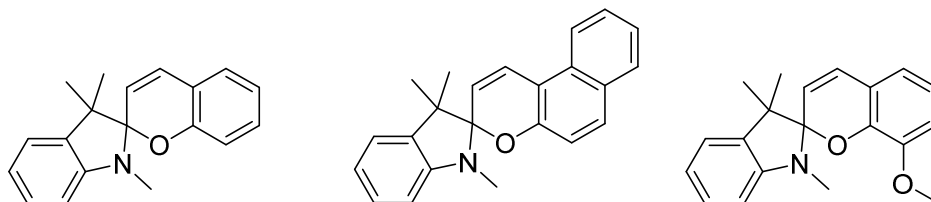


**Figure 4.4.43** Structure of 1,3,3-trimethylindolino-benzopyrylospiran (SP) (left); 1,3,3-trimethylindolino- $\beta$ -naphthopyrylospiran (SP-N) with an additional phenyl ring at the chromene moiety enlarging the  $\pi$ -electron system (middle) and 1,3,3-trimethylindolino-8'-methoxybenzo-pyrylospiran (SP-OMe) with a methoxy group at 8'-position of the chromene moiety (right).

The resulting spiropyran@MOF composite materials will be shortly described in the following, starting with SP as embedded guest molecule.

##### 4.4.2.1 SP@MOF hybrid materials

SP was embedded into four different MOFs, namely MOF-5, MIL-68(In), MIL-68(Ga) and MIL-53(Al), via a gas phase loading process. Four SP@MOF composite materials were obtained:

- (5) SP@MOF-5
- (6) SP@MIL-68(In)
- (7) SP@MIL-68(Ga)
- (8) SP@MIL-53(Al)

These SP@MOF systems were investigated by means of the ICE-principle. The results are presented in the following.

#### 4.4.2.1.1 Incorporation

The successful embedment of SP was confirmed by XRPD measurements. The XRPD pattern of SP@MOF-5 (**5**) is exemplarily shown in figure 4.4.44. For diffraction patterns of compounds **6** to **8** see figures 8.3.1 to 8.3.3 in the supplement.

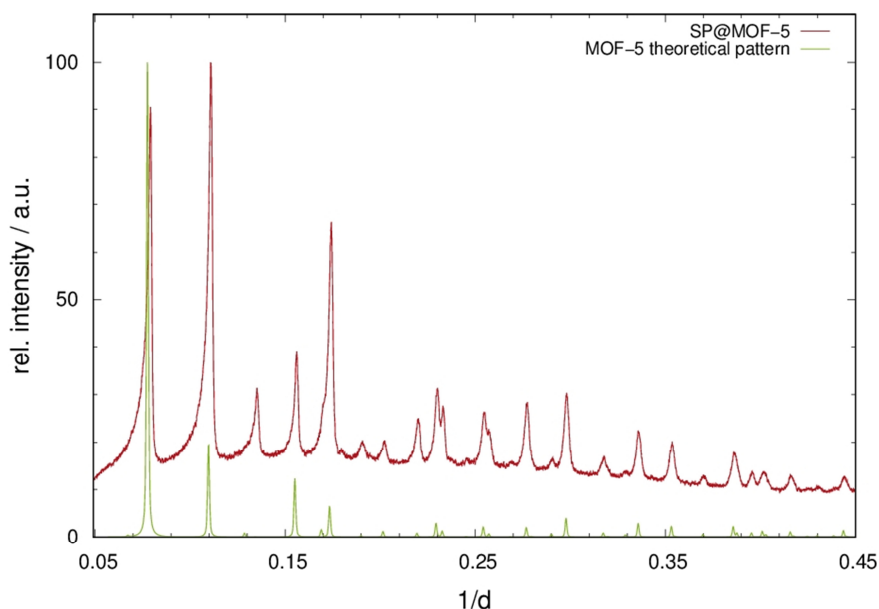


**Figure 4.4.44** XRPD pattern of **5** (red), measured at 298 K (*Huber G670*:  $\lambda = 1.54 \text{ \AA}$ ), in comparison to theoretical data of MOF-5 (green).

Notably, alterations in intensity occur, which confirm a complete incorporation of the guest molecule. Furthermore, no additional peaks are present, which excludes the presence of free dye molecules. Similar to the results of SP-Nitro, neither a change in the diffraction pattern nor intensity changes are present for SP@MIL-53(Al) (**8**) (figure 8.2.17 in the supplement). Hence, surface adsorption as an amorphous film is expected for this compound, since a change in color during the synthesis process was observed.

In order to determine changed cell volumes upon guest loading, *Le Bail* fits in *JANA2006*<sup>[194]</sup> were performed. In table 4.4.18 the results are listed and compared to the volumes of the respective unloaded host material. It has to be stated that *Le Bail* fits on the unloaded MOFs were performed with high resolution synchrotron powder diffraction data (BM01B, ESRF), while loaded MOFs were investigated by laboratory diffraction. Hence, comparison of these data is of qualitative but not quantitative value. *Le Bail* fits of **5** to **7** and the respective

unloaded MOFs are shown in figures 8.2.2 to 8.2.4, table 8.2.1 and figures 8.3.4 to 8.3.6 in the supplement.

**Table 4.4.18** Results of *Le Bail* fits of powder diffraction data of compounds **5** to **7** compared with the unit cell volumes of the respective unloaded MOF.

	(5)	(6)	(7)
T/K	298	298	298
Space Group / No.	$Fm\bar{3}m$ / 225	$Cmcm$ / 63	$Cmcm$ / 63
GOF	3.07	1.09	2.34
$R_p$	0.0476	0.0225	0.0415
$wR_p$	0.0891	0.0392	0.0677
$V/\text{\AA}^3$	17224(1)	5915(1)	5294(1)
a	25.825(2)	21.830(4)	20.837(2)
b	-	37.508(5)	38.172(5)
c	-	7.2236(8)	6.656(1)
$V/\text{\AA}^3$ (unloaded MOF)	17156.0(4)	5901.5(2)	5197.0(7)

Contrary to SP-Nitro@MOF-5 (**1**), SP loading results in an expansion of the MOF-5 framework, pointing to repulsive interactions between the guest molecule and the host lattice. SP-Nitro features an electron-withdrawing group, which is not present in SP. Hence, those two spiropyrans differ markedly in their dipole character, which could be an explanation for the different interaction with the MOF-5 scaffold that is suggested to be polar. Guest incorporation into MOFs of the MIL-68 family causes expansion of the framework, which has also been observed for SP-Nitro being embedded in MIL-68(In) and MIL-68(Ga). Since the alterations in volumes are not significant, additional methods to confirm the suggestion of attractive and repulsive host-guest interactions are indispensable in future investigations.

#### 4.4.2.1.2 Composition

The composition of the SP@MOF compounds was determined by means of XPS measurements. Areas of typical nitrogen XPS signals and the areas of the typical metal cation XPS signals were compared. In table 4.4.19 the results of the XPS measurements are listed. Peak fits of the XPS data and calculations are found in figures 8.3.7 to 8.3.10 and table 8.3.1 in the supplement.

**Table 4.4.19** Ratio of SP per formula unit of the respective MOF for **5** to **8** calculated from XPS measurements.

		SP : MOF ratio
SP <sub>x</sub> @MOF-5 ( <b>5</b> )	SP : (Zn <sub>4</sub> O(bdc) <sub>3</sub> )	1.94 : 1
SP <sub>x</sub> @MIL-68(In) ( <b>6</b> )	SP : (In(OH)(bdc))	0.30 : 1
SP <sub>x</sub> @MIL-68(Ga) ( <b>7</b> )	SP : (Ga(OH)(bdc))	0.29 : 1
SP <sub>x</sub> @MIL-53(Al) ( <b>8</b> )	SP : (Al(OH)(bdc))	0.25 : 1

According to the results of SP-Nitro@MOF systems, the highest amount of incorporated dye is found for MOF-5, followed by MIL-68(In), MIL-68(Ga) and MIL-53(Al). Interestingly, values between the MIL-68 components and MIL-53(Al) do not markedly differ from each other, even though a successful embedment of SP into MIL-53(Al) was not confirmed. Consequently, the surface of MIL-53(Al) must be attractive for the formation of amorphous dye films.

#### 4.4.2.1.3 Effects

When combined with the different porous host materials, SP-Nitro showed photochromic properties. For the obtained SP@MOF systems photoswitching properties are expected as well. In order to investigate these, UV/vis spectroscopic measurements under inert conditions were performed. Here, only the results of SP@MOF-5 (**5**) will be shortly discussed. Spectra of compounds **6** to **8** are shown in the supplement (figure 8.3.11 to 8.3.13).

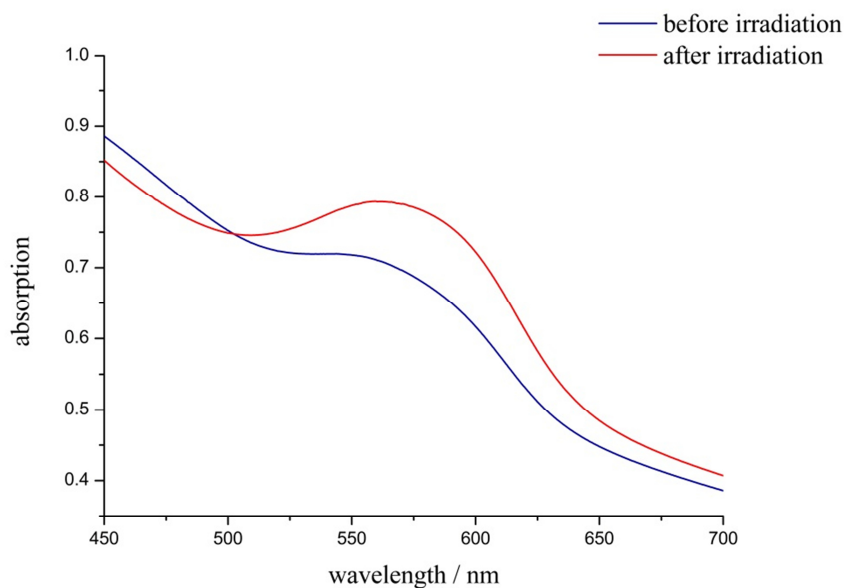


**Figure 4.4.45** Absorption spectra (298 K) of SP@MOF-5 (**5**) before (blue) and after (red) irradiation with UV light ( $\lambda = 365$  nm, 30 min).

For compound **5** the open merocyanine form is already formed without UV light exposure, which is visible in the presence of a local absorption maximum at  $\lambda = 560$  nm (see figure 4.4.45). When irradiated for 30 min with  $\lambda = 365$  nm, the absorption band at  $\lambda = 560$  nm gains in intensity pointing to a proceeding formation of the open merocyanine form, which has already been observed for SP-Nitro@MOF-5 (**1**). Hence, the assumption of MOF-5 establishing an environment being preferred by molecules with a large dipole moment such as merocyanines is further strengthened by this result. For compound **6** only a slight absorption band is formed upon UV light exposure (see figure 8.3.11 in the supplement). When embedded in MIL-68(Ga), the absorption band of SP decreases under UV light irradiation, while no switching is found for SP@MIL-53(Al) at all (figures 8.3.12 and 8.3.13 in the supplement). In figure 4.4.46 the different compounds are shown before (left) and after irradiation with UV light ( $\lambda = 385$  nm) for 1 min.

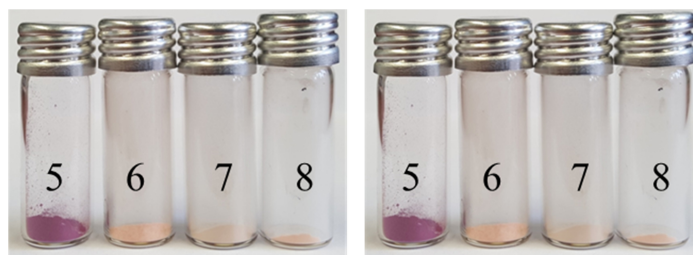


**Figure 4.4.46** Compounds **5** to **8** before (left) and after irradiation with UV light with  $\lambda = 385$  nm (right) for 1 min.

Obviously, no changes in the absorption properties before and after irradiation with UV light ( $\lambda = 365$  nm and  $\lambda = 385$  nm) are present. This could be the result of inhibited photochromism of the embedded dye molecule on the one hand. On the other hand, another excitation wavelength might be required to trigger the light induced switching. Hence, further experiments with light of different wavelengths have to be performed in future studies to investigate the switching properties of SP inside the MOF scaffolds.

#### 4.4.2.2 *SP-N@MOF hybrid materials*

SP-N was embedded into five different MOFs, namely MOF-5, MIL-68(In), MIL-68(Ga), MIL-53(Al) and HKUST-1, via a gas phase loading process. Five SP-N@MOF composite materials were obtained:

- (9) SP-N@MOF-5
- (10) SP-N@MIL-68(In)
- (11) SP-N@MIL-68(Ga)
- (12) SP-N@MIL-53(Al)
- (13) SP-N@HKUST-1

These SP-N@MOF systems were investigated by means of the ICE-principle. The results are shortly presented in the following.

##### 4.4.2.2.1 **Incorporation**

Incorporation of SP-N was followed via XRPD measurements. The XRPD pattern of SP-N@MOF-5 (9) is exemplarily shown in figure 4.4.47. The diffraction pattern does not change in position, but in intensity of the peaks in comparison to the theoretical data of MOF-5. Alterations are small, but present, showing the successful embedment of the dye molecule. Additionally, a shoulder is observed before the second peak, which does not belong to free dye molecule. This shoulder is also found for SP-OMe@MOF-5 (see chapter 4.4.2.3). The reason for this is not known yet.

For diffraction patterns of compounds 10 to 13 see figures 8.3.14 to 8.3.17 in the supplement.

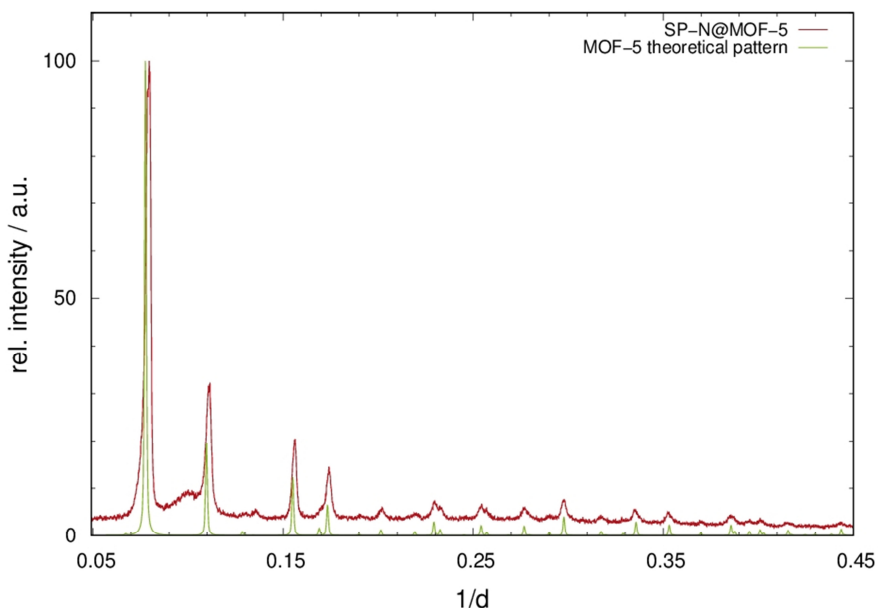


**Figure 4.4.47** XRPD pattern of **9** (red), measured at 298 K (*Stoe StadiP*:  $\lambda = 1.54 \text{ \AA}$ ), in comparison to theoretical data of MOF-5 (green).

For compound **12** additional peaks are present in the diffraction pattern (see figure 8.2.30 in the supplement), which can be assigned to the presence of free dye molecules. Even with extended heating times those free molecules could not be removed. For investigations on the composition and on occurring effects the presence of free SP-N has to be considered for compound **12**.

Changes in cell volumes upon guest loading were determined by *Le Bail* fits performed in *JANA2006*<sup>[194]</sup>. In table 4.4.20 the results are listed and compared to the volumes of the respective unloaded host material. It has to be stated that *Le Bail* fits on the unloaded MOFs except HKUST-1 were performed with high resolution synchrotron powder diffraction data (BM01B, ESRF), while loaded MOFs were investigated by laboratory diffraction. Therefore, comparison of these data is of qualitative but not quantitative value. *Le Bail* fits of **9** to **11** and **13** and the respective unloaded MOFs are shown in figures 8.2.2 to 8.2.4, table 8.2.1 and 8.3.2 and figures 8.3.19 to 8.3.22 in the supplement.

**Table 4.4.20** Results of *Le Bail* fits of powder diffraction data of compounds **9** to **11** and **13** compared with the unit cell volumes of the respective unloaded MOF.

	(9)	(10)	(11)	(13)
T/K	298	298	298	298
Space Group / No.	<i>Fm</i> $\bar{3}$ <i>m</i> / 225	<i>Cmcm</i> / 63	<i>Cmcm</i> / 63	<i>Fm</i> $\bar{3}$ <i>m</i> / 225
GOF	1.39	0.87	1.03	0.91
R <sub>p</sub>	0.0886	0.1055	0.0767	0.0701
wR <sub>p</sub>	0.126	0.1479	0.1013	0.0926
V/Å <sup>3</sup>	17427(2)	6117(2)	5462(2)	18401(2)
a	25.927(3)	22.271(6)	21.247(4)	26.401(4)
b	-	37.744(9)	37.936(8)	-
c	-	7.278(2)	6.776(1)	-
V/Å <sup>3</sup> (unloaded MOF)	17156.0(4)	5901.5(2)	5197.0(7)	18161(2)

For all compounds a profound increase in volume occurs in comparison to the respective unloaded MOF material. The expansion of the framework points to repulsive interactions between the guest molecules and the host scaffold. Nonetheless, additional methods to strengthen this suggestion of repulsive host-guest interactions are obligatory.

#### 4.4.2.2.2 Composition

Investigations on the composition of the SP-N@MOF compounds were done via of XPS measurements. Areas of typical nitrogen XPS signals and the areas of the typical metal cation XPS signals were compared. In table 4.4.21 the results of the XPS measurements are listed. Peak fits of the XPS data and calculations are found in figures 8.3.23 to 8.3.26 and table 8.3.3 in the supplement. Notably, the SP-N : MIL-53(Al) ratio is comparably high. As already mentioned, free dye molecules are present, which are responsible for this result. Further, MIL-68(Ga) is markedly higher loaded with SP-N than MIL-68(In). To understand this, additional investigations on the host-guest interactions have to be done to find the reason for this difference.

**Table 4.5.21** Ratio of SP-N per formula unit of the respective MOF for **9** to **12** calculated from XPS measurements.

		SP-N : MOF ratio
SP-N <sub>x</sub> @MOF-5 ( <b>9</b> )	SP-N : (Zn <sub>4</sub> O(bdc) <sub>3</sub> )	1.32 : 1
SP-N <sub>x</sub> @MIL-68(In) ( <b>10</b> )	SP-N : (In(OH)(bdc))	0.38 : 1
SP-N <sub>x</sub> @MIL-68(Ga) ( <b>11</b> )	SP-N : (Ga(OH)(bdc))	0.57 : 1
SP-N <sub>x</sub> @MIL-53(Al) ( <b>12</b> )	SP-N : (Al(OH)(bdc))	0.38 : 1

#### 4.4.2.2.3 Effects

In order to investigate the switching properties of SP-N embedded in different host materials, UV/vis spectroscopic measurements were performed. For all compounds very limited respectively no photoswitching was found to occur even after 30 min of UV light exposure ( $\lambda = 365$  nm). The results are exemplarily discussed for compound **9**. For compounds **10** to **12** see figure 8.3.27 to 8.3.29 in the supplement.

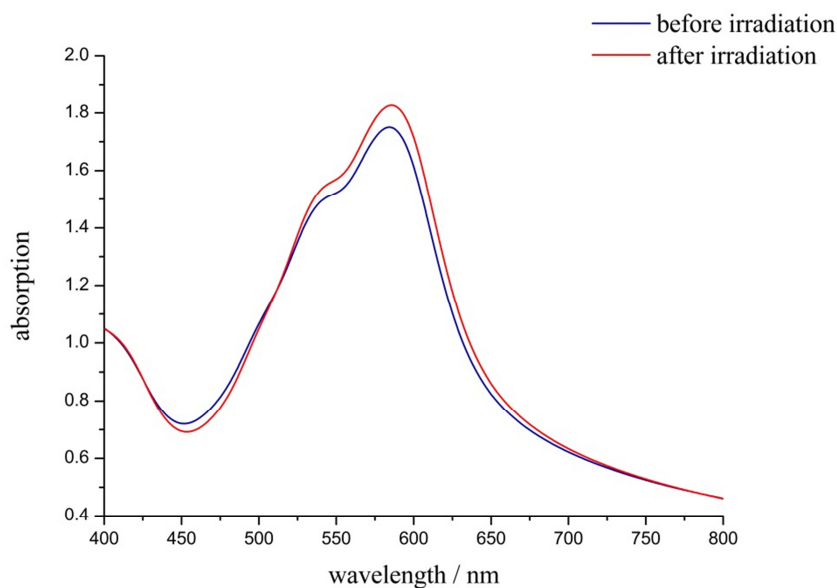


**Figure 4.4.48** Absorption spectra (298 K) of SP-N@MOF-5 (**9**) before (blue) and after (red) irradiation with UV light ( $\lambda = 365$  nm, 30 min).

Analogue to compound **5** and **9**, parts of SP-N embedded in MOF-5 are already present in its open MC-N without UV light exposure, which is obvious in the presence of the local absorption maximum at  $\lambda = 584$  nm with a shoulder at  $\sim 525$  nm (see figure 4.4.48). When dissolved in ethanol, an absorption maximum at 573 nm is found.<sup>[204]</sup> By irradiation with  $\lambda = 365$  nm for 30 min, the absorption maximum at  $\lambda = 584$  nm increases, which indicates a proceeding formation of the open merocyanine. Alteration upon excitation are rather small for the other compounds **10** to **12**: While a small increase in intensity is found for **10**, the absorption maximum of **11** slightly decreases and no changes are observed for **12** (see figures 8.2.41 to 8.2.43 in the supplement). Similar to SP@MOF systems, to fully understand decreasing and increasing absorption bands (photodegradation, complete attribution to the SP and MC form), IR spectroscopic measurements have to be applied in future investigations.

Notably, the open merocyanine form is stabilized in all compounds even without UV light exposure. In figure 4.4.49 compounds **9** to **13** are shown before (left) and after irradiation (right) with UV light ( $\lambda = 385$  nm).

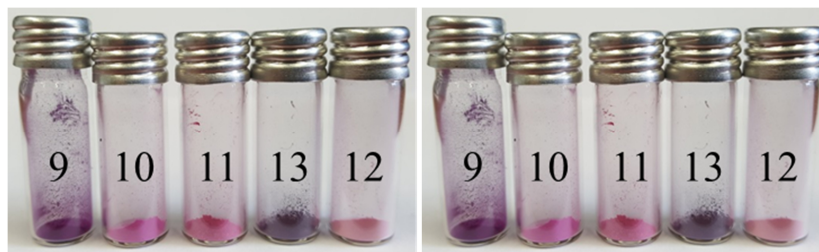


**Figure 4.4.49** Compounds **9** to **13** before (left) and after irradiation with UV light with  $\lambda = 385$  nm (right).

Apparently, irradiation does not have a profound impact on the absorption properties of SP-N embedded in the different host materials. Similar to SP, this could be the result of inhibited photochromism of the embedded dye molecule on the one hand. On the other hand, another excitation wavelength might be required to trigger the light induced switching. Hence, further experiments with light of different wavelengths have to be performed in future studies to investigate the switching properties of SP-N inside the MOF scaffolds.

#### 4.4.2.2.4 Mechanochemical Loading

In addition to gas phase loading, another embedment mechanism was performed for the incorporation of SP-N into different host materials: mechanochemical loading. Ten different dilutions were applied for the MOFs MOF-5, MIL-68(In), MIL-68(Ga) and HKUST-1. Molar ratios of  $n(\text{MOF}) : n(\text{SP-N})$  of 1:x with  $x = 0.1, \dots, 1$  in steps of 0.1 were used.

That way, 40 different SP-N@MOF compounds were obtained. The incorporation was followed by means of XRPD measurements. In figure 4.4.50 the diffraction patterns of the serial dilution of SP-N in MIL-68(Ga) are shown. The other serial dilutions can be found in figure 8.3.30 and 8.3.32 in the supplement.

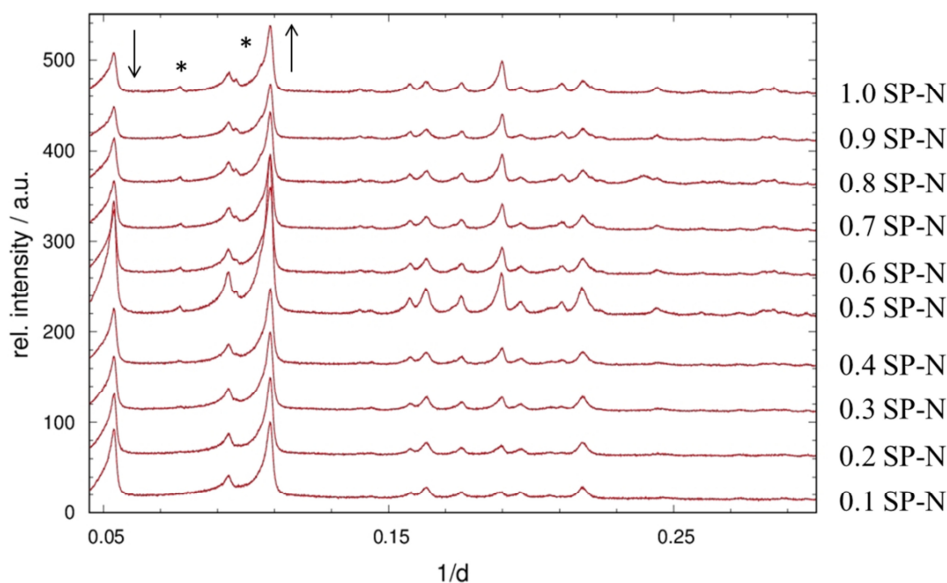


**Figure 4.4.50** Diffraction patterns of the serial dilution of MIL-68(Ga) with SP-N, measured at 298 K (*Huber G670*;  $\lambda = 1.54 \text{ \AA}$ ), with offset. Peaks of free dye molecules are marked with an “\*”. Alterations in intensity are illustrated with an arrow.

Alterations in intensity of the first and third peak are found to occur upon guest loading for representatives of the MIL-68 family. This has been comprehensively described for SP-Nitro@MIL-68(In/Ga) in chapter 4.4.1. When thoroughly ground with MIL-68(Ga) a successful and complete incorporation of SP-N is observed for  $n(\text{SP-N}) \leq 0.3$ . The first peak loses and the third gains in intensity, which confirms the embedment of the dye molecule (marked with an arrow). Interestingly, decrease and increase of the peaks are not constant, but change (e.g. for 0.5 SP-N the highest intensity is found for the third peak). This might be the result of a varying packing density of the capillaries during the XRPD measurements. For  $n(\text{SP-N}) > 0.3$  additional peaks occur, which are marked with an “\*”. They are attributed to free spiropyran, which is not embedded even for prolonged grinding times. Therefore, mechanochemical loading of MOFs with SP-N is possible. However, complete embedment is only achieved for low SP-N concentrations.

#### 4.4.2.3 SP-OMe@MOF hybrid materials

SP-OMe was embedded into five different MOFs, namely MOF-5, MIL-68(In), MIL-68(Ga), MIL-53(Al) and HKUST-1, via a gas phase loading process. Five SP-OMe@MOF composite materials were obtained:

(14) SP-OMe@MOF-5

(15) SP-OMe@MIL-68(In)

(16) SP-OMe@MIL-68(Ga)

(17) SP-OMe@MIL-53(Al)

(18) SP-OMe@HKUST-1

These SP-OMe@MOF systems were investigated by means of the ICE-principle. The results are presented in the following.

##### 4.4.2.3.1 Incorporation

The successful incorporation of the dye molecule was confirmed by means of XRPD measurements. The XRPD pattern of SP-OMe@MOF-5 (**14**) is exemplarily shown in figure 4.4.51. The peaks of the diffraction pattern do not change in position, but in intensity in comparison to the theoretical data of MOF-5. Alterations are small, but present, pointing to a successful embedment of SP-OMe. Additionally, a shoulder is present before the second peak, which has also been observed for SP-N@MOF-5 (**9**). The reason for this is not known yet. For diffraction patterns of compounds **15** to **18** see figures 8.3.33 to 8.3.36 in the supplement.

In order to determine changed cell volumes upon guest loading, *Le Bail* fits in *JANA2006*<sup>[194]</sup> were performed. In table 4.4.22 the results are listed and compared to the volumes of the respective unloaded host material. Notably, *Le Bail* fits on the unloaded MOFs except HKUST-1 were performed with high resolution synchrotron powder diffraction data (BM01B, ESRF), while loaded MOFs were investigated by laboratory diffraction. Hence, comparison of these data is of qualitative but not quantitative value. *Le Bail* fits of **14**, **15** and **18** and the respective unloaded MOFs are shown in figures 8.2.2 to 8.2.4, table 8.2.1 and 8.3.2

and figures 8.3.22, 8.3.37 to 8.3.39 in the supplement. Due to the low data quality of **16**, no *Le Bail* fits were performed on this compound.

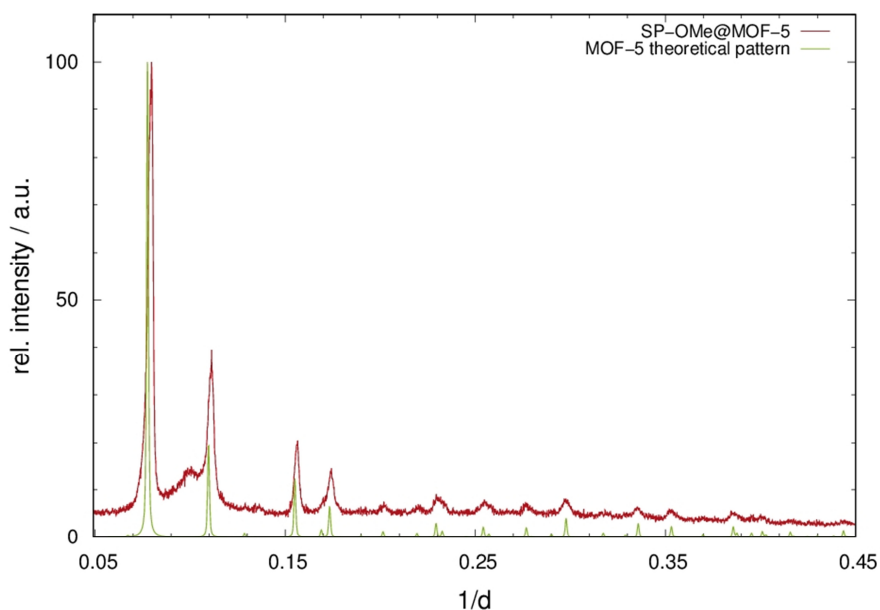


**Figure 4.4.51** XRPD pattern of **(14)** (red), measured at 298 K (*Stoe StadiP*:  $\lambda = 1.54 \text{ \AA}$ ), in comparison to theoretical data of MOF-5 (green).

**Table 4.4.22** Results of *Le Bail* fits of powder diffraction data of compounds **14**, **15** and **18** compared with the unit cell volumes of the respective unloaded MOF.

	<b>(14)</b>	<b>(15)</b>	<b>(18)</b>
T/K	298	298	298
Space Group / No.	$Fm\bar{3}m$ / 225	$Cmcm$ / 63	$Fm\bar{3}m$ / 225
GOF	1.16	0.90	0.85
$R_p$	0.083	0.1087	0.069
$wR_p$	0.1111	0.1514	0.0921
$V/\text{\AA}^3$	17425(3)	6093(2)	18464(3)
a	25.925(5)	22.105(6)	26.431(4)
b	-	37.86(1)	-
c	-	7.281(2)	-
$V/\text{\AA}^3$ (unloaded MOF)	17156.0(4)	5901.5(2)	18161(2)

For all compounds **14**, **15** and **18**, the incorporation of SP-OMe causes a significant increase in volume in comparison to the unloaded MOF framework. The expansion of the MOF scaffold upon guest loading points to repulsive host-guest interactions. This assumption has to be further strengthened by additional methods in future investigations exactly the same as for all other spiropyran@MOF composite materials.

#### 4.4.2.3.2 Composition

The composition of the SP-OMe@MOF compounds was determined by means of XPS measurements. Analogue to the other spiropyran@MOF systems the areas of typical nitrogen XPS signals and the areas of the typical metal cation XPS signals were compared. The used spiropyran possesses one nitrogen atom. Hence, only one N1s peak is expected. In table 4.4.23 the results of the XPS measurements are listed. Peak fits of the XPS data and calculations are found in figures 8.3.40 to 8.3.43 and table 8.3.4 in the supplement.

**Table 4.4.23** Ratio of SP-OMe per formula unit of the respective MOF for **14** to **17** calculated from XPS measurements.

		SP-OMe : MOF ratio
SP-OMe <sub>x</sub> @MOF-5 ( <b>14</b> )	SP-OMe : (Zn <sub>4</sub> O(bdc) <sub>3</sub> )	1.86 : 1
SP-OMe <sub>x</sub> @MIL-68(In) ( <b>15</b> )	SP-OMe : (In(OH)(bdc))	0.32 : 1
SP-OMe <sub>x</sub> @MIL-68(Ga) ( <b>16</b> )	SP-OMe : (Ga(OH)(bdc))	0.47 : 1
SP-OMe <sub>x</sub> @MIL-53(Al) ( <b>17</b> )	SP-OMe : (Al(OH)(bdc))	0.22 : 1

Analogue to the previously discussed spiropyran@MOF composites, the highest amount of embedded dye is present in MOF-5 and the lowest in MIL-53(Al). Surprisingly, the calculated ratios of SP-OMe in compound **15** and **16** significantly differ from each other, which has been observed for SP-N as well. To explain this, the type of host-guest interactions have to be determined e.g. via IR spectroscopy.

#### 4.4.2.3.3 Effects

Photoswitching of SP-OMe was only followed by means of UV/vis spectroscopy. For all compounds either limited or no photoswitching was found to occur even after 30 min of UV light exposure ( $\lambda = 365$  nm). The absorption spectrum of SP-OMe embedded in MOF-5 (compound **14**) is exemplarily shown in figure 4.4.52. All other spectra are found in figure 8.3.44 to 8.3.46 in the supplement.

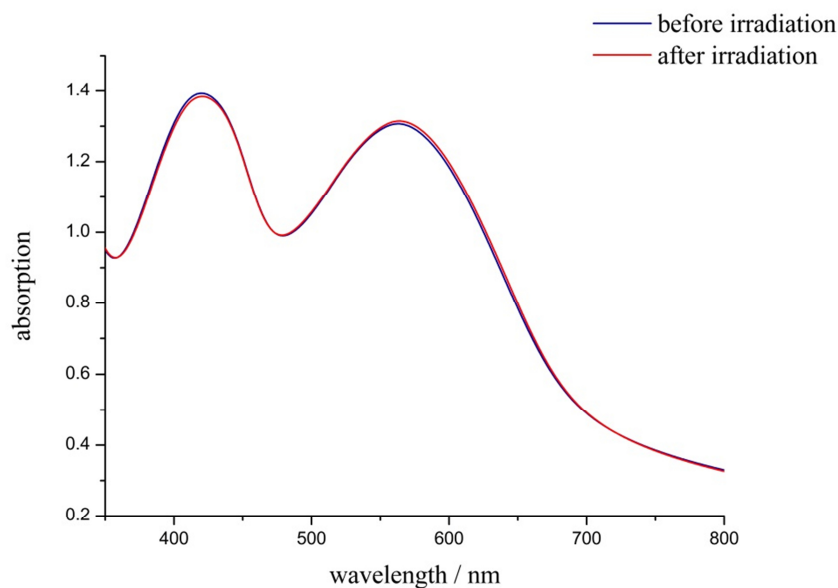


**Figure 4.4.52** Absorption spectra (298 K) of SP-OMe@MOF-5 (**14**) before (blue) and after (red) irradiation with UV light ( $\lambda = 365$  nm, 30 min).

Obviously, the open merocyanine form is already present in **14** without UV light exposure. Furthermore, extended excitation does not markedly change the absorption properties of SP-OMe embedded inside MOF-5 pointing to a full stabilization of MC-OMe, which has also been found for the other spiropyran@MOF-5 composite materials. For compound **15** a slight increase of the characteristic absorption band is observed (figure 8.2.58 in the supplement), while a slight decrease is found for **16** (figure 8.2.59 in the supplement). When combined with MIL-53(Al) (compound **17**) no response is observed (figure 8.2.60 in the supplement).



**Figure 4.4.53** Compounds **14** to **17** before (left) and after irradiation with UV light with  $\lambda = 385$  nm (right).

In figure 4.4.53 compounds **14** to **17** are shown before (left) and after (right) UV light exposure for 1 min. Similar to SP and SP-N, SP-OMe does not exhibit profound differences in its absorption properties before and after excitation. As already discussed for SP and SP-N, this could be the result of inhibited photochromism of the embedded dye molecule on the one hand. On the other hand, another excitation wavelength might be required to trigger the light induced switching. Hence, further experiments with light of different wavelengths have to be performed in future studies to investigate the switching properties of SP-OMe inside the MOF scaffolds.

#### 4.4.2.3.4 Mechanochemical Loading

Analogue to SP-N, mechanochemical embedment was performed for SP-OMe. Thereupon, ten different dilutions were applied for the MOFs MOF-5, MIL-68(In), MIL-68(Ga) and HKUST-1. Molar ratios of  $n(\text{MOF}) : n(\text{SP-OMe})$  of 1:x with  $x = 0.1, \dots, 1$  in steps of 0.1 were used.

That way, 40 different SP-OMe@MOF materials were yielded. The incorporation was followed by means of XRPD measurements. In figure 4.4.51 the diffraction patterns of the serial dilution of MIL-68(Ga) are shown. The other serial dilutions can be found in figure 8.3.47 and 8.3.49 in the supplement.

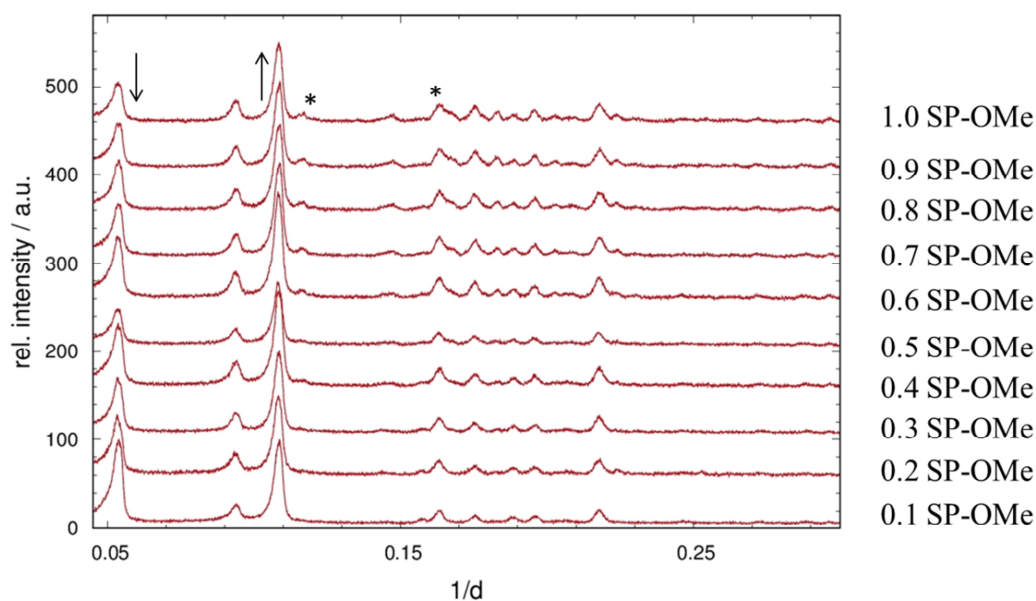


**Figure 4.4.51** Diffraction patterns of the serial dilution of MIL-68(Ga) with SP-OMe at 298 K (*Stoe StadiP*:  $\lambda = 1.54 \text{ \AA}$ ), with offset. Peaks of free dye molecules are marked with an “\*”. Loss and gain in intensity is illustrated with an arrow.

Similar to the serial dilution of SP-N@MIL-68(Ga), SP-OMe is successfully embedded into MIL-68(Ga) via a mechanochemical loading process. When thoroughly ground with MIL-68(Ga) a successful and complete incorporation of SP-OMe is observed for  $n(\text{SP-OMe}) \leq 0.2$ . The first peak loses and the third gains in intensity, which confirms the embedment of the dye molecule (marked with an arrow). Similar to the serial dilution of SP-N in different MOF matrices, peak alterations are not constant, which can be explained by a varying packing density of the capillaries. For  $n(\text{SP-OMe}) > 0.2$  additional peaks occur, which are marked with an “\*”. They belong to free spiropyran, which is not embedded into the MOF scaffold even for prolonged grinding times. Therefore, mechanochemical loading of MOFs with SP-OMe is possible, but total embedment is only achieved for low SP-OMe concentrations.

### 4.4.3 Preliminary Conclusions

Four SP-Nitro@MOF systems were synthesized and characterized according to ICE-Principle. For the resulting compounds SP-Nitro@MOF-5 (**1**), SP-Nitro@MIL-68(In) (**2**) and SP-Nitro@MIL-68(Ga) (**3**) the successful incorporation of the dye molecule was confirmed via XRPD. Composition was determined using both elemental analysis and XPS. XPS was found to be the more appropriate method for two reasons: Firstly, only characteristic elements (nitrogen for the guest molecule and the respective metal cation for the MOF matrix) are considered, which minimizes possible mistakes. Secondly, broadening of the nitrogen peaks is a further proof of SP-Nitro being embedded in the MOF matrices.

For all compounds **1** to **3** photochromic response is observed upon UV light exposure, which was followed by UV/vis and IR spectroscopy. The light induced transformation of the closed SP form to its open MC form is not sterically hindered inside the MOF pores. Thus, switching of SP-Nitro is enabled in solid state, which has previously mostly been observed in solution. SP-Nitro@MOF composites represent first switching systems with a spiropyran guest molecule showing positive photochromism in a MOF scaffold. Moreover, the absorption maxima of the excited species strongly depend on the used host material. This solvatochromic response highly resembles the behavior of SP-Nitro when dissolved in solvents of varying polarity. Therefore, solvatochromism is not only found for solvents, but also for MOFs. Hence, MOFs can be regarded as “solid solvents” for spiropyrans. Interestingly, the open MC-Nitro is stabilized inside MOF-5: the inner surface of MOF-5 exhibits a chemical environment, which is preferably chosen by molecules with a high dipole moment such as merocyanines. For all compounds, progressive photodegradation was found for repetitive and prolonged UV light irradiation.

In contrast to compounds **1** to **3**, incorporation of SP-Nitro was not found for MIL-53(Al), but surface adsorption instead. Nonetheless, SP-Nitro@MIL-53(Al) (**4**) exhibits photochromic behavior with a red-shifted absorption maximum in comparison to compounds **1** to **3**. Hence, the light induced transformation of SP-Nitro to MC-Nitro is even enabled for SP-Nitro being adsorbed on the MOF surface. Additionally, formation of *H*-aggregates occurs upon prolonged UV light exposure that retards the photodegradation process upon extended excitation.

On top of that, 14 further spiropyran@MOF systems were synthesized with SP, SP-N and SP-OMe. Similar to SP-Nitro the merocyanine form was found to be stabilized inside MOF-5 for

these three spiropyran which supports the assumption of MOF-5 being relatively polar in comparison to the other used host materials. In contrast to SP-Nitro and SP the spiropyran SP-OMe and SP-N were incorporated via both, gas phase and mechanochemical loading. A dilution series for MOF-5, MIL-68(In), MIL-68(Ga) and HKUST-1 was applied and the embedment was followed by XRPD measurements. Nonetheless, a total incorporation without the presence of free dye molecule was not achieved for high spiropyran concentrations. In contrast to SP-Nitro switching of SP, SP-N and SP-OMe is less effective inside the different host materials. Hence, SP-Nitro represents the most suitable one among the used spiropyran.

Nevertheless, the low fatigue resistance of SP-Nitro is a major drawback with respect to possible applications. In order to avoid this disadvantage, structurally related spirooxazines were chosen for further experiments. In contrast to spiropyran, spirooxazines exhibit a profound photostability. This class of photoswitchable molecules and the resulting spirooxazine@MOF systems will be part of the following chapter.

## 4.5 Spirooxazine@MOF hybrid materials

Spiropyrans and spirooxazines are closely related to each other. Both dye molecules differ in their structure by an additional nitrogen atom in the spiropyran chromene ring. Hence, the spiro carbon connects the indoline with a benzoxazine part in spirooxazines. While spiroopyrans were very intensively studied after their discovery<sup>[16,17]</sup>, the synthesis of and publications on spirooxazines somehow went unnoticed, even though they are known since 1960.<sup>[205]</sup> Only since the 1980s the class of spirooxazines has become more present, mainly due to *Chu's* discovery of the extraordinary photostability of 1,3,3-trimethylindolino-naphthospirooxazine (SP-O) and derivatives under continuous light excitation.<sup>[205]</sup> For this reason, spirooxazines are preferred in comparison to spiropyrans. The structure of SP-O is shown in figure 4.5.1.

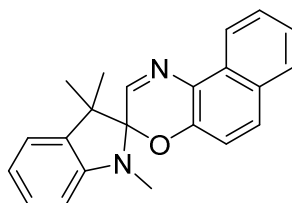


**Figure 4.5.1** Structure of 1,3,3-trimethylindolino-naphthospirooxazine (SP-O).

Upon UV light irradiation the closed spirooxazine form converts into the open strongly colored merocyanine form. The switching process has already been illustrated and comprehensively described in chapter 2.1.1. Similar to spiroopyrans, the MC form of spirooxazines occurs in four acyclic isomers with the TTC form being the most stable one according to quantum-chemical calculations (see figure 4.5.2).<sup>[206,207]</sup>

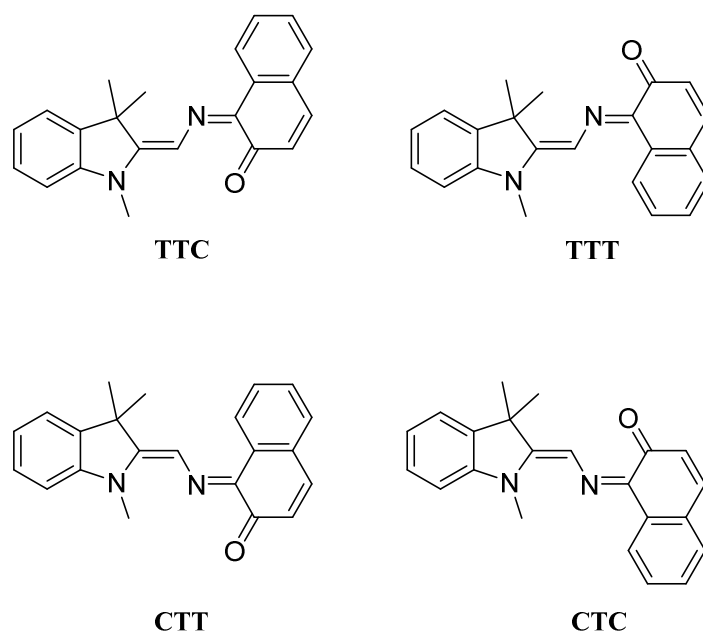


**Figure 4.5.2** Different isomers of the open merocyanine form of SP-O.

Excited spirooxazine exhibits an absorption maximum in the range of  $\lambda = 480 - 670$  nm, which is dependent on the substituent and the polarity of the surrounding medium. Besides, the absorption maxima feature an asymmetric shape with a red- or blue-shifted shoulder for different substituents under normal conditions.<sup>[205]</sup> Additionally, the position of the absorption maximum is strongly dependent on the polarity of the surrounding medium. Solvatochromism can either be positive or negative in relation to the substituents of the spirooxazine molecules. For SP-O positive solvatochromism was found to occur, which results in bathochromically shifted absorption bands.<sup>[205]</sup> The absorption maxima  $\lambda_{\max}$  of spirooxazine dissolved in solvents of varying polarity with their respective elution power  $\epsilon^0$  according to *Snyder*<sup>[193]</sup> are listed in table 4.5.1.

**Table 4.5.1** List of different solvents of varying polarity with their elution power and  $\lambda_{\max}$  of MC-O dissolved in these solvents.

solvent	$\lambda_{\max}$ of MC-O / nm <sup>[205]</sup>	elution power $\epsilon^0$ <sup>[193]</sup>
methanol	613	0.95
ethanol	610	0.88
acetonitrile	602	0.65
toluene	596	0.29
cyclohexane	556	0.04

Based on the results of SP-Nitro being embedded in different MOF hosts, a behavior of SP-O inside those frameworks similar to that when dissolved in solvents of varying polarity is expected. On that occasion, four different hybrid materials were synthesized and characterized. Notably, no spirooxazine@MOF systems are known up to now.

#### **4.5.1 SP-O@MOF hybrid materials**

SP-O was embedded into four different MOFs, namely MOF-5, MIL-68(In), MIL-68(Ga) and MIL-53(Al) via a gas phase loading process. Four SP-O@MOF composite materials were obtained:

**(19)** SP-O@MOF-5

**(20)** SP-O@MIL-68(In)

**(21)** SP-O@MIL-68(Ga)

**(22)** SP-O@MIL-53(Al)

These SP-O@MOF systems were investigated according to the ICE-principle. The results are presented in the following.

##### **4.5.1.1 Incorporation**

The successful incorporation of SP-O into the four different host matrices MOF-5, MIL-68(In), MIL-68(Ga) and MIL-53(Al) was confirmed by XRPD measurements. Analogue to the SP-Nitro@MOF systems, non-flexible MOFs are discussed first.

For SP-O@MOF-5 **(19)** marked alterations in the peak intensities are found when compared to the pattern calculated from the literature known crystal structure of MOF-5<sup>[116]</sup> (see figure 4.5.3). Especially for the second peak a profound increase in intensity points to the successful incorporation of the dye molecule.

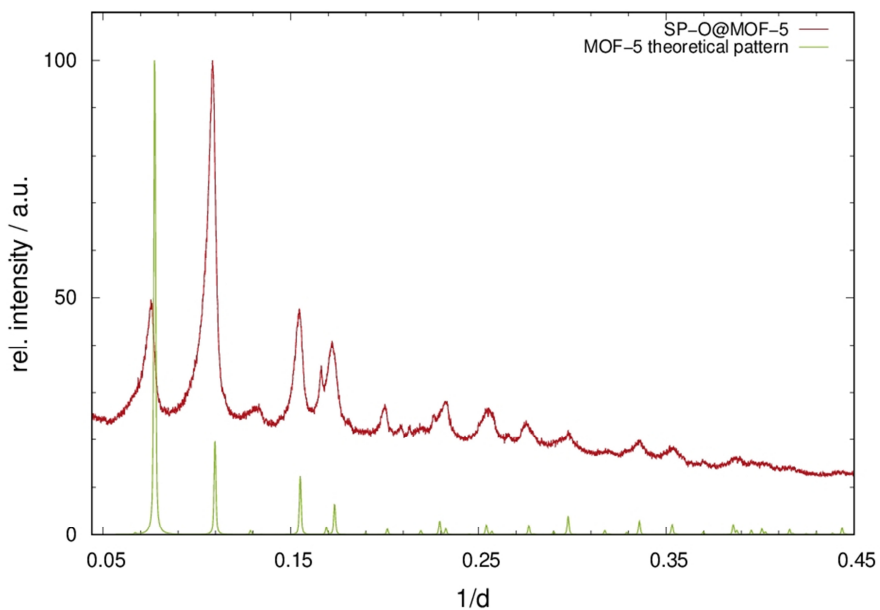


**Figure 4.5.3** XRPD pattern of **(19)** (red), measured at 298 K (*Huber G670*:  $\lambda = 1.54 \text{ \AA}$ ), in comparison to theoretical data of MOF-5 (green).

Hybrid systems of MIL-68(In) and MIL-68(Ga) containing SP-O as guest molecule exhibit similar behavior such as compounds **2** and **3** for the nitro-substituted spiropyran: A profound gain in intensity of the third peak and loss in intensity of the first one show the successful embedment for both SP-O@MIL-68(In) (**20**) and SP-O@MIL-68(Ga) (**21**). The diffraction pattern of **20** and **21** are shown in figures 4.5.4 and 4.5.5, respectively.

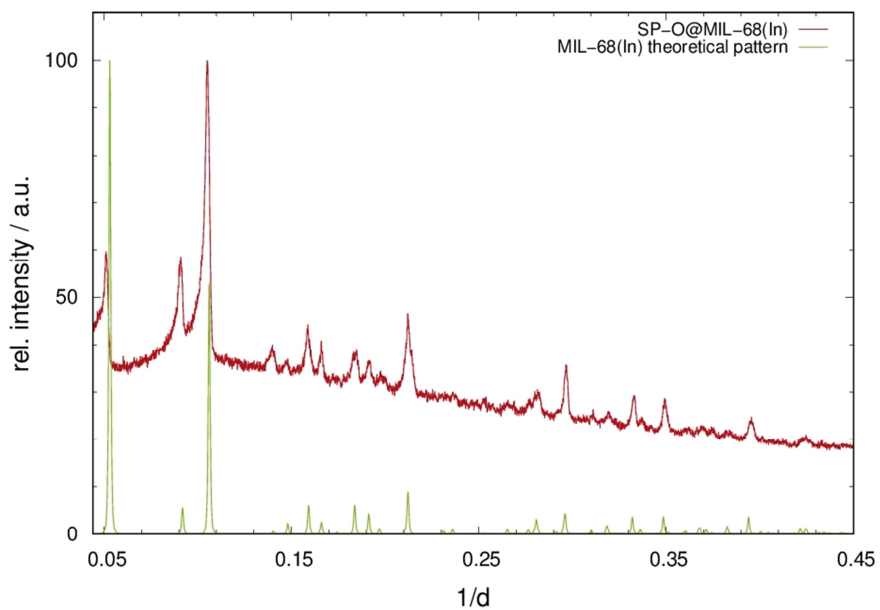


**Figure 4.5.4** XRPD pattern of **(20)** (red), measured at 298 K (*Huber G670*:  $\lambda = 1.54 \text{ \AA}$ ), in comparison to theoretical data of MIL-68(In) (green).

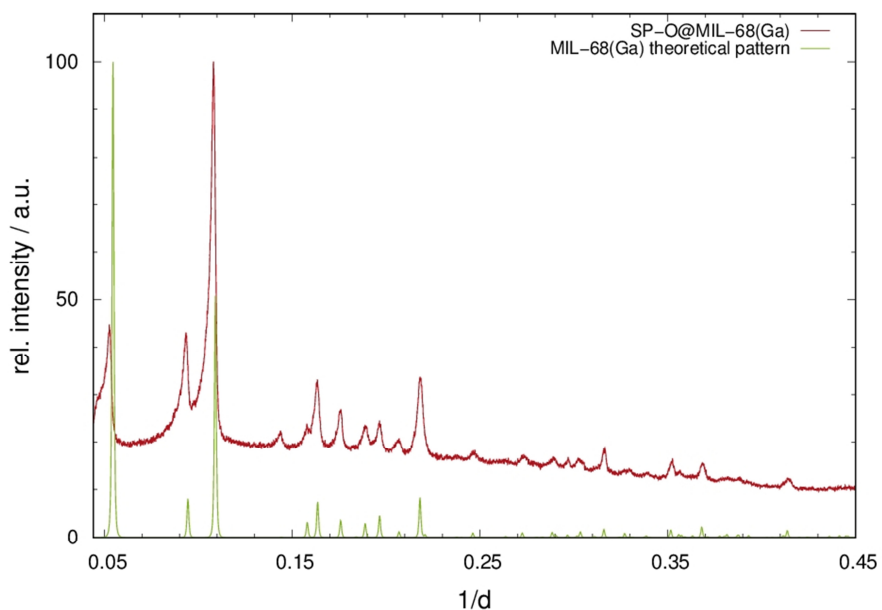


**Figure 4.5.5** XRPD pattern of **(21)** (red), measured at 298 K (*Huber G670*:  $\lambda = 1.54 \text{ \AA}$ ), in comparison to theoretical data of MIL-68(Ga) (green).

For all compounds **19** to **21** the presence of free spirooxazine can be excluded since no additional peaks occur.

In order to determine changed cell volumes upon guest loading, *Le Bail* fits in *JANA2006*<sup>[194]</sup> were performed. In table 4.5.2 the results are listed and compared to the volumes of the respective unloaded host material. It has to be stated that *Le Bail* fits on the unloaded MOFs were performed with high resolution synchrotron powder diffraction data, while loaded MOFs were investigated by laboratory diffraction. Thus, comparison of these data is of qualitative but not quantitative value. *Le Bail* fits of **19** to **21** and the respective unloaded MOFs are shown in figures 8.2.2 to 8.2.4, table 8.2.1 and figures 8.4.1 to 8.4.3 in the supplement.

**Table 4.5.2** Results of *Le Bail* fits of powder diffraction data of compounds **19** to **21** compared with the unit cell volumes of the respective unloaded MOF.

	(19)	(20)	(21)
T/K	298	298	298
Space Group / No.	$Fm\bar{3}m$ / 225	$Cmcm$ / 63	$Cmcm$ / 63
GOF	1.55	0.92	1.38
R <sub>p</sub>	0.031	0.0202	0.0276
wR <sub>p</sub>	0.0469	0.0315	0.0431
V/Å <sup>3</sup>	16502(3)	5949(1)	5073(1)
a	25.459(5)	22.425(2)	20.546(3)
b	-	37.160(4)	37.594(6)
c	-	7.1388(7)	6.568(1)
V/Å <sup>3</sup> (unloaded MOF)	17156.0(4)	5901.5(2)	5197.0(7)

For the flexible MOF MIL-53(Al) a different behavior is observed when combined with the spirooxazine. Similar to SP-Nitro the diffraction pattern remains unaltered with respect to intensity and position in comparison to the unloaded host material (see figure 4.5.6), even though a change in color occurs upon gas phase loading. For SP-Nitro@MIL-53(Al) (**4**) the results of further spectroscopic measurements pointed to the adsorption of the dye molecule as an amorphous film on the MOF surface. A similar situation is assumed for SP-O@MIL-53(Al) (**22**), which has to be further strengthened by additional measurements (presented in the following chapters). Since the combination of SP-Nitro and MIL-53(Al) also exhibits photochromic behavior for the dye being adsorbed on the host surface, further investigations on spirooxazine combined with MIL-53(Al) were performed.

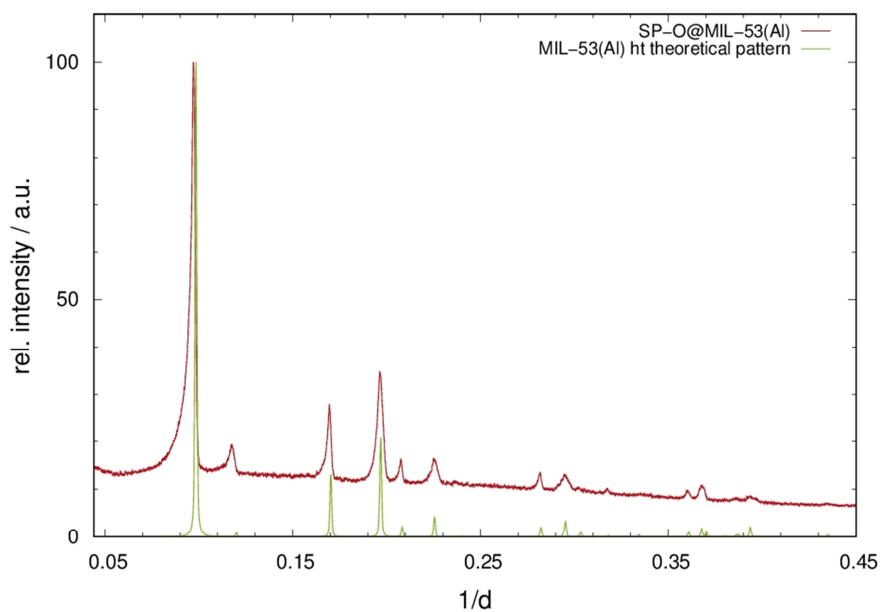


**Figure 4.5.6** XRPD pattern of **(22)** (red), measured at 298 K (*Huber G670*:  $\lambda = 1.54 \text{ \AA}$ ), in comparison to theoretical data of MIL-53(Al) (green).

It has to be stated that the quality of the diffraction patterns of compounds **19** to **22** is comparably low due to the measurement conditions of the *Huber G670* diffractometer: Peaks are asymmetric in the low-angle region, which results in values of poor quality for the *Le Bail* fits.

#### 4.5.1.2 Composition

The composition of the spirooxazine@MOF compounds was determined by means of XPS measurements. Analogue to the spiropyran@MOF systems the areas of typical nitrogen XPS signals and were compared with the areas of the typical metal cation XPS signals. The used spirooxazine features two nitrogen atoms, which can be treated electronically equal. Hence, only one N1s peak is expected. The results of the XPS measurements are listed in table 4.5.3. Peak fits of the XPS data and calculations are found in figures 8.4.4 to 8.4.7 and table 8.4.1 in the supplement.

**Table 4.5.3** Ratio of SP-O per formula unit of the respective MOF for **19** to **22** calculated from XPS measurements.

		SP-O : MOF ratio
SP-O <sub>x</sub> @MOF-5 ( <b>19</b> )	SP-O : (Zn <sub>4</sub> O(bdc) <sub>3</sub> )	2.15 : 1
SP-O <sub>x</sub> @MIL-68(In) ( <b>20</b> )	SP-O : (In(OH)(bdc))	0.19 : 1
SP-O <sub>x</sub> @MIL-68(Ga) ( <b>21</b> )	SP-O : (Ga(OH)(bdc))	0.29 : 1
SP-O <sub>x</sub> @MIL-53(Al) ( <b>22</b> )	SP-O : (Al(OH)(bdc))	0.13 : 1

Nitrogen peaks of SP-Nitro embedded in MOF-5 and the MIL-68 family showed a marked broadening, while the adsorption of the dye molecule on the surface of MIL-53(Al) did not affect the electronic structure of the spiropyran. The comparison of typical nitrogen peaks of spirooxazine being either embedded in MOF-5 and MIL-68(In/Ga) or MIL-53(Al) points to a surface adsorption of the dye on MIL-53(Al) again (figure 4.5.7). For spirooxazine combined with MIL-53(Al) only one peak is found at approx. 399 eV. In contrast to that, a slight peak splitting occurs for all other non-flexible MOFs. The nitrogen N1s peak area is exemplarily shown for SP-O@MIL-68(In) (**20**) in figure 4.5.8. In addition to the most intensive peak at 399 eV, a second one at approx. 404 eV appears which is not present for compound **22**, but for compound **21** (see figure 8.4.6 in the supplement). For spirooxazine embedded in MOF-5 peak broadening and a small shoulder at approx. 396 eV are observed (figure 8.4.4 in the supplement).

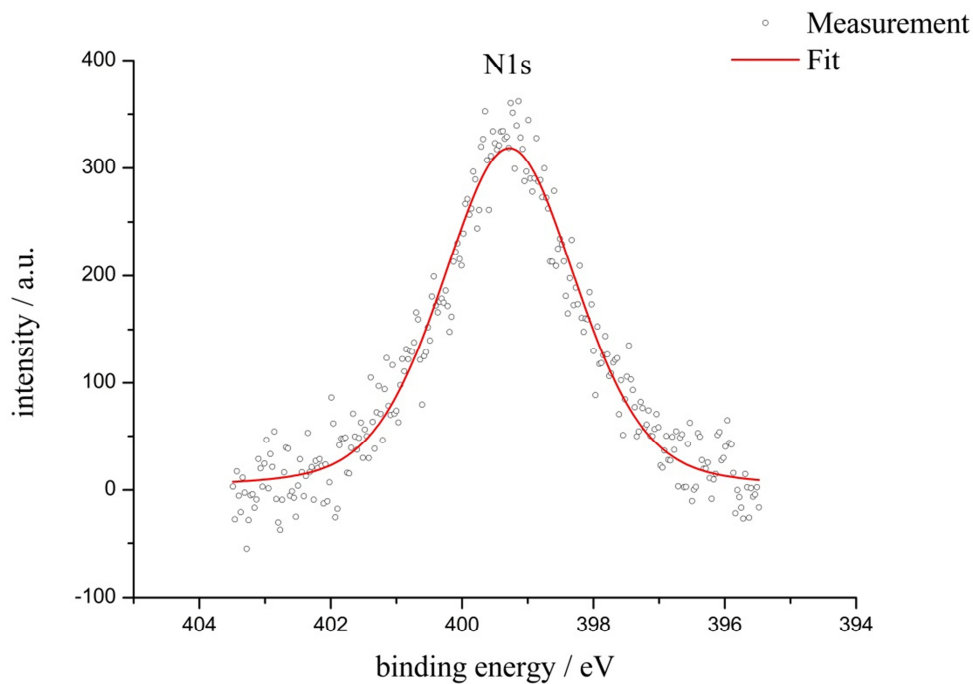


**Figure 4.5.7** XPS spectrum of the N1s peak of SP-O@MIL-53(Al) (**22**) with experimental data (dots) and fit (red).

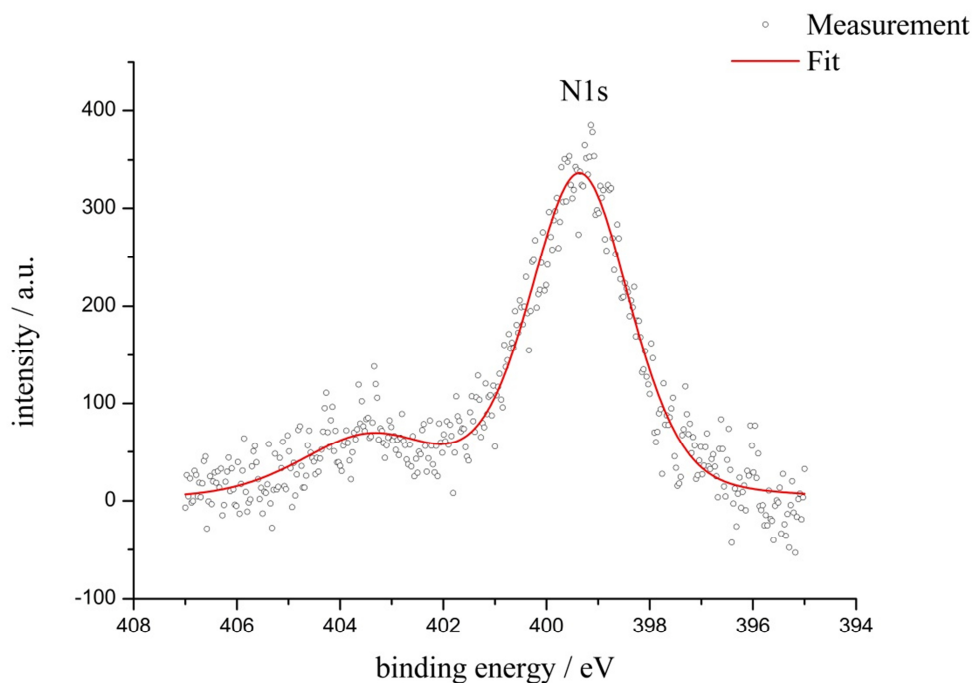


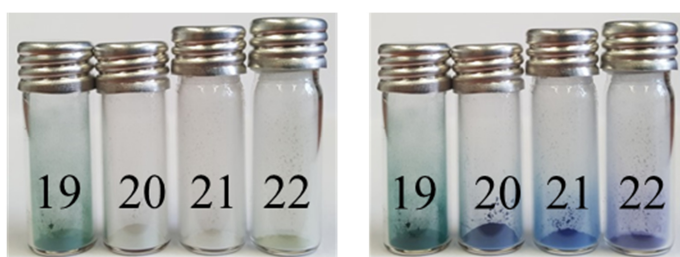
**Figure 4.5.8** XPS spectrum of the N1s peak of SP-O@MIL-68(In) (**20**) with experimental data (dots) and fit (red).

### 4.5.1.3 Effects

Besides the small structural differences between spiropyrans and spirooxazines, the last named compound is known to be highly resistant towards photodegradation – an obligatory property for possible applications. In solution, light irradiation of SP-O causes the conversion to its merocyanine form, which is strongly colored due to its planar structure and extended  $\pi$ -conjugation between the indoline and benzoxazine part (see chapter 4.5). Based on the results of SP-Nitro@MOF compounds, the spirooxazine@MOF systems were investigated focusing on the following aspects: (a) photoswitching properties and type of photochromism, (b) influence of the host matrix on the absorption properties and stabilization and (c) reversibility of switching and fatigue resistance.

#### 4.5.1.3.1 Photoswitching and Type of Photochromism

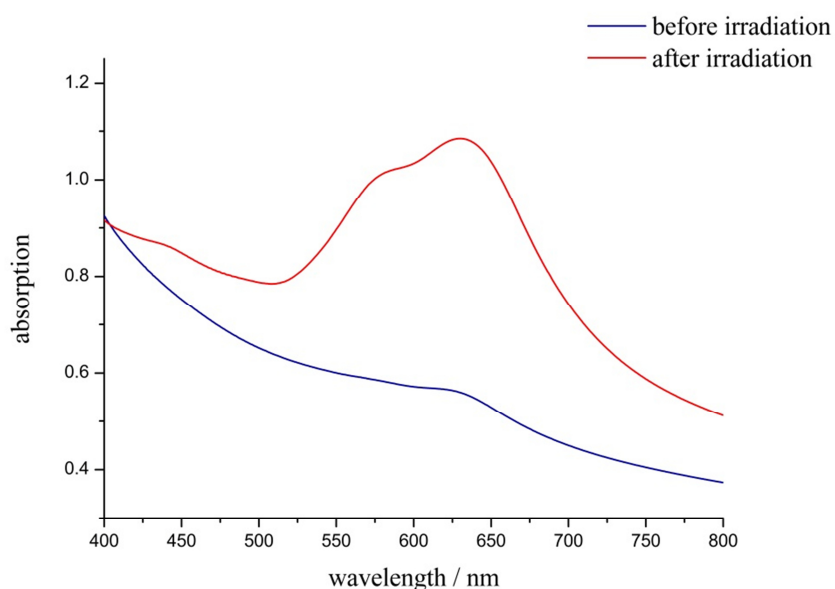
UV/vis absorption spectra before and after irradiation with UV light ( $\lambda = 365$  nm, 30 min) of all compounds **19** to **22** were recorded under inert conditions. Hence, possible influence of water because of moisture uptake can be excluded from all further considerations. The change in color upon UV light irradiation is depicted in figure 4.5.9. Obviously, incorporation of SP-O into MOF-5 already causes a stabilization of the colored merocyanine form. For the MIL-68 family and MIL-53(Al) the colored MC-O is only formed upon UV light exposure. In figures 4.5.10 to 4.5.13 the absorption spectra of the hybrid systems are shown.



**Figure 4.5.9** Compounds **19** to **22** before (left) and after irradiation with UV light with  $\lambda = 385$  nm (right), 1 min.

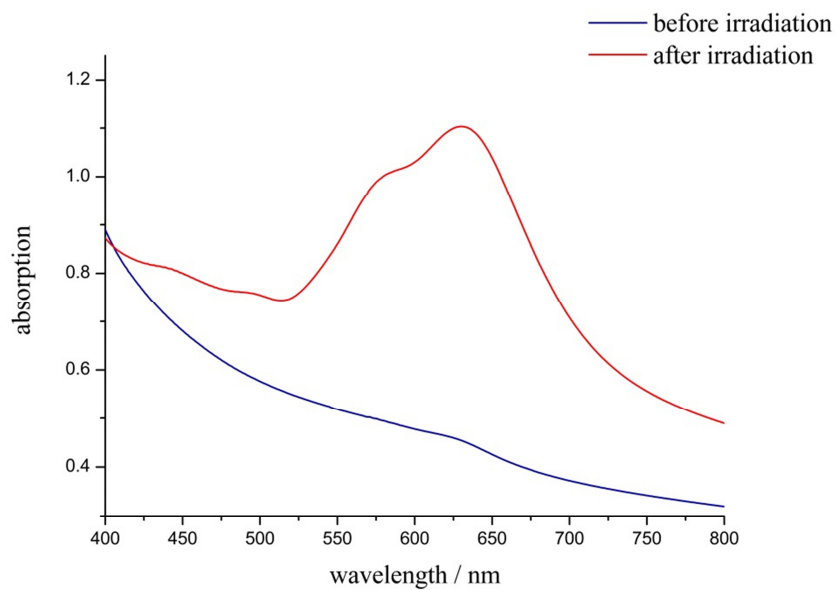
For **19** a small shoulder at  $\lambda = 631$  nm is already visible without irradiation, which is clearly attributed to the presence of spirooxazine in its merocyanine form (blue line, figure 4.5.10). When exposed to UV light a significant increase in intensity is observed, forming an absorption maximum at  $\lambda = 631$  nm with a blue-shifted shoulder at approx. 580 nm (red line, figure 4.5.10). This is the result of the proceeding formation of the merocyanine moiety upon

excitation. Similar to SP-Nitro@MOF-5 (**1**) the merocyanine form of the spirooxazine is partly stabilized - again pointing to an environment given by the MOF-5 pores being preferable for molecules with a high dipole moment such as merocyanines. In addition to that, positive photochromism occurs, since an absorption maximum is formed upon UV light irradiation.

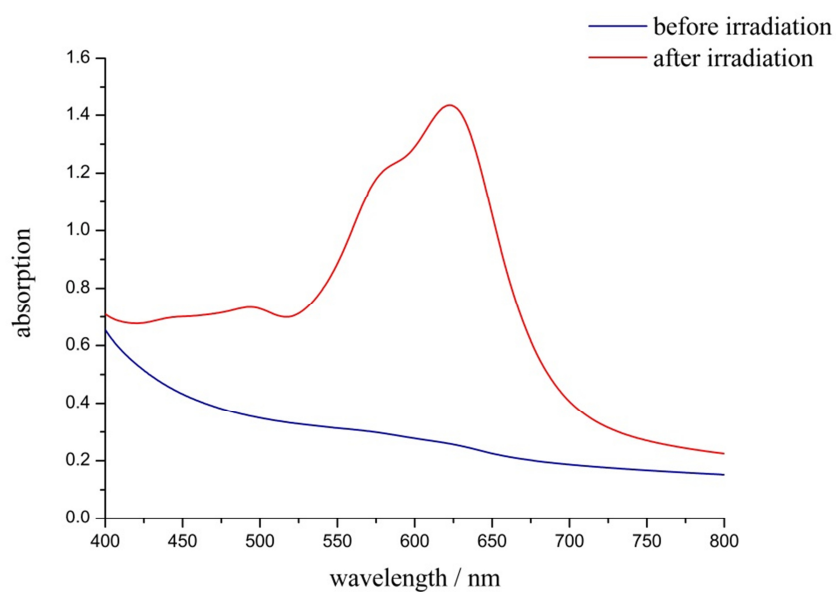


**Figure 4.5.10** Absorption spectra (298 K) of SP-O@MOF-5 (**19**) before (blue) and after (red) irradiation with UV light ( $\lambda = 365$  nm, 30 min).

For compounds **20** and **21** positive photochromism is found to occur as well. Before irradiation with UV light only a very small shoulder is observed in both cases, which does not lead to a colored product (see figure 4.5.11 and 4.5.12). When excited, the formation of MC-O can be followed by the appearance of a strong absorption band at 629 nm for compound **20** and 624 nm for compound **21**. Additionally, a blue-shifted shoulder is found to appear as well, which is positioned at 577 nm for compound **20** and at 575 nm for compound **21**. In comparison to compound **19** the absorption maxima are slightly blue-shifted. For **20** and **21** switching of the spirooxazine is not sterically hindered inside the MOF pores. This finding is similar to **19**.

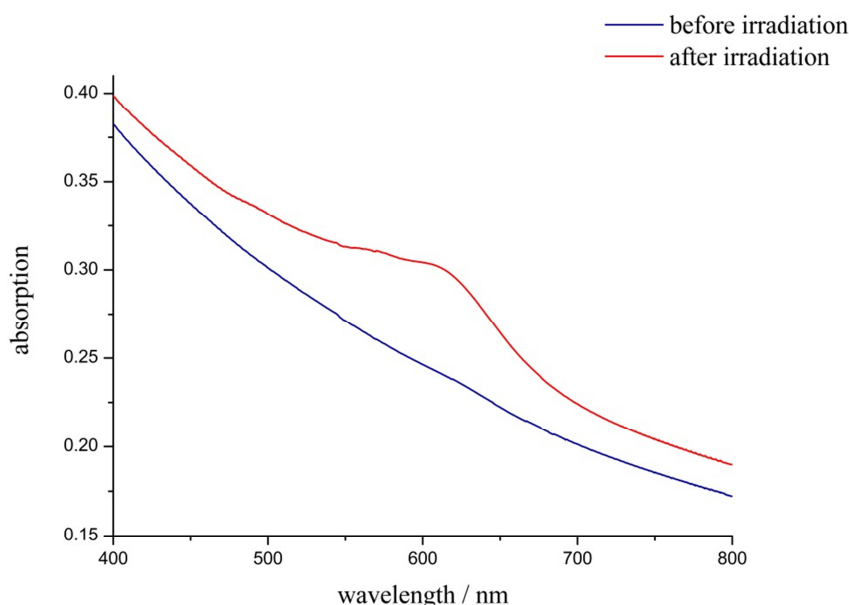


**Figure 4.5.11** Absorption spectra (298 K) of SP-O@MIL-68(In) (**20**) before (blue) and after (red) irradiation with UV light ( $\lambda = 365$  nm, 30 min).



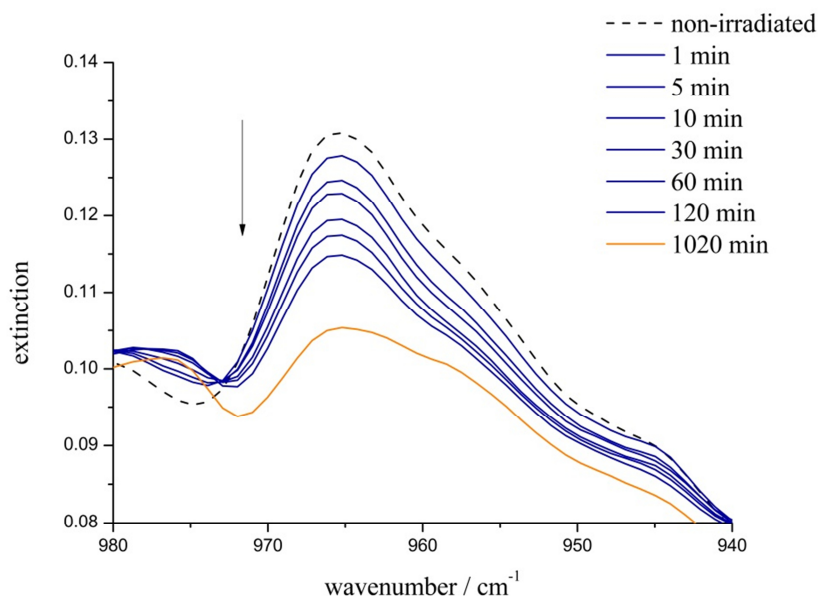
**Figure 4.5.12** Absorption spectra (298 K) of SP-O@MIL-68(Ga) (**21**) before (blue) and after (red) irradiation with UV light ( $\lambda = 365$  nm, 30 min).

Figure 4.5.13 shows the absorption spectra of non-irradiated and irradiated SP-O@MIL-53(Al) (**22**). From the XRPD and also XPS measurements a surface adsorption of the dye molecule is expected. Analogue to compound **4** the combination of spirooxazine and MIL-53(Al) exhibits photochromic behavior with an absorption maximum at approx. 613 nm, which is markedly blue-shifted in comparison to the other spirooxazine@MOF materials. Furthermore, a very small shoulder appears at around 566 nm. Additionally, the intensity of the occurring absorption maximum is rather small, indicating only a small amount of spirooxazine being adsorbed on the MOF surface, which has already been determined via XPS measurements. Nonetheless, compound **22** features positive photochromism upon UV light exposure.



**Figure 4.5.13** Absorption spectra (298 K) of SP-O@MIL-53(Al) (**22**) before (blue) and after (red) irradiation with UV light ( $\lambda = 365$  nm, 30 min).

Further investigations to understand and prove the SP to MC conversion were done by means of IR spectroscopic measurements both before and after irradiation with UV light. Exposure times varied and are given for the respective system. The conversion of SP-O to its MC-O form results in the cleavage of the  $C_{\text{Spiro-O}}$  bond. Hence, the decrease of this band at approx.  $\tilde{\nu} = 959 \text{ cm}^{-1}$  is used to follow the formation of MC-O.<sup>[198]</sup> The spectra of this fingerprint region are shown in figure 4.5.14 for compound **19**. A significant decrease for the  $C_{\text{Spiro-O}}$  band was observed with varying UV light exposure times, pointing to the successful formation of the excited state.



**Figure 4.5.14** IR spectra of **19** during irradiation with UV light ( $\lambda = 365$  nm) focusing on the decrease (the direction of the decrease is marked with an arrow) of the C<sub>Spiro</sub>-O band at approx.  $\tilde{\nu} = 959$  cm<sup>-1</sup>.

Upon irradiation with UV light, the IR bands for SP-O decrease while the ones for MC-O increase; this can be easily followed in the IR spectra. In the present work, an exact assignment of the IR bands to the respective isomer (SP-O and MC-O, respectively) was performed for SP-O combined with the four different MOF matrices. According to *Lyubimov* and co-workers<sup>[197]</sup> and *Paal and Arnold*<sup>[198]</sup> the decreasing IR bands of the SP form were assigned. Thereupon, the data of the non-irradiated species were subtracted from the irradiated ones to obtain  $\text{ext}_{\text{irrad}} - \text{ext}_{\text{ground state}}$ . The resulting spectra are found in figure 4.5.15 with changing bands colored in blue and the band for maximal irradiation colored in orange. Notably, maximum changes are accompanied by a maximum irradiation time, which indicates that no photodegradation takes place. Hence, increasing IR bands can be fully assigned to the merocyanine moiety.

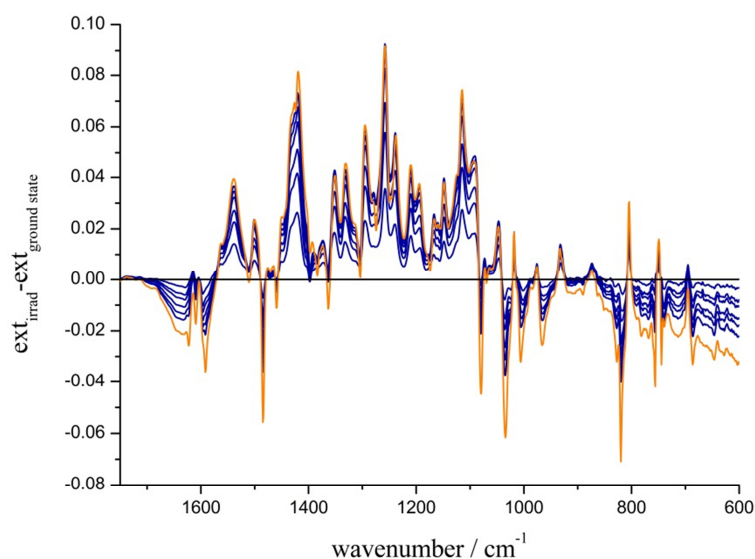


**Figure 4.5.15** Differential IR spectra of SP-O@MOF-5 (**19**). Maximum irradiation time (720 min) is colored in orange.

That way, the alterations upon UV light irradiation were detected. In the following table 4.5.4 the decreasing vibrational frequencies of SP-O@MOF-5 (**19**) and suspected assignments are listed. For a better understanding the structure of the closed spirooxazines is shown in figure 4.5.16, in which the different rings are labeled.

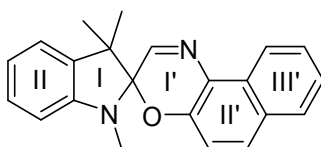


**Figure 4.5.16** Closed form of SP-O with labeled rings.

All decreasing vibrational frequencies were completely assigned to the closed form of the used spirooxazine. This points to the successful isomerization of SP-O to its MC-O form.

**Table 4.5.4** Assignment of decreasing IR bands of SP-O@MOF-5 (**19**) according to *Paal and Arnold*.<sup>[198]</sup> Theoretical data were taken from *Lyubimov and co-workers*<sup>[197]</sup>.

decreasing bands / cm <sup>-1</sup>	assignment / cm <sup>-1</sup>	vibration mode
1621	1620	$\nu(\text{C}=\text{C}), \nu(\text{C}=\text{N})$
1591	1592	ring-valence vibration $\nu(\text{C}=\text{C})$
1510	1508	ring-valence vibration $\nu(\text{C}=\text{C})$
1484	1485	ring-valence vibration $\nu(\text{C}=\text{C})$
1459	1453 1454 1461	<u>theoretical:</u> $\nu(\text{H}-\text{C}_{\text{Methyl}}-\text{H})$ (on N and C atoms) $\nu(\text{C}-\text{C})$ (II) $\nu(\text{C}-\text{N})$ (I) $\nu(\text{C}-\text{C}-\text{H})$ (II)
1362	1359	$\nu(\text{C}-\text{N})$
1079	1083	$\delta(\text{C}-\text{H})_{\text{arom.}}$
1035	1039	<u>theoretical:</u> $\nu(\text{O}-\text{C}_{\text{Spiro}}-\text{C})$ (I') $\nu(\text{C}_{\text{Spiro}}-\text{O})$ $\nu(\text{N}-\text{C}-\text{C})$ (I')
1005	1018 1022	<u>theoretical:</u> $\nu(\text{C}-\text{C})$ (II, III') $\nu(\text{C}-\text{N})$ (I, I')
966	959	$\nu(\text{O}-\text{C}_{\text{Spiro}}-\text{N})$
819	814	$\gamma(\text{C}-\text{H})$ (II', III')
756	749	$\gamma(\text{C}-\text{H})$ (II', III')
742	744	$\gamma(\text{C}-\text{H})$ benzene ring
685	682	<u>theoretical:</u> out-of-plane vibrations (I', II', III')
645	635	<u>theoretical:</u> in-plane-ring bending vibrations/bond bending vibrations of (I', II', III') and (II)

Moreover, increasing IR bands were analyzed. Unfortunately, an assignment of the open MC-O has not been published yet. Hence, an assignment was done following the one of *Lyubimov* and co-workers<sup>[197]</sup> and the one of *Paal and Arnold*<sup>[198]</sup>. Furthermore, unknown vibrational frequencies were assigned according to *Hesse, Meyer & Zeeh*<sup>[199]</sup>. Thereupon, the TTC mesomeric form of the merocyanine moiety of the spirooxazine has to be examined more precisely with respect to changing bonds in comparison to the closed SP-O. The structure is shown in figure 4.5.17 and compared to the closed SP-O form.

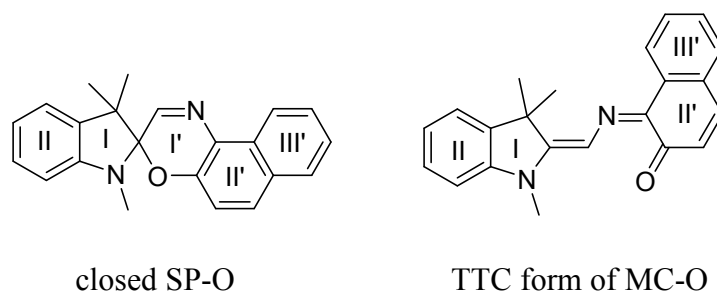


**Figure 4.5.17** Comparison of SP-O in its closed form and the TTC form of the respective merocyanine.

Obviously, the rings I, II and III' remain unaffected by the light induced cleavage of the C<sub>Spiro</sub>-O bond, whereas ring I' is completely destroyed and II' changes structurally. Therefore, all vibrational modes related to the rings I, II and III' remain. That way, all increasing bands were attributed to the respective vibrational modes pointing to a successful SP-O to MC-O conversion without the formation of any photo-by-product (table 4.5.4). The photostability of the used spirooxazine remains unaffected by the incorporation into MOF-5.

**Table 4.5.4** Assignment of increasing IR bands of SP-O@MOF-5 (**19**) according to *Lyubimov* and co-workers<sup>[197]</sup>, *Paal and Arnold*<sup>[198]</sup> and *Hesse, Meyer & Zeeh*<sup>[199]</sup>.

increasing bands / cm <sup>-1</sup>	assignment / cm <sup>-1</sup>	vibration mode
1539	1600-1500	ring-valence vibration $\nu(\text{C}=\text{C})$ <sup>[198,199]</sup>
1499	1600-1500	ring-valence vibration $\nu(\text{C}=\text{C})$ <sup>[198,199]</sup>
1475	1600-1500	ring-valence vibration $\nu(\text{C}=\text{C})$ <sup>[198,199]</sup>

1465	1453	<u>theoretical</u> <sup>[197]</sup>
	1454	$\nu(\text{C-C})$ (II)
	1461	$\nu(\text{C-N})$ (I)
	1475	$\nu(\text{C-C-H})$ (II)
1418	1420	$\delta(\text{C-H})$ neighboring $\text{C=O}$ <sup>[199]</sup>
1392	1390-1370	$\delta(\text{C-H})$ methyl-group of I <sup>[199]</sup>
1373	1390-1370	$\delta(\text{C-H})$ methyl-group of I <sup>[199]</sup>
1350	1359	$\nu(\text{C-N})$ <sup>[198]</sup>
1331	1335	<u>theoretical</u> <sup>[197]</sup>
		$\nu(\text{C-C})$ (III') $\nu(\text{C-C-H})$ (I, III')
1295	1308	<u>theoretical</u> <sup>[197]</sup>
		$\nu(\text{C-N})$ (I)
		$\nu(\text{C-C}_{\text{Methyl}})$ (I)
		$\nu(\text{C-N-C})$ (I) $\nu(\text{C-C-H})$ (II)
1258	1251	$\nu(\text{=C-O})$ <sup>[198]</sup>
1238	1238	<u>theoretical</u> <sup>[197]</sup> $\nu(\text{C-C-O})$
1209	1219	<u>theoretical</u> <sup>[197]</sup>
		$\nu(\text{C-C})$ (III')
		$\nu(\text{C-C-C})$ (III') $\nu(\text{C-C-H})$ (III')
1195	1174 1189	<u>theoretical</u> <sup>[197]</sup>
		$\nu(\text{C-C}_{\text{Methyl}})$ (I)
		$\nu(\text{C-C})$ (I)
		$\nu(\text{C-C}_{\text{Methyl-H}})$ (I)
		$\nu(\text{C-N})$ (I) $\nu(\text{N-C}_{\text{Methyl}})$ (I) $\nu(\text{N-C}_{\text{Methyl-H}})$ $\nu(\text{C}_{\text{Spiro-N}})$
1166	1168	<u>theoretical</u> <sup>[197]</sup> $\nu(\text{N-C}_{\text{Methyl}})$ (I) $\nu(\text{C-C}_{\text{Methyl}})$ (I)

1148	1149 1154	<u>theoretical</u> <sup>[197]</sup> $\nu(\text{C-C-H})$ ( III' ) $\nu(\text{C-C})$ ( III' ) $\nu(\text{C-C-H})$ ( II ) $\nu(\text{C-C})$ ( II )
1115	1119	$\delta(\text{C-H})_{\text{arom.}}$ <sup>[198]</sup>
1091	1083	$\delta(\text{C-H})_{\text{arom.}}$ <sup>[198]</sup>
1047	1039	<u>theoretical</u> <sup>[197]</sup> $\nu(\text{N-C-C})$
1018	1018 1022	<u>theoretical</u> <sup>[197]</sup> $\nu(\text{C-C})$ ( II, III' ) $\nu(\text{C-N})$ ( I )
976	945 988	<u>theoretical</u> <sup>[197]</sup> deviation of H atoms from the plane ( III' ) $\delta(\text{C}_{\text{Methyl}}\text{-H})$ $\nu(\text{C-N})$ ( I )
931	929	<u>theoretical</u> <sup>[197]</sup> $\nu(\text{C-C}_{\text{Methyl}}\text{-H})$
874	865 868	<u>theoretical</u> <sup>[197]</sup> $\nu(\text{C-N})$ ( I ) $\delta(\text{III}')$ out-of-plane vibrations ( III' )
804	794	<u>theoretical</u> <sup>[197]</sup> deviation of H atoms from the plane ( III' ) out-of-plane vibrations ( III' ) $\delta(\text{II})$ $\nu(\text{C-N})$ ( I )
749	760-740	$\gamma(\text{C-H})$ ( II, III' ) <sup>[199]</sup>

IR-spectroscopic measurements have only been done on SP-O@MOF-5 so far. For SP-O embedded in MIL-68(In) and MIL-68(Ga) and for SP-O combined with MIL-53(Al) similar results and effects are expected. Investigations on these systems still have to be done for a full characterization of SP-O embedded in different MOF host materials.

#### 4.5.1.3.2 Influence of the Host Matrices on the Absorption Properties

For SP-Nitro@MOF systems a profound impact of the surrounding host matrix on the electronic structure of the excited dye molecule was found, resulting in red- or blue-shifted absorption maxima. This has been comprehensively elucidated and is referred to as solvatochromism. Thus, similar results are expected for SP-O@MOF hybrid materials. In contrast to SP-Nitro SP-O exhibit positive solvatochromism with increasing solvent polarity. When embedded in the different host matrices MOF-5 and MIL-68(In/Ga) and when combined with MIL-53(Al) the opposite absorption behavior in comparison to compounds **1** to **4** is observed. In table 4.5.5 the absorption maxima of compounds **1** to **4** and **19** to **22** are listed and compared.

**Table 4.5.5** Comparison of the absorption maxima of MC-Nitro@MOF and MC-O@MOF systems. Data were recorded under inert conditions.

host matrix	$\lambda_{\max}$ of MC-Nitro / nm	$\lambda_{\max}$ of MC-O / nm
MOF-5	500	631 (shoulder 580 nm)
MIL-68(In)	578	629 (shoulder 577 nm)
MIL-68(Ga)	582	624 (shoulder 575 nm)
MIL-53(Al)	594	613 (shoulder 566 nm)
	<i>red-shift</i>	<i>blue-shift</i>

While MC-Nitro features red-shifted absorption bands (MOF-5 to MIL-53(Al)), absorption of MC-O is blue-shifted. By taking its property of positive solvatochromism into account, MOF-5 represents the most polar and MIL-53(Al) the least polar host matrix – analogue to the previously described results of SP-Nitro. It has to be stated that SP-O seems to be adsorbed on the surface of MIL-53(Al), which is similar to SP-Nitro.

The successful isomerization of SP-O to MC-O and the influence of the host matrix highly resemble the behavior of spirooxazine when dissolved in solvents of varying polarity. Thus, MOFs can be understood as “solid solvents” not only for spiropyran, but also for the structurally related spirooxazines.

In contrast to MC-Nitro the absorption properties of MC-O all point to the used MOFs being very polar, when only taking the local absorption maximum into account (see table 4.5.6). By

taking a closer look at the absorption spectra in figure 4.5.10 to Figure 4.5.13 a shoulder is found for all compounds **19** to **22**, blue-shifted to the local absorption maximum. If only these values are considered, all used MOFs are rather non-polar in the range of polarity of cyclohexane. For spirooxazines the appearance of asymmetric absorption maxima is known to occur, with a bathochromically or hypsochromically shifted shoulder. Hence, the local absorption maximum on the one and the respective shoulder on the other hand cannot be considered isolated. On that occasion,  $\lambda_{\text{average}}$  was calculated by  $0.5 (\lambda_{\text{max}} + \lambda_{\text{shoulder}})$  and used for the polarity determination. In the following table 4.5.6 these calculated values are listed with the attribution to the respective MOF hybrid material.

**Table 4.5.6** Comparison of  $\lambda_{\text{max}}$  (MC-O) dissolved in solvents of varying polarity with  $\lambda_{\text{max}}$  (MC-O),  $\lambda_{\text{shoulder}}$  (MC-O) and  $\lambda_{\text{average}}$  (MC-O) when combined with different MOF hosts.  $\lambda_{\text{average}}$  was calculated by  $0.5 (\lambda_{\text{max}} + \lambda_{\text{shoulder}})$ .

$\lambda_{\text{max}}$ solvent / nm <sup>[205]</sup>	$\lambda_{\text{max}}$ MOF / nm	$\lambda_{\text{shoulder}}$ MOF / nm	$\lambda_{\text{average}}$ MOF / nm
613 (methanol)	631 ( <b>19</b> )	580 ( <b>19</b> )	605.5 ( <b>19</b> )
610 (ethanol)	629 ( <b>20</b> )	577 ( <b>20</b> )	603.0 ( <b>20</b> )
602 (acetonitrile)	624 ( <b>21</b> )	575 ( <b>21</b> )	599.5 ( <b>21</b> )
596 (toluene)	613 ( <b>22</b> )	566 ( <b>22</b> )	589.5 ( <b>22</b> )
556 (cyclohexane)			

To illustrate the correlation between MOF and solvent, the absorption maxima of MC-O dissolved in different solvents were plotted as a function of the elution power  $\epsilon^0$  of the respective solvent on alumina according to *Snyder*<sup>[193]</sup> (see figure 4.5.18). The values (blue dots) were linearly fitted (blue broken line) and  $\lambda_{\text{average}}$  of **19** to **22** were added (red squares).

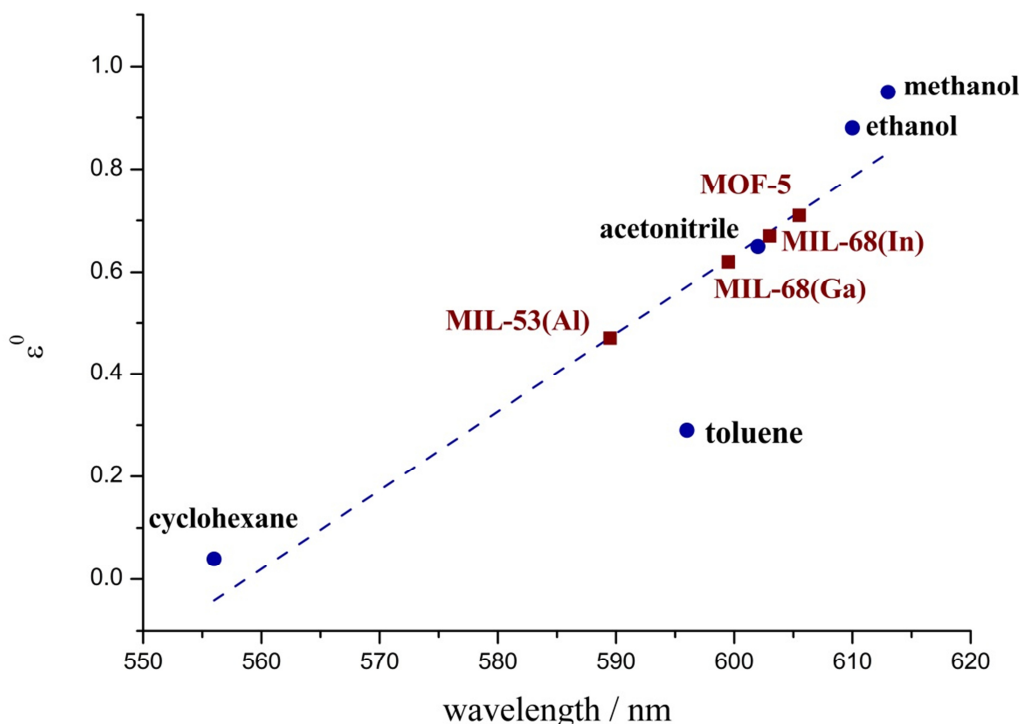


**Figure 4.5.18** Plot of the wavelength of the absorption of MC-O dissolved in different solvents (blue dots) versus the elution power  $\epsilon^0$  on alumina taken from *Snyder*<sup>[193]</sup>, classifying the polarity of the respective MOFs (red squares).

That way, the polarity of the used MOF hosts was estimated, which corresponds to the SP-Nitro@MOF compound findings. The only exception represents MOF-5, which featured an estimated polarity higher than methanol for SP-Nitro, but is less polar than ethanol for SP-O. For MIL-68(In), MIL-68(Ga) and MIL-53(Al) the resulting polarities correspond to the ones found for the SP-Nitro@MOF systems. Hence, the polarity scale MOF-5 > MIL-68(In) > MIL-68(Ga) > MIL-53(Al) is qualitatively, but not quantitatively proven.

In addition to the results of the SP-Nitro@MOF systems, these findings confirm the concept of MOFs being similar to a solvent. However, spirooxazines are structurally related to spiropyrans. Hence, the ability to switch when embedded in these host matrices and being dependent on the environment given by the MOF pore with regard to the absorption properties is not surprising. A completely different photoactive dye molecule will be considered in chapter 4.6.

#### 4.5.1.3.3 Reversibility of Switching and Photostability

Investigations on SP-Nitro as guest molecule showed profound photodegradation upon repetitive and prolonged UV light irradiation for all compounds **1** to **4**. With regard to possible applications, this low fatigue resistance is a major drawback. Spirooxazines are known for being much more resistant against photodegradation.<sup>[205]</sup> In order to determine the reversibility of switching and the photostability of SP-O combined with different MOFs all compounds **19** to **22** were investigated via UV/vis and IR spectroscopy (compound **19**). It has to be stated that all data were recorded under inert conditions and any influence of moisture uptake can be excluded from all further considerations.

In chapter 4.5.1.3.1 IR spectra of SP-O@MOF-5 (**19**) were comprehensively expounded. Upon prolonged UV light irradiation, no intensity loss was observed for previously increasing vibrational frequencies, which already alludes to photostability of the spirooxazine embedded in MOF-5 for a total UV light exposure time of 1020 min. The irradiated species (1020 min with  $\lambda = 365$  nm) was left at room temperature. After 55 min and after 105 min IR spectra were recorded to examine thermal relaxation of MC-O to its closed SP-O form. In figure 4.5.19 the IR spectra of the thermal relaxation at room temperature (RT) are compared with both the irradiated species and the non-irradiated one.

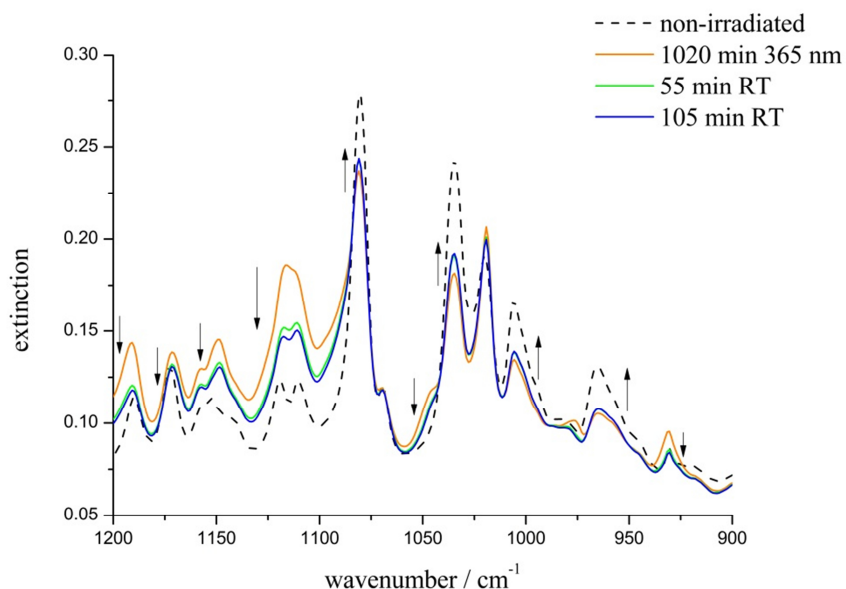


**Figure 4.5.19** IR spectra of the thermal relaxation at room temperature (green and blue solid lines) of SP-O@MOF-5 (**19**) in comparison to the non-irradiated (black broken line) and maximum irradiated species (orange solid line). Loss and gain in intensity is marked with arrows.

In contrast to SP-Nitro@MOF hybrid materials thermal relaxation at room temperature of SP-O@MOF-5 (**19**) is obvious, which can be easily followed by the loss and gain in intensity of the respective vibrational frequencies. However, the non-irradiated state is not reached after 105 min relaxation time at room temperature. From the prolonged IR spectroscopic measurements photodegradation of SP-O inside MOF-5 can be excluded. Therefore, MC-O is stabilized inside the pores of MOF-5, which has already been shown by *Zhu* and co-workers<sup>[171]</sup> for a spiroopyran. This finding presents further evidence for an environment given by MOF-5 being preferred by molecules with a large dipole moment.

Reconversion by thermal treatment for MC-O embedded in MOF-5 was shown to be only possible to a certain extent. Possibly, relaxation of the excited species preferably occurs upon irradiation. On that occasion, maximum irradiated compound **19** was exposed to electromagnetic radiation of different wavelengths (505, 590, 660, 450 and 405 nm) to induce a full reconversion to the closed SP form of the used spirooxazine. The results of this experiment are plotted in figure 4.5.20 following the order of exposure wavelength.

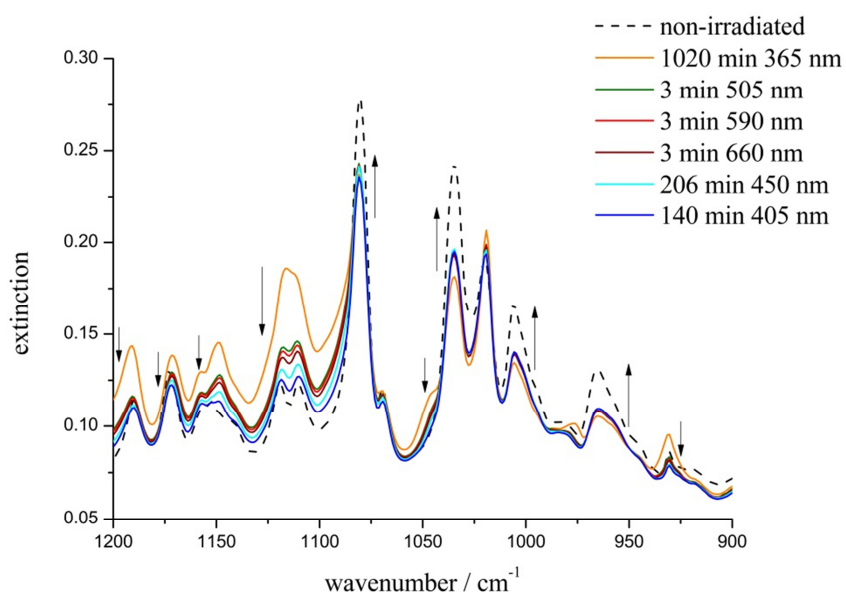


**Figure 4.5.20** IR spectra of the photochemical relaxation upon irradiation with light of different wavelengths of SP-O@MOF-5 (**19**) in comparison to the non-irradiated (black broken line) and maximum irradiated species (orange solid line). Loss and gain in intensity is marked with arrows.

According to the absorption maxima of compound **19**, wavelengths were chosen, which are located in the range of the absorption band (except 405 nm and 450 nm). For all wavelengths changes directing to the non-irradiated state are obvious. Major changes become apparent by irradiation into the left part of the absorption maximum with  $\lambda = 405$  nm. However, for long irradiation times (140 min for 405 nm and 206 min for 450 nm, respectively) thermal relaxation cannot be excluded, hence measurements at low temperatures have to be conducted to suppress thermal relaxation. Nevertheless, the initial state cannot be reached even by photochemical means. Spirooxazine in its open MC-O form is preferably present inside MOF-5.

MOF-5 represents the most polar one among the used host materials. Hence, investigations on the thermal and photochemical relaxation of compounds **20** to **22** are obligatory and have to be done in future experiments. Possibly, reconversion is probable inside those host matrices as their polarity was estimated to be lower than the one given by the chemical environment of MOF-5.

For SP-O@MOF-5 (**19**) reversibility of switching to a certain extent was shown by both thermal and photochemical treatment. The stabilization of MC-O inside MOF-5 is suggested. Furthermore, photodegradation is excluded by the findings of the IR spectroscopic measurements (see chapter 4.5.1.3.1). To fully prove this UV/vis spectroscopy was applied as a second method. Thereupon, all compounds were irradiated with UV light with  $\lambda = 365$  nm with a maximum irradiation time of 30 min. Alterations in the absorption bands were followed in the absorption spectra. For a better visualization of the occurring processes, the absorption of the non-irradiated species was subtracted from the irradiated ones. The resulting differential spectra are discussed in the following, starting with SP-O@MOF-5 (**19**).

The changes in absorption in relation to the irradiation time of compound **19** are shown in figure 4.5.21. Remarkably, the intensity of the absorption band at  $\lambda = 631$  nm increases constantly upon UV light exposure pointing to a high photostability of SP-O inside the MOF-5 matrix, which corresponds to the IR spectroscopic measurements. For compound **19** the assumption of MC-O being stabilized inside the host matrix is further proven by this. Additionally, a shoulder in the range of  $\lambda = 480$  nm appears which has not been attributed so far, but is also observed for compounds **20** and **21** for prolonged irradiation times (figures 4.5.22 and 4.5.23). Possible aggregation processes are assumed, which have to be further proven by additional analytical methods e.g. solid state NMR.

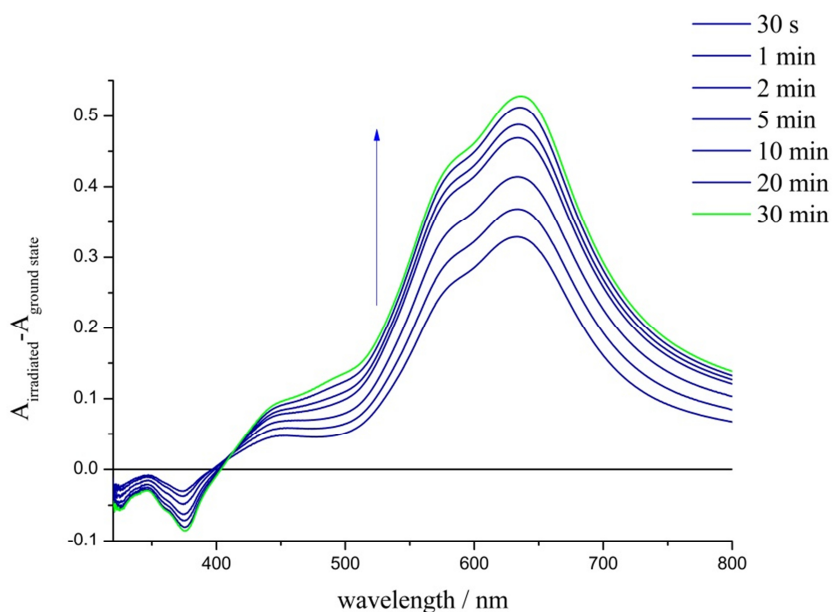


**Figure 4.5.21** Differential UV/vis spectra of SP-O@MOF-5 (**19**) for prolonged UV light irradiation ( $\lambda = 365$  nm).

In contrast to MOF-5 SP-O is less photostable when embedded in the host materials belonging to the MIL-68 family. While SP-O is perfectly stable inside MOF-5, irradiation times  $> 20$  min cause a slight decrease of the absorption band when embedded in MIL-68(In) (see figure 4.5.22).

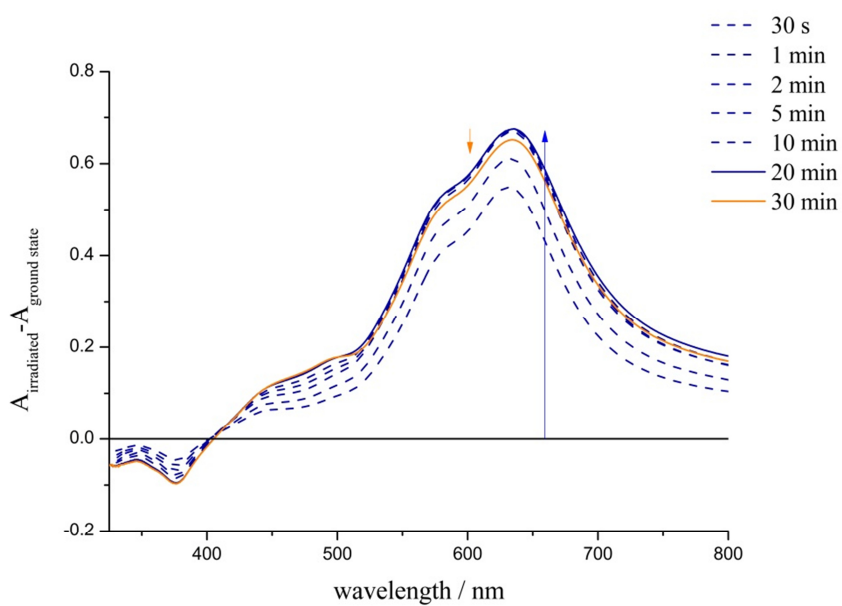


**Figure 4.5.22** Differential UV/vis spectra of SP-O@MIL-68(In) (**20**) for prolonged UV light irradiation ( $\lambda = 365$  nm). Increasing absorption is colored in blue, decreasing absorption is colored in orange.

When embedded in MIL-68(Ga) irradiation times  $> 5$  min already cause decreasing absorption (see figure 4.5.23). Loss in intensity of the absorption band is possibly caused by photodegradation, which has to be further proven by IR spectroscopic measurements.

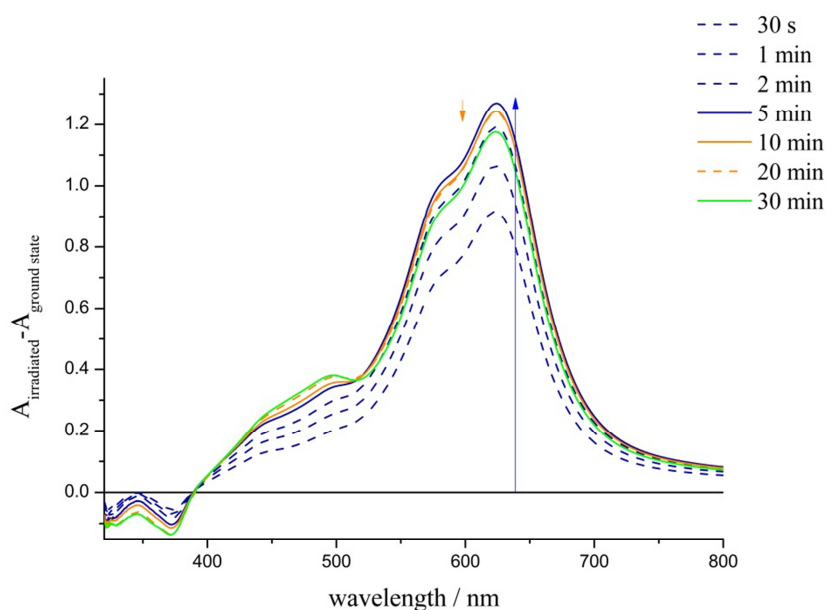


**Figure 4.5.23** Differential UV/vis spectra of SP-O@MIL-68(Ga) (**21**) for prolonged UV light irradiation ( $\lambda = 365$  nm). Increasing absorption is colored in blue, decreasing absorption is colored in orange, irradiation for 30 min is colored in green.

For SP-O@MIL-53(Al) (**22**) alterations upon UV light irradiation were found to be rather small (see figure 4.5.24). When irradiated up to 10 min the absorption band at 524 nm gains in intensity. Exposure times exceeding 20 min cause loss in intensity pointing to photodegradation of SP-O inside MIL-53(Al), which corresponds to the results of the MIL-68 family.

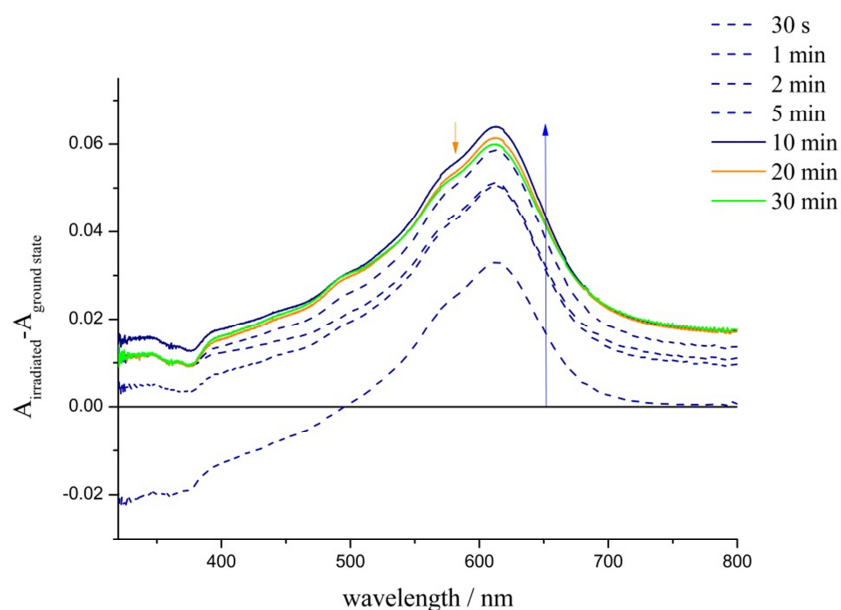


**Figure 4.5.24** Differential UV/vis spectra of SP-O@MIL-53(Al) (**22**) for prolonged UV light irradiation ( $\lambda = 365$  nm). Increasing absorption is colored in blue, decreasing absorption is colored in orange, irradiation for 30 min is colored in green.

Although spirooxazines exhibit a profound photostability, the surrounding host matrix influences the fatigue resistance significantly. Surprisingly, MOF-5 stabilizes the electronic structure in a way that photo-by-products are not produced upon prolonged UV light exposure, whereas the other used host materials do not. In order to understand the reason of this property the knowledge of the exact position of the embedded dye becomes necessary. Thus, solid-state NMR experiments, PDF as well as quantum-chemical calculations have to be conducted in future work.

## 4.5.2 Preliminary Conclusions

In the previous chapter 4.4.1 switching of the photoactive unit in spiroopyran@MOF systems was found to occur upon UV light irradiation. Inside the MOF host or when adsorbed on the MOF surface the light induced SP to MC conversion is enabled for spiroopyrans. Furthermore, the host scaffolds provide varying chemical environments of the pores that caused MOF dependent absorption maxima of the incorporated SP-Nitro, which is referred to as solvatochromism. Nonetheless, spiroopyrans exhibit low fatigue resistance upon repetitive and prolonged excitation. Due to the low photostability, a spirooxazine was now used to avoid the process of photodegradation.

The spirooxazine SP-O was successfully combined with the four different host matrices MOF-5, MIL-68(In), MIL-68(Ga) and MIL-53(Al). That way, the first spirooxazine@MOF systems were synthesized. While SP-O is embedded in MOF-5, MIL-68(In) and MIL-68(Ga), surface adsorption occurs for MIL-53(Al), which has been found for SP-Nitro as well.

All compounds feature positive photochromism and solvatochromism upon UV light irradiation, which is similar to the dissolved state of the dye molecule. The switching processes were followed by means of UV/vis spectroscopy and, additionally, IR spectroscopic measurements for SP-O@MOF-5 (**19**). IR bands of the non-irradiated species were completely assigned to the spirooxazine. Moreover, vibrational frequencies of the excited species were determined and attributed, which has not been done in the literature so far: The first IR spectroscopic data of MC-O were presented here.

According to the results of SP-Nitro embedded in MOF-5, SP-O is stabilized in its open merocyanine form in compound **19** as well. Additionally, photodegradation of the spirooxazine is completely suppressed in MOF-5 even upon prolonged UV light exposure, but was found to occur in MIL-68(In), MIL-68(Ga) and MIL-53(Al). Based on these results, further analytical methods such as solid-state NMR and quantum-chemical calculations have to be applied to fully understand the occurring properties of these host-guest systems from a structural point of view.

Up to now, structurally related dye molecules with a similar behavior upon UV light excitation were used. Firstly, spiroopyrans were examined. Apparently, a low photostability of these photoactive dyes excludes possible applications. Nevertheless, the results, especially concerning the influence of the host matrices on the electronic structure of the embedded dye,

were directing for investigations on spirooxazines. In case of MOF-5, these materials were found to be resistant towards photodegradation. Furthermore, the concept of “MOFs as solid solvents” is expanded from spiropyrans to spirooxazines.

Both spiropyrans and spirooxazines are closely related to each other. Hence, similar behavior when embedded in the MOFs was expectable. For an appropriate understanding of the host matrices' influence on the electronic structure of the guest molecule another photoactive dye molecule was applied: a polarity sensitive phthalimide, which exhibits shifted emission bands upon varying polarity of the surrounding medium. This molecule and its combination with different MOFs and porous materials will be part of the following and last chapter.

## 4.6 Phthalimide@Porous-Material composites

For the investigations on MOFs as “solid solvents for photoactive dye molecules”, another compound, which completely differs in its structure, was used to strengthen this concept. On that occasion, a photoactive phthalimide was chosen that exhibits different emission maxima in relation to the polarity of the surrounding medium. Thereupon, solvent dependence of fluorescence will be described from a theoretical point of view first, before the used phthalimide is introduced.

### 4.6.1 Solvent-Dependence of Fluorescence

For some dye molecules, the absorption properties are dependent on the polarity of the surrounding media. This has been comprehensively described in chapter 2.2. These molecules show solvatochromic behavior, which also accounts for fluorescent dyes. This is sometimes referred to as fluorosolvatochromism<sup>[208]</sup> or solvatofluorochromism<sup>[209]</sup>. In contrast to a varying shape, intensity and position of the absorption spectra by polarity alteration of the solvent, a change in shape and position of the emission spectra is supplemented by a varying life-time of the excited species.<sup>[87]</sup>

Emission of a photon occurs by relaxation of the  $S_1$  to the  $S_0$  electronic state. Usually, the  $0 \rightarrow 0$  transition is equal for both absorption and fluorescence. Due to the loss of energy (because of vibrational relaxation), the fluorescence maximum is always positioned red-shifted in comparison to the absorption maximum, which is referred to as *Stokes* rule (see Figure 4.6.1). The gap between those two maxima is called the *Stokes* shift, which provides valuable information on the excited state of the fluorophore. The *Stokes* shift is usually expressed in wavenumbers with  $\Delta\tilde{\nu} = \tilde{\nu}_A - \tilde{\nu}_F$ . If the dipole moment of a fluorescent dye is larger in the excited state than in the ground state with  $\mu_e > \mu_g$ , an increase in polarity of the solvent results in an increase of the *Stokes* shift.<sup>[210–216]</sup> This can be easily explained: the solvent molecules orient in a specific solvation shell around the fluorescent dye according to its dipole moment. If the dipole moment changes due to excitation, the solvent molecules have to rearrange around the excited fluorophore. When focusing on the solvent dependence of the position of the emission band, the finite relaxation time  $\tau_R$  for the re-orientation of the solvent molecules around the *Franck-Condon* excited state as well as the finite lifetime  $\tau_e$  of the fluorophore in the excited state have to be considered. Taking those values into account,

two scenarios occur: If  $\tau_R > \tau_e$ , emission will occur before rearrangement of the solvent molecules. Hence, the starting point of the emission process is the *Franck-Condon* excited state  $S_1'$  with the equilibrium ground state as the final state. In that case, emission and absorption wavenumbers are equal. When  $\tau_R < \tau_e$ , reorientation of the solvent molecules around the *Franck-Condon* excited state occurs before emission. A relaxed excited state  $S_1$  is obtained, which is now the initial state of the emission process. After the emission process a *Franck-Condon* ground state  $S_0'$  is achieved before the solvent molecules reorientate to the equilibrium arrangement of the ground state  $S_0$ .<sup>[87]</sup> This process is illustrated in figure 4.6.1.

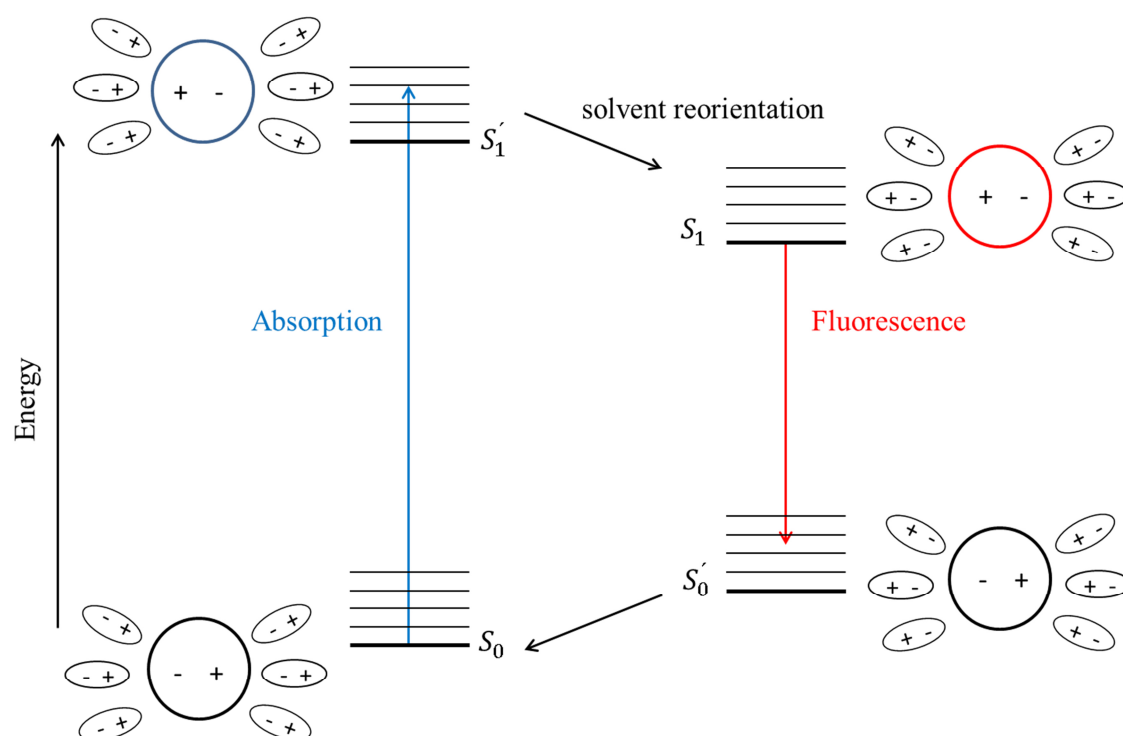


**Figure 4.6.1** Influence of the solvent reorientation on the excited state on the emission band of a dipolar molecule with a dipole flip upon excitation.  $S_1'$  and  $S_0'$  are the *Franck-Condon* excited and ground state, respectively,  $S_1$  and  $S_0$  the corresponding equilibrium states,  $\tau_R < \tau_e$ . The illustration was adapted from Reichardt.<sup>[87]</sup>

Generally, solvent effects on the emission spectra are a result of the differential solvation of the ground and excited state of the fluorophore, which is influenced by different solute-solvent interactions.<sup>[211,212,217-219]</sup> Most fluorophores exhibit an intramolecular charge transfer upon excitation that gives rise to a change in dipole moment with  $\mu_e > \mu_g$ . The relaxed *Franck-Condon* excited state  $S_1$  will be energetically more stabilized than the ground state  $S_0$ , which causes a profound red-shift in the emission band. The stronger the solute-solvent interactions, the lower the energy of the *Franck-Condon* excited state  $S_1$ . Hence, an increase

in polarity of the solvent for fluorophores with a change in dipole moment with  $\mu_e > \mu_g$  results in increasingly red-shifted fluorescence bands and corresponding *Stokes* shifts.

A very well studied example of such a strong solvatochromic fluorophore with a change in dipole moment with  $\mu_e > \mu_g$  upon excitation is 4-aminophthalimide with a *Stokes* shift of  $\Delta\tilde{\nu} = 5010 \text{ cm}^{-1}$  for diethyl ether  $\rightarrow$  water.<sup>[220–223]</sup> The structure is shown in figure 4.6.2.

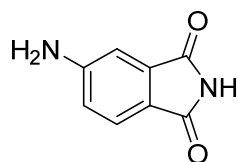


**Figure 4.6.2** Structure of 4-aminophthalimide.

In the present work, another phthalimide was used for the polarity probing of different porous host materials, which will be introduced in the following chapter 3.6.2.

#### 4.6.2 4,5-Dimethoxy-*N*-butylphthalimide

In the present work, 4,5-dimethoxy-*N*-butylphthalimide (abbreviated with Phth in the following) was used as guest molecule to confirm the concept of MOFs as “solid solvents” for dye molecules. The structure of Phth is shown in figure 4.6.3.

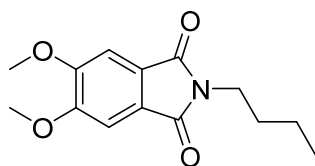


**Figure 4.6.3** Structure of 4,5-dimethoxy-*N*-butylphthalimide (Phth).

When dissolved in solvents of varying polarity, the emission maximum is increasingly red-shifted corresponding to the increasing solvent polarity. When looking at Figure 4.6.4 an emission maximum of  $\lambda_{em} = 432 \text{ nm}$  is found for toluene,  $\lambda_{em} = 439.5 \text{ nm}$  for acetone,

$\lambda_{em} = 443$  nm for DMF,  $\lambda_{em} = 444$  nm for chloroform,  $\lambda_{em} = 481$  nm for ethanol and  $\lambda_{em} = 490.5$  nm for methanol.

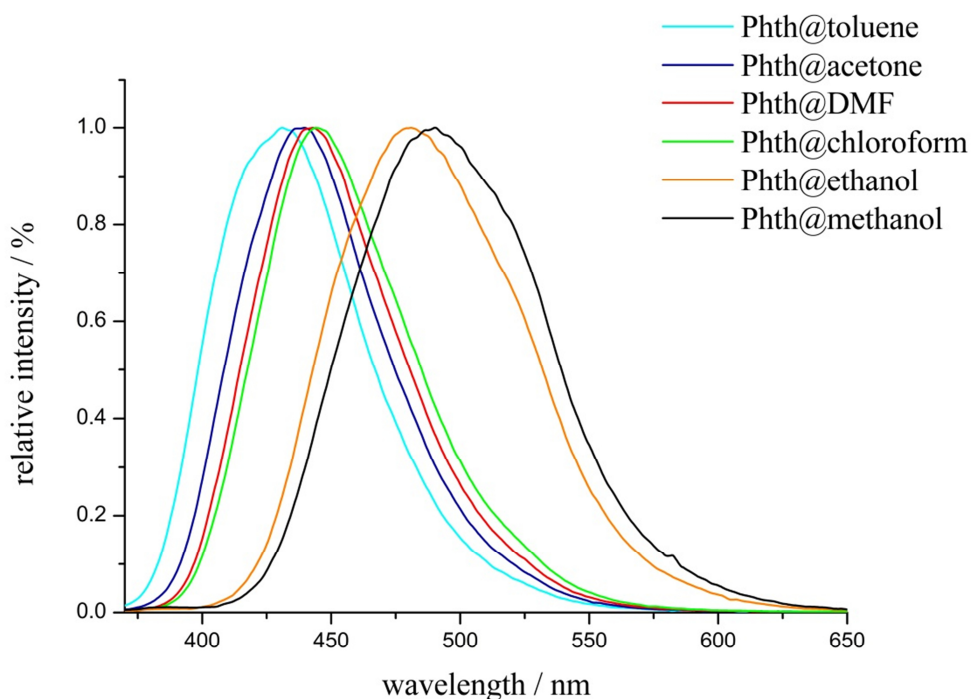


**Figure 4.6.4** Emission spectra of 4,5-dimethoxy-*N*-butylphthalimide (Phth) dissolved in solvents of varying polarity with  $\lambda_{ex} = 347$  nm.

According to the elutrope series of *Snyder*<sup>[193]</sup>, methanol is the most polar solvent, followed by ethanol, acetonitrile, acetone and finally toluene. For a better overview, the solvents with their respective elution power  $\epsilon^0$  and the emission maximum of Phth are listed in table 4.6.1. When compared to the less polar solvents, the emission maximum of Phth dissolved in methanol is significantly red-shifted.

Apparently, the emission maximum  $\lambda_{em}$  of Phth bathochromically shifts with increasing solvent polarity. This knowledge is essential for further understanding and characterizing Phth@PM systems, which are presented in the following.

**Table 4.6.1** List of the used solvents with their elution power and  $\lambda_{\max}$  of 4,5-dimethoxy-*N*-butylphthalimide (Phth).

solvent	$\lambda_{\max}$ of Phth / nm	elution power $\epsilon^{0[193]}$
methanol	490.5	0.95
ethanol	481	0.88
chloroform	444	0.44
acetone	439.5	0.56
toluene	431	0.29

### 4.6.3 Phth@Porous-Material composites

Phth was embedded into ten different porous materials (PMs), namely MOF-5, MIL-68(In), MIL-68(Ga), MIL-53(Al), HKUST-1, MIL-101(Cr), Zeolite Y, MFM-300(Ga<sub>2</sub>), F-MFM-300(Ga<sub>2</sub>) and F<sub>2</sub>-MFM-300(Ga<sub>2</sub>) via a gas phase loading process. Ten Phth@PM composite materials were obtained:

- (23) Phth@MOF-5
- (24) Phth@MIL-68(In)
- (25) Phth@MIL-68(Ga)
- (26) Phth@MIL-53(Al)
- (27) Phth@Zeolite Y
- (28) Phth@MFM-300(Ga<sub>2</sub>)
- (29) Phth@F-MFM-300(Ga<sub>2</sub>)
- (30) Phth@F<sub>2</sub>-MFM-300(Ga<sub>2</sub>)
- (31) Phth@HKUST-1
- (32) Phth@MIL-101(Cr)

These composite materials were investigated by means of the ICE-principle. The results are presented in the following. In contrast to the previously used spiropyran and spirooxazines, MOF host materials were extended with one zeolite material, which is known to be very polar due to its structure. That way an accurate und precise polarity attribution of the MOF materials is expected.

#### 4.6.3.1 Incorporation

Analogue to the previously described spiropyran/spirooxazine@MOF systems the incorporation of the phthalimide was tracked via XRPD measurements. The diffraction pattern for Phth@MOF-5 (**23**) is exemplarily shown in figure 4.6.5 and compared to the pattern calculated from the literature known crystal structure of MOF-5<sup>[116]</sup>. Apparently, alterations in the peak intensities especially in the low angle region occur upon loading with the phthalimide, which validates the successful incorporation of the dye molecule. Diffraction patterns of compounds **25** and **27** to **32** are shown in figures 8.5.1 to 8.5.7 in the supplement. Notably, a shoulder at  $1/d \sim 0.07$  is present and broad peaks at  $1/d \sim 0.23$  to  $0.25$  occur for all compounds, which might be a result of phthalimide decomposition.

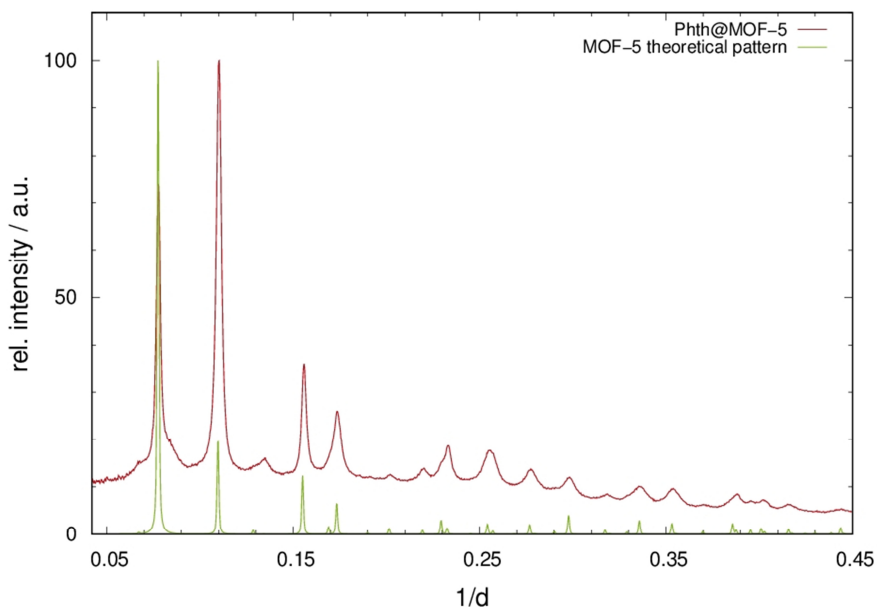


**Figure 4.6.5** XRPD pattern of Phth@MOF-5 (**23**) (red), measured at 298 K (BL9/DELTA:  $\lambda = 0.49594 \text{ \AA}$ ) in comparison to theoretical data of MOF-5 (green).

However, for MIL-68(In) as host material, no complete incorporation was found, even after extended heating times. As shown in figure 4.6.6 several additional peaks are present, which are attributed to free phthalimide after the synthesis, probably being mainly adsorbed on the surface of the MOF.

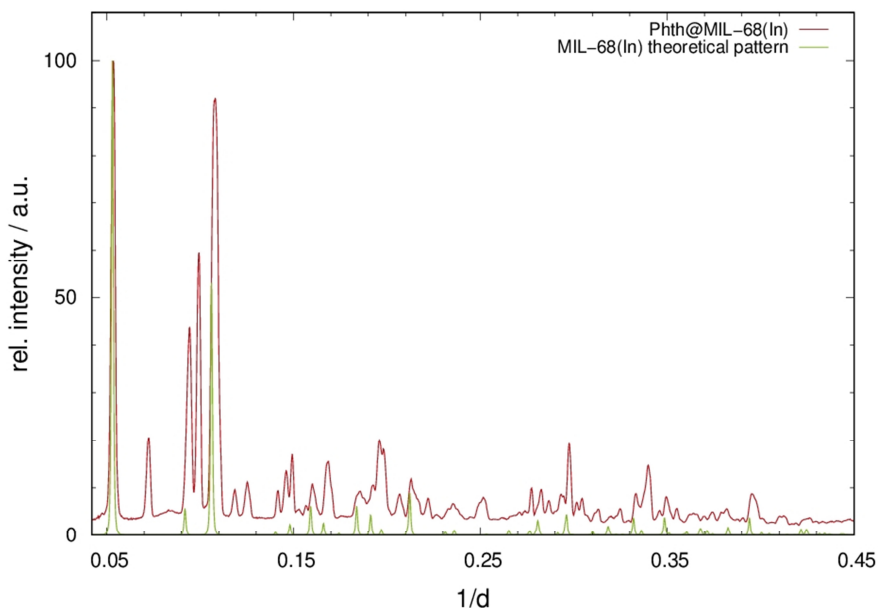


**Figure 4.6.6** XRPD pattern of Phth@MIL-68(In) (**24**) (red), measured at 298 K (BL9/DELTA:  $\lambda = 0.49594 \text{ \AA}$ ) in comparison to theoretical data of MIL-68(In) (green).

Nevertheless, further investigations on this system were carried out, mainly focusing on the influence of the MOF surface combined with the chemical environment given by the MOF pore. *Le Bail* fits of all compounds were performed with *JANA2006*<sup>[194]</sup> to determine the changed cell volumes. The results are listed in tables 4.6.2 and 4.6.3 and compared to the respective unloaded host material. For unloaded MOF-5, MIL-68(In) and MIL-68(Ga) high resolution synchrotron powder diffraction data were collected at the ESRF/Grenoble (FRA). This has to be taken into account, when comparing changes in cell volumes. The *Le Bail* fits of compounds **23** and **25** to **31** and the unloaded host materials are given in figures 8.2.2 to 8.2.4, table 8.2.1, figure 8.3.22 and table 8.3.2 and figures 8.5.8 to 8.5.17 and table 8.5.1 in the supplement.

**Table 4.6.2** Results of *Le Bail* fits of powder diffraction data of compounds **23** to **25** and **27** compared with the unit cell volumes of the respective unloaded MOF.

	(23)	(25)	(27)
T/K	298	298	298
Space Group / No.	$Fm\bar{3}m$ / 225	$Cmcm$ / 63	$Fd\bar{3}m$ / 227
GOF	1.54	1.07	3.93
R <sub>p</sub>	0.0397	0.0335	0.0527
wR <sub>p</sub>	0.0531	0.0503	0.0967
V/Å <sup>3</sup>	16945(2)	5175.0(7)	14852.8(5)
a	25.685(4)	20.999(2)	24.5812(8)
b	-	36.629(3)	-
c	-	6.7278(3)	-
V/Å <sup>3</sup> (unloaded MOF/PM)	17156.0(4)	5197.0(7)	14796(1)

**Table 4.6.3** Results of *Le Bail* fits of powder diffraction data of compounds **28** to **31** compared with the unit cell volumes of the respective unloaded MOF.

	(28)	(29)	(30)	(31)
T/K	298	298	298	298
Space Group / No.	$I4_122$ / 98	$I4_122$ / 98	$I4_122$ / 98	$Fm\bar{3}m$ / 225
GOF	3.01	3.03	4.48	1.46
R <sub>p</sub>	0.0469	0.0485	0.0692	0.098
wR <sub>p</sub>	0.0891	0.0853	0.109	0.1301
V/Å <sup>3</sup>	2647.2(3)	2650.1(4)	2665.6(8)	18528(1)
a	14.949(1)	14.961(1)	14.973(2)	26.461(2) -
b	14.949(1)	14.961(1)	14.973(2)	-
c	11.846(1)	11.839(2)	11.846(3)	-
V/Å <sup>3</sup> (unloaded MOF/PM)	2636.2(6)	2632(1)	2658(1)	18161(2)

Due to the low quality of the diffraction pattern of compound **32**, no *Le Bail* fits were performed (see figure 8.5.7 in the supplement). Nonetheless, Phth@MIL-101(Cr) was further investigated to determine occurring effects. It has to be stated that the quality of the

diffraction patterns of compounds **27** to **31** is comparably low due to the measurement conditions of the *Huber G670* diffractometer. Especially in the low-angle region peaks are asymmetric leading to relatively poor quality values for the *Le Bail* fits. Therefore, values of the fit are preliminary but not conclusive.

For MIL-53(Al) a change in the diffraction pattern was expected upon guest loading due to the “breathing effect” of the host material. When taking spiropyrans or spirooxazines as guest molecules, no additional peaks or changes in the diffraction pattern were found to occur. Since photochromic behavior of the respective dye was observed, surface adsorption of the photoswitchable molecule as an amorphous film was suggested and confirmed by means of XPS measurements. For Phth@MIL-53(Al) (**26**) a different diffraction pattern is found in comparison to the unloaded MIL-53(Al) *ht*, but with partly present free dye molecules (figure 4.6.7). By excluding these peaks, the changed space group was determined with the program package *Topas*<sup>[224]</sup> and fitted with *JANA2006*<sup>[194]</sup>. The results are listed in table 4.6.4 and the *Le Bail* fit is shown in figure 4.6.8.

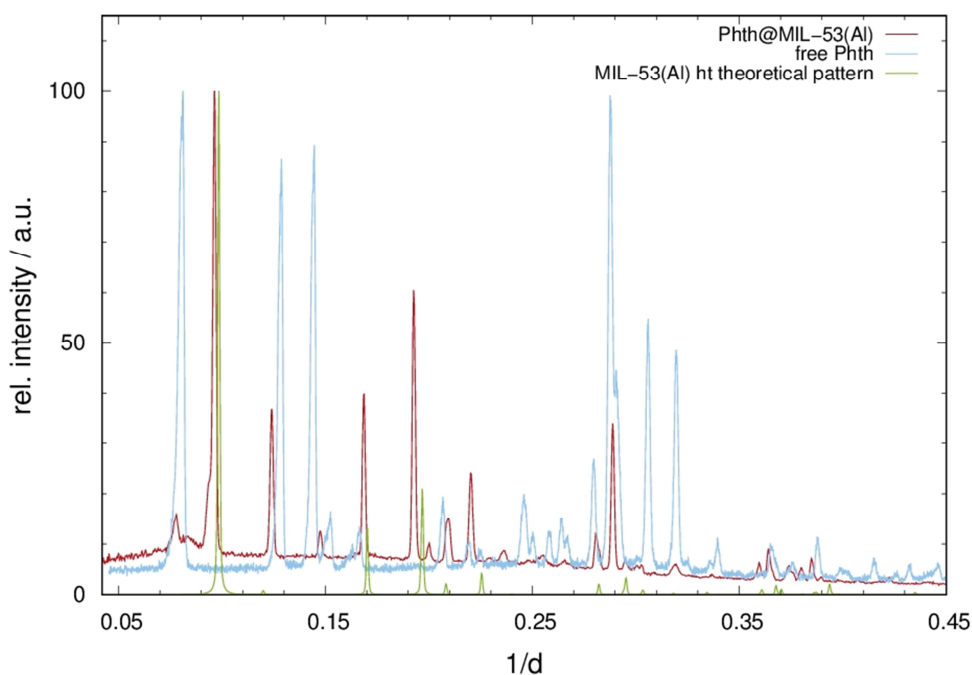


**Figure 4.6.7** XRPD pattern of Phth@MIL-53(Al) (**26**) (red), measured at 298 K (BL9/DELTA:  $\lambda = 0.49594 \text{ \AA}$ ) in comparison to free Phth (blue), measured at 298 K (*Stoe StadiP*,  $\lambda = 1.54 \text{ \AA}$ ) and theoretical data of MIL-53(Al) *ht* (green).

**Table 4.6.4** Results of the *Le Bail* fit of high resolution synchrotron powder diffraction data of Phth@MIL-53(Al) (**26**).

	( <b>26</b> )
T/K	298
Space Group / No.	<i>Imma</i> / 74
GOF	3.67
R <sub>p</sub>	0.087
wR <sub>p</sub>	0.1236
background function	Chebyshev
GW	4.07(8)
LY	19(1)
zero shift	-0.23(3)
number of data points	5228
V/Å <sup>3</sup>	1445.5(2)
a	6.6008(5)
b	16.137(1)
c	13.571(1)

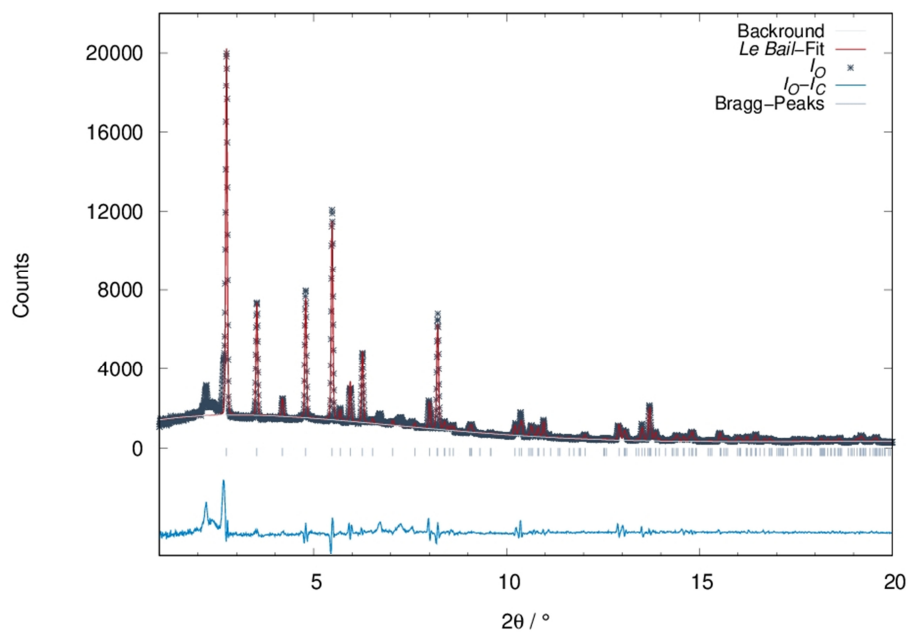


**Figure 4.6.8** *Le Bail* fit of Phth@MIL-53(Al) (**26**) (298 K, BL9/DELTA:  $\lambda = 0.49594$  Å) with measured intensities (grey, crosses), calculated intensities (red), differential curve (turquoise), *Bragg* peaks (light blue, ticks) and background of refinement (white).

When guest-free, MIL-53(Al) *ht* crystallizes in the space group *Imma* (No. 74) with a cell volume of 1411.951 Å<sup>3</sup>.<sup>[166]</sup> Upon loading with the phthalimide host-guest interaction occurs in a way that the MOF changes in its structure: Phth@MIL-53(Al) (**26**) crystallizes in the same space group *Imma* (No. 74) with a cell volume of 1445.3 Å<sup>3</sup>.

#### 4.6.3.2 Composition

For compounds **23** to **30** XPS measurements were applied to determine the composition of the Phth@PM hybrid systems. The results of the calculations are listed in table 4.6.5. The fits as well as the calculations for the XPS measurements of all compounds are found in figures 8.5.18 to 8.5.25 and tables 8.5.2 and 8.5.3 in the supplement. All  $n_{\text{PM}}:n_{\text{phthalimide}}$  ratios are reasonable, except the ones for compounds **28** to **30**. Here, a comparably high amount of phthalimide is found for the small pores of these host materials. This might be the result of DMF inside the pores, which was not fully removed during the activation of the host materials.

For compound **24** a higher amount of phthalimide is found being present in comparison to compound **25**. As known from previous XRPD measurements, free dye molecules on the surface of MIL-68(In) remained even for extended heating times. Hence, the higher  $n_{\text{PM}}:n_{\text{phthalimide}}$  ratio is plausible.

**Table 4.6.5** Ratio of Phth per formula unit of compounds **9** to **16** calculated from XPS measurements.

		Phth : MOF ratio
Phth <sub>x</sub> @MOF-5 ( <b>23</b> )	Phth : (Zn <sub>4</sub> O(bdc) <sub>3</sub> )	2.35 : 1
Phth <sub>x</sub> @MIL-68(In) ( <b>24</b> )	Phth : In(OH)(bdc)	0.48 : 1
Phth <sub>x</sub> @MIL-68(Ga) ( <b>25</b> )	Phth : Ga(OH)(bdc)	0.37 : 1
Phth <sub>x</sub> @MIL-53(Al) ( <b>26</b> )	Phth : Al(OH)(bdc)	0.40 : 1
Phth <sub>x</sub> @Zeolite Y ( <b>27</b> )	Phth : (SiO <sub>2</sub> ) <sub>5.1</sub> :Al <sub>2</sub> O <sub>3</sub>	0.74 : 1
Phth@MFM-300(Ga <sub>2</sub> ) ( <b>28</b> )	Phth : Ga <sub>2</sub> (OH) <sub>2</sub> (bptc)	0.86 : 1
Phth@F-MFM-300(Ga <sub>2</sub> ) ( <b>29</b> )	Phth : Ga <sub>2</sub> (OH) <sub>2</sub> (F-bptc)	0.95 : 1
Phth@F <sub>2</sub> -MFM-300(Ga <sub>2</sub> ) ( <b>30</b> )	Phth : Ga <sub>2</sub> (OH) <sub>2</sub> (F <sub>2</sub> -bptc)	1.10 : 1

#### 4.6.3.3 Effects

For spiropyran/spirooxazine@MOF systems a profound impact of the surrounding host matrix on the electronic structure of the excited dye molecule was found, resulting in red- or blue-shifted absorption maxima. This has been comprehensively elucidated and is referred to as solvatochromism. Phthalimides feature a high sensitivity of their emission bands on the polarity of the solvent. This fluorosolvatochromism has been described in chapter 4.6.1. A profound red-shift of the emission bands with increasing polarity of the solvent is observed. When embedded in porous materials, alterations in the fluorescence bands are found. The emission spectra of all compounds **23** to **32** are compared in figure 4.6.9.

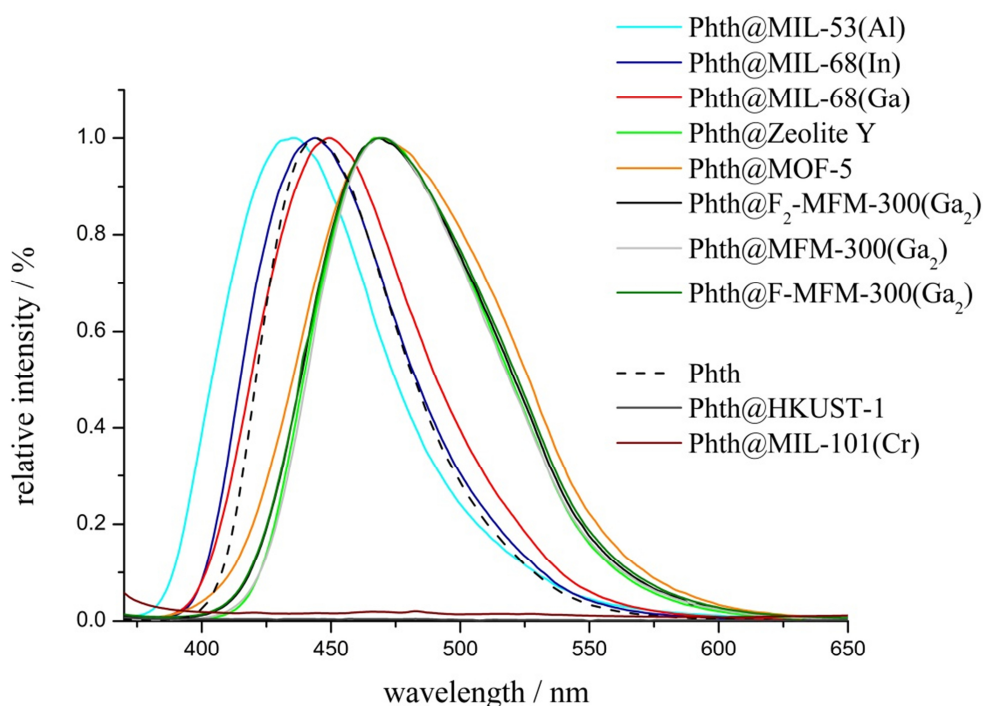


**Figure 4.6.9** Emission bands of Phth embedded in different porous host matrices with  $\lambda_{\text{ex}} = 347$  nm.

Additionally, the emission spectrum of pure phthalimide was recorded (black broken line). Emission bands of embedded Phth are presented in colored solid lines and will be discussed in the following going from low to high wavelength emission.

For Phth@MIL-53(Al) (**26**) an emission maximum of  $\lambda_{\text{em}} = 435.5$  nm is found, which is markedly blue-shifted in comparison to the other host materials and to pure phthalimide. When embedded in MIL-68(In) and MIL-68(Ga) Phth exhibits an emission maximum at  $\lambda_{\text{em}} = 444$  nm and  $\lambda_{\text{em}} = 449.5$  nm, respectively. Compounds **23** and **27** to **30** feature emission

maxima in the range of  $\lambda_{em} = 469$  nm being significantly red-shifted when compared to the emission band of pure phthalimide. As previously described, increasing polarity of the surrounding medium is accompanied by red-shifted emission bands. Consequently, MOF-5 as well as MFM-300(Ga<sub>2</sub>) and its fluorinated derivatives and zeolite Y represent the most polar host materials in this study, followed by the MIL-68 family and finally MIL-53(Al), which is again the least polar porous material. In contrast to the spiropyran/spirooxazine@MOF systems, MIL-68(In) is less polar than MIL-68(Ga) when phthalimide is embedded inside its pores. However, incorporation has not been completely successful, as previously described in chapter 4.6.3.1, which is assumed to be the reason for this difference. In table 4.6.6 the exact values of the emission maxima  $\lambda_{em}$  of **23** to **30** are listed.

**Table 4.6.6** Emission maxima of Phth embedded in different porous host materials.

host matrix	$\lambda_{em}$ of Phth@PM / nm
MIL-53(Al)	435.5
MIL-68(In)	444
MIL-68(Ga)	449.5
Zeolite Y	467.5
MOF-5	468.5
F <sub>2</sub> -MFM-300(Ga <sub>2</sub> )	468.5
MFM-300(Ga <sub>2</sub> )	469.5
F-MFM-300(Ga <sub>2</sub> )	469.5

Notably, the values for MFM-300(Ga<sub>2</sub>) and its fluorinated derivatives do not differ markedly. This is somewhat surprising, since a higher degree of fluorination is considered to lead to a more hydrophobic inner surface of the MOF pore, which has been firstly emphasized by *Omary* and co-workers in 2011.<sup>[225]</sup> Therefore, an increase in fluorination of MFM-300(Ga<sub>2</sub>) was expected to result in blue-shifted emission bands. However, alterations in the emission bands were not observed, which is probably due to the position of the fluorine anion (which does not stick into the pores) and additionally due to the relatively moderate degree of fluorination. Nevertheless, phthalimides offer the possibility to determine the polarity of the MOFs inner surface and, therefore, are suitable candidates to experimentally prove the change in hydrophobicity in relation to the degree of fluorination.

Notably, no emission was detected for compounds **31** and **32**. Fluorescence quenching is known to occur in presence of copper(II) cations, which has been examined e.g. by *Krämer*<sup>[226]</sup>. Hence, a coordination of Phth to the unsaturated coordination side on the paddle-wheel of HKUST-1 is expected, which explains the absence of fluorescence even though the dye molecule was successfully incorporated. For Phth@MIL-101(Cr) (**32**) absence of the characteristic emission band is plausible as a result of present chromium(III) cations in the MOF structure. Analogue to copper(II) cations, the presence of chromium(III) cations causes fluorescence quenching.<sup>[227]</sup> Unfortunately, the polarity of the inner surface of HKUST-1 in comparison to its fluorinated derivatives UHM-31<sup>[228]</sup> and higher fluorinated representatives<sup>[229]</sup> cannot be investigated by the incorporation of fluorescent dyes because of the quenching effects of copper(II) cations.

To illustrate the correlation between porous hosts and solvent, the emission maxima of Phth dissolved in different solvents were plotted as a function of the elution power  $\epsilon^0$  of the respective solvent on alumina according to *Snyder*<sup>[193]</sup> (see figure 4.6.10). The values of Phth dissolved in different solvents (blue dots) were linearly fitted (blue broken line) and  $\lambda_{em}$  of **23** to **30** were added (red squares).

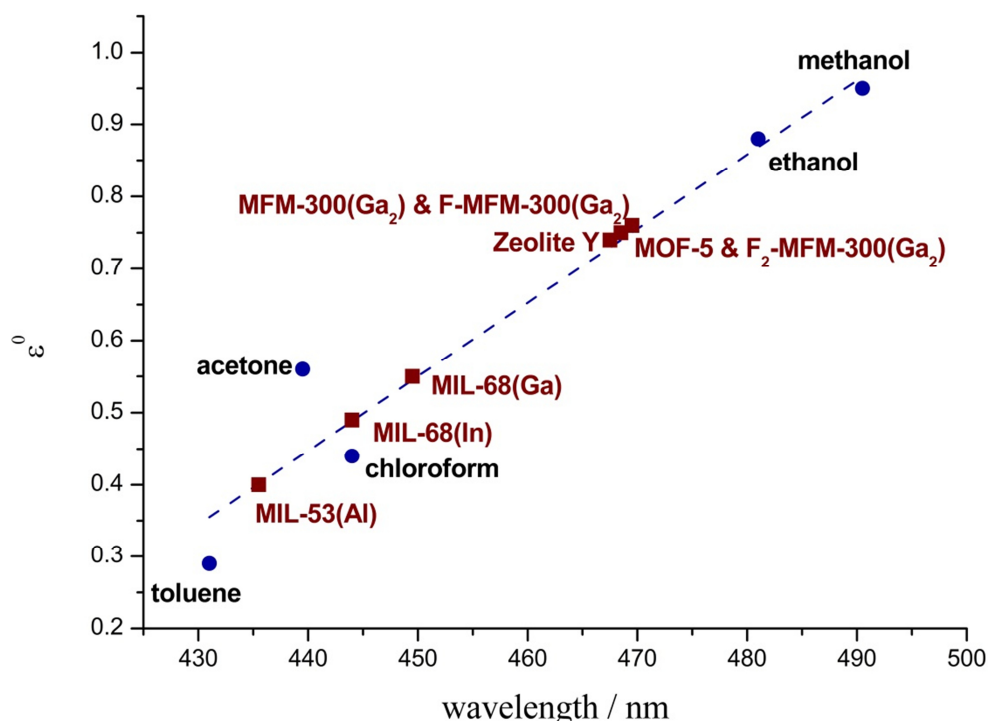


**Figure 4.6.10** Plot of the emission maxima of Phth dissolved in different solvents (blue dots) versus the elution power  $\epsilon^0$  on alumina taken from *Snyder*<sup>[193]</sup>, classifying the polarity of the respective MOFs and porous materials (red squares).

According to the results of the previously described spiropyran/spirooxazine@MOF hybrid systems, MOF-5 represents the most polar and MIL-53(Al) the least polar host material. Nevertheless, the polarity values differ from a quantitative but not qualitative point of view. In order to fully determine the electric fields of the porous materials, UV/vis spectroscopic measurements under inert conditions have to be carried out to elucidate the *Stokes* shifts of the phthalimide when embedded in different porous host materials. That way, a quantitative statement regarding polarity can be drawn.

#### 4.6.4 Dilution of Phth in MOF-5 and MIL-68(Ga)

Only host-guest interactions were considered up to now. Possible guest-guest interactions and the influence on the absorption (for spiropyrans and spirooxazines) and on the emission properties (phthalimides) have not been elucidated so far. For this reason, two host materials, one with a high symmetry (MOF-5) and one with a lower symmetry (MIL-68(Ga)), were chosen for a dilution with Phth. Three dilutions were applied with a  $n_{\text{MOF}}:n_{\text{phthalimide}}$  ratio of a) 1:0.1, b) 1:0.25 and c) 1:0.5, respectively. The results of this dilution will be discussed in the following, mainly focusing on the occurring effects.

##### 4.6.4.1 Incorporation

The incorporation of Phth in different ratios was successfully confirmed by means of XRPD measurements. Since the electron-density rises with increasing the amount of phthalimide, alterations in the peak intensities should be obvious following the embedded guest ratio. In figure 4.6.11 the diffraction patterns for the serial dilution of Phth in MOF-5 are presented, showing the successful incorporation of the photoactive dye molecule. Furthermore, no additional peaks are present pointing to the absence of free phthalimide.

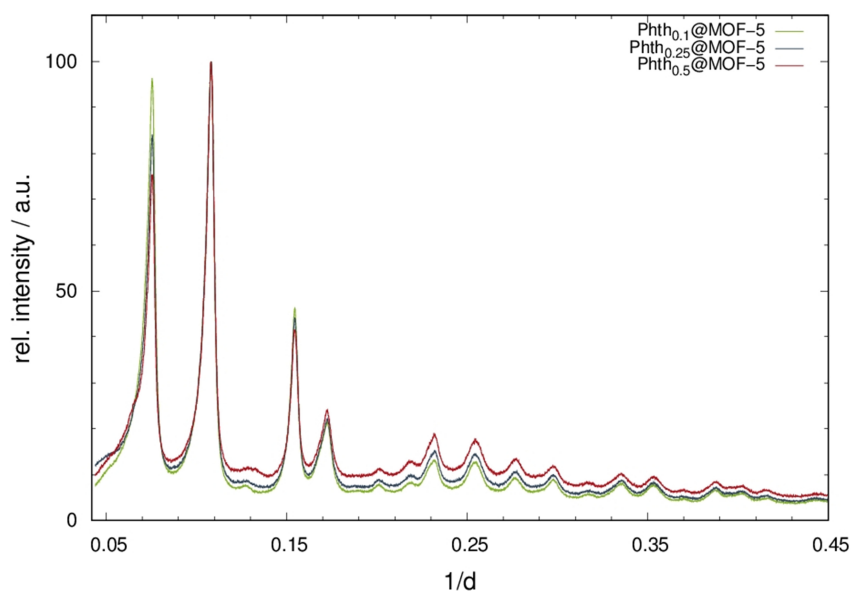


**Figure 4.6.11** XRPD patterns of the serial dilution of Phth in MOF-5, measured at 298 K (*Huber G670*:  $\lambda = 1.54 \text{ \AA}$ ).

Focusing on the low angle area (figure 4.6.12) the constant decrease of the first peak with increasing amount of incorporated guest is observed.

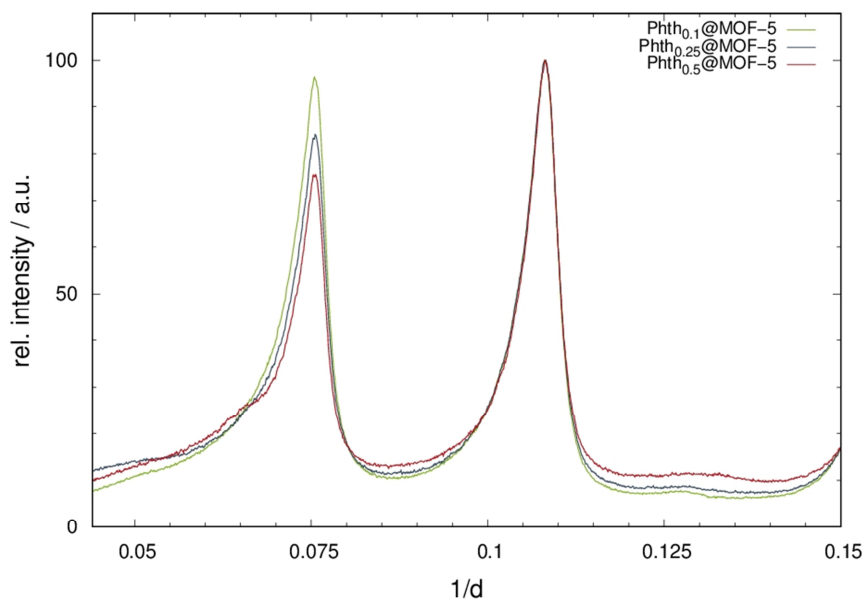


**Figure 4.6.12** Detailed view on the low angle region of the XRPD patterns of the serial dilution of Phth in MOF-5, measured at 298 K (*Huber G670*:  $\lambda = 1.54 \text{ \AA}$ ).

In order to determine the changing volumes in relation to the amount of embedded guest molecules, *Le Bail* fits in *JANA2006*<sup>[194]</sup> were performed. The results are listed in table 4.6.7 and in figures 8.5.26 to 8.5.28 in the supplement. Notably, no significant changes in the cell volumes are observed for different degrees of loading.

Notably, the quality of the diffraction patterns of the serial dilution of MOF-5 is comparably low due to the measurement conditions of the *Huber G670* diffractometer. Especially in the low-angle region peaks are asymmetric resulting in relatively poor quality values for the *Le Bail* fits. Hence, values of the fits are preliminary but not conclusive.

**Table 4.6.7** Results of *Le Bail* fits of powder diffraction data of the serial dilution of Phth in MOF-5.

	<b>0.1</b>	<b>0.25</b>	<b>0.5</b>
T/K	298	298	298
Space Group / No.	<i>Fm</i> $\bar{3}$ <i>m</i> / 225	<i>Fm</i> $\bar{3}$ <i>m</i> / 225	<i>Fm</i> $\bar{3}$ <i>m</i> / 225
GOF	6.01	5.24	4.42
R <sub>p</sub>	0.0785	0.0677	0.0617
wR <sub>p</sub>	0.1159	0.1017	0.0924
V/Å <sup>3</sup>	16176 (3)	16226(3)	16174(3)
a	25.290(4)	25.317(4)	25.289(4)

Corresponding to the results of the Phth@MOF-5 serial dilution, different loading degrees result in peak intensity alterations for MIL-68(Ga) as host material as well. Furthermore, no additional peaks are found, pointing to the absence of free dye molecules. An overview of the different XRPD patterns is given in figure 4.6.13.

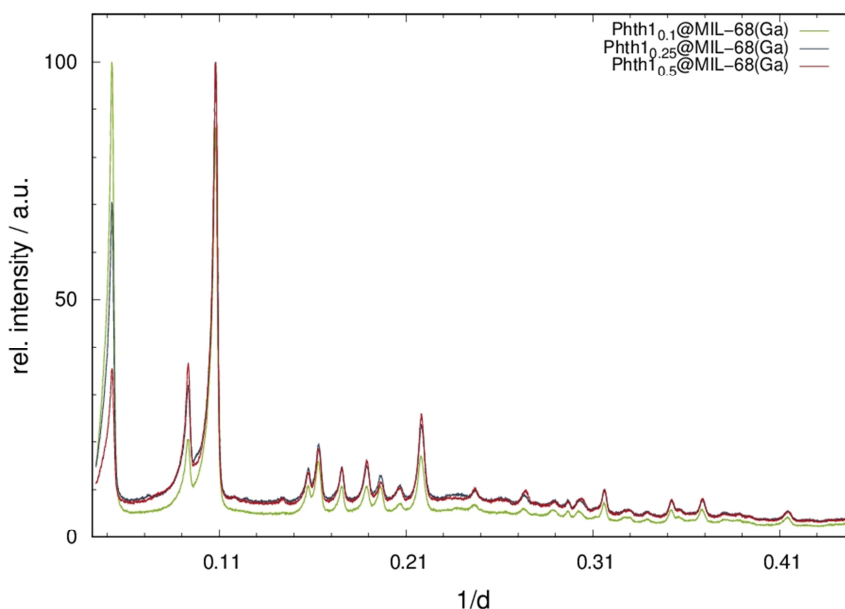


**Figure 4.6.13** XRPD patterns of the serial dilution of Phth in MIL-68(Ga), measured at 298 K (*Huber G670*:  $\lambda = 1.54 \text{ \AA}$ ).

By taking a closer look at the low angle region, an increase of the Phth amount is accompanied by both a decrease of the first peak and an increase of the third one (see figure

4.6.14). Hence, the amount of incorporation can be followed by intensity alterations, similar to the serial dilution of Phth in MOF-5.

Determination of the changes in volume in relation to the amount of embedded guest were done by *Le Bail* fits in *JANA2006*<sup>[194]</sup>. Details are listed in table 4.6.8. Fits are found in figures 8.5.29 to 8.5.31 in the supplement. Notably, no trends or significant differences in volume are observed. Hence, the host lattice remains mainly unaffected by the amount of embedded guest.

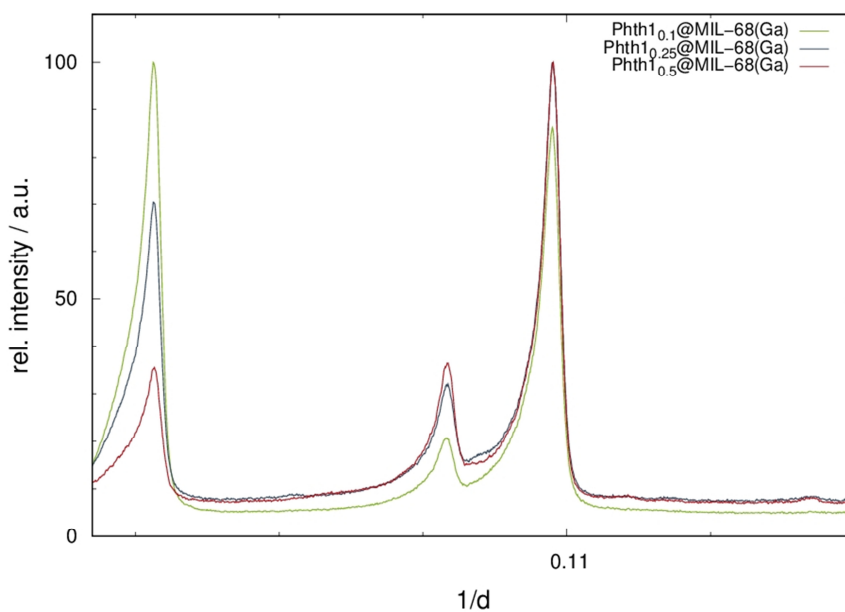


**Figure 4.6.14** Detailed view on the low angle region of the XRPD patterns of the serial dilution of MIL-68(Ga), measured at 298 K (*Huber G670*:  $\lambda = 1.54 \text{ \AA}$ ).

**Table 4.6.8** Results of *Le Bail* fits of powder diffraction data of the serial dilution of Phth in MIL-68(Ga).

	<b>0.1</b>	<b>0.25</b>	<b>0.5</b>
T/K	298	298	298
Space Group / No.	<i>Cmcm</i> / 63	<i>Cmcm</i> / 63	<i>Cmcm</i> / 63
GOF	5.20	3.88	3.66
R <sub>p</sub>	0.0709	0.0525	0.0501
wR <sub>p</sub>	0.1103	0.0854	0.0796
V/Å <sup>3</sup>	5126(1)	5075(1)	5088(1)
a	20.542(2)	20.519(2)	20.564(2)
b	37.865(6)	37.640(5)	37.616(4)
b	6.591(1)	6.571(1)	6.5776(8)

Similar to all data recorded with the *Huber G670* diffractometer, the quality of the diffraction patterns of the serial dilution of MIL-68(Ga) is comparably low due to the measurement conditions. Especially in the low-angle region peaks are asymmetric leading to relatively bad quality values for the *Le Bail* fits. Therefore, values of the fits are preliminary but not conclusive.

#### 4.6.4.2 Composition

Although specific molar ratios were applied during the syntheses procedure, the n<sub>MOF</sub>:n<sub>phthalimide</sub> ratio was determined by means of XPS measurements. In table 4.6.9 and 4.6.10 the respective values are listed. Detailed information on the calculations is given in tables 8.5.4 and 8.5.5 and in figures 8.5.32 to 8.5.37 in the supplement. Notably, all nitrogen signals were very broad, pointing to a successful incorporation of the photoactive dye inside. Unfortunately, fitting of these data turned out to be difficult because of the high signal-to-noise ratio and the low nitrogen concentrations.

**Table 4.6.9** Ratio of Phth per formula unit of the serial dilution of Phth in MOF-5 calculated from XPS measurements.

		Phth : MOF ratio
Phth <sub>0.1</sub> @MOF-5	Phth : (Zn <sub>4</sub> O(bdc) <sub>3</sub> )	0.11 : 1
Phth <sub>0.25</sub> @MOF-5	Phth : (Zn <sub>4</sub> O(bdc) <sub>3</sub> )	0.20 : 1
Phth <sub>0.5</sub> @MOF-5	Phth : (Zn <sub>4</sub> O(bdc) <sub>3</sub> )	0.43 : 1

The results of the XPS measurements are in good agreement with the amount of educts used for the serial dilution of Phth in MOF-5. For MIL-68(Ga) marked discrepancies are found for  $n_{\text{MOF}}:n_{\text{phthalimide}}$  of 1:0.1 and 1:0.5. For Phth<sub>0.1</sub>@MIL-68(Ga) the high signal-to-noise ratio might be responsible for the higher calculated amount of phthalimide. Since the embedment of the dye molecules was done by a gas phase loading process, some phthalimide probably left the pores of the host material during the synthesis process. Hence, a lower guest-to-host ratio is the result of the synthesis conditions.

**Table 4.6.10** Ratio of Phth per formula unit of the serial dilution of Phth in MIL-68(Ga) calculated from XPS measurements.

		Phth : MOF ratio
Phth <sub>0.1</sub> @ MIL-68(Ga)	Phth : (Ga(OH)(bdc))	0.22 : 1
Phth <sub>0.25</sub> MIL-68(Ga)	Phth : (Ga(OH)(bdc))	0.25 : 1
Phth <sub>0.5</sub> @ MIL-68(Ga)	Phth : (Ga(OH)(bdc))	0.32 : 1

Interestingly, the influence of both host matrices on the electronic structure differs significantly, which can be seen in the respective nitrogen peaks. Exemplarily, the nitrogen peak areas of the  $n_{\text{MOF}}:n_{\text{phthalimide}}$  ratio of 1:0.25 are compared in figure 4.6.15 and 4.6.16. While the nitrogen signal of Phth inside MOF-5 is very broad, peak splitting occurs inside MIL-68(Ga).

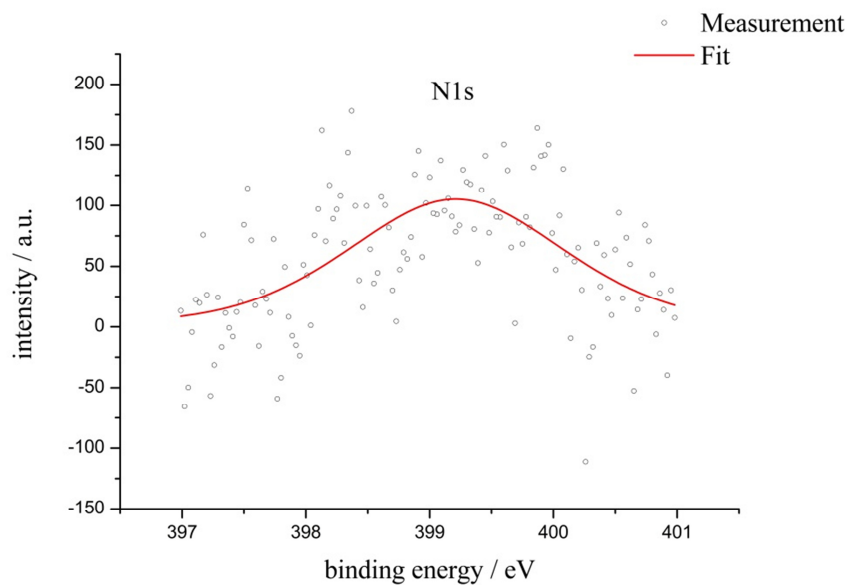


**Figure 4.6.15** XPS spectrum of the N1s peak of Phth<sub>0.25</sub>@MOF-5 with experimental data (dots) and fit (red).

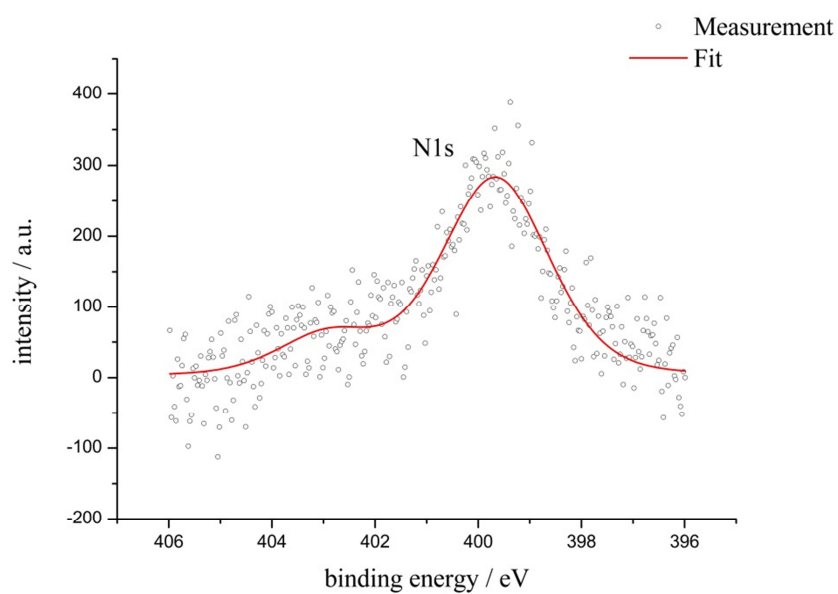


**Figure 4.6.16** XPS spectrum of the N1s peak of Phth<sub>0.25</sub>@MIL-68(Ga) with experimental data (dots) and fit (red).

#### 4.6.4.3 Effects

Possible influence of the degree of filling on the emission bands was investigated by means of fluorescence spectroscopy. For MOF-5 and MIL-68(Ga) a different response is expected because of one MOF being highly symmetric (MOF-5, cubic) and one featuring a lower symmetry (MIL-68(Ga), orthorhombic). In figure 4.6.17 and 4.6.18 the emission spectra of the serial dilution of Phth in MOF-5 and in MIL-68(Ga) are shown, respectively.

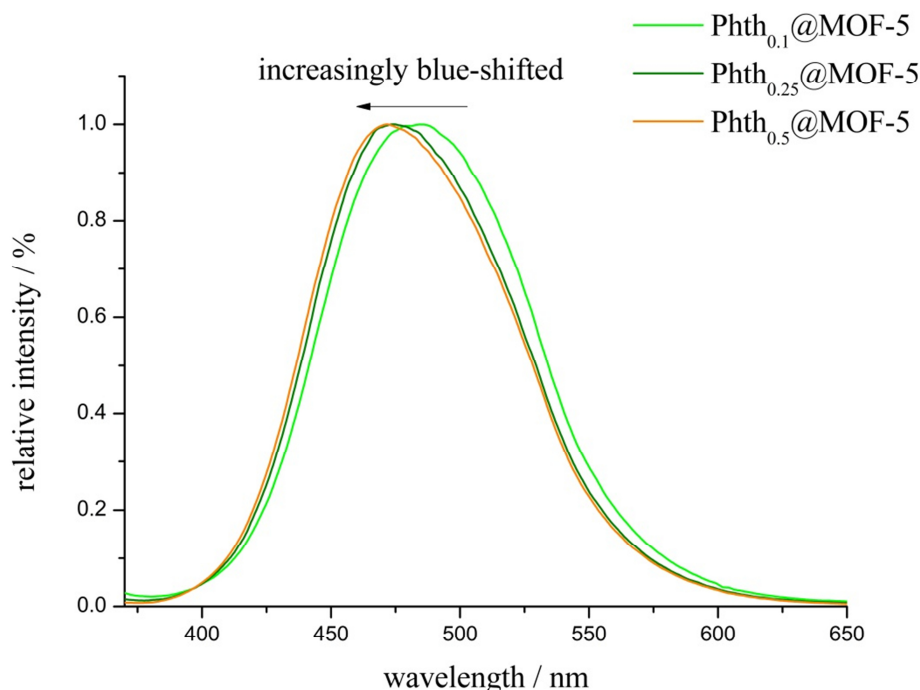


**Figure 4.6.17** Emission spectra of the serial dilution of Phth in MOF-5 with  $\lambda_{\text{ex}} = 347$  nm.

When embedded in MOF-5 rise of the amount of embedded Phth is accompanied by increasingly blue-shifted emission bands, pointing to varying orientations of the guest molecule upon different degrees of loading inside the MOFs pore (see figure 4.6.17). At low concentrations of Phth ( $n = 0.1$ ) the emission band with  $\lambda_{\text{em}} = 484.5$  nm is significantly red-shifted in comparison to both other concentrations 0.25 ( $\lambda_{\text{em}} = 473.5$  nm) and 0.5 ( $\lambda_{\text{em}} = 471.5$  nm), respectively. This might be the result of the phthalimide being mainly oriented close to the metal-nodes  $[\text{Zn}_4\text{O}]^{6+}$  of the MOF scaffold, which feature a comparably high charge. If the quantity of embedded phthalimide is raised, the guest molecules possibly move to lower charged areas inside the host lattice, leading to blue-shifted emission bands. These findings are somewhat surprising, since a disordered orientation inside the cubic pores of MOF-5 was expected being independent from the degree of filling. However, the metal

nodes seem to be attractive in a way that Phth might be preferably positioned close to those. However, raising the phthalimide concentration guest-guest interactions become more attractive, which results in changes in the emission bands to a certain degree.

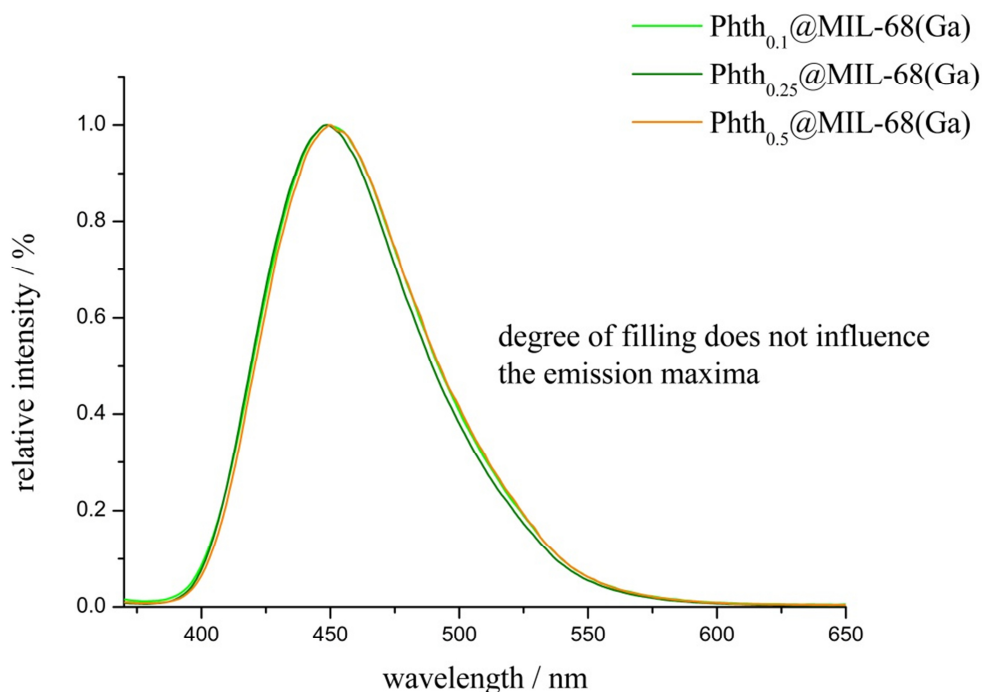


**Figure 4.6.18** Emission spectra of the serial dilution of Phth in MIL-68(Ga) with  $\lambda_{\text{ex}} = 347$  nm.

In contrast to the serial dilution of MOF-5 profound alterations in the emission bands of varying phthalimide concentrations are not found in MIL-68(Ga) (figure 4.6.18). For the dilutions with  $n_{\text{Phth}} = 0.1$  and  $n_{\text{Phth}} = 0.25$  an emission maximum at  $\lambda_{\text{em}} = 448.5$  nm and for  $n_{\text{Phth}} = 0.5$  at  $\lambda_{\text{em}} = 450$  nm is observed. A disparity of  $\lambda = 1.5$  nm is not significant, since small differences in values can be the result of discrepancies during the measurement. Hence, orientation and position of the guest molecules inside MIL-68(Ga) is not influenced by the amount of guest being incorporated. In the structure of MIL-68(Ga) infinite chains consisting of octahedral with  $\text{MO}_4(\text{OH})_2$  are present. They propagate through the complete channels and thus ensure a relatively constant and diffuse charge distribution: The distance between those infinite chains measures  $17 \text{ \AA}$  in maximum, when taking the diameter of the entrance window into account. Furthermore, the wall of the channel is bordered by six such chains. Consequently, there are no large charge distribution differences within the channel, so the position of the guest molecule has no profound impact on the emission properties.

In contrast, the electric charge in MOF-5 is confined to four positions within the pore, exactly in the corners. This results in three possible positions for a small guest molecule: one in the highly charged corners or orientation near the linker molecules as well as centered inside the pore.

To fully prove these assumptions further investigations on the exact position of the guest molecules have to be conducted. Solid state NMR and structure solution via diffraction are recommended in ongoing studies. Besides, the electric field given by the MOFs pore has to be determined, which has not been done so far but might be performed via quantum-chemical calculations.

#### 4.6.5 Preliminary Conclusions

When embedded in different MOF matrices, light induced transformation of spiropyrans and spirooxazines was enabled in solid state. Moreover, the excited state of both dyes showed alterations in their absorption maxima, which are caused by a varying physicochemical environment inside the MOF pores. This influence on the electronic structure was further investigated by the incorporation of 4,5-dimethoxy-*N*-butylphthalimide to understand the occurring effects in greater detail.

The phthalimide 4,5-dimethoxy-*N*-butylphthalimide was successfully combined with ten different host matrices MOF-5, MIL-68(In), MIL-68(Ga), MIL-53(Al), Zeolite Y, MFM-300(Ga<sub>2</sub>) and two fluorinated derivatives as well as HKUST-1 and MIL-101(Cr). The incorporation was confirmed by XRPD measurements for all compounds except of MIL-68(In), where free dye molecule, possibly adsorbed on the MOF surface, could not be removed even after extended heating times.

Instead of the previously used spiropyran and spirooxazine dyes phthalimides are not photochromic, but sensitive to solvent polarity, which influences the position of their emission bands. That way, the shifts of the emission maxima in relation to the used porous host material were determined by means of fluorescence spectroscopy: The results for polarity determination correspond to the previous assignments by the spiropyran and spirooxazine embedment, but only from a qualitative point of view. For precise polarity analysis, however, the *Stokes* shift must also be included, which has to be done in future investigations.

Additionally, dilutions of Phth in two different MOF hosts were performed to take possible guest-guest interactions and, furthermore, different orientations in relation to varying guest concentrations into account. It was suggested that the phthalimide is preferably positioned near to the highly charged metal node of MOF-5 for very low concentrations, which results in a significantly red-shifted emission band in comparison to higher amounts of embedded dye molecule. On the contrary, such shifts were not observed when embedded in MIL-68(Ga). Hence, emission bands seem to be only influenced by guest concentration in host materials with a large charge distribution, such as MOF-5, but not in MIL-68(Ga).



## 5 Conclusion and Future Perspectives

The interest in hybrid materials consisting of photoactive dye molecules and various host materials has become a central point of research in recent years. In order to fully understand and characterize such systems a principle was set up in this thesis, which provides a logical and precise pathway for analysis. The so-called **ICE**-principle with “**I**” defined as Incorporation, “**C**” as Composition and “**E**” as Effects clearly addresses the following questions and recommends possible analytical methods to answer those: First: Was the incorporation successful? Second: What is the composition of the hybrid material? And third: Does the combination of photoactive dye and host material result in new properties – which effects do occur? The establishment and application of such a principle is indispensable for an adequate characterization and a complete understanding of the hybrid dye@MOF materials, which have been presented in this work.

In the present thesis, the embedment of photoactive and polarity sensitive dye molecules into various porous materials mainly focusing on MOFs has been performed. Thereupon, nine MOFs were chosen: MOF-5, MIL-68(In), MIL-68(Ga), MIL-53(Al), HKUST-1, MFM-300(Ga<sub>2</sub>), F-MFM-300(Ga<sub>2</sub>), F<sub>2</sub>-MFM-300(Ga<sub>2</sub>) and MIL-101(Cr). Additionally, the porous material Zeolite Y was applied as a host matrix. Embedment of the dye molecules into the porous host matrices was either performed by gas phase or by mechanochemical loading processes under inert conditions to exclude any solvent molecule from all further considerations. Following the ICE-principle 32 new light responsive composite materials were systematically characterized:

**Table 5.1** Overview of the synthesized dye@MOF/PM systems in the present thesis.

	SP-Nitro	SP	SP-N	SP-OMe	SP-O	Phth
MOF-5	<b>1</b>	<b>5</b>	<b>9</b>	<b>14</b>	<b>19</b>	<b>23</b>
MIL-68(In)	<b>2</b>	<b>6</b>	<b>10</b>	<b>15</b>	<b>20</b>	<b>24</b>
MIL-68(Ga)	<b>3</b>	<b>7</b>	<b>11</b>	<b>16</b>	<b>21</b>	<b>25</b>
MIL-53(Al)	<b>4</b>	<b>8</b>	<b>12</b>	<b>17</b>	<b>22</b>	<b>26</b>
Zeolite Y	-	-	-	-	-	<b>27</b>
MFM-300(Ga <sub>2</sub> )	-	-	-	-	-	<b>28</b>
F-MFM-300(Ga <sub>2</sub> )	-	-	-	-	-	<b>29</b>
F <sub>2</sub> -MFM-300(Ga <sub>2</sub> )	-	-	-	-	-	<b>30</b>
HKUST-1	-	-	<b>13</b>	<b>18</b>	-	<b>31</b>
MIL-101(Cr)	-	-	-	-	-	<b>32</b>

Fundamental investigations on these hybrid systems were focused on in this work. Additionally, the correlation between the MOF scaffold and solvents was shown, since the former can be applied as “solid solvents” for photoswitchable molecules concerning two aspects: photochromic and solvatochromic response.

In a first step, a nitro-substituted spiropyran was used as guest molecule, since spiropyrans offer both photochromic and solvatochromic properties. Thus, both the light induced SP to MC conversion within the MOF and the polarity of the host scaffold were investigated. Four different hybrid systems, namely SP-Nitro@MOF-5 (**1**), SP-Nitro@MIL-68(In) (**2**), SP-Nitro@MIL-68(Ga) (**3**) and SP-Nitro@MIL-53(Al) (**4**), were obtained and fully characterized according to the ICE-principle. The successful embedment was confirmed for all compounds except MIL-53(Al). Here, surface adsorption of the spiropyran occurs. When embedded in MOF-5, the merocyanine form of SP-Nitro is already present without UV light exposure. This points to a chemical environment of the MOF pore, which is preferred by molecules with a high dipole moment such as merocyanines. For host lattices of the MIL series, positive photochromism was observed when SP-Nitro is embedded in or combined with the respective porous host. The successful isomerization of SP-Nitro to its MC-Nitro form was followed by UV/vis and IR spectroscopic measurements. An assignment of all increasing and decreasing vibrational bands was performed to confirm the SP to MC conversion. Notably, MC-Nitro associates into *H*-aggregates in compound **4** upon prolonged UV light exposure.



**Figure 5.1** Left: photography of compounds **1** to **4** after irradiation with UV light ( $\lambda = 365$  nm, 1 min); right: photography of MC-Nitro dissolved in solvents of varying polarity.

Interestingly, the absorption properties of MC-Nitro strongly depend on the MOF host lattice, which is illustrated in figure 5.1, left. In relation to the used host materials, MC-Nitro exhibits

different absorption maxima. Hence, solvatochromic behavior is not only observed in solution (figure 5.1, right), but also in solid state. The ability to successfully isomerize from SP-Nitro to MC-Nitro upon UV light irradiation and dependence of the absorption properties on the used host material are similar to the dissolved state. Taking these two aspects into account, MOFs can be understood as “solid solvents” for this class of photoactive molecules.

Due to its solvatochromic response inside the MOF scaffold, SP-Nitro was applied as a polarity sensor to classify the MOF pores according to the elutrope series of solvents on alumina taken from *Snyder*<sup>[193]</sup>. MOF-5 represents the most polar porous material, followed by MIL-68(In), MIL-68(Ga) and MIL-53(Al). For MIL-53(Al) surface adsorption has to be considered. The correlation between MOF and solvent is shown in figure 5.2.

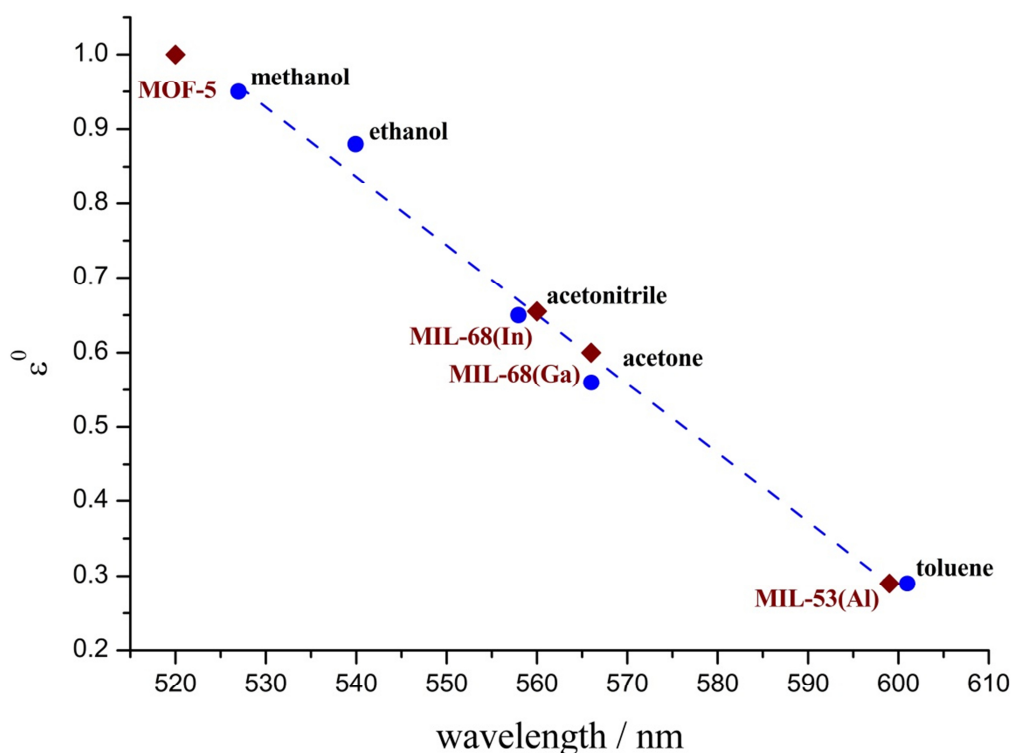


**Figure 5.2** Plot of the wavelength of the absorption maxima of MC-Nitro dissolved in different solvents (blue dots) versus the elution power  $\epsilon^0$  on alumina taken from *Snyder*<sup>[193]</sup>, classifying the polarity of the respective MOFs (red squares). The values of SP-Nitro dissolved in different solvents (blue dots) were linearly fitted (blue broken line).

Reconversion of MC-Nitro to the closed SP form was found to be possible upon heat supply. However, repetitive and prolonged UV light exposure causes destruction of the embedded spiropyran.

Additionally, three further spiropyrans were embedded into different MOF materials. Similar to SP-Nitro@MOF-5 (**1**), the merocyanine form of SP, SP-N and SP-OMe is already stabilized without excitation inside MOF-5. In contrast to SP-Nitro and SP, mechanochemical loading was found to be possible for SP-N and SP-OMe, but only for low dye concentrations. However, SP to MC conversion upon UV light exposure ( $\lambda = 365$  nm and  $\lambda = 385$  nm) was only observed to limited extent for SP, SP-N and SP-OMe, making them unsuitable for the construction of switching hybrid materials.

The low fatigue resistance of SP-Nitro and low photochromic response of SP, SP-N and SP-OMe are a major drawback with respect to potential applications. In order to avoid this disadvantage, structurally related spirooxazines were chosen and SP-O was embedded into MOF-5 (**19**), MIL-68(In) (**20**), MIL-68(Ga) (**21**) and MIL-53(Al) (**22**) via a gas phase loading process. All compounds feature photochromic behavior with positive photochromism and positive solvatochromism upon UV light irradiation. The switching processes were followed by means of UV/vis spectroscopy and, additionally, IR spectroscopic measurements for SP-O@MOF-5 (**19**). That way, all IR bands of the non-irradiated species were assigned to the spirooxazine. Moreover, vibrational frequencies of the excited species were determined and attributed, which has not been done in the literature so far. Thus, first IR spectroscopic data of MC-O are presented here. According to the results of SP-Nitro embedded in MOF-5, SP-O is also stabilized in its open merocyanine form, which confirms that MOF-5 is preferred by molecules with a large dipole moment. Moreover, photodegradation of the spirooxazine is completely suppressed in MOF-5 even upon prolonged UV light exposure, but was found to occur in MIL-68(In), MIL-68(Ga) and when combined with MIL-53(Al). Analogue to SP-Nitro, SP-O was applied as a polarity sensor for the determination of the physicochemical environment of the host matrices. That way, the polarity of the MOF hosts was determined. The results correspond to the SP-Nitro@MOF compound findings except MOF-5, which featured an estimated polarity higher than methanol for SP-Nitro, but is less polar than ethanol for SP-O. For MIL-68(In), MIL-68(Ga) and MIL-53(Al) as host materials the resulting polarities are in agreement with the results of the SP-Nitro@MOF systems. Hence, the polarity scale MOF-5 > MIL-68(In) > MIL-68(Ga) > MIL-53(Al) is qualitatively, but not quantitatively proven.

In order to proof the concept of MOFs as “solid solvents” with a structurally different molecule, a phthalimide was chosen. Phthalimides are not photochromic, but sensitive to solvent polarity, which influences the position of their emission bands. That way, the shifts of the emission maxima in relation to the used porous host material were determined. The

obtained results for polarity correspond to the previous assignments by the spiropyran as well as spirooxazine embedment, but only from a qualitative point of view. For precise polarity analysis, however, the *Stokes* shifts must also be included, which has to be done in future investigations. Moreover, dilutions of Phth in two different MOF hosts were investigated to understand possible guest-guest interactions and, furthermore, different orientations inside the MOF pore in relation to varying guest concentrations. It was assumed that the phthalimide is preferably positioned close to the highly charged metal node of MOF-5 for very low concentrations, which results in a significantly red-shifted emission band in comparison to higher amounts of dye molecule. On the contrary, such shifts were not observed when embedded in MIL-68(Ga). Therefore, emission bands seem to be only influenced by guest concentration in host materials with a large charge distribution, such as MOF-5, but not in MIL-68(Ga). These assumptions are preliminary and have yet to be confirmed by further investigations.

With regard to the fundamental questions formulated in the objective, the following answers can be summarized:

- **Photochromism**

Spiroyrans and spirooxazines exhibit photochromic properties when embedded in or combined with different MOF matrices. For both guest molecules positive photochromism is found to occur.

- **Solvatochromism**

Spiroyrans and spirooxazines feature solvatochromic behavior depending on the respective host. Spiroyrans show negative and spirooxazines positive solvatochromism inside the MOF scaffold, which is similar to the behavior when dissolved in solvents of varying polarity. Therefore, MOFs can be understood as “solid solvents” for these switchable dye molecules.

- **Stabilization of ground and excited state**

When embedded in MOF-5, all switchable guests are stabilized in their open merocyanine form even without UV light exposure: an environment established by the MOF pore is suggested, which is preferred by molecules with a high dipole moment like merocyanines.

- **Formation of aggregates**

The formation of aggregates was only found for compound **4**, where SP-Nitro is adsorbed on the surface of MIL-53(Al). Here, association into *H*-aggregates takes place, which results in an increased resistance towards photodegradation.

- **Photostability**

Upon repetitive and prolonged UV light exposure photodegradation occurs for embedded SP-Nitro. For the spirooxazine photostability was only observed inside MOF-5.

- **Polarity of the host materials**

Depending on the metal node, the used MOF matrices feature varying polarity, which was determined by the incorporation of solvatochromic spiropyrans and spirooxazines and, additionally, a polarity sensitive phthalimide. That way, a polarity order was established.

In summary, the obtained guest@MOF composite materials are of great potential for understanding the influence of the host material on the photochromic and solvatochromic properties of the embedded guest molecule. Photoswitching as well as solvatochromic response was shown for spiropyrans and spirooxazines embedded in the porous host matrices. Nonetheless, determination of the exact position of the incorporated guest molecules inside the MOF pores is obligatory to completely understand the light induced response. The presented results describe the effects, but only explain them to a certain extent. However, structure solution even via high resolution synchrotron powder diffraction was not possible, since the embedded dye molecules are, in contrast to azobenzene<sup>[164]</sup> e.g., too complex for such investigations. In a next step, complementary methods such as solid state NMR and PDF in combination with quantum-chemical calculations have to be applied for an exact determination of the dye position. That way, the mobility of the embedded guest molecule inside the host cages can be determined to answer the following questions: Is the dye molecule located at a particular position inside the host scaffold or randomly ordered? Do positions change during the light induced isomerization processes? The dipole moments of both spiropyrans and spirooxazines markedly differ when converted to their merocyanine form. Thus, varying positions inside the host scaffold are expected for the non-irradiated and excited species.

The preparation of MOF bulk materials is comparably simple, but characterization especially with regard to determining the guest position and structure solution is not straightforward. Synthesis of guest@MOF single crystals would overcome this problem. *Benedict* and co-workers already presented a dye@MOF single crystal composite material.<sup>[168]</sup> However, identification of the exact position of the used diarylethene inside the pore has not been successful: The guest molecule is strongly disordered in the pores of the tetragonal DMOF-1. Therefore, synthesis of such loaded single crystals with a comparably simple photoswitch like azobenzene and host lattices with low symmetry has to be done in the future. Both position and isomerization processes of the embedded guest molecule inside the host scaffold could be followed in those loaded single crystals.

Up to now, the polarity of the used porous host materials has been experimentally determined by the incorporation of dyes being sensitive to the surrounding medium. This represents a simple and descriptive way, as the polarities of the host matrices can be tracked via changes in absorption and emission spectra. However, exact polarity values still have to be determined. This has been nicely introduced for solvents via a solvent polarity scale established by *Rodríguez* and co-workers<sup>[230]</sup> with 2-(dimethylamino)-7-nitrofluorene and its homomorph 2-fluoro-7-nitrofluorene as polarity probes. In a next step, a MOF polarity scale could be introduced, which offers the opportunity to systematically tune the absorption and emission properties of potential guest molecules. That way, smart guest@MOF systems can be designed.

With respect to possible applications the synthesis of dye@MOF materials as thin films is indispensable. Such systems are already known with azobenzene and fluorinated derivatives<sup>[170]</sup> and a spiropyran<sup>[171]</sup>. The systematic design of dye@MOF systems with desired properties combined with the preparation of those as thin films will be future directing for functional and light responsive hybrid materials.



## 6 Experimental

### 6.1 General Remarks

In the following, the synthesis procedures are listed and described. Detailed information on the synthesis strategies for the host matrices and hybrid materials are given in chapter 6.2

For investigations on solvatochromism of the different spiropyrans and the spirooxazine, the respective dye was dissolved in different solvents by a concentration of  $10^{-1}$  mol/l and irradiated with UV light ( $\lambda = 385$  nm) for 1 min. To determine the polarity dependent emission of 4,5-dimethoxy-*N*-butylphthalimide, a concentration of  $10^{-5}$  mol/l was chosen based on the sensitivity of the fluorescence spectrometer's detector. The UV/vis spectra were recorded by means of qualitative, but not quantitative analysis.

In collaboration with the work group of *Griesbeck* (Institute of Organic Chemistry, University of Cologne) investigations on a fluorescent phthalimide were carried out to further understand the polarity/electric fields inside different MOF and zeolite matrices. 4,5-dimethoxy-*N*-butylphthalimide was synthesized by *M. Atar* and *M. Vollmer*. The detailed description of the synthesis is found here<sup>[231]</sup>.

To investigate the polarity of the inner surface in relation to the degree of fluorination, isostructural MOFs with none, one and two fluorine atoms in the linker backbone were loaded with 4,5-dimethoxy-*N*-butylphthalimide. The required MOFs MFM-300(Ga<sub>2</sub>) and its fluorinated derivatives F-MFM-300(Ga<sub>2</sub>) and F<sub>2</sub>-MFM-300(Ga<sub>2</sub>) were synthesized by *C. Stastny*. The exact protocol is found here<sup>[186]</sup>.

Parts of the synthesis of dye@MOF-5 systems were done with MOF-5 provided by the *BASF*.

The following Table 6.1 lists the chemicals with their supply source and purity used in this work.

**Table 6.1** List of the used chemicals with their supply source and information on purity.

<b>Chemical</b>	<b>sum formula</b>	<b>supply source</b>	<b>purity</b>
Aluminum(III)-nitrate-nonahydrate	$\text{Al}(\text{NO}_3)_3 \cdot 9\text{H}_2\text{O}$	ABCR	> 98%
MOF-5	$\text{Zn}_4\text{C}_{24}\text{O}_{13}\text{H}_{12}$	BASF	n.s.
N,N-dimethylformamide	$\text{C}_5\text{H}_7\text{NO}$	Fischer	HPLC grade
Ethanol	$\text{CH}_3\text{CH}_2\text{OH}$	Brennerei Hoffmann	reinst.
Gallium(III)-nitrate-monohydrate	$\text{Ga}(\text{NO}_3)_3 \cdot x\text{H}_2\text{O}$	ABCR	99.99%
Indium(III)-nitrate-hydrate	$\text{In}(\text{NO}_3)_3 \cdot x\text{H}_2\text{O}$	ABCR	99.99%
Methanol	$\text{CH}_3\text{OH}$	BCD Chemie	n.s.
Nitric acid	$\text{HNO}_3$	n.s.	n.s.
Terephthalic acid	$\text{C}_8\text{O}_4\text{H}_6$	Alfa Aesar	> 98%
1,3,3- Trimethylindolino-6'-nitro-benzopyrylospiran	$\text{C}_{19}\text{H}_{18}\text{N}_2\text{O}_3$	TCI	> 98%
1,3,3-Trimethylindolino- $\beta$ -naphthopyrylospiran	$\text{C}_{23}\text{H}_{21}\text{NO}$	TCI	> 98%
1,3,3-Trimethylindolino-8'-methoxybenzo-pyrylospiran	$\text{C}_{20}\text{H}_{21}\text{NO}_2$	TCI	> 98%
1,3,3-Trimethylindolino-benzopyrylospiran	$\text{C}_{19}\text{H}_{19}\text{NO}$	TCI	> 98%
1,3,3-Trimethylindolino-naphthospirooxazine	$\text{C}_{22}\text{H}_{20}\text{N}_2\text{O}$	TCI	> 98%
Toluene	$\text{C}_7\text{H}_8$	Fischer Chemicals	HPLC grade
Acetonitrile	$\text{C}_2\text{H}_3\text{N}$	Fischer Chemicals	HPLC grade
Acetone	$\text{C}_3\text{H}_6\text{O}$	n.s.	n.s.
Copper(II)-hydroxide	$\text{Cu}(\text{OH})_2$	Sigma Aldrich	n.s.
Trimesic acid	$\text{C}_9\text{H}_6\text{O}_6$	Sigma Aldrich	95%
Zeolite Y	$\text{SiO}_2:\text{Al}_2\text{O}_3$ 5.1:1 mole ratio	Alfa Aesar	n.s.
Trimethylamine	$\text{C}_3\text{H}_9\text{N}$	n.s.	n.s.
Zinc(II)-acetate-dihydrate	$\text{Zn}(\text{OAc})_2 \cdot 2\text{H}_2\text{O}$	n.s.	n.s.

## 6.2 Syntheses methods

### 6.2.1 Syntheses of Host Materials

The host materials of the MIL-series were produced solvothermally. The corresponding metal salts, terephthalic acid and DMF or water were mixed in a 23 ml Teflon lined autoclave. The Teflon inlays were screwed tight in an acid digestion bomb (*Parr Company*) and heated in the oven (*Memmert Company*<sup>[232]</sup>). Heating programs were controlled by the program *Celsius 2005*. The removal of excess terephthalic acid and DMF was performed in ovens of the *HTM Reetz GmbH* in air.

MOF-5 and HKUST-1 were synthesized by stirring a solution of the respective metal-salt and terephthalic respectively trimesic acid over a certain time.

In order to get the solvent-free metal-organic frameworks, all compounds were heated under reduced pressure to remove all solvent and water molecules and stored under an argon atmosphere to prevent absorption of humidity and decomposition.

#### **MIL-68(In)**

408.20 mg  $\text{In}(\text{NO}_3)_3 \cdot 5 \text{H}_2\text{O}$  (1.04 mmol) and 200.00 mg terephthalic acid (1.20 mmol) were mixed with 5.0 ml DMF in a 23 ml teflon lined autoclave. The mixture was heated to 100 °C with a rate of 20 °C/h, kept at this temperature for 48 h, and afterwards cooled down to room temperature with a rate of 5 °C/h. The resulting colorless powder was washed several times with DMF and dried in air. To remove the embedded DMF molecules, the powder was heated in air at 200 °C for 12 h, then at 100 °C for 1 h under reduced pressure and was stored afterwards under an argon atmosphere in the glovebox to prevent absorption of humidity.

#### **MIL-68(Ga)**

207.40 mg  $\text{Ga}(\text{NO}_3)_3 \cdot x \text{H}_2\text{O}$  (0.81 mmol) and 100.00 mg terephthalic acid (0.60 mmol) were mixed with 5.0 ml DMF in a 23 ml teflon lined autoclave. The mixture was heated to 100 °C with a rate of 20 °C/h, kept at this temperature for 48 h, and afterwards cooled down to room temperature with a rate of 5 °C/h. The resulting colorless powder was washed several times with DMF and dried in air. To remove the embedded DMF molecules, the residue was heated in air at 200 °C for 12 h, then at 100 °C for 1 h under reduced pressure and was stored afterwards under an argon atmosphere in the glovebox to prevent absorption of humidity.

### **MIL-53(Al)**

1.95 g  $\text{Al}(\text{NO}_3)_3 \cdot 9 \text{H}_2\text{O}$  (5.20 mmol) und 432.00 mg terephthalic acid (2.60 mmol) were mixed with 5.0 ml deionized water in a 23 ml teflon lined autoclave. The mixture was heated to 180 °C with a rate of 10 °C/h, kept at this temperature for 72 h and afterwards cooled down to room temperature with a rate of 5 °C/h. The resulting colorless powder was washed with deionized water several times and dried in air. To remove the embedded terephthalic acid molecules, the residue was heated in air at 350 °C for 7 days followed by 3 days of heating at 400 °C. Finally, the resulting powder was heated at 100 °C for 1 h under reduced pressure and stored under an argon atmosphere in the Glovebox to prevent absorption of humidity.

### **MIL-101(Cr)**

0.400 g  $\text{Cr}(\text{NO}_3)_3 \cdot 9 \text{H}_2\text{O}$  (1.0 mmol), 0.160 g terephthalic acid (1.0 mmol), 0.07 ml 65%  $\text{HNO}_3$  and 5 ml deionized water were filled into a Teflon lined autoclave and heated to 220 °C with a rate of 25 °C/h, kept at this temperature for 8 h and cooled down to room temperature at 30 °C/h. The obtained suspension was centrifuged and the solvent decanted. 5 ml DMF were added to the green solid and the suspension was sonicated for 1 h at 80 °C, again centrifuged, the solvent decanted and the obtained green precipitate transferred into a 25 ml glass beaker. 10 ml  $\text{H}_2\text{O}$  were added and the mixture was stirred for 5 h at 70 °C. After centrifugation and removal of the solvent the resulting precipitate was transferred to a 25 ml glass beaker, mixed with 10 ml ethanol and stirred for 5 h at 70 °C. The suspension was centrifuged, decanted and the precipitate dried at 120 °C and a reduced pressure for 2 h. MIL-101(Cr) was obtained as dark green powder, which was stored under an argon atmosphere in the glovebox to prevent absorption of humidity.

### **HKUST-1**

0.42 g  $\text{Cu}(\text{OH})_2$  (4.31 mmol) and 0.5 g trimesic acid (2.38 mmol) were dissolved in 4.2 ml dest. water and 11 ml ethanol, respectively. Both suspensions were united and stirred at room temperature for 2 h. The resulting residue was filtered and washed with ethanol several times. To remove the embedded solvent molecules, the turquoise powder was dried in the oven at 100 °C overnight. Finally, the resulting powder was heated at 100 °C for 1 h under reduced pressure and stored under an argon atmosphere in the glovebox to prevent absorption of humidity.

## **MOF-5**

1.266 g terephthalic acid (7.62 mmol) and trimethylamine (2.13 ml) were dissolved in 100 ml of DMF. 4.25 g  $\text{Zn}(\text{OAc})_2 \cdot 2 \text{H}_2\text{O}$  (19.35 mmol) was dissolved in 125 ml DMF. While stirring, the zinc salt solution was added dropwise to the organic solution over 15 min. The mixture was stirred for 2.5 h. The precipitate was filtered and immersed in 62.5 ml DMF overnight. It was then filtered again and immersed in 87.5 ml  $\text{CHCl}_3$ . The solvent was exchanged 3 times over 7 days: after 2 days, 3 days, and 7 days. Finally, the bulk of the solvent was decanted. To remove all solvent molecules, the resulting powder was heated at 100 °C for 12 h under reduced pressure and stored under an argon atmosphere in the glovebox to prevent absorption of humidity and decomposition by contact with moisture.

## 6.2.2 Syntheses of dye@MOF systems

To exclude any solvent molecule from all further considerations, the embedment of the guest molecules was either done by gas phase loading or by mechanochemical loading processes. In both cases, all compounds were handled in an inert atmosphere to prevent absorption of humidity.

### 6.2.2.1 Gas phase loading

A mixture of the respective activated MOF and the respective dye molecule was thoroughly ground under an argon atmosphere. The resulting homogenous powder was placed into a small glass vessel inside a *Schlenk* tube and heated at a specific temperature (exact temperatures are given at the detailed synthesis for the respective systems) and a reduced pressure of  $\sim 5 \cdot 10^{-2}$  mbar for several hours. The excess of dye molecule resublimed at the top of the glass tube. Afterwards, all compounds were stored under an argon atmosphere in the glovebox to prevent the absorption of water and decomposition upon contact with air and moisture. Usually, molar ratios of  $n_{\text{guest}}:n_{\text{MOF}}$  of 1:1 (for MOF-5  $n_{\text{guest}}:n_{\text{MOF}}$  of 5:1) were applied according to the results of different azobenzene@MOF composite materials.<sup>[163,164]</sup>

### SP-Nitro@MOF

In table 6.2 the weights for the syntheses of SP-Nitro@MOF materials are listed. Molar ratios were calculated for the solvent free metal-organic frameworks. In a typical synthesis, the respective mixture of spiropyran and MOF was heated at 140 °C to 150 °C and a reduced pressure for several hours. The syntheses were stopped, when no excess spiropyran resublimed at the top of the glass tube anymore. All compounds were stored under an argon atmosphere afterwards for further characterization.

**Table 6.2** Weights for the syntheses of the SP-Nitro@MOF compounds.

compound	m(MOF) / mg	n(MOF) / mmol	m(SP-Nitro) / mg	n(SP-Nitro) / mmol
SP-Nitro@MOF-5	60	0.08	126	0.40
SP-Nitro@MIL-68(In)	60	0.20	64	0.20
SP-Nitro@MIL-68(Ga)	60	0.24	77	0.24
SP-Nitro@MIL-53(Al)	60	0.28	92	0.28

### SP@MOF

In a typical synthesis, the respective mixture of spiropyran and MOF was heated at 150 °C and a reduced pressure for several hours. The syntheses were stopped, when no excess spiropyran resublimed at the top of the glass tube anymore. All compounds were stored under an argon atmosphere afterwards for further characterization.

**Table 6.3** Weights for the syntheses of the SP@MOF compounds.

compound	m(MOF) / mg	n(MOF) / mmol	m(SP) / mg	n(SP) / mmol
SP@MOF-5	60	0.08	108.00	0.40
SP@MIL-68(In)	60	0.20	56.25	0.20
SP@MIL-68(Ga)	60	0.24	66.37	0.24
SP@MIL-53(Al)	60	0.28	80.00	0.28

### SP-O@MOF

In a typical synthesis, the respective mixture of spirooxazine and MOF was heated at 70 °C to 110 °C and a reduced pressure for several hours. The syntheses were stopped, when no excess spirooxazine resublimed at the top of the glass tube anymore. All compounds were stored under an argon atmosphere afterwards for further characterization.

**Table 6.4** Weights for the syntheses of the SP-O@MOF compounds.

compound	m(MOF) / mg	n(MOF) / mmol	m(SP-O) / mg	n(SP-O) / mmol
SP-O@MOF-5	60	0.08	128.5	0.40
SP-O@MIL-68(In)	60	0.20	66.60	0.20
SP-O@MIL-68(Ga)	60	0.24	78.60	0.24
SP-O@MIL-53(Al)	60	0.28	47.37	0.28

### SP-OMe@MOF and SP-N@MOF

In a typical synthesis, the respective mixture of the respective spiropyran and MOF was heated at 110 °C to 120 °C and a reduced pressure for several hours.

**Table 6.5** Weights for the syntheses of the spiropyran@MIL-53(Al) compounds.

compound	m(MOF) / mg	n(MOF) / mmol	m(spiro) / mg	n(spiro) / mmol
SP-OMe@MIL-53(Al)	60	0.28	94.46	0.28
SP-N@MIL-53(Al)	60	0.28	88.68	0.28

### Phth@MOF/PM

Similar to the spiropyran and spirooxazine@MOF-systems, Phth@MOF/PM composites were synthesized as follows: in a typical synthesis, the respective mixture of phthalimide and MOF was heated at 120 °C to 130 °C and a reduced pressure for several hours.

**Table 6.6** Weights for the syntheses of the Phth@PM compounds.

compound	m(PM) / mg	n(PM) / mmol	m(Phth) / mg	n(Phth) / mmol
Phth@MOF-5	60	0.08	61.0	0.24
Phth@MIL-68(In)	60	0.20	53.4	0.20
Phth@MIL-68(Ga)	60	0.24	63.0	0.24
Phth@MIL-53(Al)	60	0.28	75.9	0.28
Phth@HKUST-1	60	0.10	21.1	0.10
Phth@MIL-101(Cr)	10	0.01	3.6	0.01
Phth@Zeolite Y	60	0.14	97.5	0.14
Phth@MFM-300(Ga <sub>2</sub> )	30	0.06	16.0	0.06
Phth@F-MFM-300(Ga <sub>2</sub> )	30	0.057	15.0	0.057
Phth@F <sub>2</sub> -MFM-300(Ga <sub>2</sub> )	60	0.11	29.4	0.11

In addition to the influence of the host matrices (host-guest interactions), possible guest-guest interactions were investigated for different loading degrees. MOF-5 and MIL-68(Ga) were chosen, since MOF-5 represents a highly symmetric MOF (cubic crystal system). MIL-

68(Ga) crystallizes in a orthorhombic space group and is therefore less symmetric. In table 6.7 and table 6.8 the exact weights for this dilution are given.

**Table 6.7** Weights for the dilution of MOF-5.

compound	m(PM) / mg	n(PM) / mmol	m(Phth) / mg	n(Phth) / mmol
Phth <sub>0.1</sub> @MOF-5	60	0.08	2	0.008
Phth <sub>0.25</sub> @MOF-5	60	0.08	5	0.02
Phth <sub>0.5</sub> @MOF-5	60	0.08	10	0.04

**Table 6.8** Weights for the dilution of MIL-68(Ga).

compound	m(PM) / mg	n(PM) / mmol	m(Phth) / mg	n(Phth) / mmol
Phth <sub>0.1</sub> @MIL-68(Ga)	60	0.24	6	0.024
Phth <sub>0.25</sub> @MIL-68(Ga)	60	0.24	15.7	0.06
Phth <sub>0.5</sub> @MIL-68(Ga)	60	0.24	31.5	0.12

For any syntheses of Phth@MOF/PM composite materials, the syntheses were stopped, when no excess phthalimide resublimed at the top of the glass tube anymore. All compounds were stored under an argon atmosphere afterwards for further characterization.

### 6.2.2.2 Mechanochemical Loading

For the mechanochemical loading processes, the respective activated MOF and Spiro-OMe or Spiro-N were thoroughly ground under an argon atmosphere. Ten different  $n_{\text{Spiro}}:n_{\text{MOF}}$  molar ratios were used for that purpose in 0.1 steps (0.1 to 1.0). Exact weights are given in the detailed synthesis descriptions of the respective systems.

#### SP-OMe@MOF

SP-OMe was incorporated into four different MOFs by means of mechanochemical loading. As suitable host matrices MOF-5, MIL-68(In), MIL-68(Ga) and HKUST-1 were chosen, since their window of the pores was estimated to be big enough for the dye molecules to enter. The mixture of the respective colorless or blue MOF and colorless dye was thoroughly ground until no significant change in color was observed anymore. In tables 6.9 to 6.12 the exact weights of dye and respective MOF are given.

**Table 6.9** Weights for the mechanochemical syntheses of the SP-OMe@MOF-5 compounds.

compound	m(MOF) / mg	n(MOF) / mmol	m(SP-OMe) / mg	n(SP-OMe) / mmol
SP-OMe <sub>0.1</sub> @MOF-5	30	0.04	1.2	0.004
SP-OMe <sub>0.2</sub> @MOF-5	30	0.04	2.4	0.008
SP-OMe <sub>0.3</sub> @MOF-5	30	0.04	3.6	0.012
SP-OMe <sub>0.4</sub> @MOF-5	30	0.04	4.8	0.016
SP-OMe <sub>0.5</sub> @MOF-5	30	0.04	6.0	0.020
SP-OMe <sub>0.6</sub> @MOF-5	30	0.04	7.2	0.024
SP-OMe <sub>0.7</sub> @MOF-5	30	0.04	8.4	0.028
SP-OMe <sub>0.8</sub> @MOF-5	30	0.04	9.6	0.032
SP-OMe <sub>0.9</sub> @MOF-5	30	0.04	10.8	0.036
SP-OMe <sub>1.0</sub> @MOF-5	30	0.04	12.0	0.040

**Table 6.10** Weights for the mechanochemical syntheses of the SP-OMe@MIL-68(In) compounds.

compound	m(MOF) / mg	n(MOF) / mmol	m(SP-OMe) / mg	n(SP-OMe) / mmol
SP-OMe <sub>0.1</sub> @MIL-68(In)	30	0.10	3	0.01
SP-OMe <sub>0.2</sub> @MIL-68(In)	30	0.10	6	0.02
SP-OMe <sub>0.3</sub> @MIL-68(In)	30	0.10	9	0.03
SP-OMe <sub>0.4</sub> @MIL-68(In)	30	0.10	12	0.04
SP-OMe <sub>0.5</sub> @MIL-68(In)	30	0.10	15	0.05
SP-OMe <sub>0.6</sub> @MIL-68(In)	30	0.10	18	0.06
SP-OMe <sub>0.7</sub> @MIL-68(In)	30	0.10	21	0.07
SP-OMe <sub>0.8</sub> @MIL-68(In)	30	0.10	24	0.08
SP-OMe <sub>0.9</sub> @MIL-68(In)	30	0.10	27	0.09
SP-OMe <sub>1.0</sub> @MIL-68(In)	30	0.10	30	0.10

**Table 6.11** Weights for the mechanochemical syntheses of the SP-OMe@MIL-68(Ga) compounds.

compound	m(MOF) / mg	n(MOF) / mmol	m(SP-OMe) / mg	n(SP-OMe) / mmol
SP-OMe <sub>0.1</sub> @MIL-68(Ga)	30	0.12	3.7	0.012
SP-OMe <sub>0.2</sub> @MIL-68(Ga)	30	0.12	7.4	0.024
SP-OMe <sub>0.3</sub> @MIL-68(Ga)	30	0.12	11.1	0.036
SP-OMe <sub>0.4</sub> @MIL-68(Ga)	30	0.12	14.8	0.048
SP-OMe <sub>0.5</sub> @MIL-68(Ga)	30	0.12	18.5	0.060
SP-OMe <sub>0.6</sub> @MIL-68(Ga)	30	0.12	22.2	0.072
SP-OMe <sub>0.7</sub> @MIL-68(Ga)	30	0.12	25.9	0.084
SP-OMe <sub>0.8</sub> @MIL-68(Ga)	30	0.12	29.6	0.096
SP-OMe <sub>0.9</sub> @MIL-68(Ga)	30	0.12	33.3	0.108
SP-OMe <sub>1.0</sub> @MIL-68(Ga)	30	0.12	37.0	0.120

**Table 6.12** Weights for the mechanochemical syntheses of the SP-OMe@HKUST-1 compounds.

compound	m(MOF) / mg	n(MOF) / mmol	m(SP-OMe) / mg	n(SP-OMe) / mmol
SP-OMe <sub>0.1</sub> @HKUST-1	30	0.05	1.5	0.005
SP-OMe <sub>0.2</sub> @HKUST-1	30	0.05	3.0	0.010
SP-OMe <sub>0.3</sub> @HKUST-1	30	0.05	4.5	0.015
SP-OMe <sub>0.4</sub> @HKUST-1	30	0.05	6.0	0.020
SP-OMe <sub>0.5</sub> @HKUST-1	30	0.05	7.5	0.025
SP-OMe <sub>0.6</sub> @HKUST-1	30	0.05	9.0	0.030
SP-OMe <sub>0.7</sub> @HKUST-1	30	0.05	10.5	0.035
SP-OMe <sub>0.8</sub> @HKUST-1	30	0.05	12.0	0.040
SP-OMe <sub>0.9</sub> @HKUST-1	30	0.05	13.5	0.045
SP-OMe <sub>1.0</sub> @HKUST-1	30	0.05	15.0	0.050

After characterization of the respective serial dilution, all moieties were united and heated at 120 °C and a reduced pressure for several hours. The gas phase loading was stopped, when no excess spiropyran resublimed at the top of the glass tube anymore. All compounds were stored under an argon atmosphere afterwards for further characterization.

## SP-N@MOF

Similar to SP-OMe, SP-N was incorporated into four different MOFs by means of mechanochemical loading. Again, MOF-5, MIL-68(In), MIL-68(Ga) and HKUST-1 were chosen as suitable host matrices, since their window of the pores was estimated to be big enough for the dye molecules to enter. The mixture of the respective colorless or blue MOF and colorless dye was thoroughly ground until no significant change in color was observed anymore. In tables 6.13 to 6.16 the exact weights of dye and respective MOF are given.

**Table 6.13** Weights for the mechanochemical syntheses of the SP-N@MOF-5 compounds.

compound	m(MOF) / mg	n(MOF) / mmol	m(SP-N) / mg	n(SP-N) / mmol
SP-N <sub>0.1</sub> @MOF-5	30	0.04	1.3	0.004
SP-N <sub>0.2</sub> @MOF-5	30	0.04	2.6	0.008
SP-N <sub>0.3</sub> @MOF-5	30	0.04	3.9	0.012
SP-N <sub>0.4</sub> @MOF-5	30	0.04	5.2	0.016
SP-N <sub>0.5</sub> @MOF-5	30	0.04	6.5	0.020
SP-N <sub>0.6</sub> @MOF-5	30	0.04	7.8	0.024
SP-N <sub>0.7</sub> @MOF-5	30	0.04	9.1	0.028
SP-N <sub>0.8</sub> @MOF-5	30	0.04	10.4	0.032
SP-N <sub>0.9</sub> @MOF-5	30	0.04	11.7	0.036
SP-N <sub>1.0</sub> @MOF-5	30	0.04	13.0	0.040

**Table 6.16** Weights for the mechanochemical syntheses of the SP-N@MIL-68(In) compounds.

compound	m(MOF) / mg	n(MOF) / mmol	m(SP-N) / mg	n(SP-N) / mmol
SP-N <sub>0.1</sub> @MIL-68(In)	30	0.10	3.3	0.01
SP-N <sub>0.2</sub> @MIL-68(In)	30	0.10	6.6	0.02
SP-N <sub>0.3</sub> @MIL-68(In)	30	0.10	9.9	0.03
SP-N <sub>0.4</sub> @MIL-68(In)	30	0.10	13.2	0.04
SP-N <sub>0.5</sub> @MIL-68(In)	30	0.10	16.5	0.05
SP-N <sub>0.6</sub> @MIL-68(In)	30	0.10	19.8	0.06
SP-N <sub>0.7</sub> @MIL-68(In)	30	0.10	23.1	0.07
SP-N <sub>0.8</sub> @MIL-68(In)	30	0.10	26.4	0.08
SP-N <sub>0.9</sub> @MIL-68(In)	30	0.10	29.7	0.09
SP-N <sub>1.0</sub> @MIL-68(In)	30	0.10	33.0	0.10

**Table 6.17** Weights for the mechanochemical syntheses of the SP-N@MIL-68(Ga) compounds.

compound	m(MOF) / mg	n(MOF) / mmol	m(SP-N) / mg	n(SP-N) / mmol
SP-N <sub>0.1</sub> @MIL-68(Ga)	30	0.12	3.9	0.012
SP-N <sub>0.2</sub> @MIL-68(Ga)	30	0.12	7.8	0.024
SP-N <sub>0.3</sub> @MIL-68(Ga)	30	0.12	11.7	0.036
SP-N <sub>0.4</sub> @MIL-68(Ga)	30	0.12	15.6	0.048
SP-N <sub>0.5</sub> @MIL-68(Ga)	30	0.12	19.5	0.060
SP-N <sub>0.6</sub> @MIL-68(Ga)	30	0.12	23.4	0.072
SP-N <sub>0.7</sub> @MIL-68(Ga)	30	0.12	27.3	0.084
SP-N <sub>0.8</sub> @MIL-68(Ga)	30	0.12	31.2	0.096
SP-N <sub>0.9</sub> @MIL-68(Ga)	30	0.12	35.1	0.108
SP-N <sub>1.0</sub> @MIL-68(Ga)	30	0.12	39.0	0.120

**Table 6.18** Weights for the mechanochemical syntheses of the SP-N@HKUST-1 compounds.

compound	m(MOF) / mg	n(MOF) / mmol	m(SP-N) / mg	n(SP-N) / mmol
SP-N <sub>0.1</sub> @HKUST-1	30	0.05	1.6	0.005
SP-N <sub>0.2</sub> @HKUST-1	30	0.05	3.2	0.010
SP-N <sub>0.3</sub> @HKUST-1	30	0.05	4.8	0.015
SP-N <sub>0.4</sub> @HKUST-1	30	0.05	6.4	0.020
SP-N <sub>0.5</sub> @HKUST-1	30	0.05	8.0	0.025
SP-N <sub>0.6</sub> @HKUST-1	30	0.05	9.6	0.030
SP-N <sub>0.7</sub> @HKUST-1	30	0.05	11.2	0.035
SP-N <sub>0.8</sub> @HKUST-1	30	0.05	12.8	0.040
SP-N <sub>0.9</sub> @HKUST-1	30	0.05	14.4	0.045
SP-N <sub>1.0</sub> @HKUST-1	30	0.05	16.0	0.050

After characterization of the respective serial dilution, all moieties were united and heated at 120 °C and a reduced pressure for several hours. The gas phase loading was stopped, when no excess spiropyran resublimed at the top of the glass tube anymore. All compounds were stored under an argon atmosphere afterwards for further characterization.

## 6.3 Characterization

### 6.3.1 Incorporation

#### 6.3.1.1 Laboratory XRPD measurements

Laboratory measurements were carried out on either a *STOE StadiP* powder diffractometer (Debye-Scherrer geometry, Ge (111) monochromator, PSD detector) or a *Huber G670* powder diffractometer (Guinier geometry, Ge (111) monochromator, image plate detector). In both cases samples were irradiated with  $\text{CuK}_{\alpha 1}$  radiation.

For each measurement, samples were prepared under an argon atmosphere to prevent absorption of humidity and decomposition. For that purpose, the respective MOF or hybrid system was thoroughly ground and filled about 2 cm high into *Lindemann* glass capillaries (diameter of 0.7 to 1.0 mm). The filled capillaries were sealed with the help of a glow wire and closed airtight with pizine. Samples were adjusted on a goniometer head in a way that the substance was in the beam the whole time while rotating.

For measurements on the *STOE StadiP* diffractometer, data were collected at RT between  $4^\circ$  and  $80.70^\circ$  in  $2\Theta$  with steps of  $0.01^\circ$  and a measurement time of 5 s/step. For each sample seven such scans were added.

Measurements of the *Huber G670* diffractometer were carried out with the identical increment, but a measurement time of 2 s/step. The measuring time was 60 min.

#### 6.3.1.2 High Resolution Synchrotron Powder Diffraction

High resolution synchrotron powder diffraction measurements were carried out on selected and suitable samples. The respective samples were thoroughly ground and filled about 2 cm high into *Hilgenberg* glass capillaries (diameter of 0.7 to 1.0 mm). To prevent absorption of humidity, glass powder was placed on top of the sample powder. Afterwards, the filled capillaries were sealed with the help of a glow wire and closed airtight with pizine. Samples were adjusted horizontally on a goniometer head in a way that the substance was in the beam the whole time while rotating.

### **ESRF (Grenoble)**

High-resolution synchrotron powder diffraction data of pristine and loaded MOFs were recorded at the *Swiss Norwegian BeamLine* (SNBL, BM01B) at the European Synchrotron (ESRF, Grenoble/France) in 2015 and 2016. The wavelength was calibrated with a Si standard NIST 640c to 0.50561 Å and 0.50447723 Å, respectively. The diffractometer is equipped with five counting channels, delivering five complete patterns collected with a small 1.1 degree offset in  $2\theta$ . A Si(111) analyzer crystal is mounted in front of each NaI scintillator/photomultiplier detector.

Data were collected at 298 K between 1.1° and 25° in  $2\theta$  with steps of 0.002° and 100 ms integration time per data point. Typical recording times were ~20 min per scan. For each sample five scans were added. Data from all detectors and scans were averaged and added to one pattern with local software.

Further data were collected at the SpLine beamline in 2017. The wavelength was calibrated with a Si standard NIST 640c to 0.56383 Å. The diffractometer is equipped with ten single point detectors. Nine of them were employed for measurements delivering nine complete patterns collected with a small 2° offset in  $2\theta$ . A Si(111) analyzer crystal is mounted in front of each NaI scintillator/photomultiplier detector.

Data were collected at 298 K between 1.1° and 25° in  $2\theta$  with steps of 0.002° and 100 ms integration time per data point. Typical recording times were ~20 min per scan. For each sample nine scans were added. Data from all detectors and scans were averaged and added to one pattern with local software.

### **DELTA (Dortmund)**

Additional high resolution diffraction data were recorded at *BL9* at the *Dortmunder Elektronen-Speicherring-Anlage* (DELTA) in 2017. Data were collected at room temperature with a wavelength of 0.49594 Å using a PILATUS100K detector between 2.8° and 25° in  $2\theta$  with steps of 0.01° and 10 s integration time per data point.

## 6.3.2 Composition

### 6.3.2.1 Elemental analysis

Elemental analysis of carbon, hydrogen and nitrogen was carried out with a *HEKAtech GmbH EuroEA 3000* Analyzer at University of Cologne. Approximately 2 mg of each compound was filled into a tin cartridge under argon atmosphere. For each sample three measurements were carried out for better statistics, from which a mean value was calculated. To estimate the dye to MOF/PM ratio the following procedure was applied: as only the guest molecules contain nitrogen, x in dye<sub>x</sub>@MOF/PM was optimized in a way that calculated and found nitrogen contents agree as good as possible.

### 6.3.2.2 X-ray Photoelectron Spectroscopy

For XPS measurements, dye@MOF/PM powders were placed on adhesive copper foil. Measurements were performed in a multi-chamber UHV system at a pressure of  $5 \cdot 10^{-10}$  mbar using a Phoibos 100 hemispherical analyzer (Specs). As excitation source a MgK<sub>α</sub> anode was used ( $h \cdot \nu = 1252.6$  e, probing depth ~10 nm).

Due to charging effects during measurements caused by the low conductivity of the powder samples, the binding energy scale as measured by XPS was shifted to higher values by a few eV for the different samples. To account for this, the binding energies were corrected in a way that adventitious carbon is positioned at 284.8 eV. Integrated peak areas of characteristic core level excitations were used to calculate the embedded amount of dye inside the MOF/PM matrices. For this, the peak areas of N, Zn, In, Ga, and Al were evaluated and corrected by their relative sensitivity factors (RSF)<sup>[233]</sup>.

### 6.3.3 Effects

#### 6.3.3.1 UV/vis Spectroscopy

##### Absorption Spectroscopy

UV/vis spectra of the dye@MOF-systems were recorded using transparent KBr pellets with a *Varian CARY 4000* spectrometer in Nancy, France.

Transparent pellets were prepared as follows: half a spatula of the substance was thoroughly ground with six spatulas of dried KBr. The mixture was pressed for 30 min at a pressure of ~530 bar yielding a thin transparent slightly colored pellet. The KBr pellet was placed into the sample holder and the sample chamber was evacuated to  $10^{-5}$  mbar. Spectra were recorded before and after irradiation with UV light ( $\lambda = 365$  nm). For thermal relaxation, the pellet was placed in a furnace; details of the irradiation and relaxation times as well as applied temperatures are listed for the respective compound in chapter 4.

UV/vis spectra of the different spiropyrans and the spirooxazine dissolved in several solvents were measured on a *Varian Cary50 Scan* photospectrometer.

##### Reflection Spectroscopy

Measurements were carried out with a *Perkin Elmer Lambda 1050* spectrometer. Samples were measured on an adhesive film in the range 250 nm to 750 nm. Data were recorded before and after irradiation with UV light ( $\lambda = 365$  nm, 1 min).

#### 6.3.3.2 IR Spectroscopy

In order to understand the occurring host-guest interactions and to quantify the amount of switching, the different systems were analyzed via IR spectroscopy. Measurements were carried out on a *Nicolet7500* FT-IR-Spectrometer at the *Faculté de Science and Technologies* in Nancy under climated atmosphere. Samples were prepared as follows: half a spatula of substance was thoroughly ground with six spatulas of KBr. Afterwards the mixture was pressed for 30 min at a pressure of ~530 bar yielding a thin and transparent light colored pellet. The pellet was placed into the sample holder. The sample chamber was evacuated to  $10^{-5}$  mbar in order to improve the resulting spectra and for keeping the quality of the pellet high. Scans were done in the range of  $360\text{ cm}^{-1}$  to  $4000\text{ cm}^{-1}$  with a resolution of  $2\text{ cm}^{-1}$  and

90 scans per sample. Backgrounds were measured after every sample replacement to ensure the results being as exact as possible. The samples underwent different irradiation and heating programs. These are listed for the respective compounds in chapter 4.

As the KBr pellet possesses a certain thickness, light penetration is limited. Furthermore, especially as the pellet is very planar and symmetric, interference occurs, which leads to “noise” in the spectra. For quantitative conclusions this has to be taken into account. Furthermore, light penetration is limited by the absorption properties of the merocyanine moiety. Molecules at the surface of the pellet are switched. Due to their high UV absorption, merocyanine molecules inside the pellet don't receive any light and therefore stay in the non-irradiated ground state. To reduce this problem the pellet was irradiated from both sides to ensure an almost complete isomerization.

#### **6.3.3.3 Fluorescence Spectroscopy**

Solid State Fluorescence Spectra of Phth@PM samples were recorded on a *Perkin Elmer LS-50B* Fluorescence Spectrometer. The samples were placed into the sample holder under Argon atmosphere and kept there right before the measurement started. Scans were done in the range of 350 nm to 700 nm with an excitation wavelength of  $\lambda_{\text{ex}} = 347$  nm.

Solid State Fluorescence measurements of SP-Nitro@MOF-5 (**1**) samples were carried out on a *Horiba Jobin Yvon Fluorolog-3* Fluorescence Spectrometer in Siegen. Excitation spectra were corrected for the lamp intensity with respect to a Rhodamine 6G standard and emission spectra were corrected for the sensitivity of the photomultiplier tube.

Liquid State Fluorescence Spectra of the phthalimide were recorded on a *Perkin-Elmer LS-50B* Fluorescence Spectrometer. A concentration of  $10^{-5}$  mol/l was chosen based on the sensitivity of the fluorescence spectrometer's detector.

#### **6.3.3.4 DSC/TGA Measurements**

DSC/TGA measurements were carried out on a *Mettler Toledo TGA/DSC STAR1E* ( $\text{Al}_2\text{O}_3$  crucible; Ar stream with 30 ml/min; heating rate  $10$  °C/min). Samples of approx. 2 - 6 mg

were weighed out and handled under inert conditions (glovebox) to avoid absorption of humidity.

## 6.4 Interpretation of Data

### 6.4.1 JANA2006

To determine the unit cell parameters precisely, *Le Bail* fits in *Jana2006*<sup>[194]</sup> were performed refining the lattice parameters, zero shifts, background (manual background function with 50 points) and profile parameters (TCH profile function with GW and LY as refined parameters). If not stated differently, in all *Le Bail* fits the same set of parameters was used.

As a criterion for the quality of the *Le Bail* fit, values calculated with equation were given for the respective fits.

$$R_P = \frac{\sum_i |y_{o,i} - y_{c,i}|}{\sum_i y_{o,i}} \quad (1)$$

$$wR_P = \sqrt{\frac{\sum_i w_i (y_{o,i} - y_{c,i})^2}{\sum_i w_i (y_{o,i})^2}} \quad (2)$$

$$w_i = \frac{1}{\sigma^2[y_{o,i}]} \quad (3)$$

$$\chi^2 = \frac{1}{N} \frac{\sum_i (y_{c,i} - y_{o,i})^2}{\sigma^2[y_{o,i}]} \quad (4)$$

$$\text{GOF} = \sqrt{\chi^2} \quad (5)$$

$$R_B = \frac{\sum_i |I_o - I_c|}{\sum_i I_o} \quad (6)$$

$y_{o,i}$ : observed intensity at step i,  $y_{c,i}$ : calculated intensity at step i,  $I = mF^2$ ,  $m$ : multiplicity,  $F$ : structure factor,  $w_i$ : weighting,  $N$ : amount of data points,  $\sigma$ : standard deviation.

#### 6.4.2 XPS Peak Fit: Determination of Composition

Analysis and interpretation of XPS data was done with the program *XPSPeakFit42*. On that occasion, the data were fitted using mixed Gaussian/Lorentzian peak shapes and the peak areas. The resulting peak areas were compared to calculate the composition of the guest@MOF systems. For this, the peak intensities were corrected by the relative sensitivity factors.<sup>[233]</sup>

#### 6.4.3 Further programs

Powder diffraction data were edited with the program package *WinXPow*<sup>[234]</sup>. Visualization of all crystal structures was done by the program package *Diamond 4.4*<sup>[173]</sup>. Visualization of X-ray powder diffraction data and the DSC/TGA measurements was done with *Gnuplot*<sup>[235]</sup>. For clarity, all patterns are shown with  $1/d$  instead of  $2\theta$ . Editing and visualization of UV/vis-, IR- and XPS data was done with the program package *Origin8.5*<sup>[236]</sup>. The program package *ChemDraw Professional 15.0* was applied for the visualization of the organic molecules and photo-isomerization processes.

## 7 References

- [1] Y. Hirshberg, *C. R. Hebd. Seances Acad. Sci.* **1950**, *116*, 903–904.
- [2] N. A. Campbell, J. B. Reece, *Biologie*, Pearson Studium, München, **2009**.
- [3] H. Bouas-Laurent, H. Dürr, *Pure Appl. Chem.* **2001**, *73*, 639–665.
- [4] J. Fritzsche, *C. R. Hebd. Seances Acad. Sci.* **1867**, *69*, 1035.
- [5] M. Buchs, C. A. Daul, P. T. Manoharan, C. W. Schlöpfer, *Int. J. Quantum Chem.* **2003**, *91*, 418–431.
- [6] H. Zöllner, W. Krasser, T. Woike, S. Haussühl, *Chem. Phys. Lett.* **1989**, *161*, 497–501.
- [7] S. Haussühl, G. Schetter, T. Woike, *Opt. Commun.* **1995**, *114*, 219–222.
- [8] T. Woike, H. Zöllner, W. Krasser, S. Haussühl, *Solid State Commun.* **1990**, *73*, 149–152.
- [9] D. Schaniel, J. Schefer, B. Delley, M. Imlau, T. Woike, *Phys. Rev. B - Condens. Matter Mater. Phys.* **2002**, *66*, 85103-1-85103–10.
- [10] Z. Tahri, R. Lepski, K.-Y. Hsieh, E.-E. Bendeif, S. Pillet, P. Durand, T. Woike, D. Schaniel, *Phys. Chem. Chem. Phys.* **2012**, *14*, 3775.
- [11] B. Cormary, S. Ladeira, K. Jacob, P. G. Lacroix, T. Woike, D. Schaniel, I. Malfant, *Inorg. Chem.* **2012**, *51*, 7492–7501.
- [12] D. H. Waldeck, *Chem. Rev.* **1991**, *91*, 415–436.
- [13] G. S. Hartley, *Nature* **1937**, *140*, 281–281.
- [14] G. S. Hartley, *J. Chem. Soc.* **1938**, 633–642.
- [15] J. M. Robertson, *J. Chem. Soc.* **1939**, *0*, 232.
- [16] E. Fischer, Y. Hirshberg, *J. Chem. Soc.* **1952**, 4522–4524.
- [17] O. Chaudé, R. Rumpf, *C. R. Hebd. Seances Acad. Sci.* **1953**, *236*, 697–699.

- [18] G. Berkovic, V. Krongauz, V. Weiss, *Chem. Rev.* **2000**, *100*, 1741–1754.
- [19] M. Irie, *Chem. Rev.* **2000**, *100*, 1685–1716.
- [20] Y. Yokoyama, *Chem. Rev.* **2000**, *100*, 1717–1739.
- [21] R. N. Macnair, *Photochem. Photobiol.* **1967**, *6*, 779–797.
- [22] H. Kamogawa, T. Masui, S. Amemiya, *J. Polym. Sci. Polym. Chem. Ed.* **1984**, *22*, 383–390.
- [23] E. Hadjoudis, I. M. Mavridis, T. Dziembowska, Z. Rozwadowski, R. Anulewicz, *Mol. Eng.* **1998**, *8*, 97–104.
- [24] M. Irie, *Photochem. Photobiol. Sci.* **2010**, *9*, 1535–1542.
- [25] D. Hermann, H. A. Schwartz, U. Ruschewitz, *ChemistrySelect* **2017**, *2*, 11846–11852.
- [26] M. Natali, S. Giordani, *Chem. Soc. Rev.* **2012**, *41*, 4010–4029.
- [27] D. A. Parthenopoulos, P. M. Rentzepis, *Science* **1989**, *245*, 843–845.
- [28] F. Zhao, A. Bonasera, U. Nöchel, M. Behl, D. Bléger, *Macromol. Rapid Commun.* **2018**, *39*, 1700527-1-1700527-5.
- [29] D. Bléger, *Macromol. Chem. Phys.* **2016**, *217*, 189–198.
- [30] C.-L. Lee, T. Liebig, S. Hecht, D. Bléger, J. P. Rabe, *ACS Nano* **2014**, *8*, 11987–11993.
- [31] K. Kumar, C. Knie, D. Bléger, M. A. Peletier, H. Friedrich, S. Hecht, D. J. Broer, M. G. Debije, A. P. H. J. Schenning, *Nat. Commun.* **2016**, *7*, 11975.
- [32] N. Koumura, R. W. J. Zijlstra, R. A. van Delden, N. Harada, B. L. Feringa, *Nature* **1999**, *401*, 152–155.
- [33] M. Moniruzzaman, C. J. Sabey, G. F. Fernando, *Polymer (Guildf)*. **2007**, *48*, 255–263.
- [34] N. W. Tyer, R. S. Becker, *J. Am. Chem. Soc.* **1970**, *92*, 1289–1294.
- [35] H. Görner, *Phys. Chem. Chem. Phys.* **2001**, *3*, 416–423.

- [36] S. A. Krysanov, M. V. Alfimov, *Chem. Phys. Lett.* **1982**, *91*, 77–80.
- [37] Z. Tian, W. Wu, W. Wan, A. D. Q. Li, *J. Am. Chem. Soc.* **2011**, *133*, 16092–16100.
- [38] J. T. C. Wojtyk, A. Wasey, P. M. Kazmaier, S. Hoz, Erwin Buncel, *J. Phys. Chem. A* **2000**, *104*, 9046–9055.
- [39] W. Fuß, C. Kosmidis, W. E. Schmid, S. A. Trushin, *Angew.Chem.Int. Ed.* **2004**, *43*, 4178–4182.
- [40] J. Henzl, M. Mehlhorn, H. Gawronski, K.-H. Rieder, K. Morgenstern, *Angew.Chem.Int. Ed.* **2006**, *45*, 603–606.
- [41] M. Irie, A. Menju, K. Hayashi, *Macromolecules* **1979**, *12*, 1176–1180.
- [42] C. Lenoble, R. S. Becker, *J. Phys. Chem.* **1986**, *90*, 62–65.
- [43] S. M. Aldoshin, *Russ. Chem. Rev.* **1990**, *59*, 663–684.
- [44] N. P. Ernsting, T. Arthen-Engeland, *J. Phys. Chem.* **1991**, *95*, 5502–5509.
- [45] K. Patel, A. Castillo-Muzquiz, M. C. Biewer, *Tetrahedron Lett.* **2002**, *43*, 5933–5935.
- [46] L. Florea, A. Hennart, D. Diamond, F. Benito-Lopez, *Sensors Actuators B Chem.* **2012**, *175*, 92–99.
- [47] L. Florea, A. McKeon, D. Diamond, F. Benito-Lopez, *Langmuir* **2013**, *29*, 2790–2797.
- [48] M. Levitus, G. Glasser, D. Neher, P. F. Aramendía, *Chem. Phys. Lett.* **1997**, *277*, 118–124.
- [49] M. Bletz, U. Pfeifer-Fukumura, U. Kolb, W. Baumann, *J. Phys. Chem. A* **2002**, *106*, 2232–2236.
- [50] J. Chen, F. Zeng, S. Wu, *ChemPhysChem* **2010**, *11*, 1036–1043.
- [51] A. A. García, S. Cherian, J. Park, D. Gust, F. Jahnke, R. Rosario, *J. Phys. Chem. A* **2000**, *104*, 6103–6107.
- [52] V. A. Krongauz, E. S. Goldburt, *Nature* **1978**, *271*, 43–45.

- [53] T. Seki, K. Ichimura, E. Ando, *Langmuir* **1988**, *4*, 1068–1069.
- [54] H. Tachibana, Y. Yamanaka, H. Sakai, M. Abe, M. Matsumoto, *J. Lumin.* **2000**, *87–89*, 800–802.
- [55] P. Uznanski, *Synth. Met.* **2000**, *109*, 281–285.
- [56] Y. Unuma, A. Miyata, *Thin Solid Films* **1989**, *179*, 497–502.
- [57] E. Ando, J. Miyazaki, K. Morimoto, H. Nakahara, K. Fukuda, *Thin Solid Films* **1985**, *133*, 21–28.
- [58] I. Cabrera, V. Krongauz, *Macromolecules* **1987**, *20*, 2713–2717.
- [59] E. Goldburt, V. Krongauz, *Macromolecules* **1986**, *19*, 246–247.
- [60] E. Goldburt, F. Shvartsman, S. Fishman, V. Krongauz, *Macromolecules* **1984**, *17*, 1225–1230.
- [61] G. Favaro, F. Masetti, U. Mazzucato, G. Ottavi, P. Allegrini, V. Malatesta, *J. Chem. Soc. Faraday Trans.* **1994**, *90*, 333.
- [62] P. Tardieu, R. Dubest, J. Aubard, A. Kellmann, F. Tfibel, A. Samat, R. Gugliemetti, *Helv. Chim. Acta* **1992**, *75*, 1185–1197.
- [63] M. Sakuragi, K. Aoki, T. Tamaki, K. Ichimura, *Bull. Chem. Soc. Jpn.* **1990**, *63*, 74–79.
- [64] J. Whelan, J. T. C. Wojtyk, E. Buncel, *Chem. Mater.* **2008**, *20*, 3797–3799.
- [65] A. Radu, R. Byrne, N. Alhashimy, M. Fusaro, S. Scarmagnani, D. Diamond, *J. Photochem. Photobiol. A Chem.* **2009**, *206*, 109–115.
- [66] J. D. Winkler, K. Deshayes, B. Shao, *J. Am. Chem. Soc.* **1989**, *111*, 769–770.
- [67] M. Inouye, Y. Noguchi, K. Isagawa, *Angew. Chemie Int. Ed. English* **1994**, *33*, 1163–1166.
- [68] J. D. Winkler, Corinne M. Bowen, V. Michelet, *J. Am. Chem. Soc.* **1998**, *120*, 3237–3242.

- [69] J. T. C. Wojtyk, P. M. Kazmaier, E. Buncel, *Chem. Mater.* **2001**, *13*, 2547–2551.
- [70] M. Tanaka, M. Nakamura, M. A. A. Salhin, T. Ikeda, K. Kamada, H. Ando, Y. Shibutani, K. Kimura, *J. Org. Chem.* **2001**, *66*, 1533–1537.
- [71] M. Tanaka, T. Ikeda, Q. Xu, H. Ando, Y. Shibutani, M. Nakamura, H. Sakamoto, S. Yajima, K. Kimura, *J. Org. Chem.* **2002**, *67*, 2223–2227.
- [72] Roni A. Kopelman, S. M. Snyder, N. L. Frank, *J. Am. Chem. Soc.* **2003**, *125*, 13684–13685.
- [73] X. Guo, D. Zhang, G. Zhang, D. Zhu, *J. Phys. Chem. B* **2004**, *108*, 11942–11945.
- [74] C. Zhang, Z. Zhang, M. Fan, W. Yan, *Dye. Pigment.* **2008**, *76*, 832–835.
- [75] J. Tao, Y. Li, P. Zhao, J. Li, Y. Duan, W. Zhao, R. Yang, *Biosens. Bioelectron.* **2014**, *62*, 151–157.
- [76] X. Guo, D. Zhang, H. Tao, D. Zhu, *Org. Lett.* **2004**, *6*, 2491–2494.
- [77] I. Shimizu, H. Kokado, E. Inoue, *Bull. Chem. Soc. Jpn.* **1969**, *42*, 1726–1729.
- [78] I. Shimizu, H. Kokado, E. Inoue, *Bull. Chem. Soc. Jpn.* **1969**, *42*, 1730–1734.
- [79] S. Schneider, H. Grau, J. Ringer, *Mol. Cryst. Liq. Cryst. Sci. Technol. Sect. A. Mol. Cryst. Liq. Cryst.* **1994**, *246*, 267–274.
- [80] C. Roxburgh, *Dye. Pigment.* **1995**, *27*, 63–69.
- [81] E. B. Gaeva, V. Pimienta, S. Delbaere, A. V. Metelitsa, N. A. Voloshin, V. I. Minkin, G. Vermeersch, J. C. Micheau, *J. Photochem. Photobiol. A Chem.* **2007**, *191*, 114–121.
- [82] A. Sugahara, N. Tanaka, A. Okazawa, N. Matsushita, N. Kojima, *Chem. Lett.* **2014**, *43*, 281–283.
- [83] Y. Ito, N. Sugimura, O. H. Kwon, Y. Imanishi, *Nat. Biotechnol.* **1999**, *17*, 73–75.
- [84] E. A. Osborne, B. R. Jarrett, C. Tu, A. Y. Louie, *J. Am. Chem. Soc.* **2010**, *132*, 5934–5935.

- [85] X. Wang, J. Hu, G. Liu, J. Tian, H. Wang, M. Gong, S. Liu, *J. Am. Chem. Soc.* **2015**, *137*, 15262–15275.
- [86] A. Doron, E. Katz, G. Tao, I. Willner, *Langmuir* **1997**, *13*, 1783–1790.
- [87] C. Reichardt, *Solvents and Solvent Effects in Organic Chemistry*, WILEY VCH Verlag GmbH, Weinheim, **2003**.
- [88] S. Dähne, *Chimia (Aarau)*. **1991**, *45*, 288–296.
- [89] S. Dähne, *Zeitschrift für Chemie* **2010**, *5*, 441–451.
- [90] J. Fabian, H. Hartman, *J. Mol. Struct.* **1975**, *27*, 67–78.
- [91] S. Dähne, D. Leupold, H. E. Nikolajewski, R. Radeaglia, *Zeitschrift für Naturforsch. B* **1965**, *20*, 1006–1007.
- [92] R. Radeaglia, S. Dähne, *J. Mol. Struct.* **1970**, *5*, 399–411.
- [93] J. E. Brady, P. W. Carr, *J. Phys. Chem.* **1985**, *89*, 5759–5766.
- [94] B. S. Brunshwig, S. Ehrenson, N. Sutin, *J. Phys. Chem.* **1987**, *91*, 4714–4723.
- [95] N. S. Bayliss, E. G. McRae, *J. Phys. Chem.* **1954**, *58*, 1002–1006.
- [96] E. U. Condon, *Phys. Rev.* **1928**, *32*, 858–872.
- [97] J. Franck, E. G. Dymond, *Trans. Faraday Soc.* **1926**, *21*, 536–542.
- [98] S. Scarmagnani, *PhD Thesis*, University Of Dublin, **2010**.
- [99] R. Klajn, *Chem. Soc. Rev.* **2014**, *43*, 148–184.
- [100] A. V. Metelitsa, V. Lokshin, J. C. Micheau, A. Samat, R. Guglielmetti, V. I. Minkin, *Phys. Chem. Chem. Phys.* **2002**, *4*, 4340–4345.
- [101] C. Li, Y. Zhang, J. Hu, J. Cheng, S. Liu, *Angew. Chem. Int. Ed.* **2010**, *49*, 5120–5124.
- [102] B. Liao, P. Long, B. He, S. Yi, B. Ou, S. Shen, J. Chen, *J. Mater. Chem. C* **2013**, *1*, 3716–3721.

- [103] J. Chen, F. Zeng, S. Wu, J. Zhao, Q. Chen, Z. Tong, *Chem. Commun.* **2008**, *13*, 5580–5582.
- [104] L. Zhu, M.-Q. Zhu, J. K. Hurst, A. D. Q. Li, *J. Am. Chem. Soc.* **2005**, *127*, 8968–8970.
- [105] D.-J. Chung, Y. Ito, Y. Imanishi, *J. Appl. Polym. Sci.* **1994**, *51*, 2027–2033.
- [106] H. R. Allcock, C. Kim, *Macromolecules* **1991**, *24*, 2846–2851.
- [107] Y. J. Oh, J. A. Nam, A. Al-Nahain, S. Lee, I. In, S. Y. Park, *Macromol. Rapid Commun.* **2012**, *33*, 1958–1963.
- [108] P. K. Kundu, G. L. Olsen, V. Kiss, R. Klajn, *Nat. Commun.* **2014**, *5*, 1–9.
- [109] D. Samanta, D. Galaktionova, J. Gemen, L. J. W. Shimon, Y. Diskin-Posner, L. Avram, P. Král, R. Klajn, *Nat. Commun.* **2018**, *9*, 1–9.
- [110] F. Marlow, K. Hoffmann, J. Caro, *Adv. Mater.* **1997**, *9*, 567–570.
- [111] K. Weh, M. Noack, K. Hoffmann, K.-P. Schröder, J. Caro, *Microporous Mesoporous Mater.* **2002**, *54*, 15–26.
- [112] K. Hoffmann, U. Resch-Genger, F. Marlow, *Microporous Mesoporous Mater.* **2000**, *41*, 99–106.
- [113] I. Casades, M. Alvaro, H. García, M. N. Pillai, *Photochem. Photobiol. Sci.* **2002**, *1*, 219–223.
- [114] I. Casades, S. Constantine, D. Cardin, H. García, A. Gilbert, F. Márquez, *Tetrahedron* **2000**, *56*, 6951–6956.
- [115] C. Schomburg, M. Wark, Y. Rohlfing, G. Schulz-Ekloff, D. Wöhrle, *J. Mater. Chem.* **2001**, *11*, 2014–2021.
- [116] H. Li, M. Eddaoudi, M. O’Keeffe, O. M. Yaghi, *Nature* **1999**, *402*, 276–279.
- [117] J.-C. Tan, B. Civalieri, *CrystEngComm* **2015**, *17*, 197–198.
- [118] S. R. Batten, N. R. Champness, X.-M. Chen, J. Garcia-Martinez, S. Kitagawa, L. Öhrström, M. O’Keeffe, M. P. Suh, J. Reedijk, *Pure Appl. Chem* **2013**, *85*, 1715–

1724.

- [119] B. F. Abrahams, B. F. Hoskins, D. M. Michail, R. Robson, *Nature* **1994**, *369*, 727–729.
- [120] B. F. Hoskins, R. Robson, *J. Am. Chem. Soc.* **1989**, *111*, 5962–5964.
- [121] H. Li, M. Eddaoudi, A. Thomas L. Groy, O. M. Yaghi, *J. Am. Chem. Soc.* **1998**, *120*, 8571–8572.
- [122] M. Kondo, T. Yoshitomi, H. Matsuzaka, S. Kitagawa, K. Seki, *Angew. Chemie Int. Ed. English* **1997**, *36*, 1725–1727.
- [123] C. Ninclaus, C. Serre, D. Riou, G. Férey, *C. R. Acad. Sci., Ser. IIC Chim.* **1998**, *1*, 551–556.
- [124] C. Zlotea, R. Campesi, F. Cuevas, E. Leroy, P. Dibandjo, C. Volkringer, T. Loiseau, G. Férey, M. Latroche, *J. Am. Chem. Soc.* **2010**, *132*, 2991–2997.
- [125] M. P. Suh, H. J. Park, T. K. Prasad, D.-W. Lim, *Chem. Rev.* **2012**, *112*, 782–835.
- [126] H. Wu, R. S. Reali, D. A. Smith, M. C. Trachtenberg, J. Li, *Chem. Eur. J.* **2010**, *16*, 13951–13954.
- [127] J.-R. Li, J. Sculley, H.-C. Zhou, *Chem. Rev.* **2012**, *112*, 869–932.
- [128] L. Alaerts, M. Maes, L. Giebeler, P. A. Jacobs, J. A. Martens, J. F. M. Denayer, C. E. A. Kirschhock, D. E. De Vos, *J. Am. Chem. Soc.* **2008**, *130*, 14170–14178.
- [129] M. Maes, F. Vermoortele, L. Alaerts, S. Couck, C. E. A. Kirschhock, J. F. M. Denayer, D. E. De Vos, *J. Am. Chem. Soc.* **2010**, *132*, 15277–15285.
- [130] J. Lee, O. K. Farha, J. Roberts, K. A. Scheidt, S. T. Nguyen, J. T. Hupp, *Chem. Soc. Rev.* **2009**, *38*, 1450–1459.
- [131] P. Horcajada, T. Chalati, C. Serre, B. Gillet, C. Sebrie, T. Baati, J. F. Eubank, D. Heurtaux, P. Clayette, C. Kreuz, et al., *Nat. Mater.* **2010**, *9*, 172–178.
- [132] P. Horcajada, C. Serre, M. Vallet-Regí, M. Sebban, F. Taulelle, G. Férey, *Angew. Chem. Int. Ed.* **2006**, *45*, 5974–5978.

- [133] V. Stavila, A. A. Talin, M. D. Allendorf, *Chem. Soc. Rev.* **2014**, 5994–6010.
- [134] M. D. Allendorf, A. Schwartzberg, V. Stavila, A. A. Talin, *Chem. Eur. J.* **2011**, *17*, 11372–11388.
- [135] Y. Inokuma, T. Arai, M. Fujita, *Nat. Chem.* **2010**, *2*, 780–783.
- [136] R. Brkljača, B. Schneider, W. Hidalgo, F. Otálvaro, F. Ospina, S. Lee, M. Hoshino, M. Fujita, S. Urban, *Molecules* **2017**, *22*, 211.
- [137] S. Lee, M. Hoshino, M. Fujita, S. Urban, *Chem. Sci.* **2017**, *8*, 1547–1550.
- [138] Y. Inokuma, K. Matsumura, S. Yoshioka, M. Fujita, *Chem. - An Asian J.* **2017**, *12*, 208–211.
- [139] N. Zigon, T. Kikuchi, J. Ariyoshi, Y. Inokuma, M. Fujita, *Chem. - An Asian J.* **2017**, *12*, 1057–1061.
- [140] F. Sakurai, A. Khutia, T. Kikuchi, M. Fujita, *Chem. Eur. J.* **2017**, *23*, 15035–15040.
- [141] M. Hoshino, A. Khutia, H. Xing, Y. Inokuma, M. Fujita, *IUCrJ* **2016**, *3*, 139–151.
- [142] Y. Inokuma, S. Yoshioka, J. Ariyoshi, T. Arai, Y. Hitora, K. Takada, S. Matsunaga, K. Rissanen, M. Fujita, *Nature* **2013**, *495*, 461–466.
- [143] M. Eddaoudi, J. Kim, N. Rosi, D. Vodak, J. Wachter, M. O’Keeffe, O. M. Yaghi, *Science* **2002**, *295*, 469–472.
- [144] H. Deng, S. Grunder, K. E. Cordova, C. Valente, H. Furukawa, M. Hmadeh, F. Gandara, A. C. Whalley, Z. Liu, S. Asahina, et al., *Science* **2012**, *336*, 1018–1023.
- [145] A. Schaate, P. Roy, T. Preusse, S. J. Lohmeier, A. Godt, P. Behrens, *Chem. Eur. J.* **2011**, *17*, 9320–9325.
- [146] S. Castellanos, F. Kapteijn, J. Gascon, *CrystEngComm* **2016**, *18*, 4006–4012.
- [147] A. Schaate, S. Dühren, G. Platz, S. Lilienthal, A. M. Schneider, P. Behrens, *Eur. J. Inorg. Chem.* **2012**, *2012*, 790–796.
- [148] C. C. Epley, K. L. Roth, S. Lin, S. R. Ahrenholtz, T. Z. Grove, A. J. Morris, *Dalt.*

- Trans.* **2017**, *46*, 4917–4922.
- [149] J. Zhang, L. Wang, N. Li, J. Liu, W. Zhang, Z. Zhang, N. Zhou, X. Zhu, *CrystEngComm* **2014**, *16*, 6547–6551.
- [150] A. Modrow, D. Zargarani, R. Herges, N. Stock, *Dalt. Trans.* **2011**, *40*, 4217.
- [151] J. Park, D. Yuan, K. T. Pham, J.-R. Li, A. Yakovenko, H.-C. Zhou, *J. Am. Chem. Soc.* **2012**, *134*, 99–102.
- [152] X. Yu, Z. Wang, M. Buchholz, N. Füllgrabe, S. Grosjean, F. Bebensee, S. Bräse, C. Wöll, L. Heinke, *Phys. Chem. Chem. Phys.* **2015**, *17*, 22721–22725.
- [153] A. Modrow, D. Zargarani, R. Herges, N. Stock, *Dalt. Trans.* **2012**, *41*, 8690.
- [154] L. Heinke, M. Cakici, M. Dommaschk, S. Grosjean, R. Herges, S. Bräse, C. Wöll, *ACS Nano* **2014**, *8*, 1463–1467.
- [155] L. Heinke, *J. Phys. D. Appl. Phys.* **2017**, *50*, 193004.
- [156] Z. Wang, A. Knebel, S. Grosjean, D. Wagner, S. Bräse, C. Wöll, J. Caro, L. Heinke, *Nat. Commun.* **2016**, *7*, 13872.
- [157] K. Müller, J. Helfferich, F. Zhao, R. Verma, A. B. Kanj, V. Meded, D. Bléger, W. Wenzel, L. Heinke, *Adv. Mater.* **2018**, 1706551.
- [158] Z. Wang, L. Heinke, J. Jelic, M. Cakici, M. Dommaschk, R. J. Maurer, H. Oberhofer, S. Grosjean, R. Herges, S. Bräse, et al., *Phys. Chem. Chem. Phys.* **2015**, *17*, 14582–14587.
- [159] K. Ohara, Y. Inokuma, M. Fujita, *Angew.Chem.Int. Ed.* **2010**, *49*, 5507–5509.
- [160] D. N. Dybtsev, H. Chun, K. Kim, *Angew.Chem.Int. Ed.* **2004**, *43*, 5033–5036.
- [161] N. Yanai, T. Uemura, M. Inoue, R. Matsuda, T. Fukushima, M. Tsujimoto, S. Isoda, S. Kitagawa, *J. Am. Chem. Soc.* **2012**, *134*, 4501–4504.
- [162] T. Uemura, G. Washino, N. Yanai, S. Kitagawa, *Chem. Lett.* **2013**, *42*, 222–223.
- [163] D. Hermann, H. Emerich, R. Lepski, D. Schaniel, U. Ruschewitz, *Inorg. Chem.* **2013**,

52, 2744–2749.

- [164] D. Hermann, *PhD Thesis*, University of Cologne, **2013**.
- [165] C. Volkringer, M. Meddouri, T. Loiseau, N. Guillou, J. Marrot, G. Férey, M. Haouas, F. Taulelle, N. Audebrand, M. Latroche, *Inorg. Chem.* **2008**, *47*, 11892–11901.
- [166] T. Loiseau, C. Serre, C. Huguenard, G. Fink, F. Taulelle, M. Henry, T. Bataille, G. Férey, *Chem. Eur. J.* **2004**, *10*, 1373–1382.
- [167] C. Volkringer, T. Loiseau, N. Guillou, G. Férey, E. Elkaïm, A. Vimont, *Dalton Trans.* **2009**, *53*, 2241–2249.
- [168] I. M. Walton, J. M. Cox, J. A. Coppin, C. M. Linderman, D. G. (Dan) Patel, J. B. Benedict, H. Ren, G. Zhu, *Chem. Commun.* **2013**, *49*, 8012–8014.
- [169] A. Knebel, L. Sundermann, A. Mohmeyer, I. Strauß, S. Friebe, P. Behrens, J. Caro, *Chem. Mater.* **2017**, *29*, 3111–3117.
- [170] K. Müller, J. Wadhwa, J. Singh Malhi, L. Schöttner, A. Welle, H. Schwartz, D. Hermann, U. Ruschewitz, L. Heinke, *Chem. Commun.* **2017**, *53*, 8070–8073.
- [171] F. Zhang, X. Zou, W. Feng, X. Zhao, X. Jing, F. Sun, H. Ren, G. Zhu, *J. Mater. Chem.* **2012**, *22*, 25019–25026.
- [172] H. A. Schwartz, *Staatsexamensarbeit*, University of Cologne, **2014**.
- [173] K. Brandenburg, *Diamond 4.4*, Crystal Impact GbR, Bonn, **2017**.
- [174] D. J. Tranchemontagne, J. R. Hunt, O. M. Yaghi, *Tetrahedron* **2008**, *64*, 8553–8557.
- [175] W. Clegg, N. C. Norman, T. Flood, L. Sallans, W. S. Kwak, P. L. Kwiatkowski, J. G. Lasch, *Acta Crystallogr. Sect. C Cryst. Struct. Commun.* **1991**, *47*, 817–824.
- [176] F. Millange, C. Serre, N. Guillou, G. Férey, R. I. Walton, *Angew. Chem. Int. Ed.* **2008**, *47*, 4100–4105.
- [177] T. Devic, F. Salles, S. Bourrelly, B. Moulin, G. Maurin, P. Horcajada, C. Serre, A. Vimont, J.-C. Lavalley, H. Leclerc, et al., *J. Mater. Chem.* **2012**, *22*, 10266.

- [178] J. P. S. Mowat, V. R. Seymour, J. M. Griffin, S. P. Thompson, A. M. Z. Slawin, D. Fairen-Jimenez, T. Düren, S. E. Ashbrook, P. A. Wright, *Dalt. Trans.* **2012**, *41*, 3937–3941.
- [179] C. Serre, F. Millange, C. Thouvenot, M. Noguès, G. Marsolier, D. Louër, G. Férey, *J. Am. Chem. Soc.* **2002**, *124*, 13519.
- [180] G. Férey, *Chem. Soc. Rev.* **2008**, *37*, 191–214.
- [181] S. S.-Y. Chui, S. M.-F. Lo, J. P. H. Charmant, A. G. Orpen, I. D. Williams, *Science* **1999**, *283*, 1148–50.
- [182] G. Majano, J. Pérez-Ramírez, *Adv. Mater.* **2013**, *25*, 1052–1057.
- [183] G. Férey, C. Mellot-Draznieks, C. Serre, F. Millange, J. Dutour, S. Surblé, I. Margiolaki, G. Férey, *Science* **2005**, *309*, 2040–2042.
- [184] T. Zhao, F. Jeremias, I. Boldog, B. Nguyen, S. K. Henninger, C. Janiak, *Dalt. Trans.* **2015**, *44*, 16791–16801.
- [185] C. P. Krap, R. Newby, A. Dhakshinamoorthy, H. García, I. Cebula, T. L. Easun, M. Savage, J. E. Eyley, S. Gao, A. J. Blake, et al., *Inorg. Chem.* **2016**, *55*, 1076–1088.
- [186] C. Stastny, *PhD Thesis*, University, **2018**.
- [187] J. Scherzer, *Catal. Rev.* **1989**, *31*, 215–354.
- [188] D. W. Breck, *Crystalline Zeolite Y*, **1964**, U.S. Patent 3130007.
- [189] J. A. Hriljac, M. M. Eddy, A. K. Cheetham, J. A. Donohue, G. J. Ray, *J. Solid State Chem.* **1993**, *106*, 66–72.
- [190] J. Scherzer, in *Catal. Mater. Relatsh. Between Struct. React.*, ACS Symposium Series, **1984**, pp. 157–200.
- [191] Y. Sheng, J. Leszczynski, A. A. Garcia, R. Rosario, D. Gust, J. Springer, *J. Phys. Chem. B* **2004**, *108*, 16233–16243.
- [192] J. B. Flannery, *J. Am. Chem. Soc.* **1968**, *90*, 5660–5671.

- [193] L. R. Snyder, *High Performance Liquid Chromatography*, Academic Press, New York, **1983**.
- [194] V. Petriček, M. Dušek, L. Palatinus, *Jana2006: The Crystallographic Computing System*, Institute Of Physics, Praha: The Czech Republic, **2006**.
- [195] G. Arnold, C. Schiele, *Zeitschrift für Naturforsch. B* **1967**, *22*, 1228–1230.
- [196] Y. Futami, M. L. S. Chin, S. Kudoh, M. Takayanagi, M. Nakata, *Chem. Phys. Lett.* **2003**, *370*, 460–468.
- [197] L. L. Gladkov, Y. D. Khamchukov, I. Y. Sychev, A. V. Lyubimov, *J. Appl. Spectrosc.* **2012**, *79*, 31–37.
- [198] G. Arnold, G. Paal, *Tetrahedron* **1971**, *27*, 1699–1713.
- [199] M. Hesse, H. Meyer, B. Zeeh, *Spektroskopische Methoden in Der Organischen Chemie*, Georg Thieme Verlag, Stuttgart, **2002**.
- [200] R. Gautron, *Bull. Soc. Chim. Fr.* **1968**, 3190–3200.
- [201] M. Suchý, P. Kutschy, K. Monde, H. Goto, N. Harada, M. Takasugi, Milan Dzurilla, E. Balentová, *J. Org. Chem.* **2001**, *66*, 3940–3947.
- [202] K. Pfoertner, K. Bernauer, *Helv. Chim. Acta* **1968**, *51*, 1787–1794.
- [203] J. Yang, A. Grzech, F. M. Mulder, T. J. Dingemans, *Chem. Commun. Chem. Commun* **2011**, *47*, 5244–5246.
- [204] R. V. Tyurin, B. S. Lukyanov, A. V. Chernyshev, V. I. Malay, A. S. Kozlenko, N. S. Tkacheva, O. N. Burov, M. B. Lukyanova, *Dokl. Chem.* **2016**, *470*, 268–273.
- [205] V. Lokshin, A. Samat, A. V. Metelitsa, *Russ. Chem. Rev.* **2002**, *71*, 893–916.
- [206] F. Maurel, J. Aubard, M. Rajzmann, R. Guglielmetti, A. Samat, *J. Chem. Soc. Perkin Trans. 2* **2002**, *0*, 1307–1315.
- [207] T. Horii, Y. Abe, R. Nakao, *J. Photochem. Photobiol. A Chem.* **2001**, *144*, 119–129.
- [208] N. Tyutyulkov, J. Fabian, A. Mehlhorn, F. Dietz, A. Tadjer, *Polymethine Dyes -*

*Structure and Properties*, St. Kliment Ohridski University Press, Sofia, **1991**.

- [209] A. A. Ishchenko, *Constitution and Spectral-Luminescent Properties of Polymethine Dyes*, Naukova Dumka, Kiev, **1994**.
- [210] B. Valeur, *Molecular Fluorescence - Principles and Applications*, **2001**.
- [211] W. Schmidt, *Optische Spektroskopie*, WILEY VCH Verlag GmbH, Weinheim, **2000**.
- [212] A. K. Sharma, S. G. Schulman, *Introduction to Fluorescence Spectroscopy*, WILEY VCH Verlag GmbH, Chirchester, **1999**.
- [213] O. S. Wolfbeis, *Fluorescence Spectroscopy – New Methods and Applications*, Springer, Berlin, **1992**.
- [214] G. Van der Zwan, J. T. Hynes, *J. Phys. Chem.* **1985**, *89*, 4181–4188.
- [215] E. M. Kosower, H. Kanety, H. Dodiuk, G. Striker, T. Jovin, H. Boni, D. Huppert, *J. Phys. Chem.* **1983**, *87*, 2479–2484.
- [216] E. M. Kosower, *J. Am. Chem. Soc.* **1985**, *107*, 1114–1118.
- [217] P. Suppan, N. Gonheim, *Solvatochromism*, Royal Society Of Chemistry, Cambridge, **1997**.
- [218] E. Lippert, W. Lüder, F. Moll, W. Nägele, H. Boos, H. Prigge, I. Seibold-Blankenstein, *Angew. Chemie* **1961**, *73*, 695–706.
- [219] B. Valeur, *Molecular Fluorescence - Principles and Applications*, **2001**.
- [220] H. Langhals, *Tetrahedron* **1987**, *43*, 1771–1774.
- [221] P. Suppan, *J. Chem. Soc. Faraday Trans. 1 Phys. Chem. Condens. Phases* **1987**, *83*, 495.
- [222] T. Soujanya, R. W. Fessenden, A. Samanta, *J. Phys. Chem.* **1996**, *100*, 3507–3512.
- [223] D. E. Wetzler, C. Chesta, R. Fernández-Prini, P. F. Aramendía, *Pure Appl. Chem.* **2001**, *73*, 405–409.

- [224] Bruker Corporation, *TOPAS, Version 5, Billerica* **2014**.
- [225] C. Yang, U. Kaipa, Q. Z. Mather, X. Wang, V. Nesterov, A. F. Venero, M. A. Omary, *J. Am. Chem. Soc.* **2011**, *133*, 18094–18097.
- [226] R. Krämer, *Angew.Chem.Int. Ed.* **1998**, *37*, 772–773.
- [227] J. L. Mass, J. M. Burlitch, D. E. Budil, J. H. Freed, D. B. Barber, C. R. Pollock, M. Higuchi, R. Dieckmann, *Chem. Mater.* **1995**, *7*, 1008–1014.
- [228] K. Peikert, F. Hoffmann, M. Fröba, *CrystEngComm* **2015**, *17*, 353–360.
- [229] J. Krautwurst, *PhD Thesis*, University Of Cologne, **2017**.
- [230] J. Catalán, V. López, P. Pérez, R. Martin-Villamil, J.-G. Rodríguez, *Liebigs Ann.* **1995**, *1995*, 241–252.
- [231] M. Atar, *PhD Thesis*, University of Cologne, **2018**.
- [232] *Celsius 2005 Version 6.1*, Memmert GmbH&CoKG, Schwabach, **2005**.
- [233] J. H. Scofield, *J. Electron Spectros. Relat. Phenomena* **1976**, *8*, 129–137.
- [234] *STOE WinXPow Version 3.01.03*, STOE & Cie GmbH, Darmstadt, **2009**.
- [235] T. Williams, C. Kelley, R. Lang, *Gnuplot 4.6*, **2012**.
- [236] OriginLab Corporation, *OriginPro 8.50G*, MA 01060 USA, Northhampton, **2010**.



## 8 Supplement

For a better overview, figures and tables are listed according to the synthesized compounds (host materials and dye@MOF/PM, respectively).

### 8.1 Host Materials

#### MOF-5

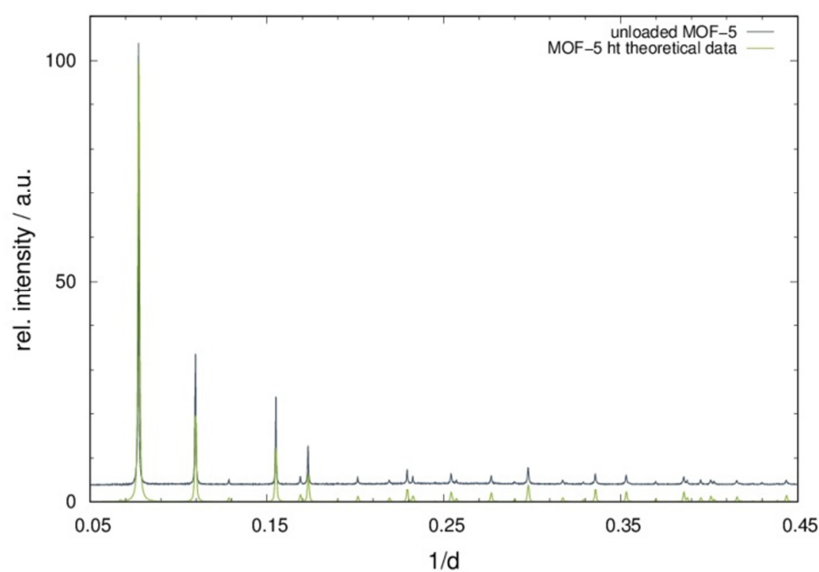


**Figure 8.1.1** XRPD pattern of unloaded MOF-5 (blue-grey), measured at 298 K (BM01B/ESRF:  $\lambda = 0.504477 \text{ \AA}$ ) in comparison to theoretical data of MOF-5 (green). A small offset along  $y$  (+ 4%) was applied in order to enhance readability.

## HKUST-1

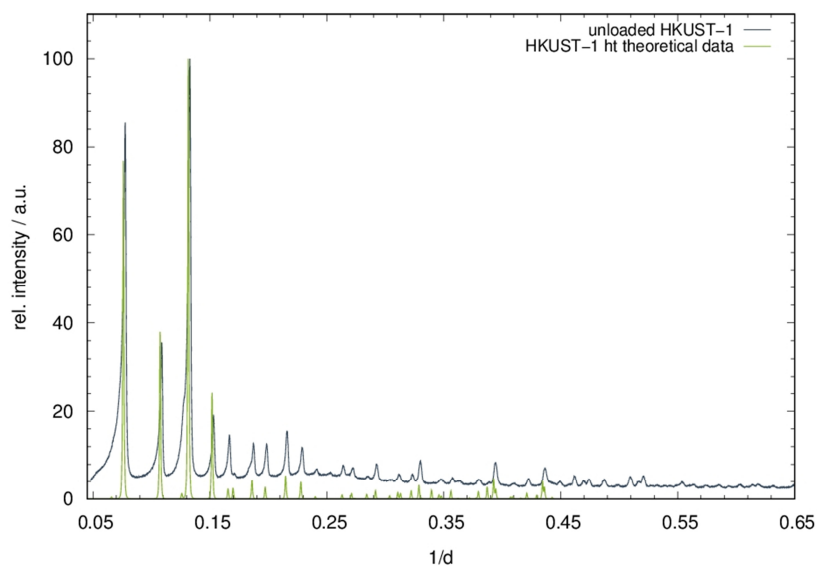


**Figure 8.1.2** XRPD pattern of unloaded HKUST-1 (blue-grey), measured at 298 K (*Stoe Stadi P*;  $\lambda = 1.54 \text{ \AA}$ ) in comparison to theoretical data of HKUST-1 (green).

## MIL-101(Cr)

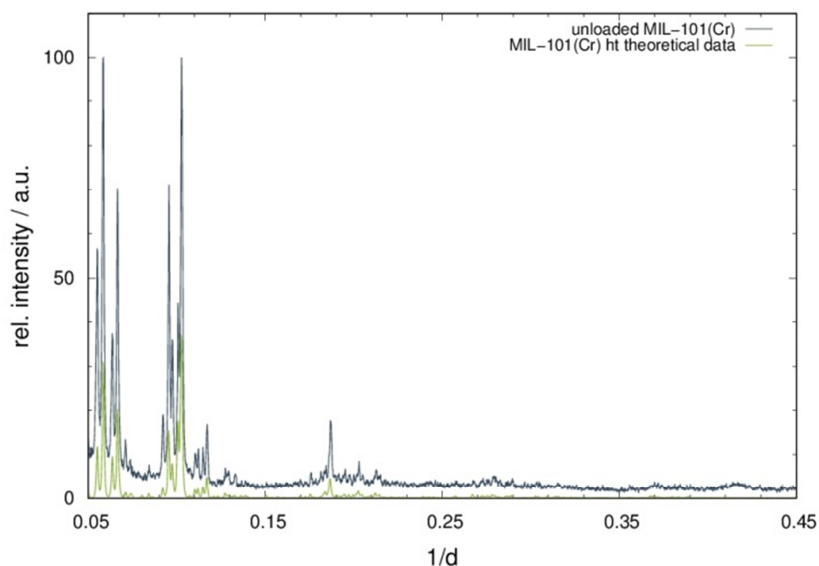


**Figure 8.1.3** XRPD pattern of unloaded MIL-101(Cr) (blue-grey), measured at 298 K (*SpLine/ESRF*;  $\lambda = 0.56383 \text{ \AA}$ ) in comparison to theoretical data of MIL-101(Cr) (green).

## MFM-300(Ga<sub>2</sub>) and fluorinated derivatives

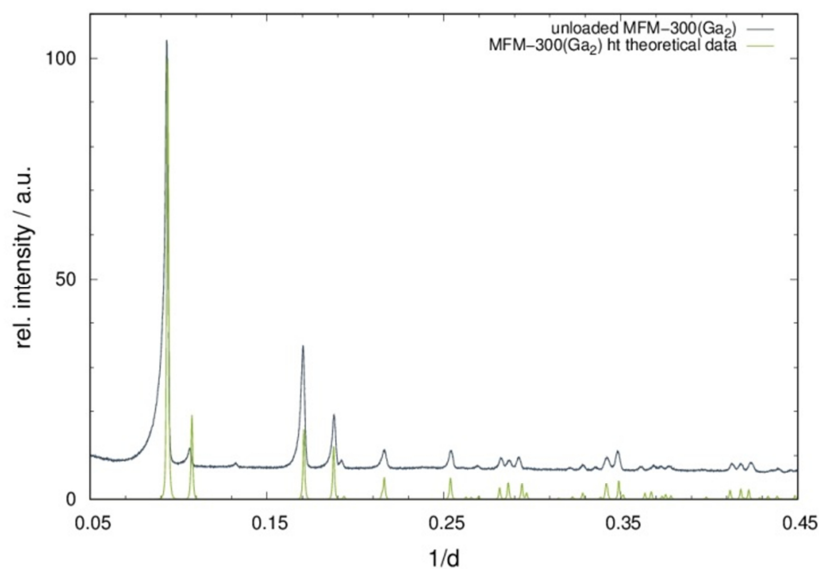


**Figure 8.1.4** XRPD pattern of MFM-300(Ga<sub>2</sub>) (blue-grey), measured at 298 K (*Huber G670*:  $\lambda = 1.54 \text{ \AA}$ ) in comparison to theoretical data of MFM-300(Ga<sub>2</sub>) (green).

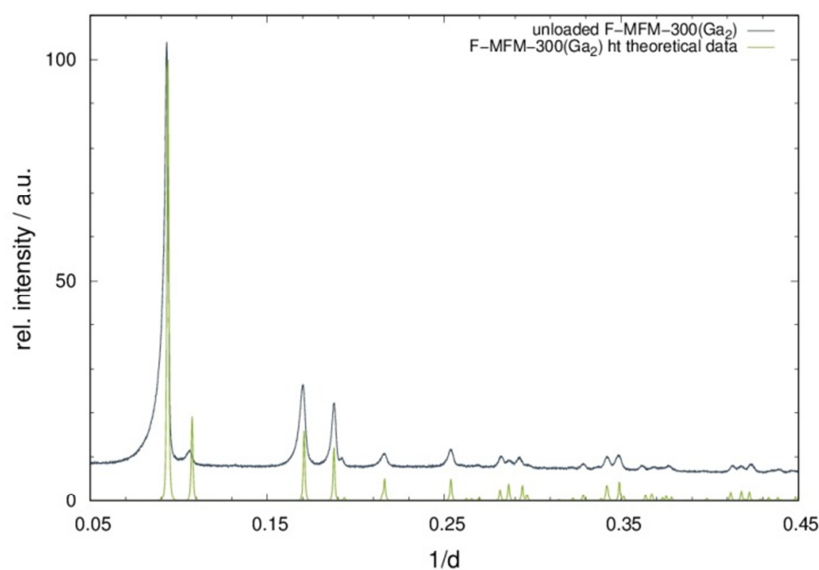


**Figure 8.1.5** XRPD pattern of F-MFM-300(Ga<sub>2</sub>) (blue-grey), measured at 298 K (*Huber G670*:  $\lambda = 1.54 \text{ \AA}$ ) in comparison to theoretical data of F-MFM-300(Ga<sub>2</sub>) (green).

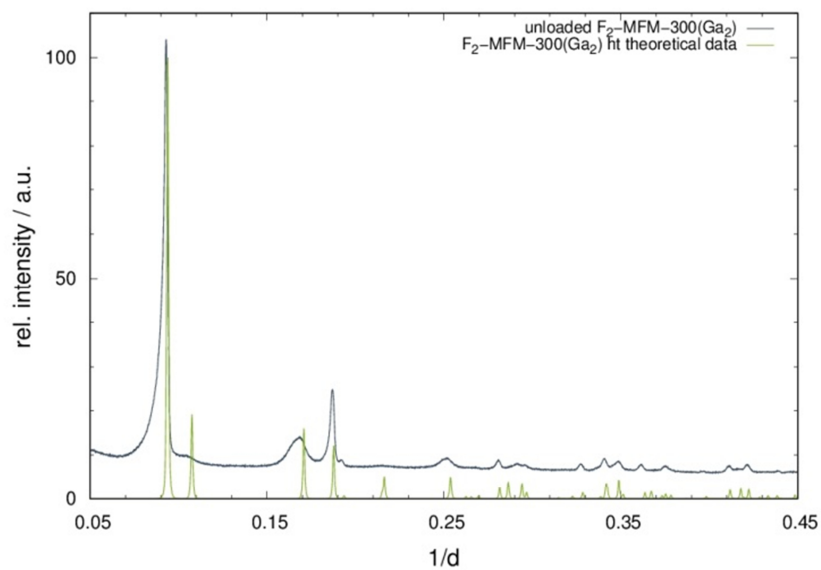


**Figure 8.1.6** XRPD pattern of  $F_2$ -MFM-300( $Ga_2$ ) (blue-grey), measured at 298 K (*Huber G670*:  $\lambda = 1.54 \text{ \AA}$ ) in comparison to theoretical data of  $F_2$ -MFM-300( $Ga_2$ ) (green).

### Zeolite Y

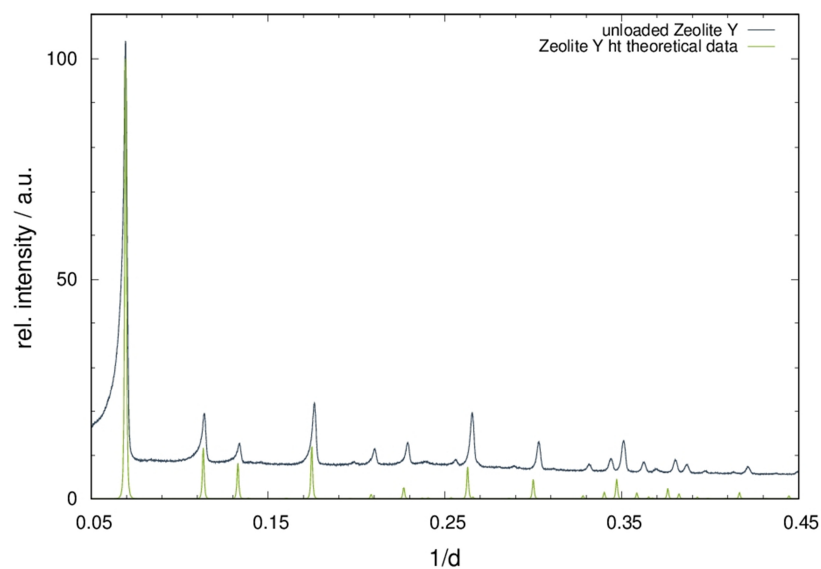


**Figure 8.1.7** XRPD pattern of Zeolite Y (blue-grey), measured at 298 K (*Huber G670*:  $\lambda = 1.54 \text{ \AA}$ ) in comparison to theoretical data of Zeolite Y (green).

## 8.2 SP-Nitro@MOF hybrid materials

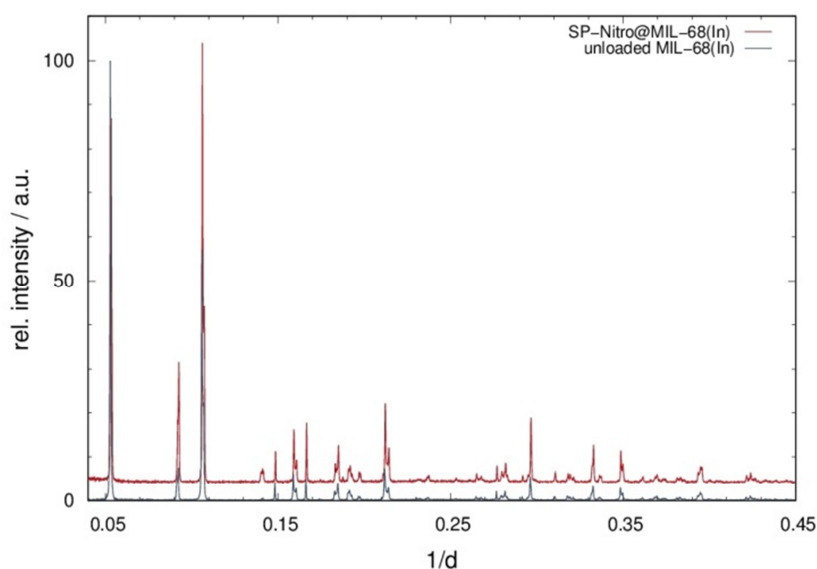


**Figure 8.2.1** XRPD patterns of **(2)** (red) and unloaded MIL-68(In) (blue-grey), measured at 298 K (BM01B/ESRF:  $\lambda = 0.50561 \text{ \AA}$  (**2**) and  $\lambda = 0.504477 \text{ \AA}$  (unloaded MIL-68(In)). As both patterns were recorded with different wavelengths  $1/d$  was chosen as  $x$  axis and a small offset along  $y$  (+ 4%) was applied in order to enhance readability.

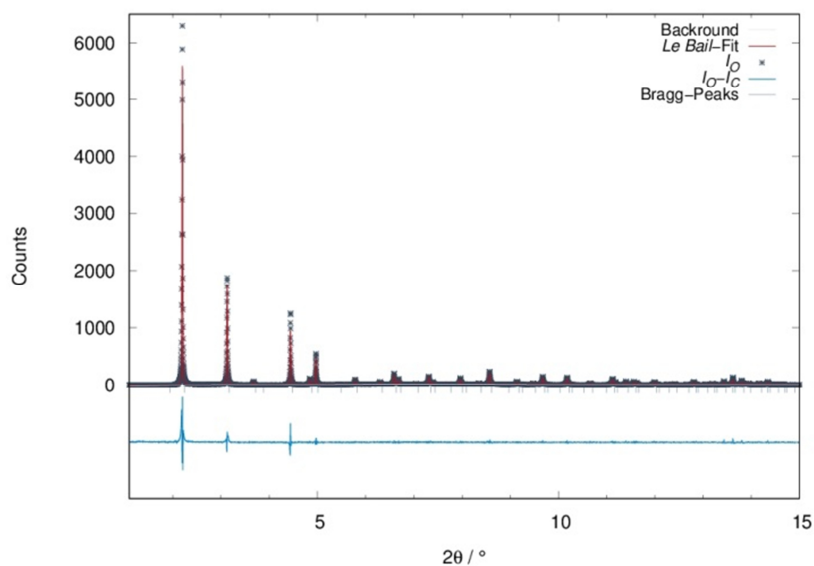


**Figure 8.2.2** *Le Bail* fit of MOF-5 (298 K, BM01B/ESRF,  $\lambda = 0.504477 \text{ \AA}$ ) with measured intensities (grey, crosses), calculated intensities (red), differential curve (turquoise), *Bragg* peaks (light blue, ticks) and background of refinement (white).

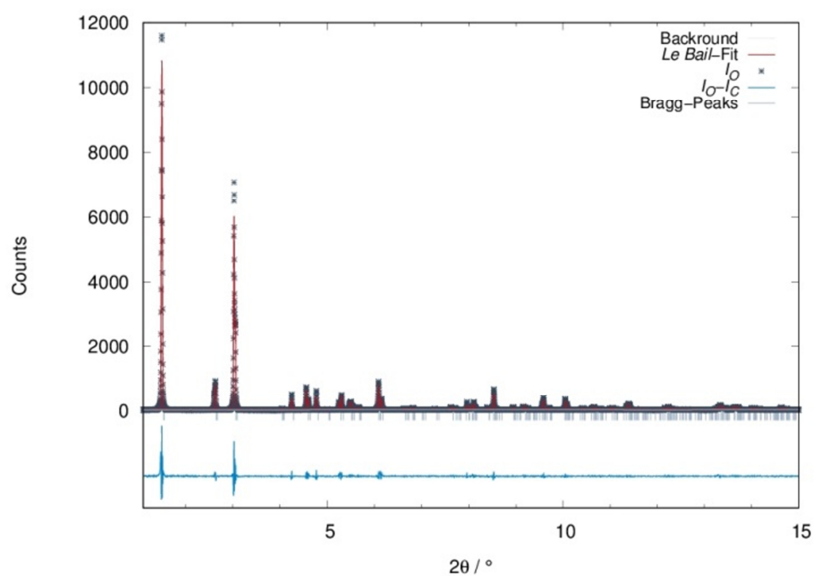


**Figure 8.2.3** *Le Bail* fit of MIL-68(In) (298 K, BM01B/ESRF,  $\lambda = 0.504477 \text{ \AA}$ ) with measured intensities (grey, crosses), calculated intensities (red), differential curve (turquoise), *Bragg* peaks (light blue, ticks) and background of refinement (white).

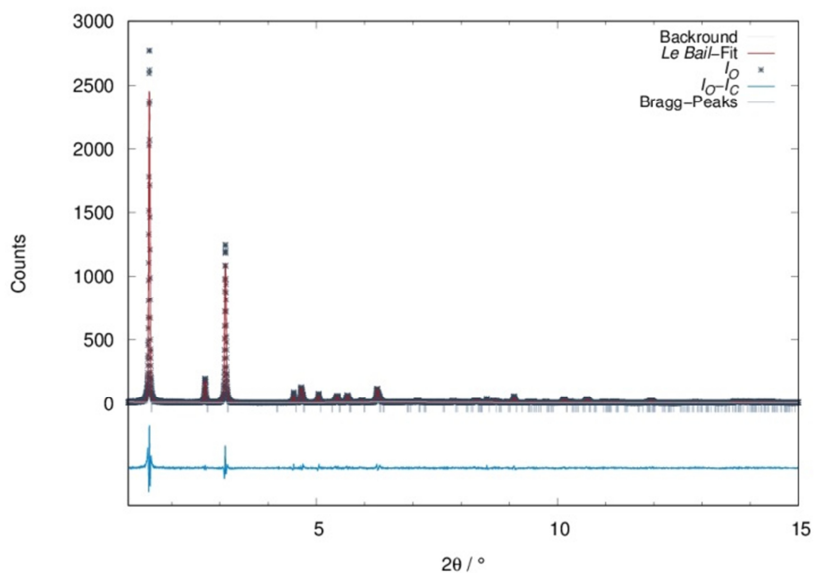


**Figure 8.2.4** *Le Bail* fit of MIL-68(Ga) (298 K, BM01B/ESRF,  $\lambda = 0.504477 \text{ \AA}$ ) with measured intensities (grey, crosses), calculated intensities (red), differential curve (turquoise), *Bragg* peaks (light blue, ticks) and background of refinement (white).

**Table 8.2.1** Results of *Le Bail* fits of high resolution synchrotron powder diffraction data of MOF-5, MIL-68(In) and MIL-68(Ga).

	MOF-5	MIL-68(In)	MIL-68(Ga)
T/K	298	298	298
Space Group / No.	$Fm\bar{3}m$ / 225	$Cmcm$ / 63	$Cmcm$ / 63
GOF	1.43	1.31	0.89
$R_p$	0.1665	0.1311	0.1591
$wR_p$	0.3172	0.1840	0.237
$V/\text{\AA}^3$	17156(4)	5901.5(2)	5197.0(7)
a	25.7912(6)	21.8387(5)	21.044(2)
b	-	37.3912(8)	36.656(2)
b	-	7.2271(1)	6.7373(4)

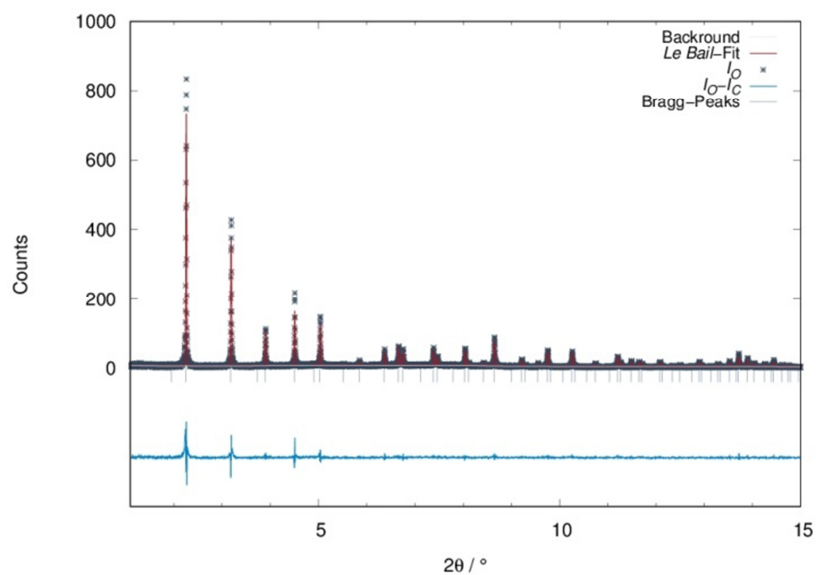


**Figure 8.2.5** *Le Bail* fit of SP-Nitro@MOF-5 (1) (298 K, BM01B/ESRF,  $\lambda = 0.504477 \text{ \AA}$ ) with measured intensities (grey, crosses), calculated intensities (red), differential curve (turquoise), *Bragg* peaks (light blue, ticks) and background of refinement (white).

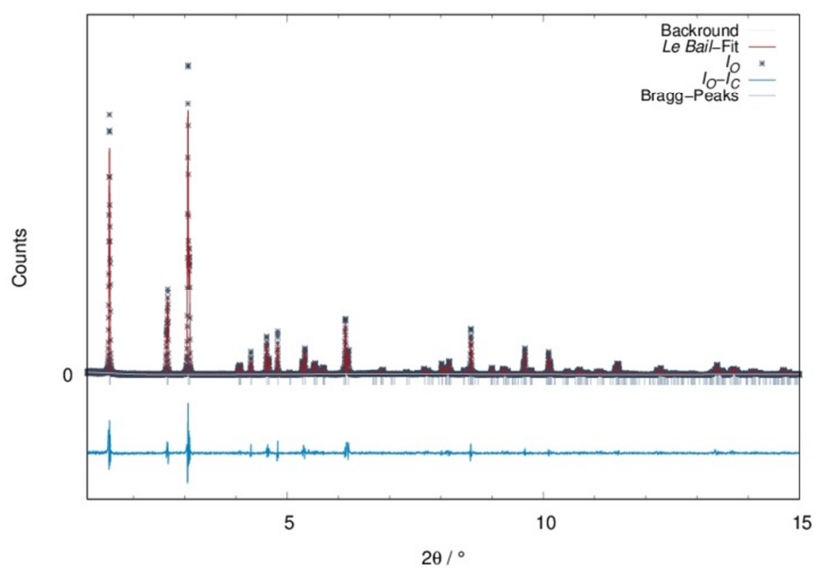


**Figure 8.2.6** *Le Bail* fit of SP-Nitro@MIL-68(In) (**2**) (298 K, BM01B/ESRF,  $\lambda = 0.504477 \text{ \AA}$ ) with measured intensities (grey, crosses), calculated intensities (red), differential curve (turquoise), *Bragg* peaks (light blue, ticks) and background of refinement (white).

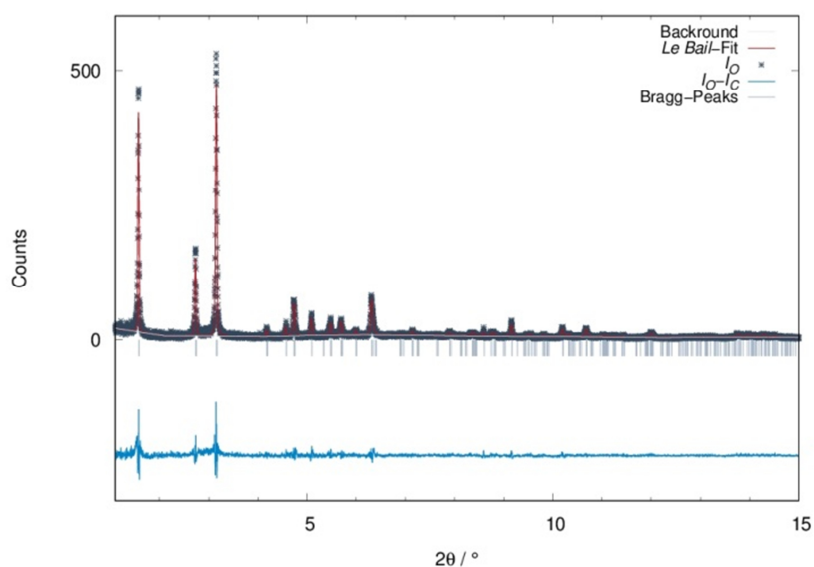


**Figure 8.2.7** *Le Bail* fit of SP-Nitro@MIL-68(Ga) (**3**) (298 K, BM01B/ESRF,  $\lambda = 0.504477 \text{ \AA}$ ) with measured intensities (grey, crosses), calculated intensities (red), differential curve (turquoise), *Bragg* peaks (light blue, ticks) and background of refinement (white).

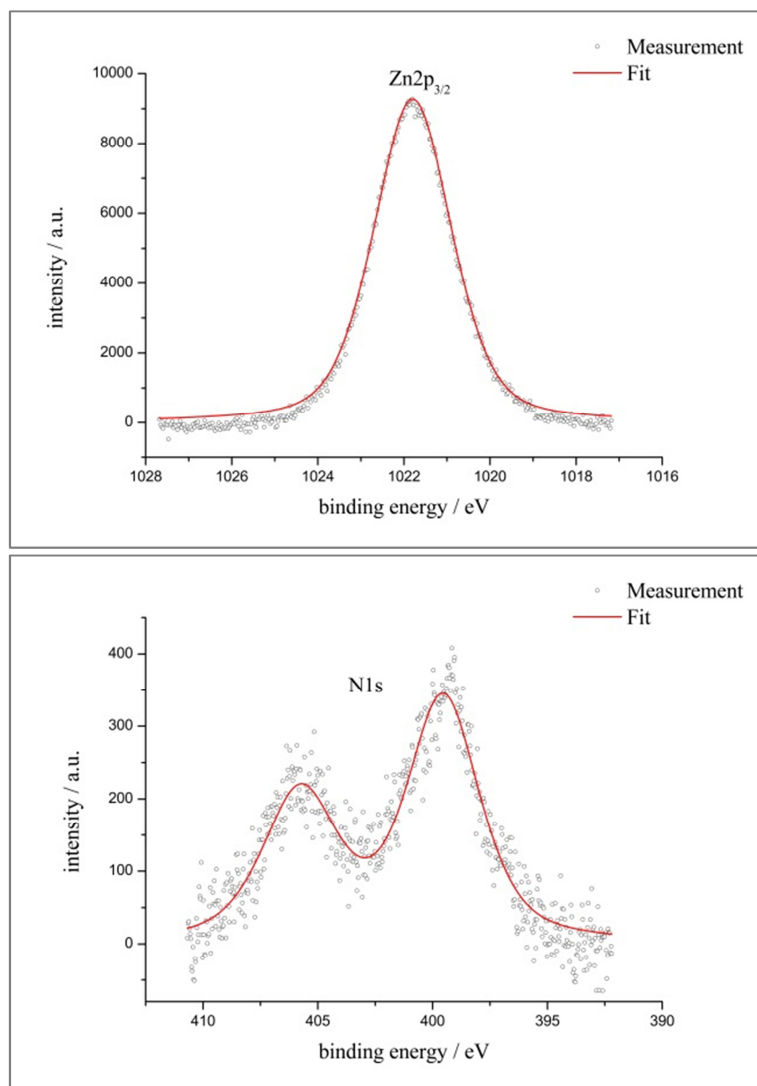


**Figure 8.2.8** XPS spectrum of the Zn2p<sub>3/2</sub> (top) and N1s peak (bottom) of SP-Nitro@MOF-5 (1) with experimental data (dots) and fit (red).

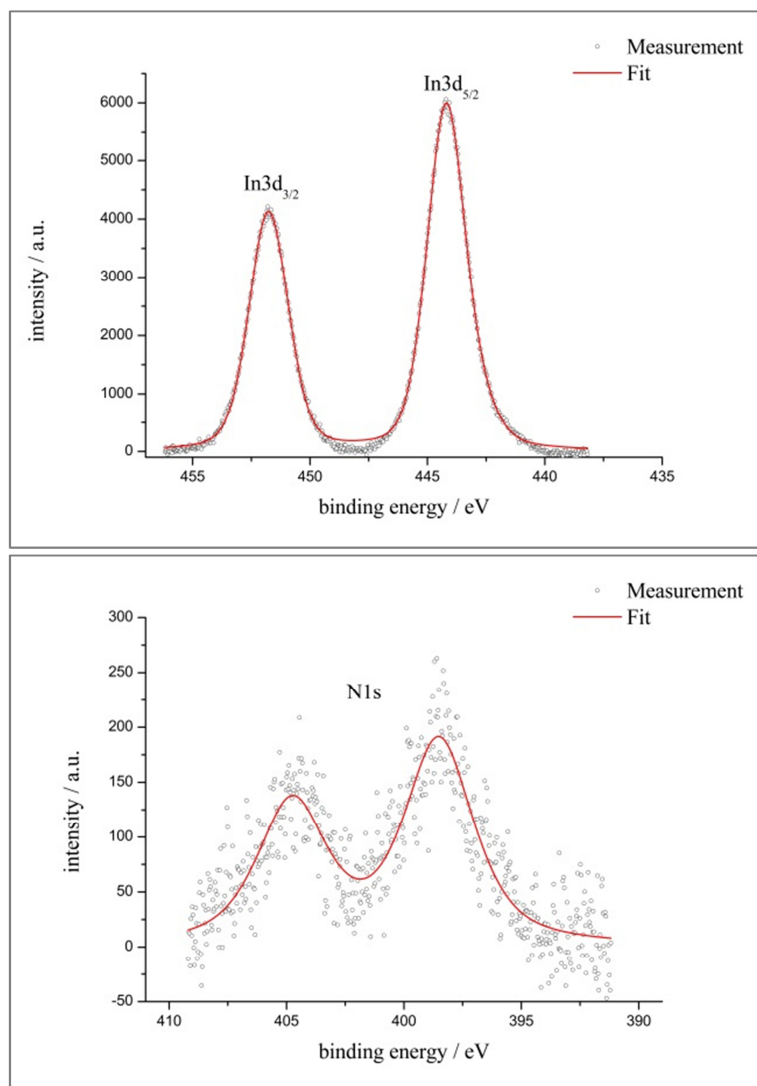


**Figure 8.2.9** XPS spectrum of the In3d<sub>5/2</sub> (top) and N1s peak (bottom) of SP-Nitro@MIL-68(In) (2) with experimental data (dots) and fit (red).

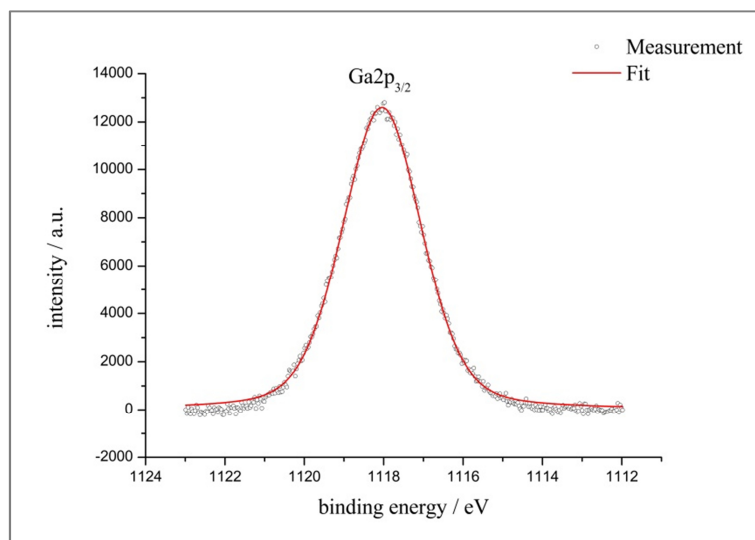


**Figure 8.2.10** XPS spectrum of the Ga<sub>2p<sub>3/2</sub></sub> of SP-Nitro@MIL-68(Ga) (**3**) with experimental data (dots) and fit (red).

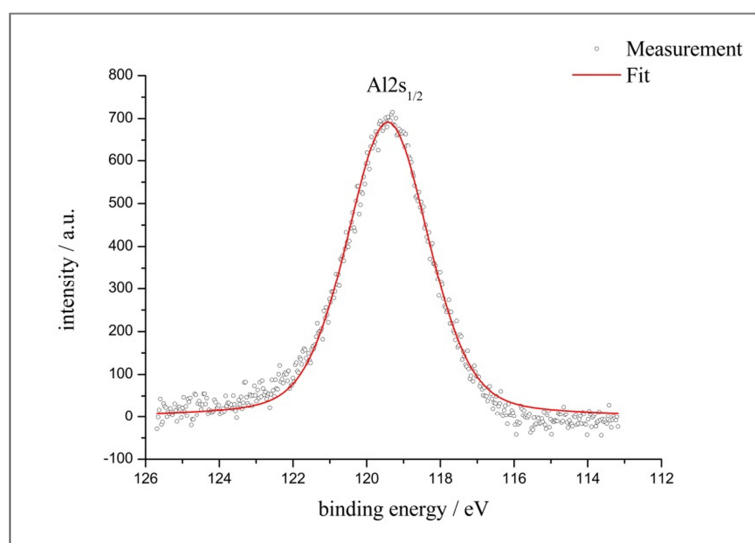


**Figure 8.2.11** XPS spectrum of the Al<sub>2s<sub>1/2</sub></sub> of SP-Nitro@MIL-53(Al) (**4**) with experimental data (dots) and fit (red).

**Table 8.2.2** Calculation of the composition of compounds **1** to **4** via XPS.

	<b>1</b>	<b>2</b>	<b>3</b>	<b>4</b>
Nitrogen atoms per formula unit of SP-Nitro	2	2	2	2
Metal atoms per formula unit of the respective MOF	4 [Zn <sub>4</sub> O(bdc) <sub>3</sub> ]	1 [In(OH)(bdc)]	1 [Ga(OH)(bdc)]	1 [Al(OH)(bdc)]
RSF factor for nitrogen	1.77 N1s	1.77 N1s	1.77 N1s	1.77 N1s
RSF factor for the respective metal	18.01 (Zn 2p <sub>3/2</sub> )	13.23 (In 3d <sub>5/2</sub> )	20.47 (Ga 2p <sub>3/2</sub> )	0.681 (Al 2s <sub>1/2</sub> )
Peak area for nitrogen	2783	1173	1482	1120
Peak area for the respective metal	25042	14732	36181	2229
SP-Nitro : MOF	2.26 : 1	0.30 : 1	0.24 : 1	0.10 : 1

**Table 8.2.3** Calculated and measured amounts (%) of N, C and H for SP-Nitro<sub>x</sub>@MOF-5 (1) with x = 2.4.

	N	C	H
calculated (%)	4.36	54.16	3.60
found (%)	4.33	54.41	3.80

**Table 8.2.4** Calculated and measured amounts (%) of N, C and H for SP-Nitro<sub>x</sub>@MIL-68(In) (2) with x = 0.45.

	N	C	H
calculated (%)	2.88	45.16	3.00
found (%)	2.86	46.88	2.74

**Table 8.2.5** Calculated and measured amounts (%) of N, C and H for SP-Nitro<sub>x</sub>@MIL-68(Ga) (3) with x = 0.25.

	N	C	H
calculated (%)	2.11	46.20	2.89
found (%)	2.17	44.04	2.78

**Table 8.2.6** Calculated and measured amounts (%) of N, C and H for SP-Nitro<sub>x</sub>@MIL-53(Al) (4) with x = 0.06.

	N	C	H
calculated (%)	0.77	38.35	2.70
found (%)	0.77	34.92	2.19

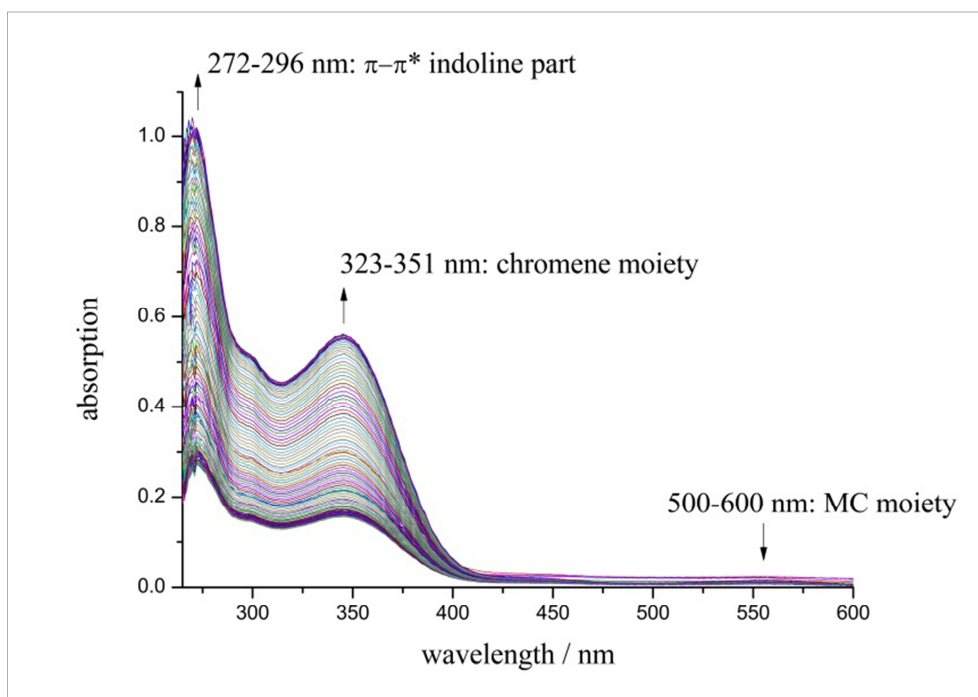


**Figure 8.2.12** Long-time UV/vis measurements on SP-Nitro@MIL-68(In) (**2**) dispersed in DMF.

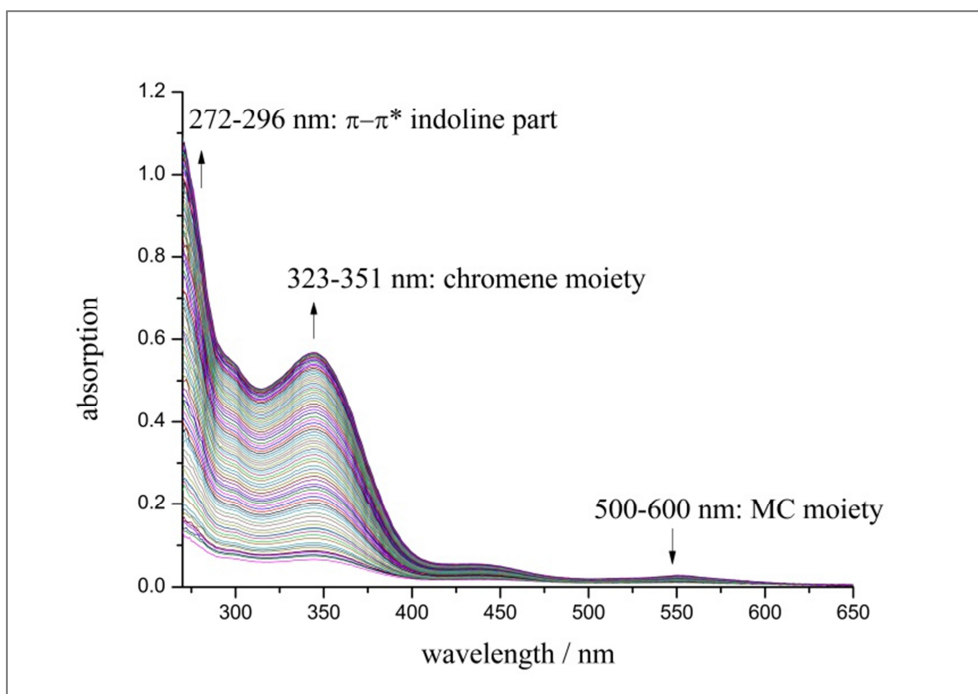


**Figure 8.2.13** Long-time UV/vis measurements on SP-Nitro@MIL-68(Ga) (**3**) dispersed in DMF.

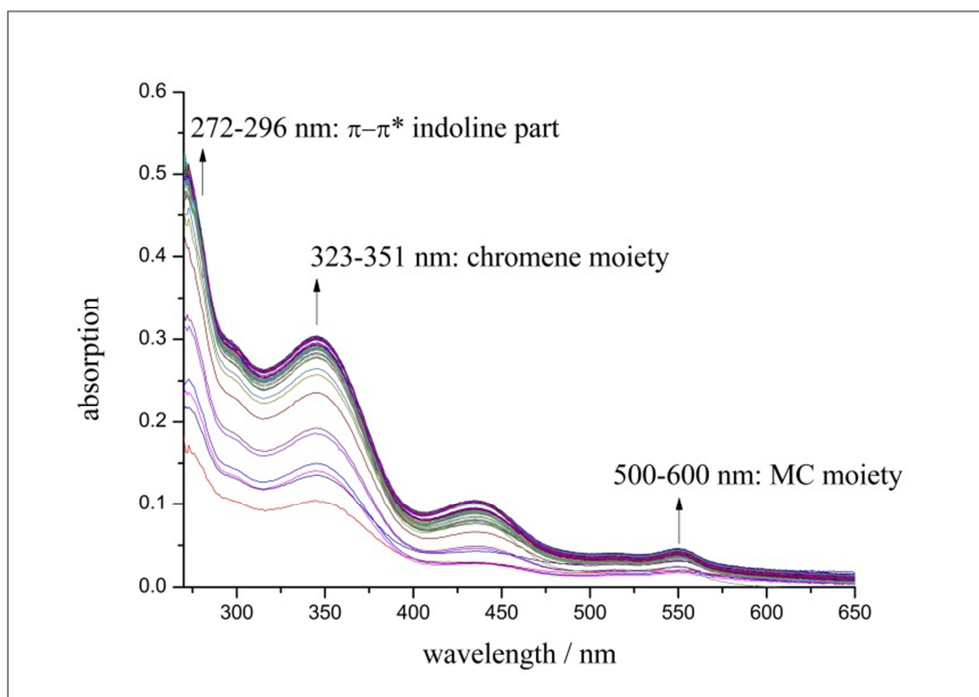


**Figure 8.2.14** Long-time UV/vis measurements on SP-Nitro@MIL-53(Al) (4) dispersed in DMF.

## 8.3 Further spiropyran@MOF-systems

### 8.3.1 SP@MOF systems

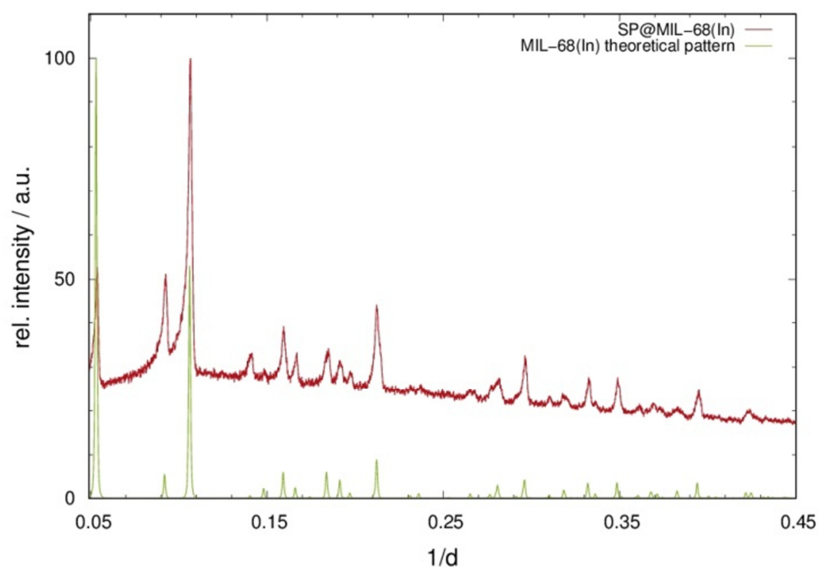


**Figure 8.3.1** XRPD pattern of (6) (red), measured at 298 K (*Huber G670*:  $\lambda = 1.54 \text{ \AA}$ ), in comparison to theoretical data of MIL-68(In) (green).

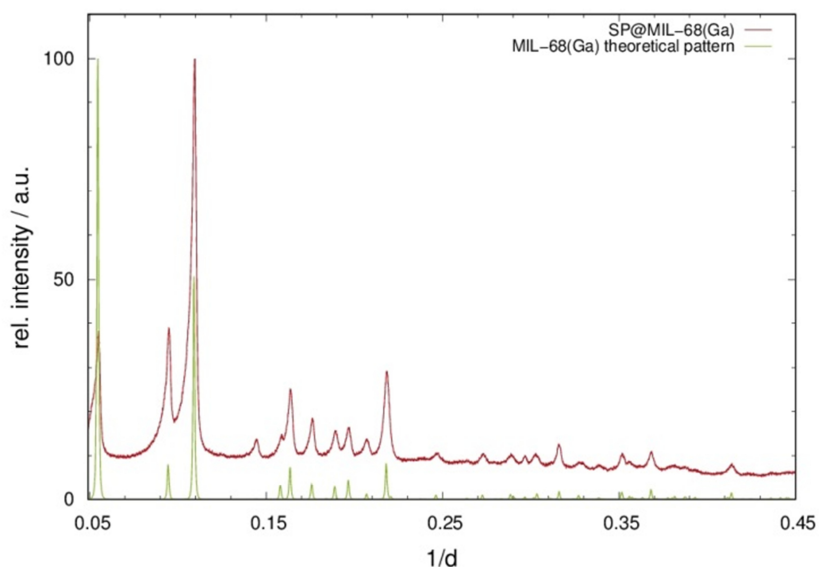


**Figure 8.3.2** XRPD pattern of (7) (red), measured at 298 K (*Huber G670*:  $\lambda = 1.54 \text{ \AA}$ ), in comparison to theoretical data of MIL-68(Ga) (green).

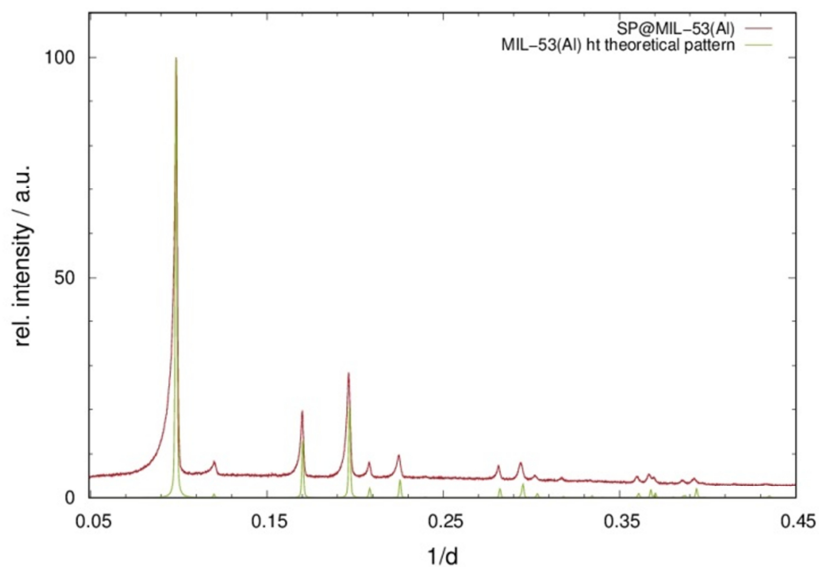


**Figure 8.3.3** XRPD pattern of **(8)** (red), measured at 298 K (*Huber G670*:  $\lambda = 1.54 \text{ \AA}$ ), in comparison to theoretical data of MIL-53(Al) *ht* (green).

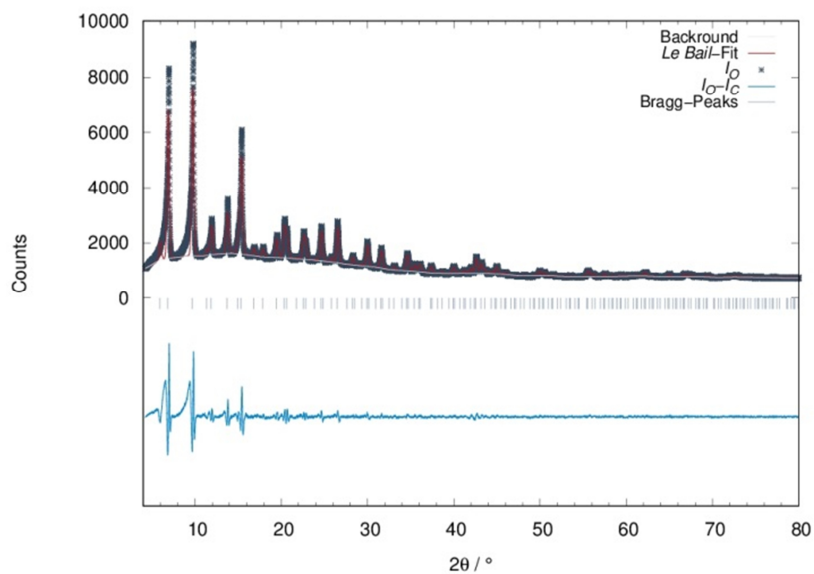


**Figure 8.3.4** *Le Bail* fit of SP@MOF-5 **(5)** (298 K, *Stoe StadiP*,  $\lambda = 1.54 \text{ \AA}$ ) with measured intensities (grey, crosses), calculated intensities (red), differential curve (turquoise), *Bragg* peaks (light blue, ticks) and background of refinement (white).

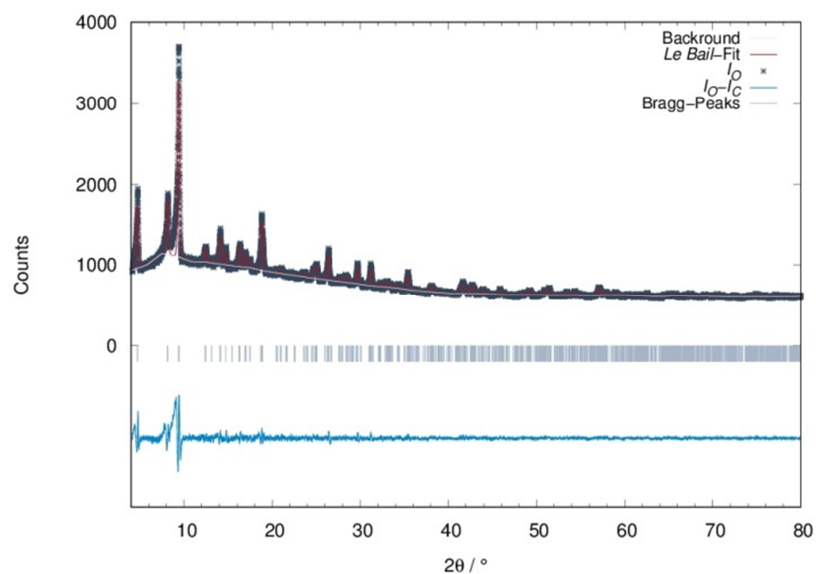


**Figure 8.3.5** *Le Bail* fit of SP@MIL-68(In) (6) (298 K, *Stoe StadiP*,  $\lambda = 1.54 \text{ \AA}$ ) with measured intensities (grey, crosses), calculated intensities (red), differential curve (turquoise), *Bragg* peaks (light blue, ticks) and background of refinement (white).

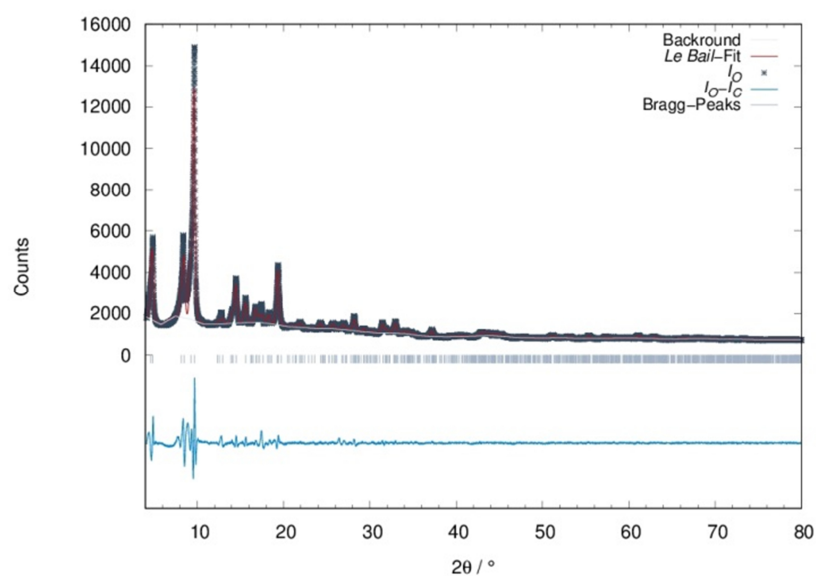


**Figure 8.3.6** *Le Bail* fit of SP@MIL-68(Ga) (7) (298 K, *Stoe StadiP*,  $\lambda = 1.54 \text{ \AA}$ ) with measured intensities (grey, crosses), calculated intensities (red), differential curve (turquoise), *Bragg* peaks (light blue, ticks) and background of refinement (white).

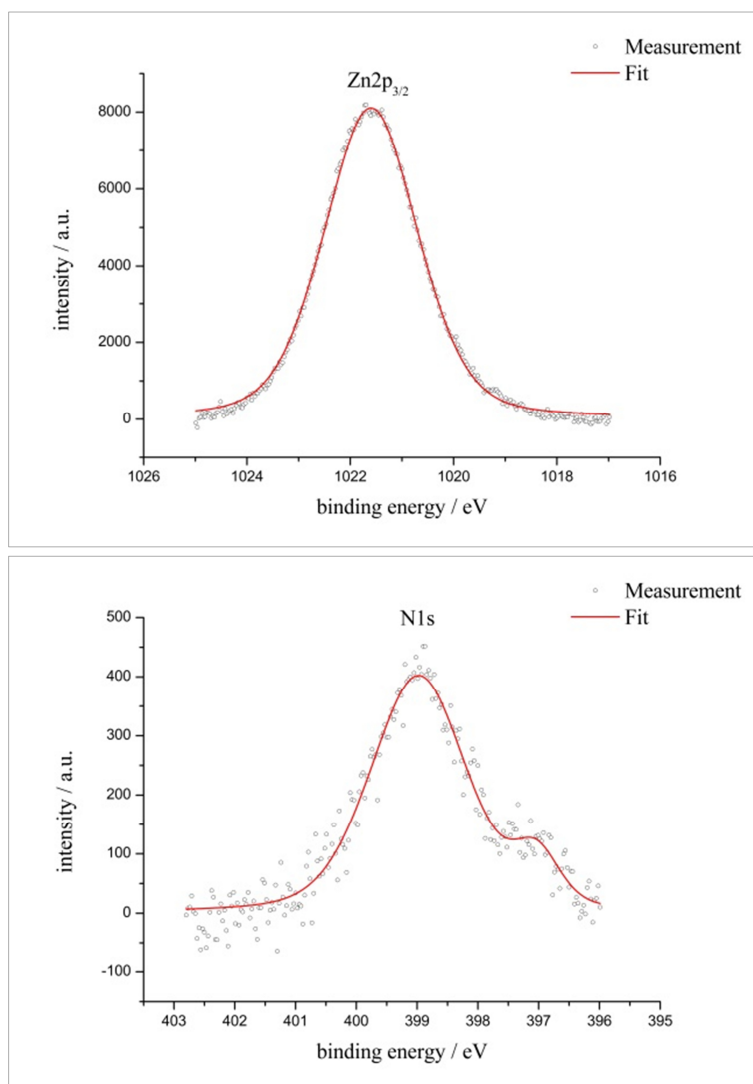


**Figure 8.3.7** XPS spectrum of the Zn2p<sub>3/2</sub> (top) and N1s peak (bottom) of SP@MOF-5 (5) with experimental data (dots) and fit (red).

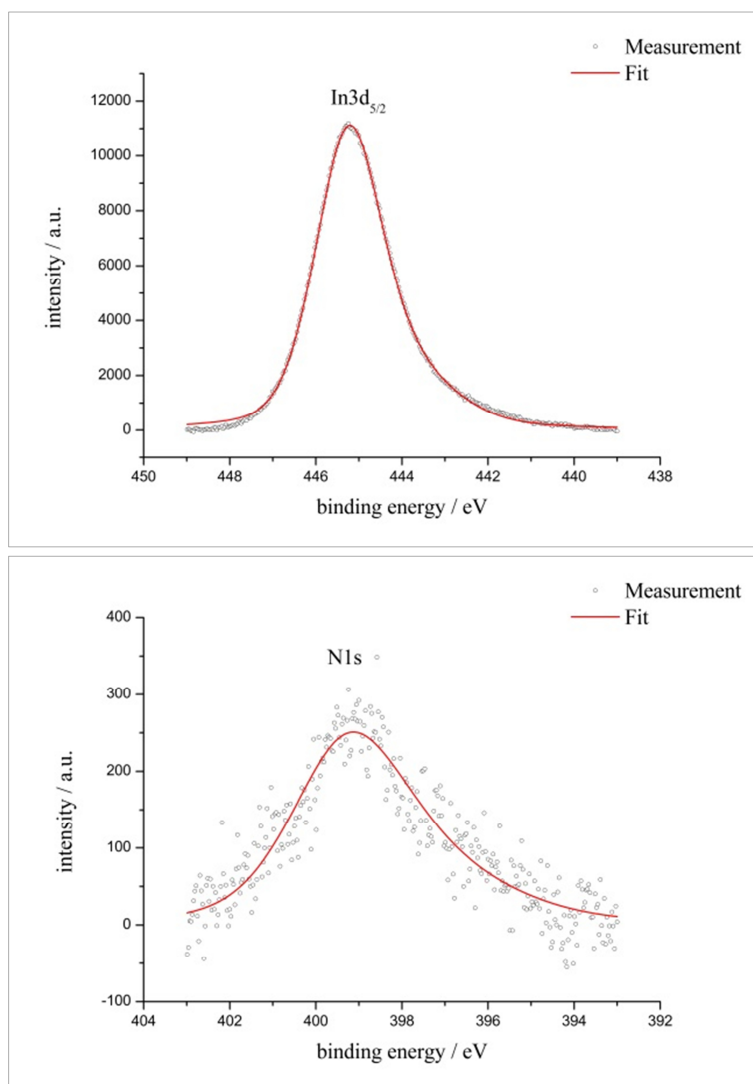


**Figure 8.3.8** XPS spectrum of the In<sub>3d</sub><sub>5/2</sub> (top) and N<sub>1s</sub> peak (bottom) of SP@MIL-68(In) (6) with experimental data (dots) and fit (red).

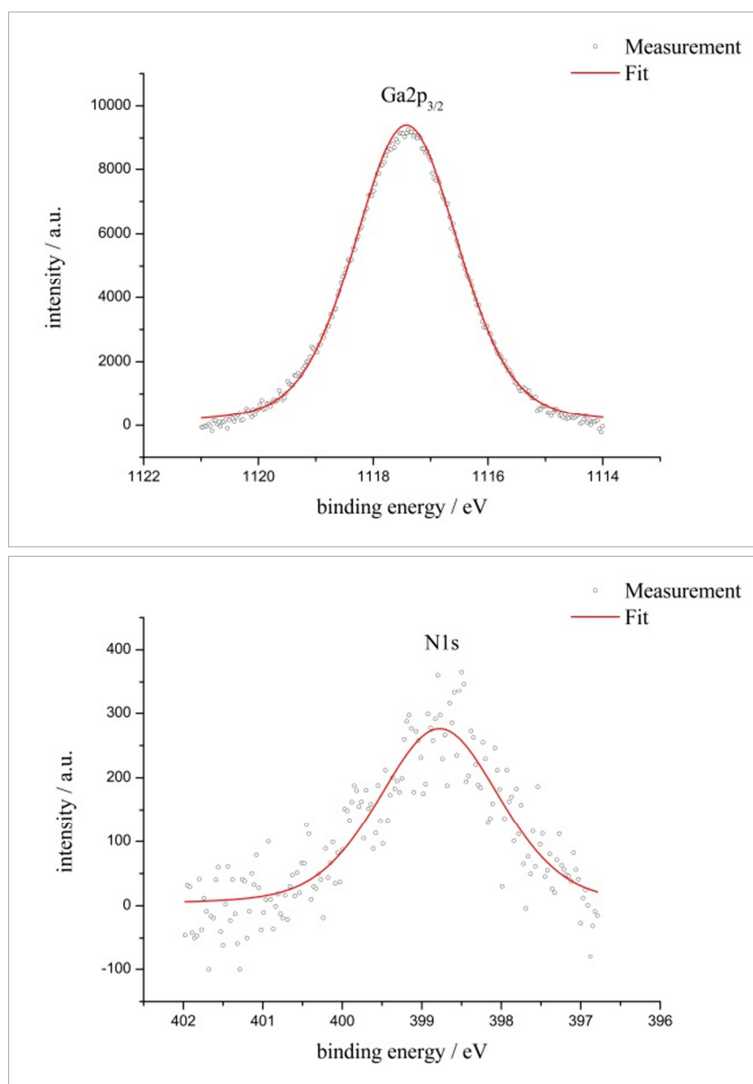


**Figure 8.3.9** XPS spectrum of the Ga<sub>2p<sub>3/2</sub></sub> (top) and N1s peak (bottom) of SP@MIL-68(Ga) (7) with experimental data (dots) and fit (red).

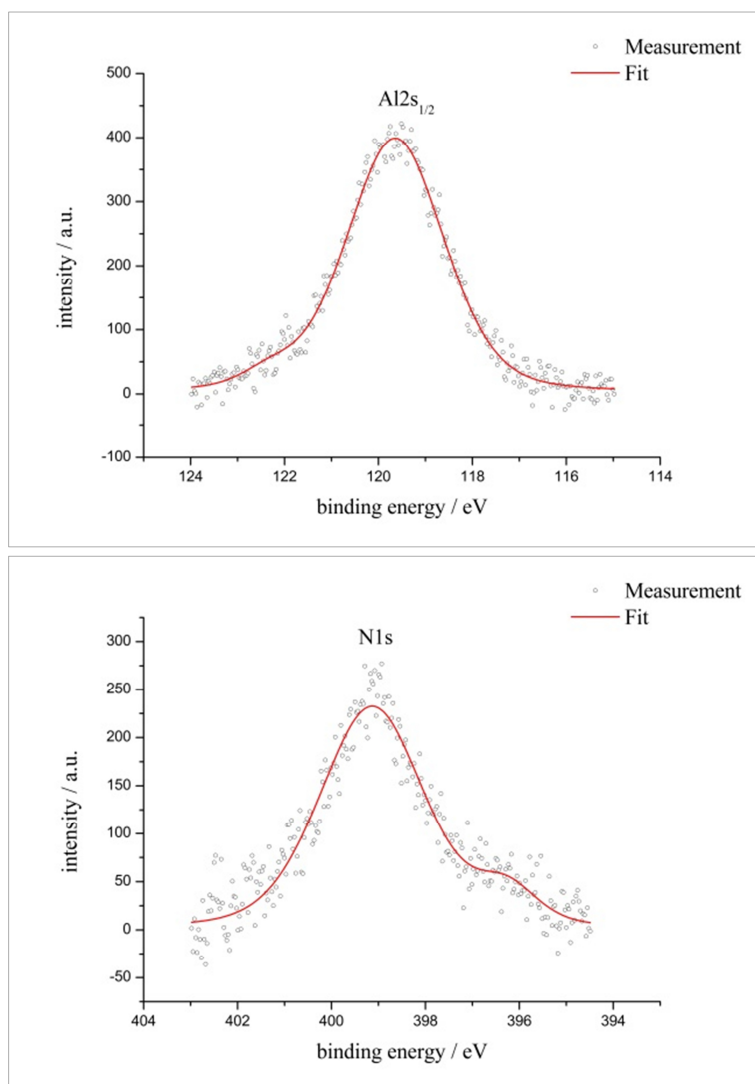


**Figure 8.3.10** XPS spectrum of the Al<sub>2s<sub>1/2</sub></sub> (top) and N1s peak (bottom) of SP@MIL-53(Al) (8) with experimental data (dots) and fit (red).

**Table 8.3.1** Calculation of the composition of compounds **5** to **8** via XPS.

	<b>5</b>	<b>6</b>	<b>7</b>	<b>8</b>
Nitrogen atoms per formula unit of SP	1	1	1	1
Metal atoms per formula unit of the respective MOF	4 [Zn <sub>4</sub> O(bdc) <sub>3</sub> ]	1 [In(OH)(bdc)]	1 [Ga(OH)(bdc)]	1 [Al(OH)(bdc)]
RSF factor for nitrogen	1.77 N1s	1.77 N1s	1.77 N1s	1.77 N1s
RSF factor for the respective metal	18.01 (Zn 2p <sub>3/2</sub> )	13.23 (In 3d <sub>5/2</sub> )	20.47 (Ga 2p <sub>3/2</sub> )	0.681 (Al 2s <sub>1/2</sub> )
Peak area for nitrogen	1009	1154	612	816
Peak area for the respective metal	21220	28348	24469	1246
SP : MOF	1.94: 1	0.30 : 1	0.29: 1	0.25 : 1

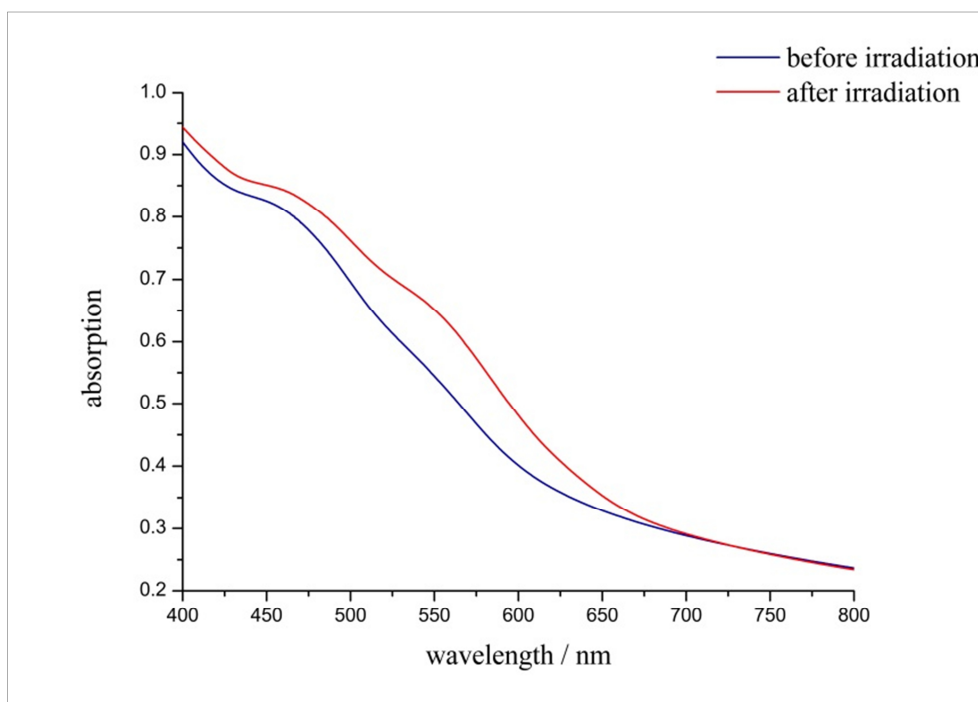


**Figure 8.3.11** Absorption spectra (298 K) of SP@MIL-68(In) (6) before (blue) and after (red) irradiation with UV light ( $\lambda = 365$  nm, 30 min).

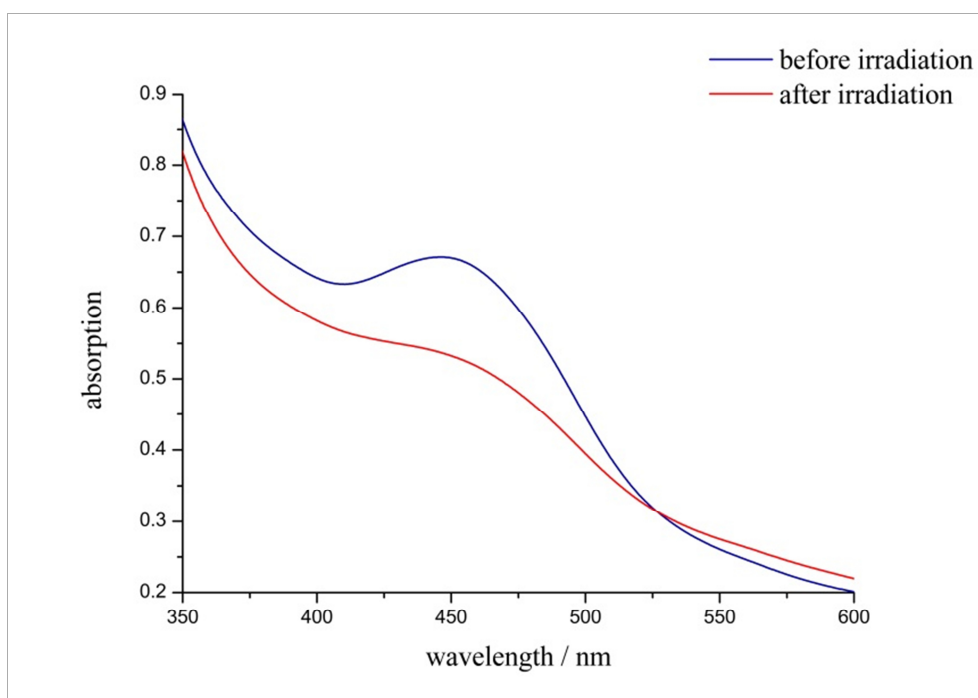


**Figure 8.3.12** Absorption spectra (298 K) of SP@MIL-68(Ga) (7) before (blue) and after (red) irradiation with UV light ( $\lambda = 365$  nm, 30 min).

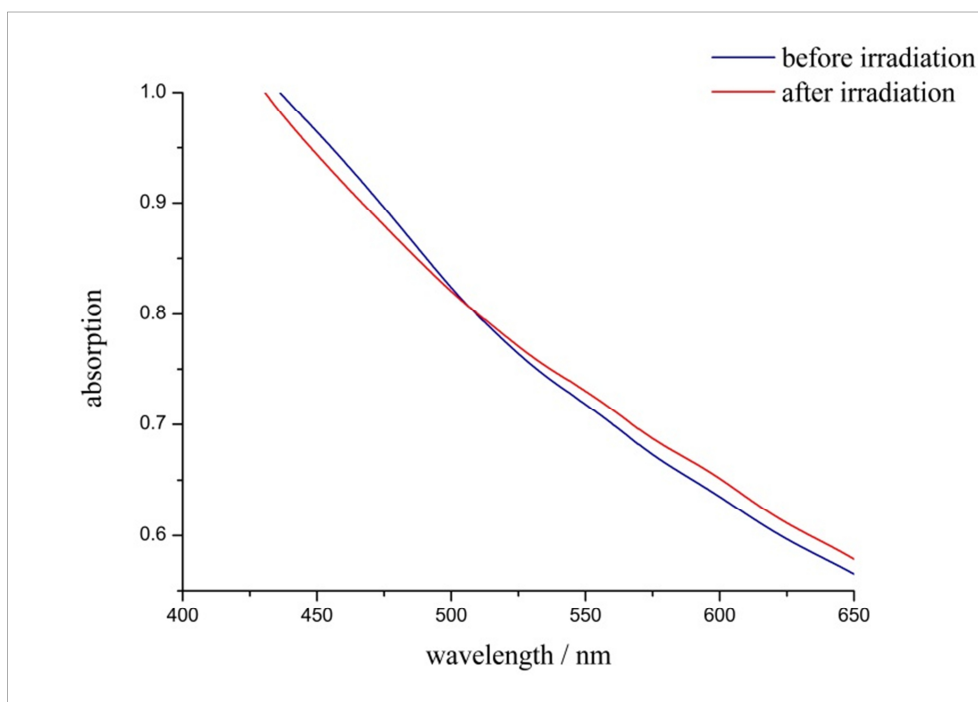


**Figure 8.3.13** Absorption spectra (298 K) of SP@MIL-53(Al) (**8**) before (blue) and after (red) irradiation with UV light ( $\lambda = 365$  nm, 30 min).

### 8.3.2 SP-N@MOF systems

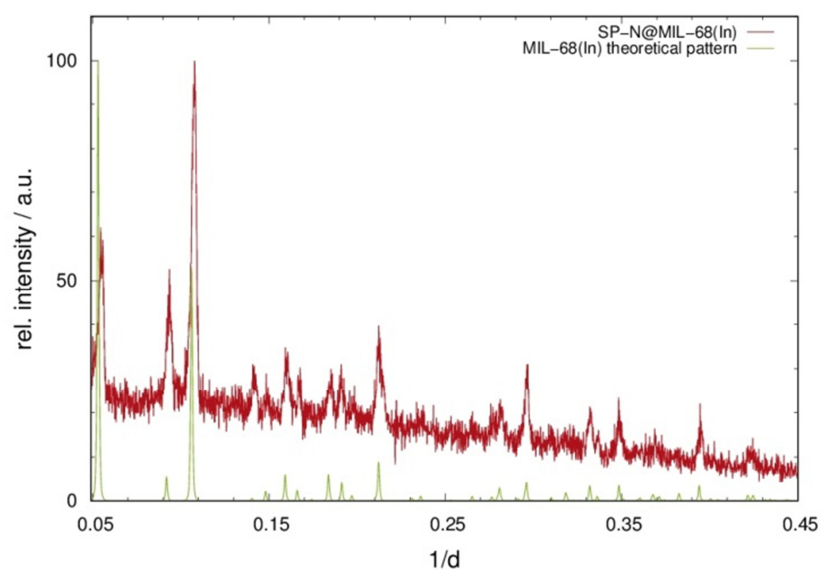


**Figure 8.3.14** XRPD pattern of **(10)** (red), measured at 298 K (*Stoe StadiP*:  $\lambda = 1.54 \text{ \AA}$ ), in comparison to theoretical data of MIL-68(In) (green).

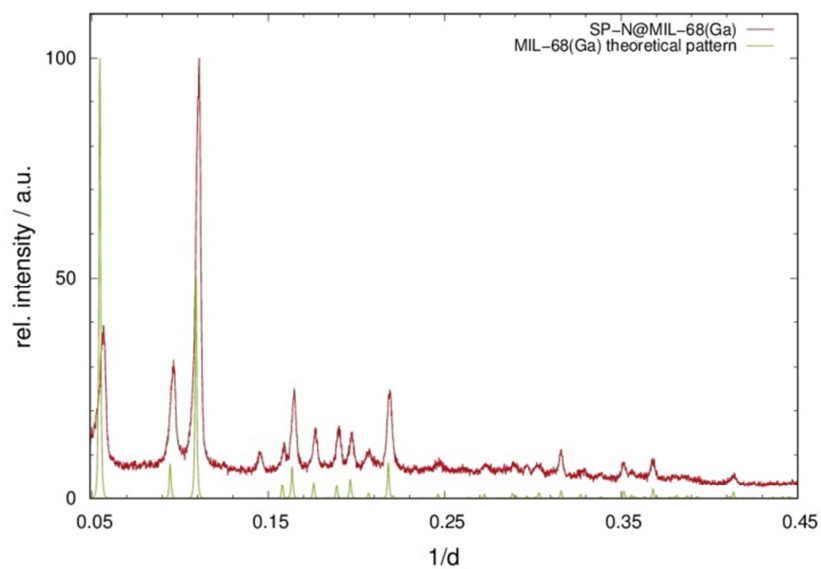


**Figure 8.3.15** XRPD pattern of **(11)** (red), measured at 298 K (*Stoe StadiP*:  $\lambda = 1.54 \text{ \AA}$ ), in comparison to theoretical data of MIL-68(Ga) (green).

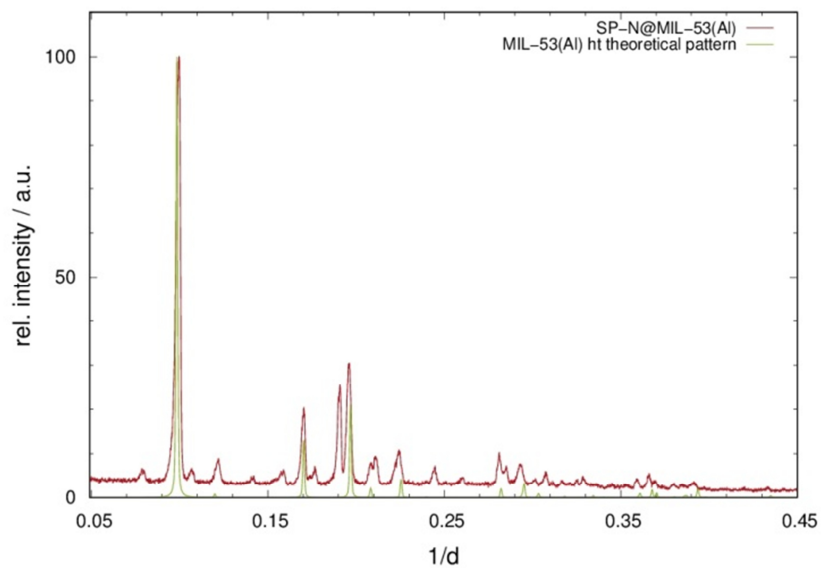


**Figure 8.3.16** XRPD pattern of **(12)** (red), measured at 298 K (*Stoe StadiP*:  $\lambda = 1.54 \text{ \AA}$ ), in comparison to theoretical data of MIL-53(Al) *ht* (green).

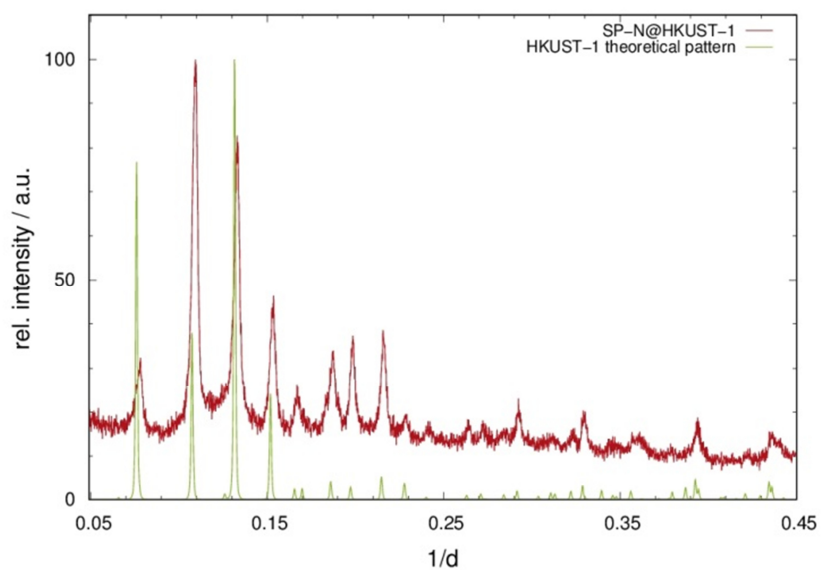


**Figure 8.3.17** XRPD pattern of **(13)** (red), measured at 298 K (*Stoe StadiP*:  $\lambda = 1.54 \text{ \AA}$ ), in comparison to theoretical data of HKUST-1 (green).

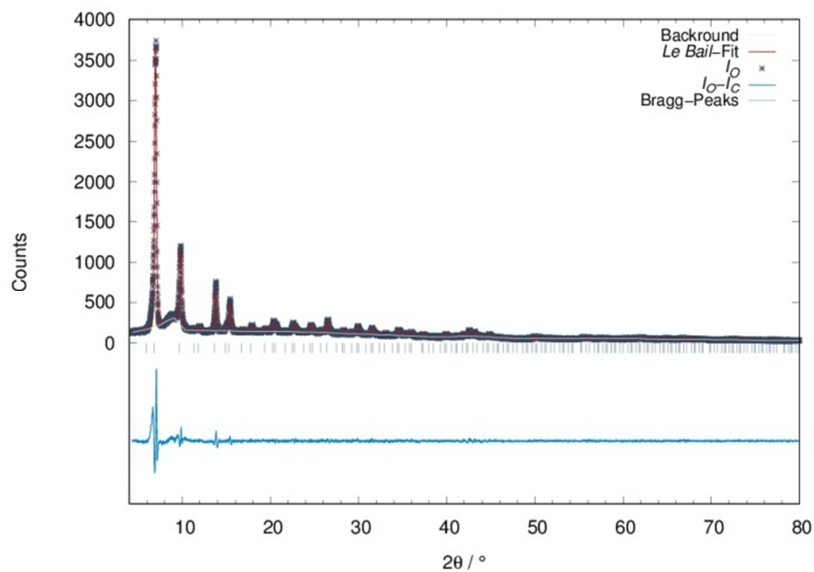


**Figure 8.3.18** *Le Bail* fit of SP-N@MOF-5 (**9**) (298 K, *Stoe StadiP*,  $\lambda = 1.54 \text{ \AA}$ ) with measured intensities (grey, crosses), calculated intensities (red), differential curve (turquoise), *Bragg* peaks (light blue, ticks) and background of refinement (white).

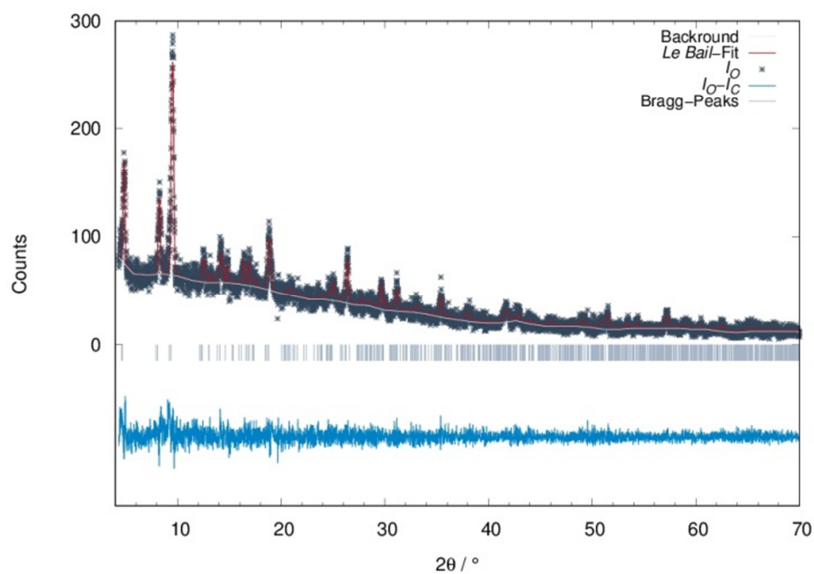


**Figure 8.3.19** *Le Bail* fit of SP-N@MIL-68(In) (**10**) (298 K, *Stoe StadiP*,  $\lambda = 1.54 \text{ \AA}$ ) with measured intensities (grey, crosses), calculated intensities (red), differential curve (turquoise), *Bragg* peaks (light blue, ticks) and background of refinement (white).

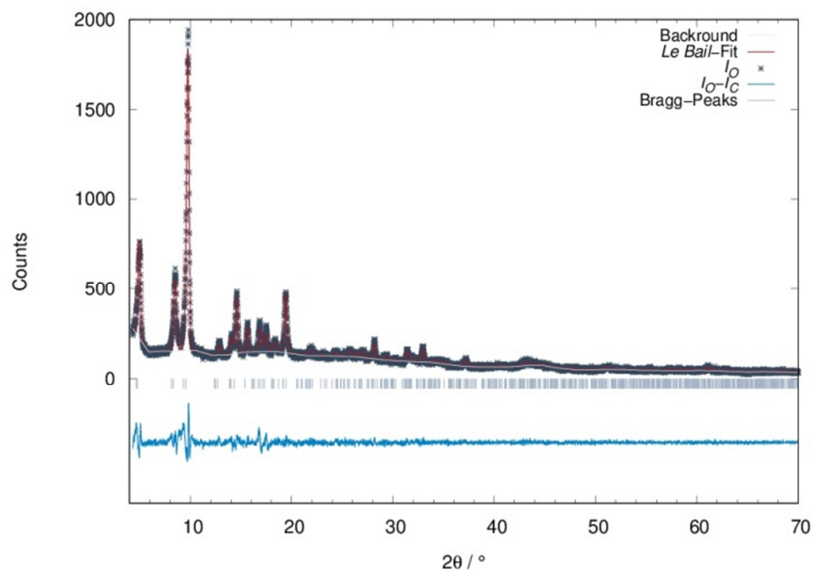


**Figure 8.3.20** *Le Bail* fit of SP-N@MIL-68(Ga) (**11**) (298 K, *Stoe StadiP*,  $\lambda = 1.54 \text{ \AA}$ ) with measured intensities (grey, crosses), calculated intensities (red), differential curve (turquoise), *Bragg* peaks (light blue, ticks) and background of refinement (white).

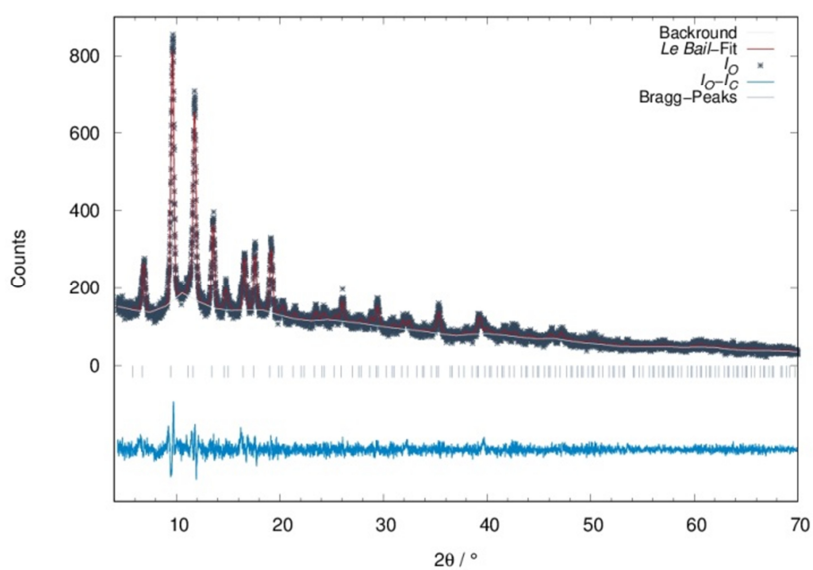


**Figure 8.3.21** *Le Bail* fit of SP-N@HKUST-1 (**13**) (298 K, *Stoe StadiP*,  $\lambda = 1.54 \text{ \AA}$ ) with measured intensities (grey, crosses), calculated intensities (red), differential curve (turquoise), *Bragg* peaks (light blue, ticks) and background of refinement (white).

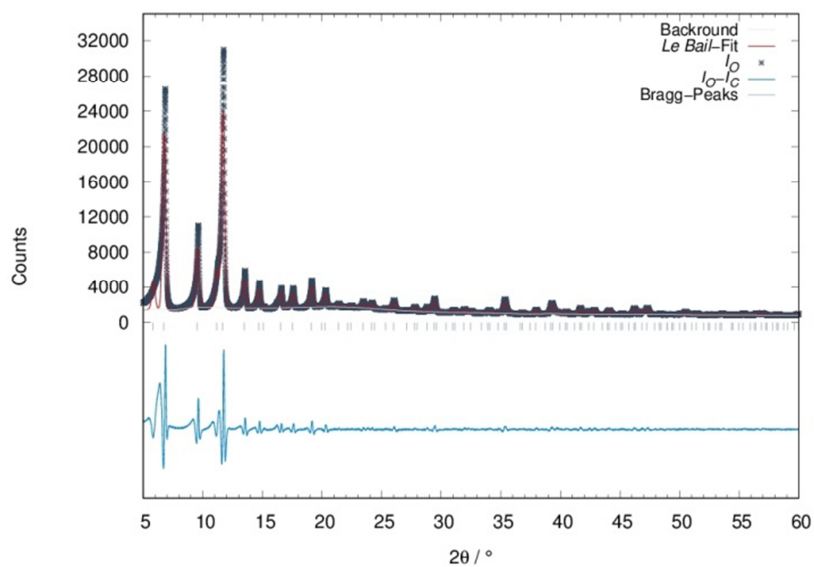


**Figure 8.3.22** *Le Bail* fit of HKUST-1 (298 K, *Stoe StadiP*,  $\lambda = 1.54 \text{ \AA}$ ) with measured intensities (grey, crosses), calculated intensities (red), differential curve (turquoise), *Bragg* peaks (light blue, ticks) and background of refinement (white).

**Table 8.3.2** Results of *Le Bail* fit of powder diffraction data of HKUST-1.

	HKUST-1
T/K	298
Space Group / No.	$Fm\bar{3}m$ / 225
GOF	6.55
$R_p$	0.1002
$wR_p$	0.1674
$V/\text{\AA}^3$	18161(2)
a	26.285(2)
b	-
b	-

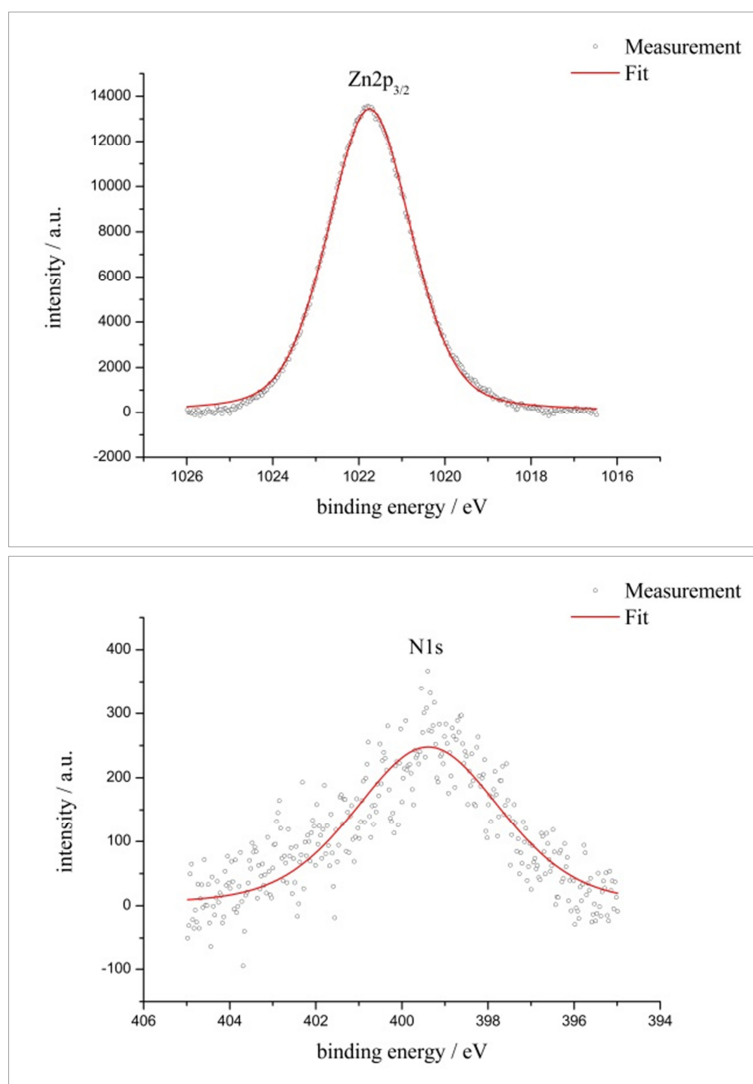


**Figure 8.3.23** XPS spectrum of the Zn2p<sub>3/2</sub> (top) and N1s peak (bottom) of SP-N@MOF-5 (9) with experimental data (dots) and fit (red).

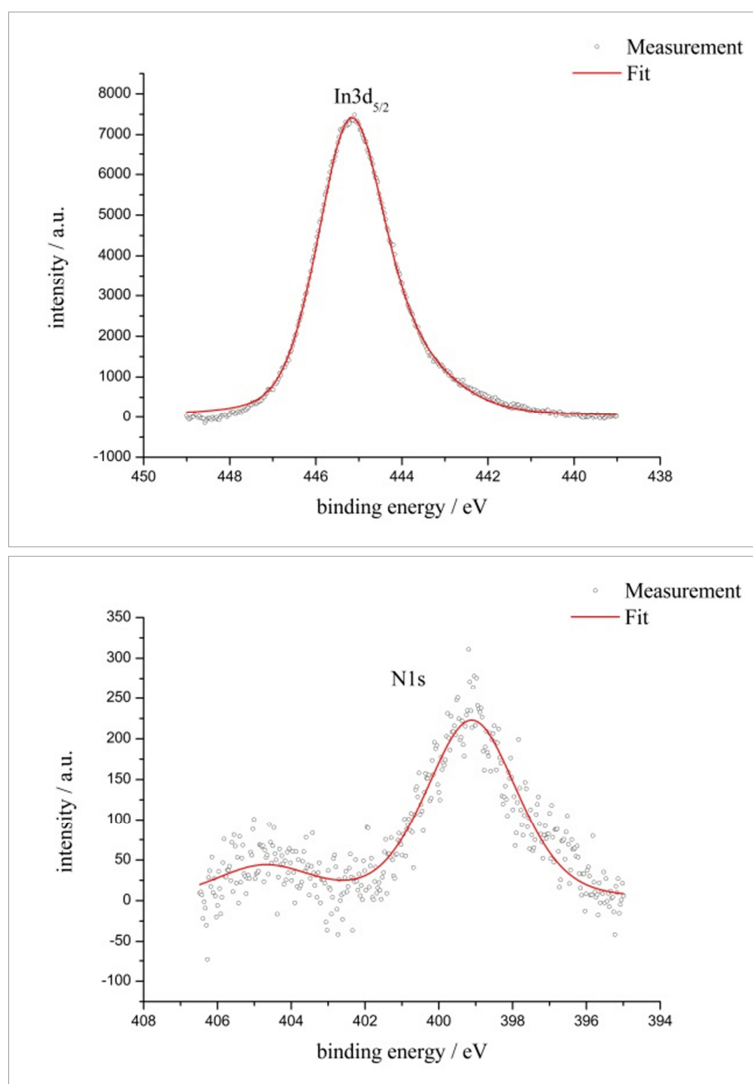


**Figure 8.3.24** XPS spectrum of the In<sub>3d</sub><sub>5/2</sub> (top) and N<sub>1s</sub> peak (bottom) of SP-N@MIL-68(In) (10) with experimental data (dots) and fit (red).

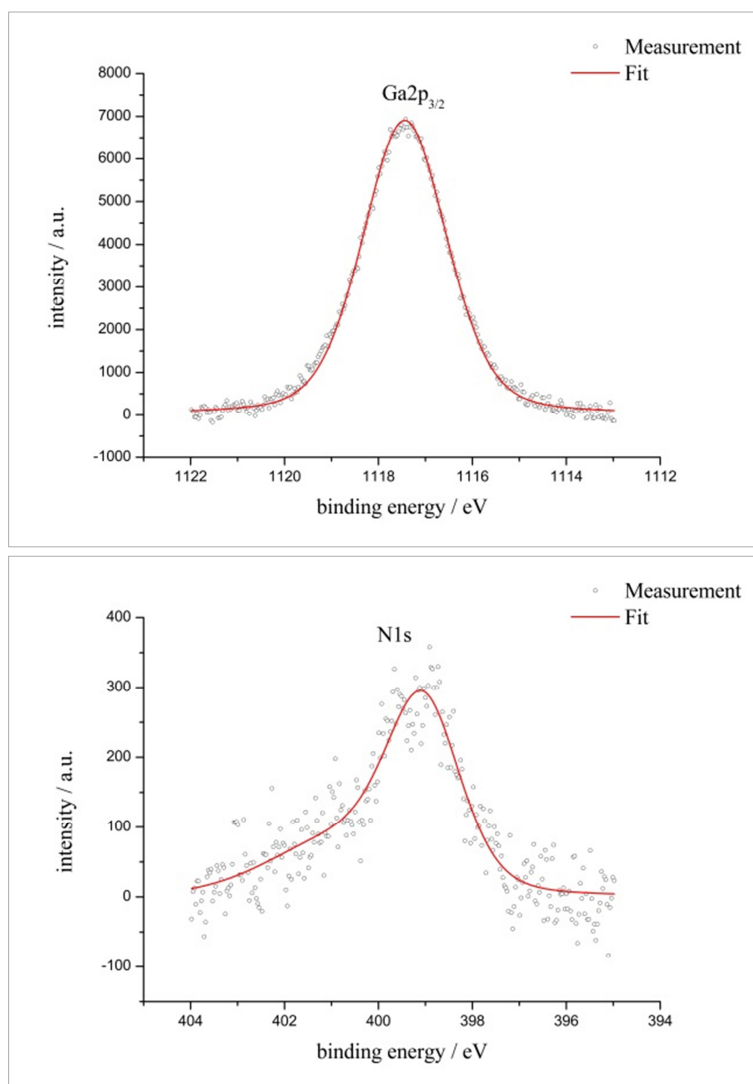


**Figure 8.3.25** XPS spectrum of the Ga<sub>2p<sub>3/2</sub></sub> (top) and N<sub>1s</sub> peak (bottom) of SP-N@MIL-68(Ga) (**11**) with experimental data (dots) and fit (red).

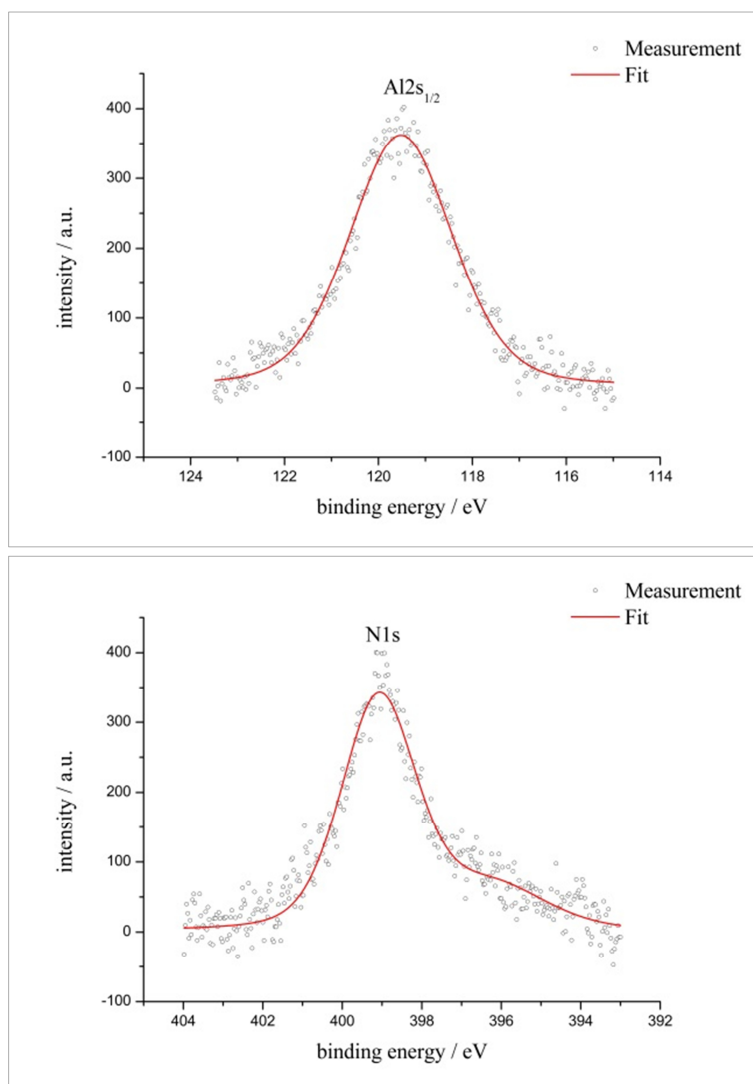


**Figure 8.3.26** XPS spectrum of the Al<sub>2s<sub>1/2</sub></sub> (top) and N<sub>1s</sub> peak (bottom) of SP-N@MIL-53(Al) (12) with experimental data (dots) and fit (red).

**Table 8.3.3** Calculation of the composition of compounds **9** to **12** via XPS.

	<b>9</b>	<b>10</b>	<b>11</b>	<b>12</b>
Nitrogen atoms per formula unit of SP-N	1	1	1	1
Metal atoms per formula unit of the respective MOF	4 [Zn <sub>4</sub> O(bdc) <sub>3</sub> ]	1 [In(OH)(bdc)]	1 [Ga(OH)(bdc)]	1 [Al(OH)(bdc)]
RSF factor for nitrogen	1.77 N1s	1.77 N1s	1.77 N1s	1.77 N1s
RSF factor for the respective metal	18.01 (Zn 2p <sub>3/2</sub> )	13.23 (In 3d <sub>5/2</sub> )	20.47 (Ga 2p <sub>3/2</sub> )	0.681 (Al 2s <sub>1/2</sub> )
Peak area for nitrogen	1218	948	884	1153
Peak area for the respective metal	37404	18548	17867	1149
SP-N : MOF	1.32 : 1	0.38 : 1	0.57 : 1	0.38 : 1

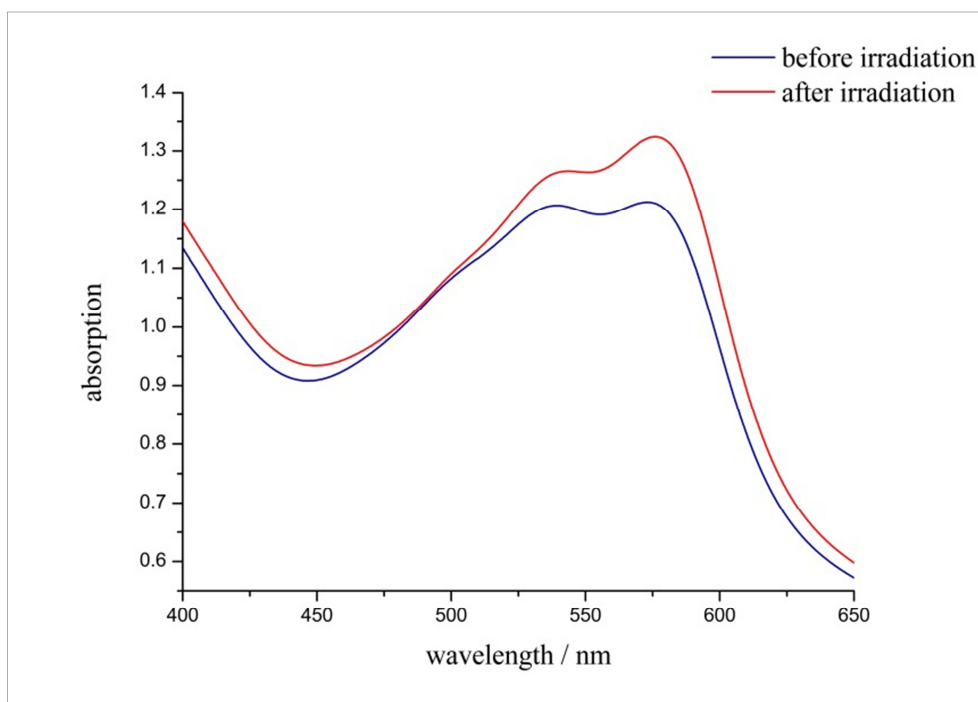


**Figure 8.3.27** Absorption spectra (298 K) of SP-N@MIL-68(In) (**10**) before (blue) and after (red) irradiation with UV light ( $\lambda = 365$  nm, 30 min).

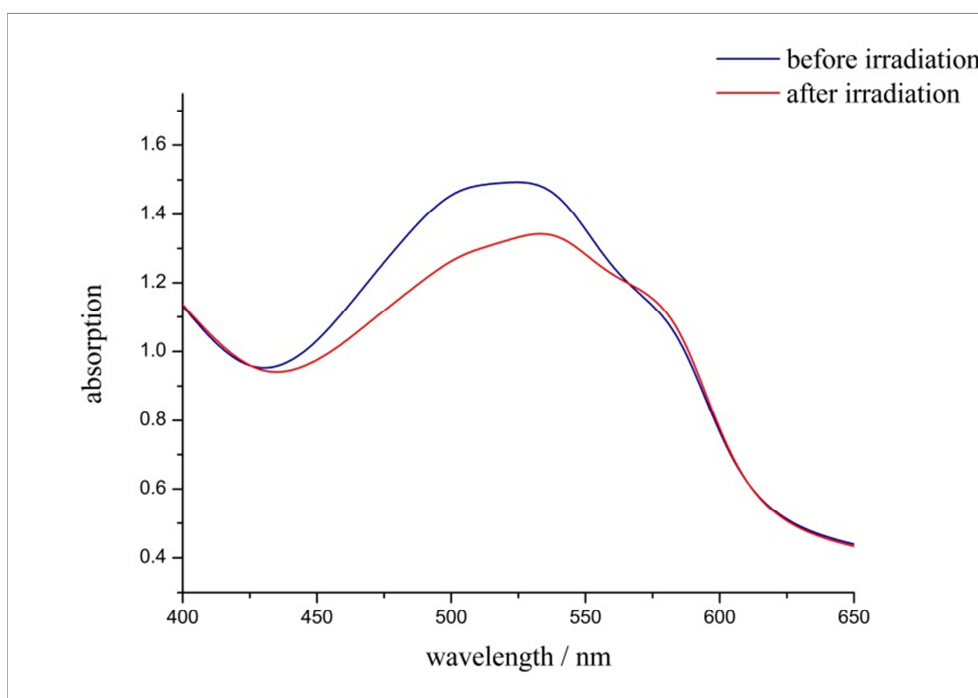


**Figure 8.3.28** Absorption spectra (298 K) of SP-N@MIL-68(Ga) (**11**) before (blue) and after (red) irradiation with UV light ( $\lambda = 365$  nm, 30 min).

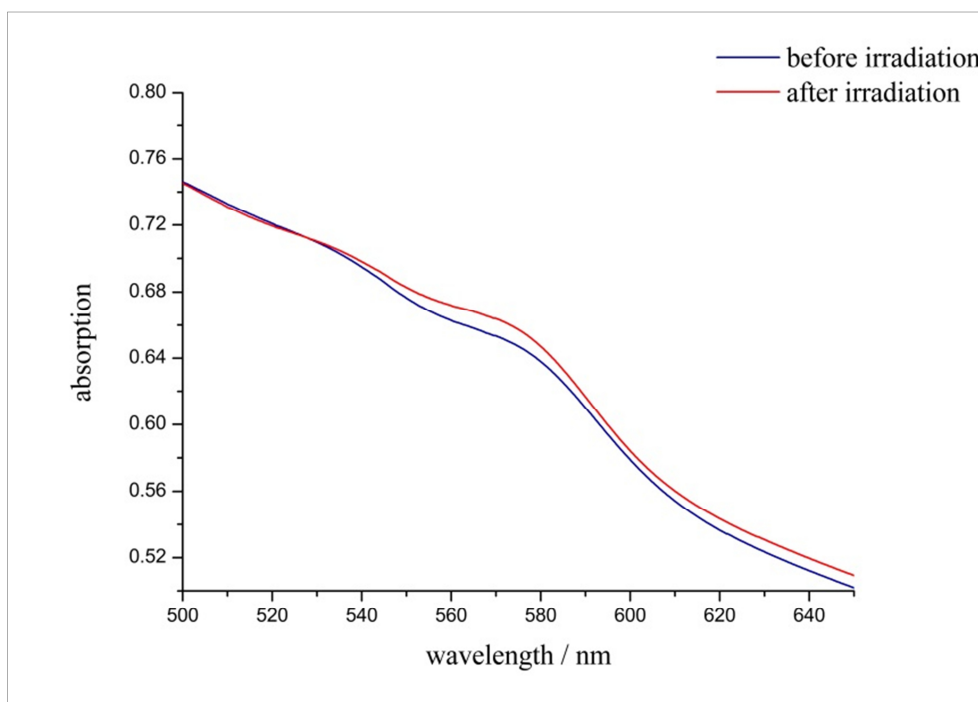


**Figure 8.3.29** Absorption spectra (298 K) of SP-N@MIL-53(Al) (**12**) before (blue) and after (red) irradiation with UV light ( $\lambda = 365$  nm, 30 min).

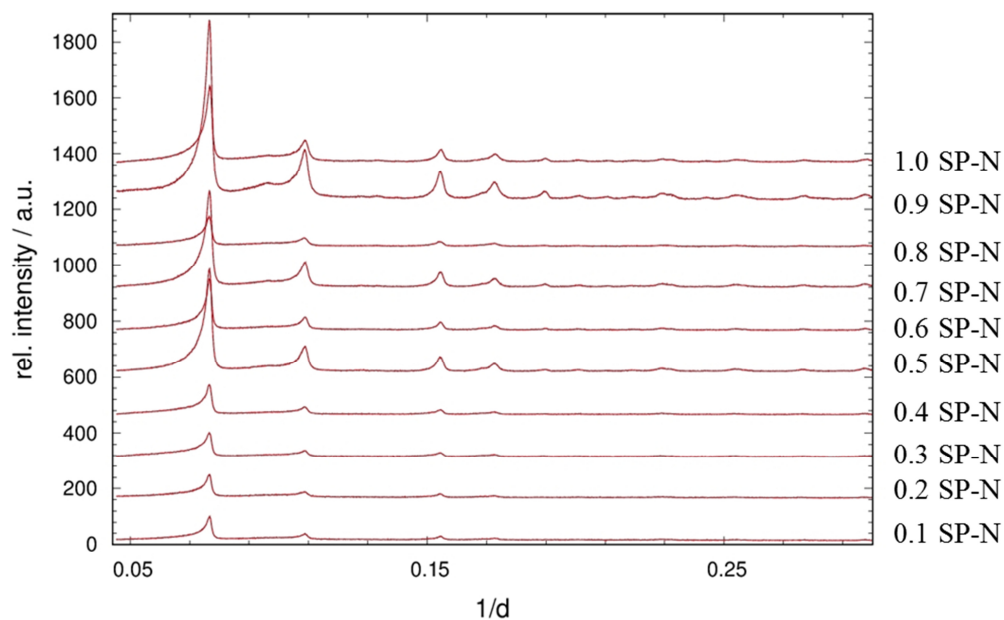


**Figure 8.3.30** Diffraction patterns of the serial dilution of MOF-5 with SP-N.

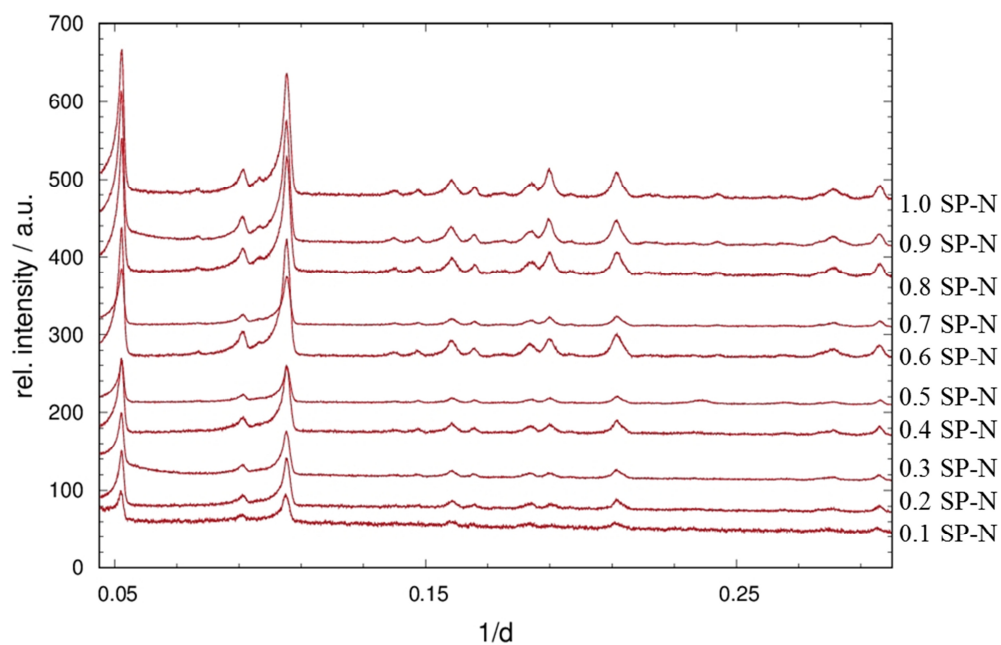


**Figure 8.3.31** Diffraction patterns of the serial dilution of MIL-68(In) with SP-N.

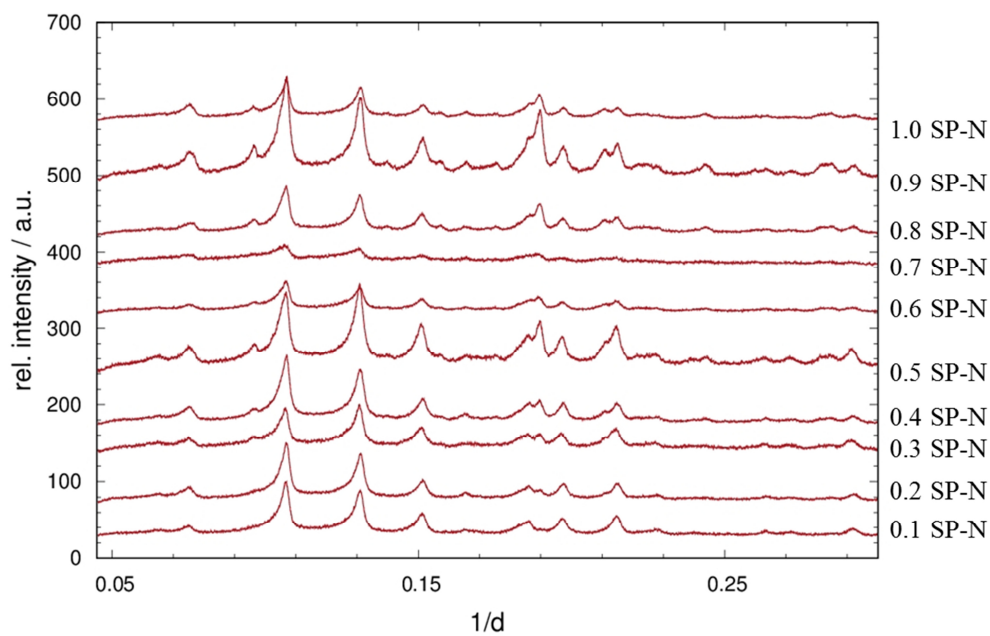


**Figure 8.3.32** Diffraction patterns of the serial dilution of HKUST-1 with SP-N.

### 8.3.3 SP-OMe@MOF systems

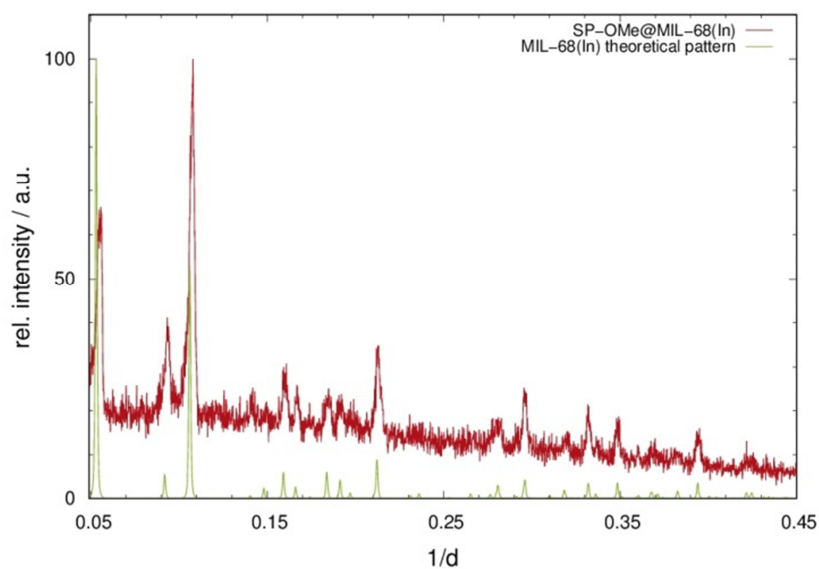


**Figure 8.3.33** XRPD pattern of **(15)** (red), measured at 298 K (*Stoe StadiP*:  $\lambda = 1.54 \text{ \AA}$ ), in comparison to theoretical data of MIL-68(In) (green).

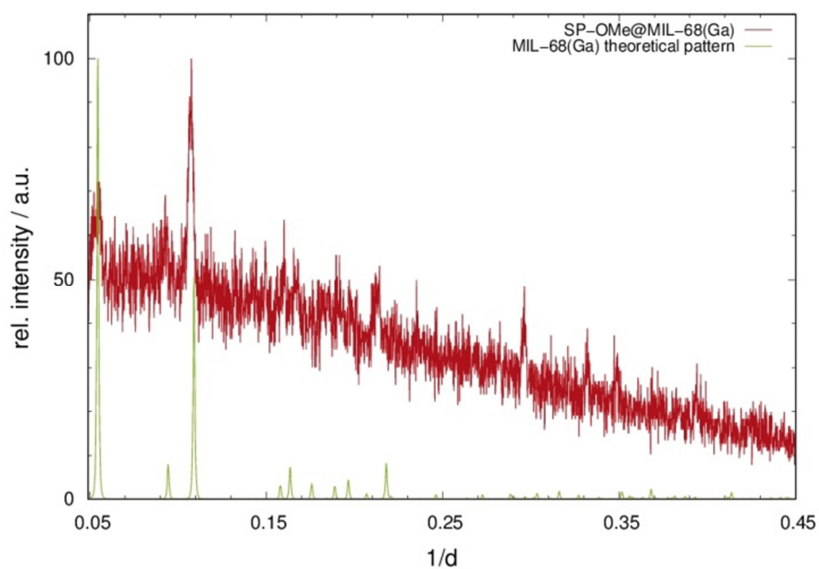


**Figure 8.3.34** XRPD pattern of **(16)** (red), measured at 298 K (*Stoe StadiP*:  $\lambda = 1.54 \text{ \AA}$ ), in comparison to theoretical data of MIL-68(In) (green).

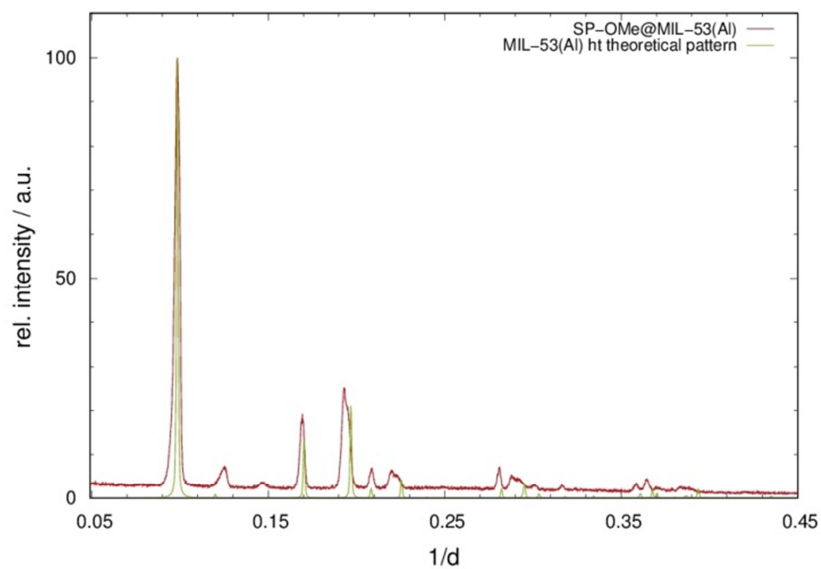


**Figure 8.3.35** XRPD pattern of **(17)** (red), measured at 298 K (*Stoe StadiP*:  $\lambda = 1.54 \text{ \AA}$ ), in comparison to theoretical data of MIL-53(Al) *ht* (green).

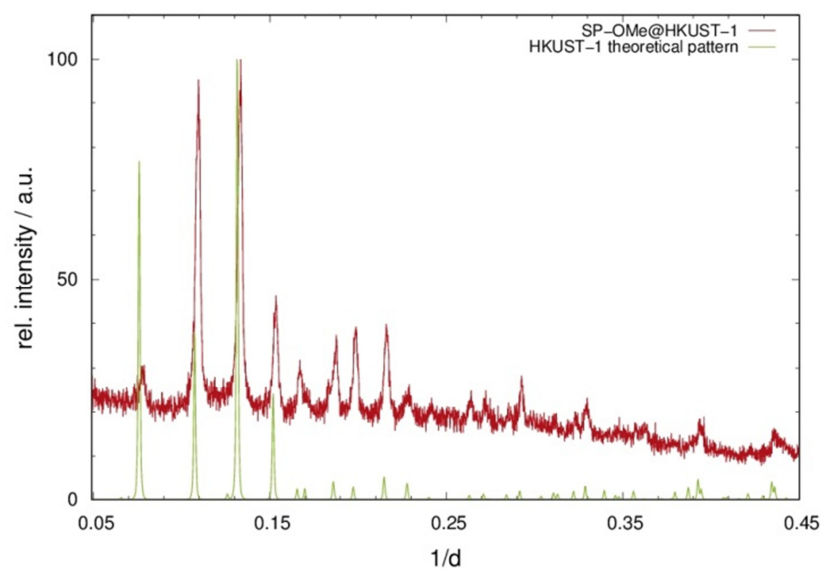


**Figure 8.3.36** XRPD pattern of **(18)** (red), measured at 298 K (*Stoe StadiP*:  $\lambda = 1.54 \text{ \AA}$ ), in comparison to theoretical data of HKUST-1 (green).

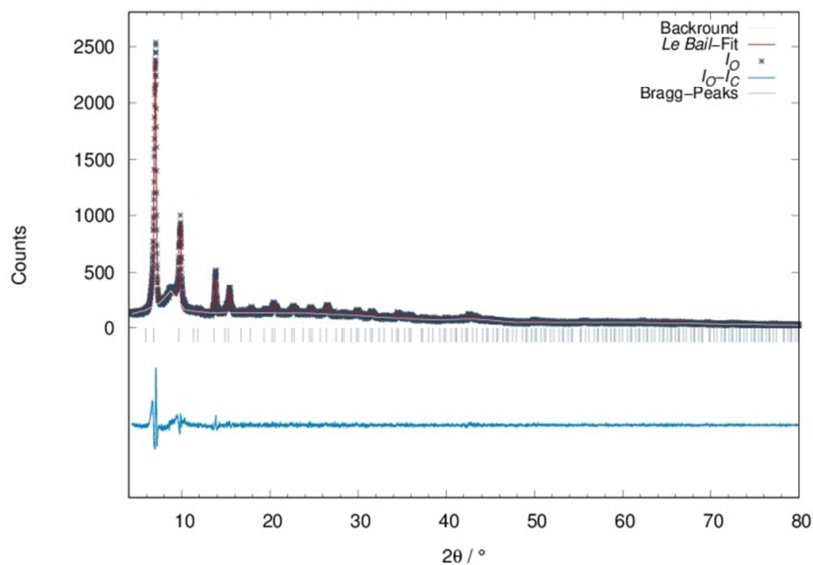


**Figure 8.3.37** *Le Bail* fit of SP-OMe@MOF-5 (**14**) (298 K, *Stoe StadiP*,  $\lambda = 1.54 \text{ \AA}$ ) with measured intensities (grey, crosses), calculated intensities (red), differential curve (turquoise), *Bragg* peaks (light blue, ticks) and background of refinement (white).

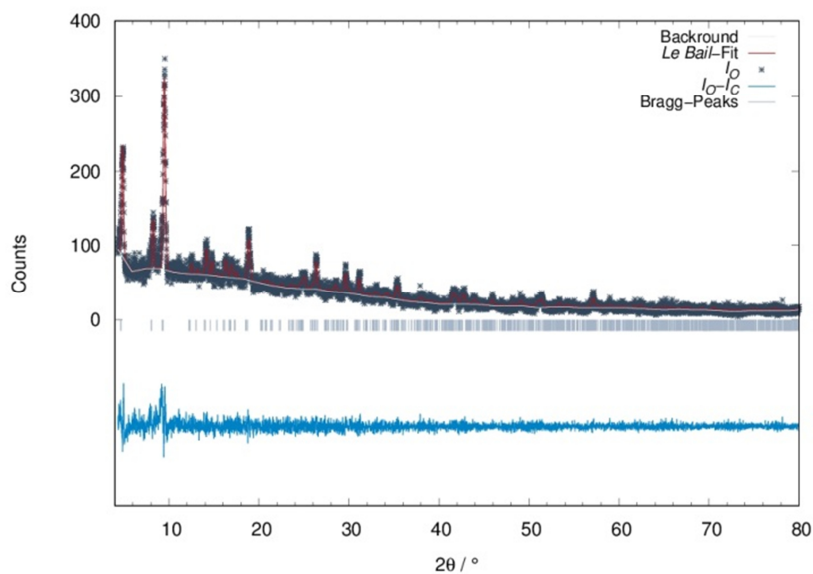


**Figure 8.3.38** *Le Bail* fit of SP-OMe@MIL-68(In) (**15**) (298 K, *Stoe StadiP*,  $\lambda = 1.54 \text{ \AA}$ ) with measured intensities (grey, crosses), calculated intensities (red), differential curve (turquoise), *Bragg* peaks (light blue, ticks) and background of refinement (white).

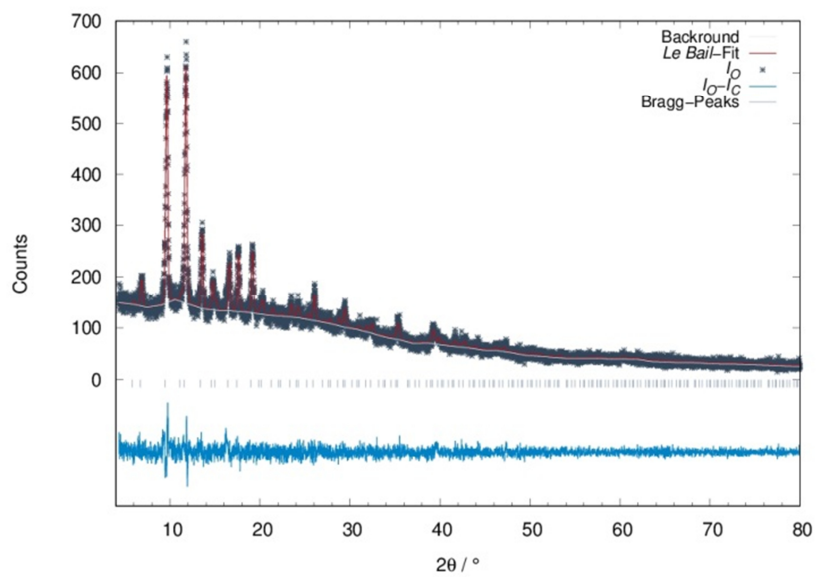


**Figure 8.3.39** *Le Bail* fit of SP-OMe@HKUST-1 (**18**) (298 K, *Stoe StadiP*,  $\lambda = 1.54 \text{ \AA}$ ) with measured intensities (grey, crosses), calculated intensities (red), differential curve (turquoise), *Bragg* peaks (light blue, ticks) and background of refinement (white).

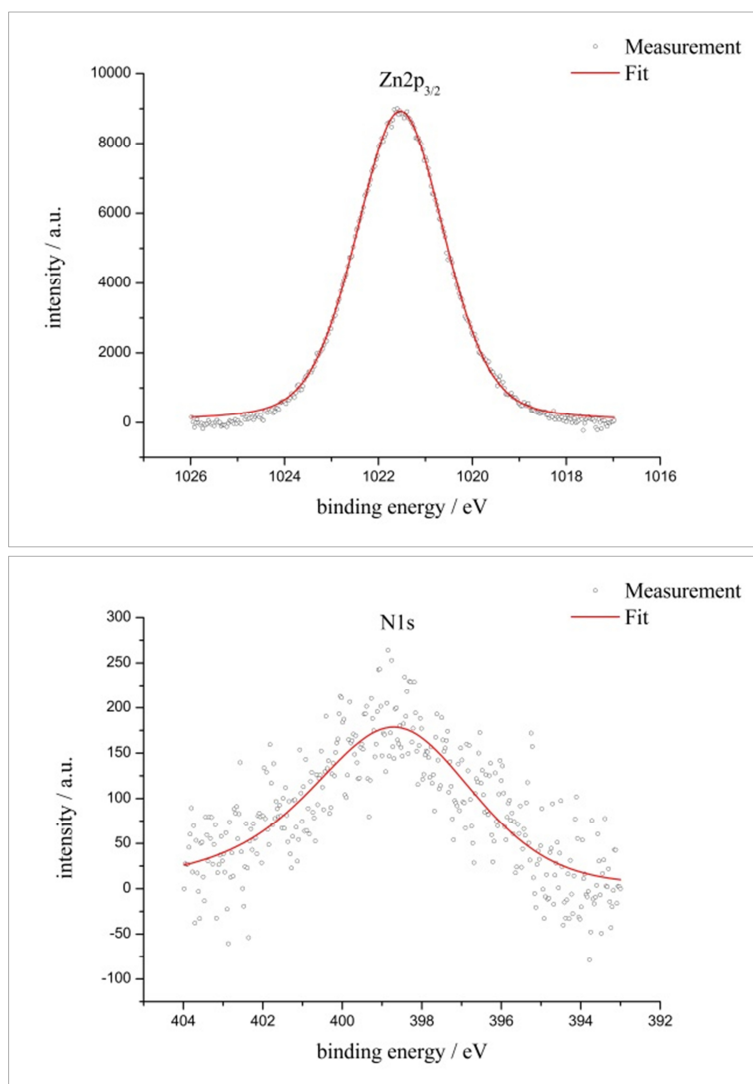


**Figure 8.3.40** XPS spectrum of the Zn2p<sub>3/2</sub> (top) and N1s peak (bottom) of SP-OMe@MOF-5 (14) with experimental data (dots) and fit (red).

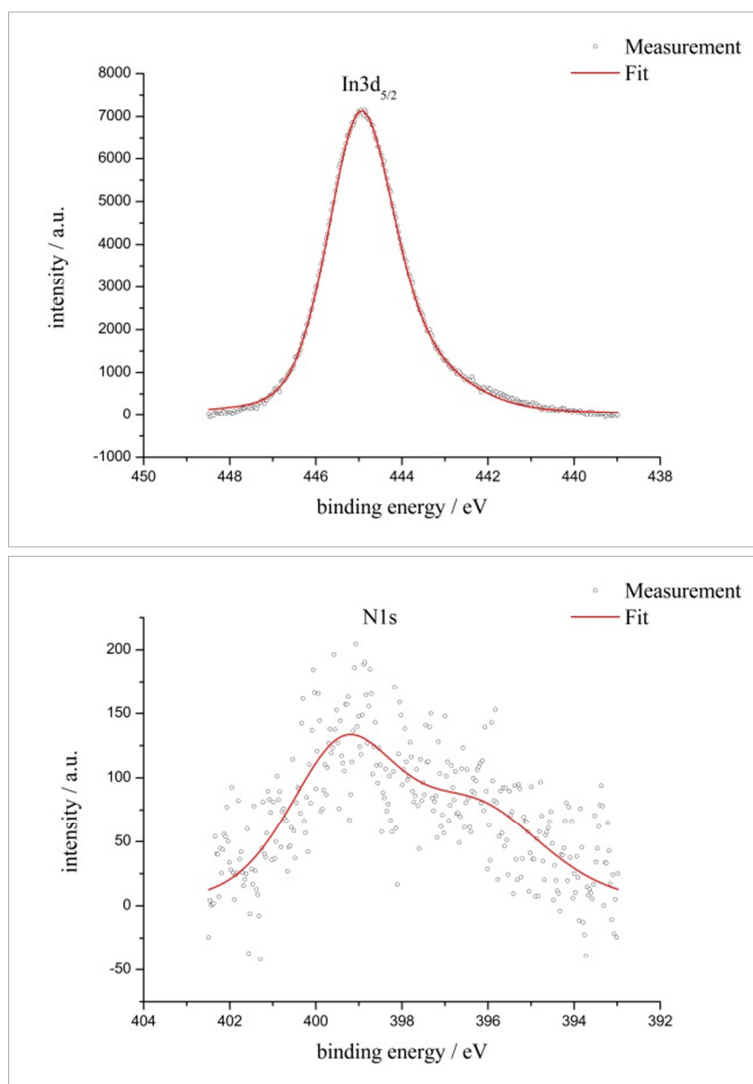


**Figure 8.3.41** XPS spectrum of the In<sub>3d<sub>5/2</sub></sub> (top) and N<sub>1s</sub> peak (bottom) of SP-OMe@MIL-68(In) (**15**) with experimental data (dots) and fit (red).

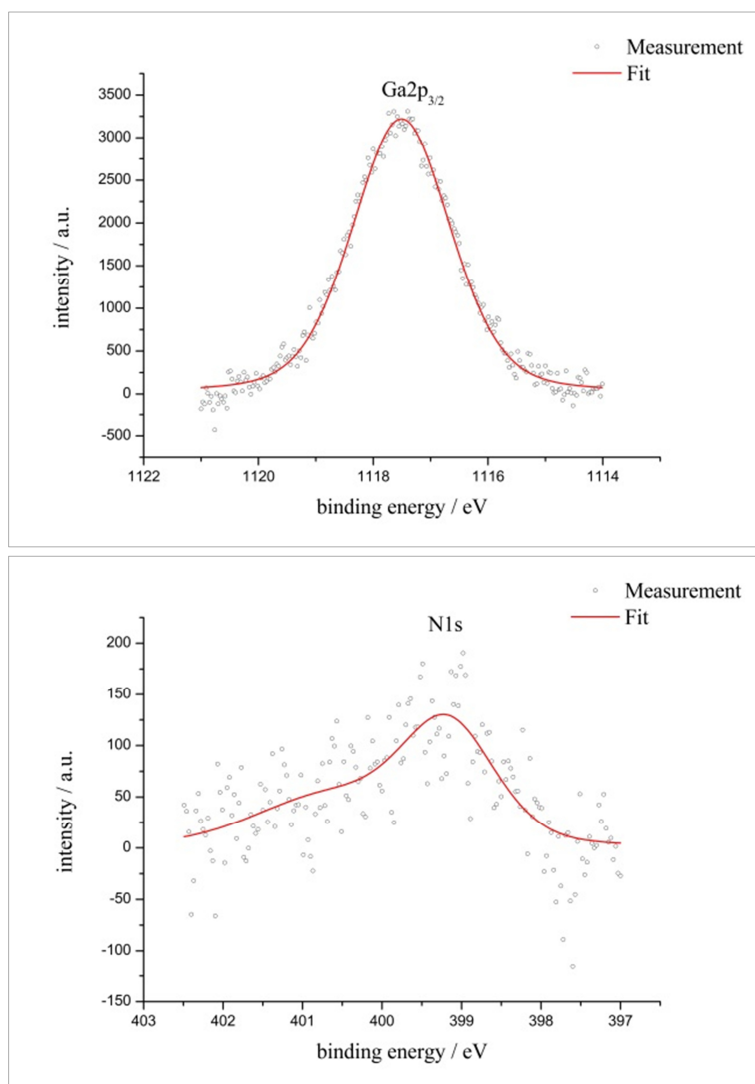


**Figure 8.3.42** XPS spectrum of the Ga<sub>2p<sub>3/2</sub></sub> (top) and N1s peak (bottom) of SP-OMe@MIL-68(Ga) (**16**) with experimental data (dots) and fit (red).

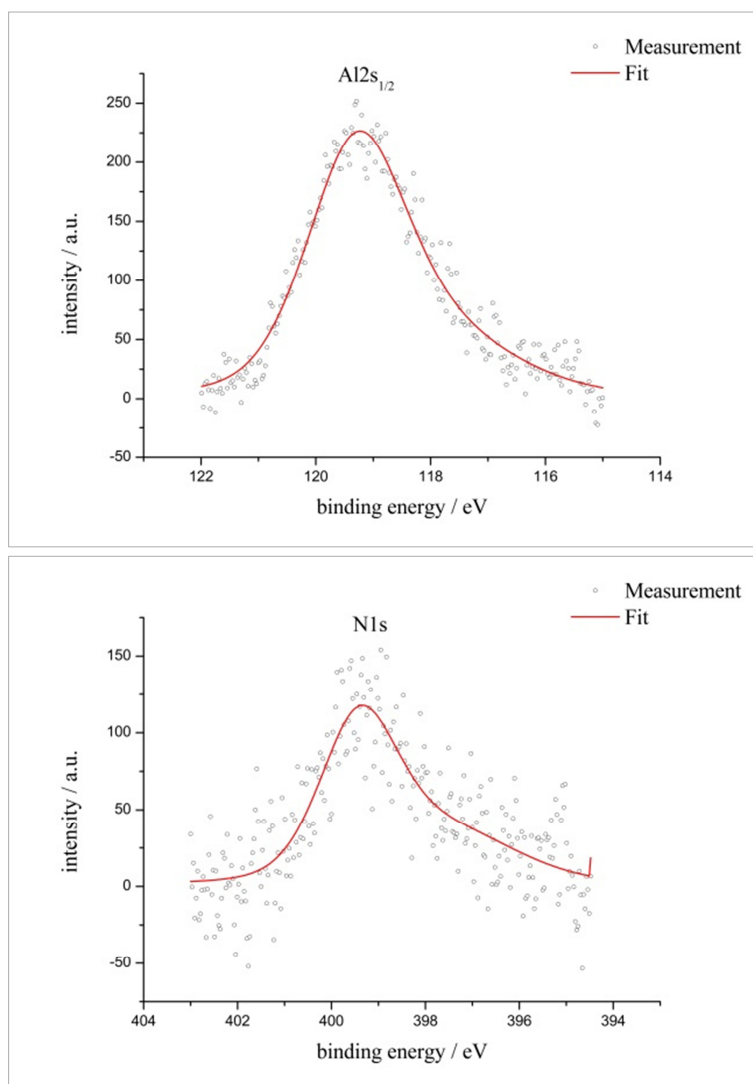


**Figure 8.3.43** XPS spectrum of the  $Al2s_{1/2}$  (top) and  $N1s$  peak (bottom) of SP-OMe@MIL-53(Al) (17) with experimental data (dots) and fit (red).

**Table 8.3.4** Calculation of the composition of compounds **14** to **17** via XPS.

	<b>14</b>	<b>15</b>	<b>16</b>	<b>17</b>
Nitrogen atoms per formula unit of SP-OMe	1	1	1	1
Metal atoms per formula unit of the respective MOF	4 [Zn <sub>4</sub> O(bdc) <sub>3</sub> ]	1 [In(OH)(bdc)]	1 [Ga(OH)(bdc)]	1 [Al(OH)(bdc)]
RSF factor for nitrogen	1.77 N1s	1.77 N1s	1.77 N1s	1.77 N1s
RSF factor for the respective metal	18.01 (Zn 2p <sub>3/2</sub> )	13.23 (In 3d <sub>5/2</sub> )	20.47 (Ga 2p <sub>3/2</sub> )	0.681 (Al 2s <sub>1/2</sub> )
Peak area for nitrogen	1106	763	328	392
Peak area for the respective metal	24214	17591	7956	675
SP-OMe : MOF	1.86 : 1	0.32 : 1	0.47 : 1	0.22 : 1

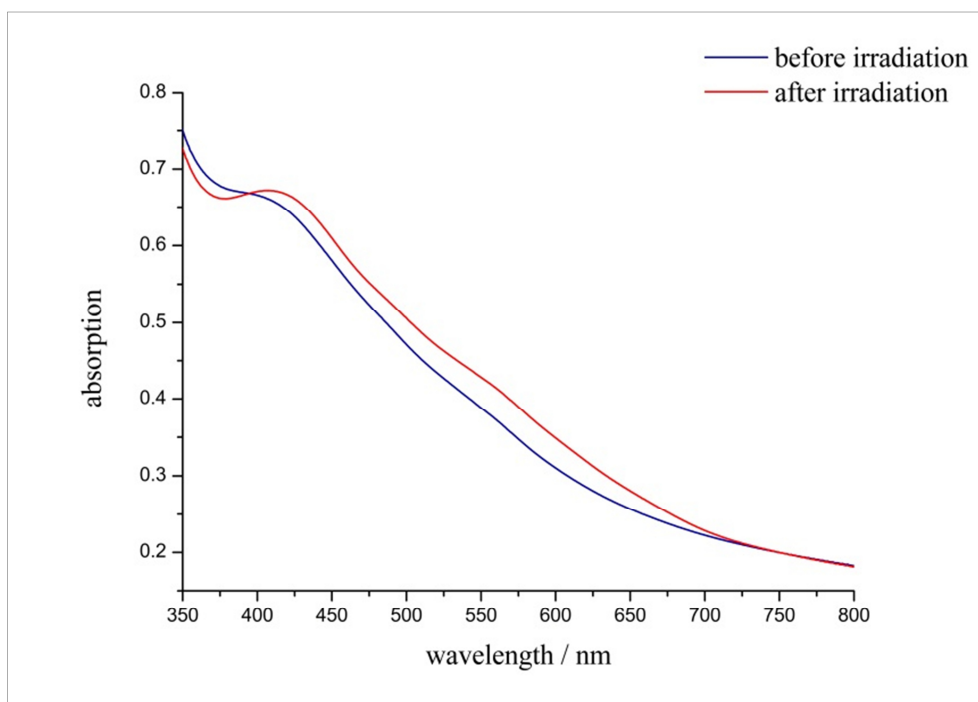


**Figure 8.3.44** Absorption spectra (298 K) of SP-OMe@MIL-68(In) (**15**) before (blue) and after (red) irradiation with UV light ( $\lambda = 365$  nm, 30 min).

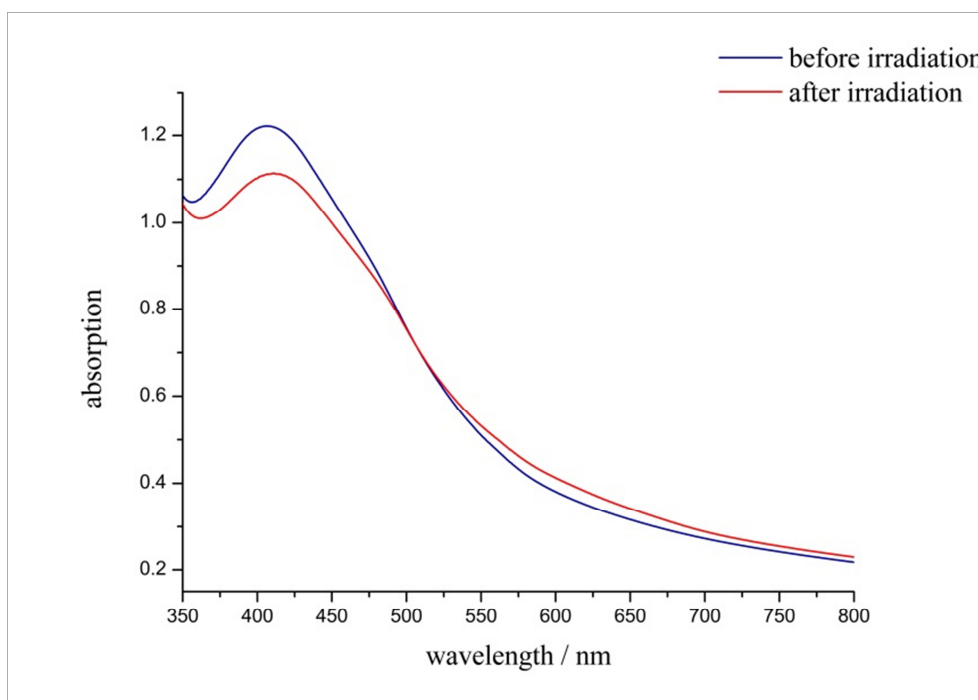


**Figure 8.3.45** Absorption spectra (298 K) of SP-OMe@MIL-68(Ga) (**16**) before (blue) and after (red) irradiation with UV light ( $\lambda = 365$  nm, 30 min).

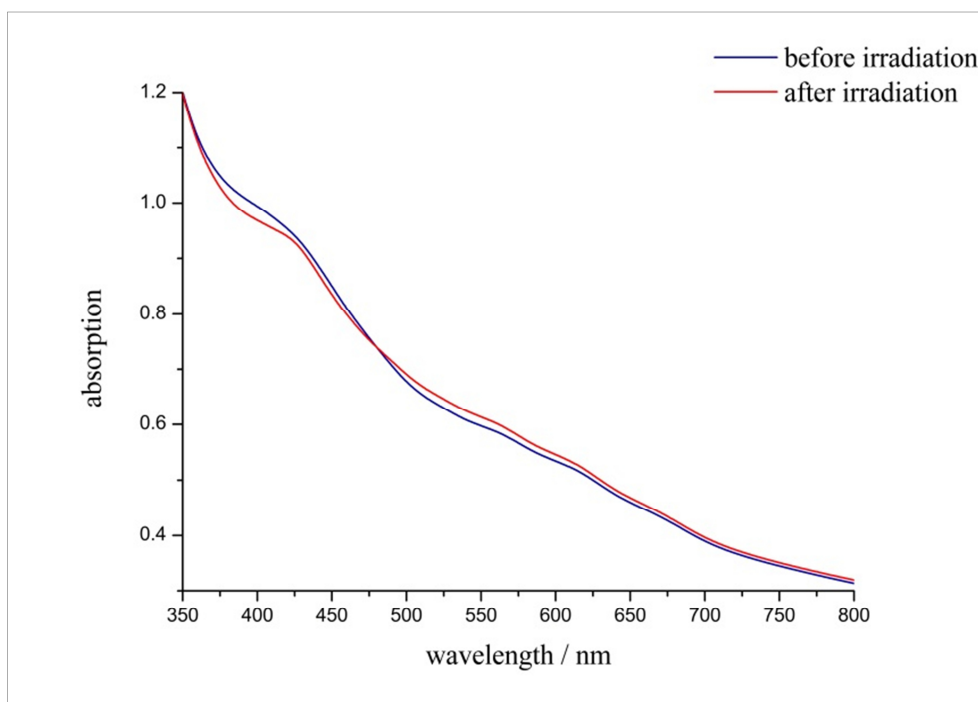


**Figure 8.3.46** Absorption spectra (298 K) of SP-OMe@MIL-53(Al) (**17**) before (blue) and after (red) irradiation with UV light ( $\lambda = 365$  nm, 10 min).

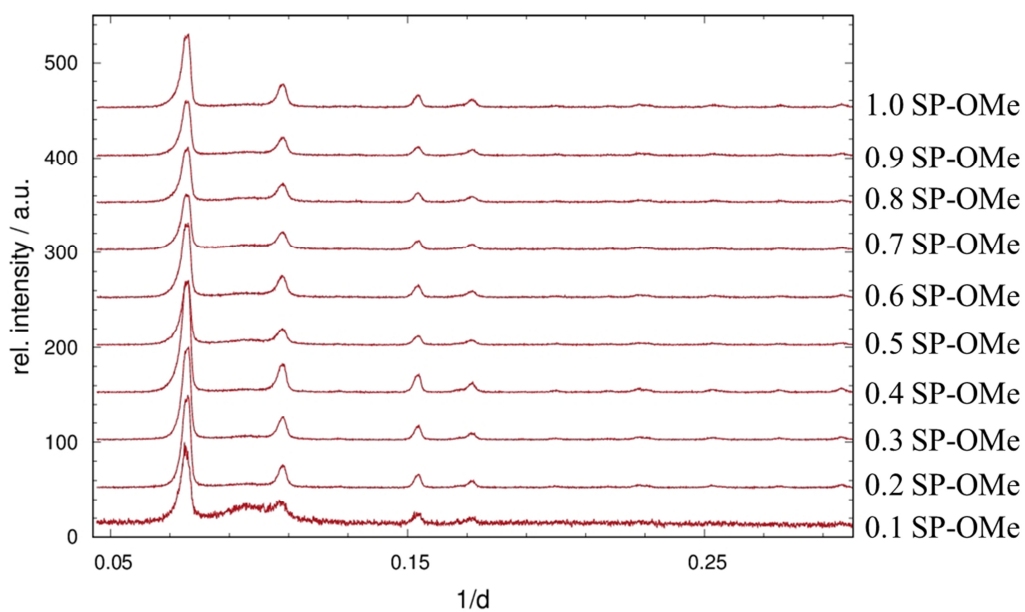


**Figure 8.3.47** Diffraction patterns of the serial dilution of MOF-5 with SP-OMe.

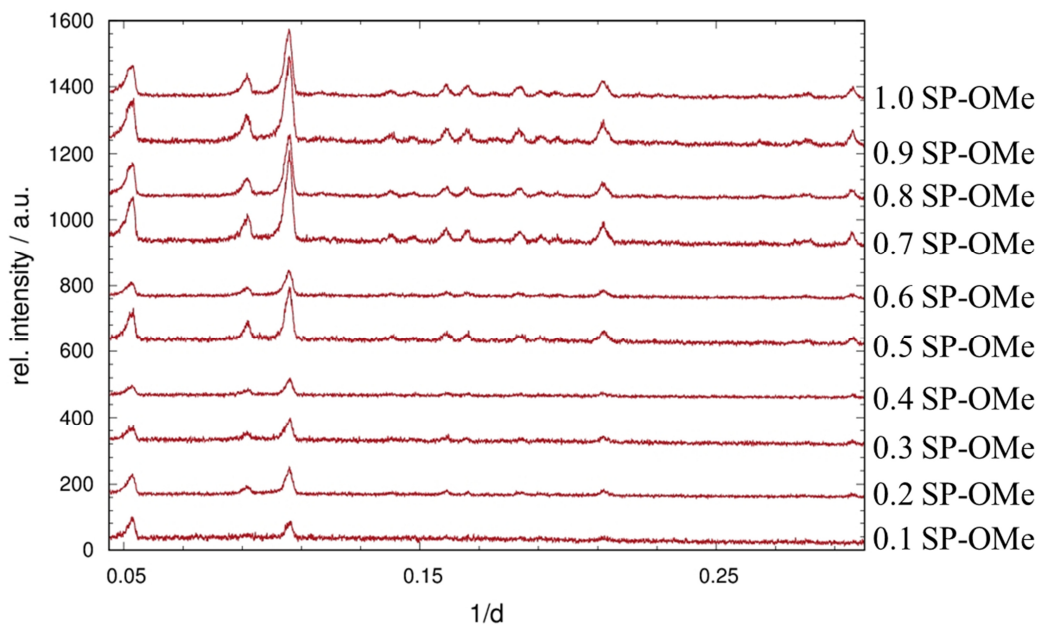


**Figure 8.3.48** Diffraction patterns of the serial dilution of MIL-68(In) with SP-OMe.

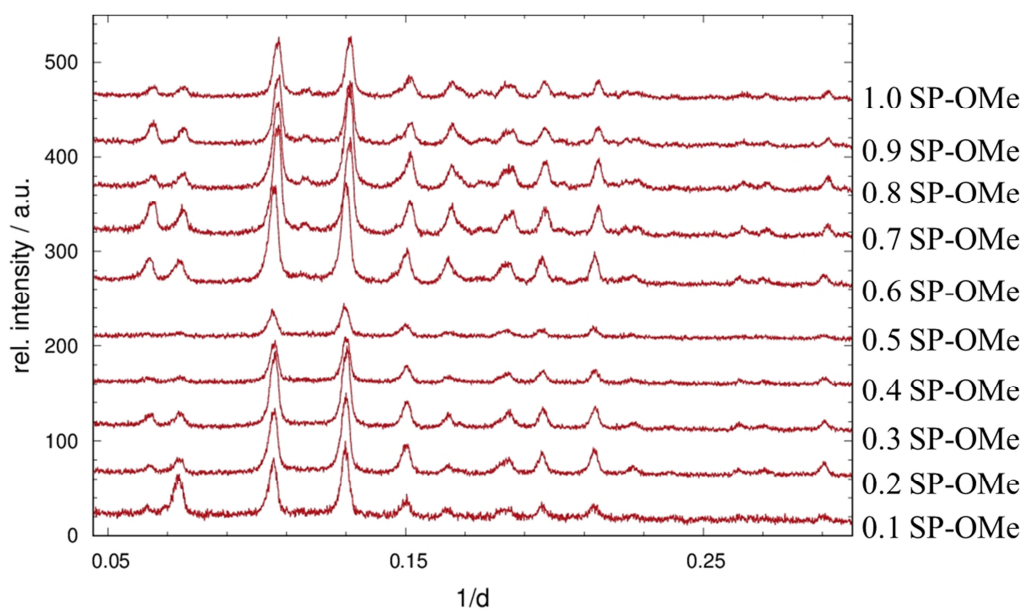


**Figure 8.3.49** Diffraction patterns of the serial dilution of HKUST-1 with SP-OMe.

## 8.4 SP-O@MOF hybrid materials

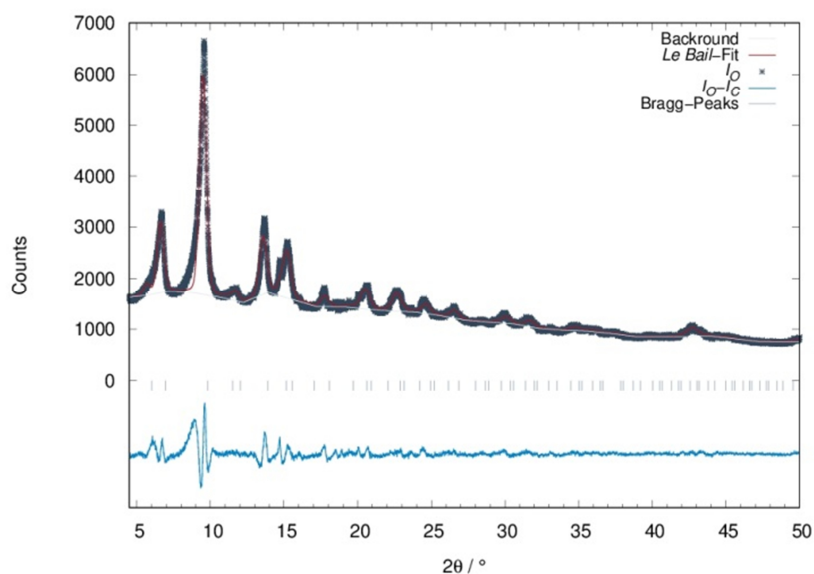


**Figure 8.4.1** *Le Bail* fit of SP-O@MOF-5 (**19**) (298 K, *Huber G670*,  $\lambda = 1.54 \text{ \AA}$ ) with measured intensities (grey, crosses), calculated intensities (red), differential curve (turquoise), *Bragg* peaks (light blue, ticks) and background of refinement (white).

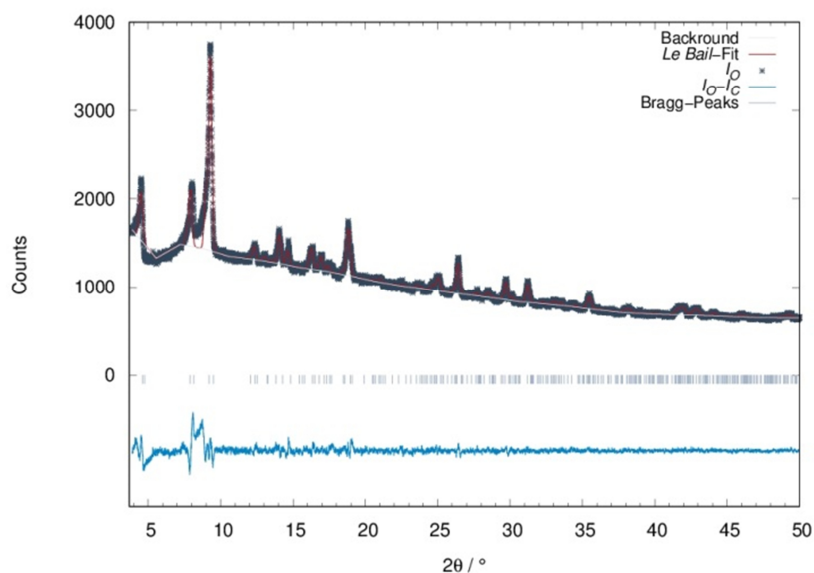


**Figure 8.4.2** *Le Bail* fit of SP-O@MIL-68(In) (**20**) (298 K, *Huber G670*,  $\lambda = 1.54 \text{ \AA}$ ) with measured intensities (grey, crosses), calculated intensities (red), differential curve (turquoise), *Bragg* peaks (light blue, ticks) and background of refinement (white).

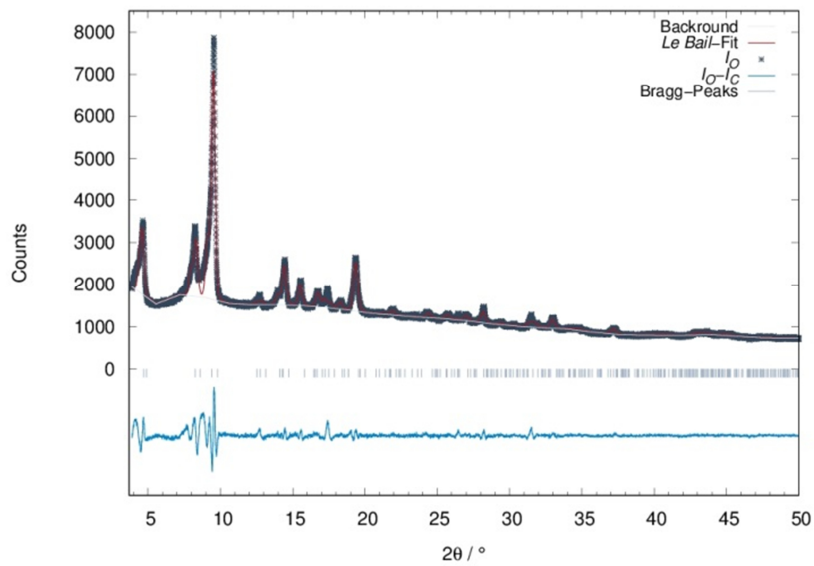


**Figure 8.4.3** *Le Bail* fit of SP-O@MIL-68(Ga) (**21**) (298 K, *Huber G670*,  $\lambda = 1.54 \text{ \AA}$ ) with measured intensities (grey, crosses), calculated intensities (red), differential curve (turquoise), *Bragg* peaks (light blue, ticks) and background of refinement (white).

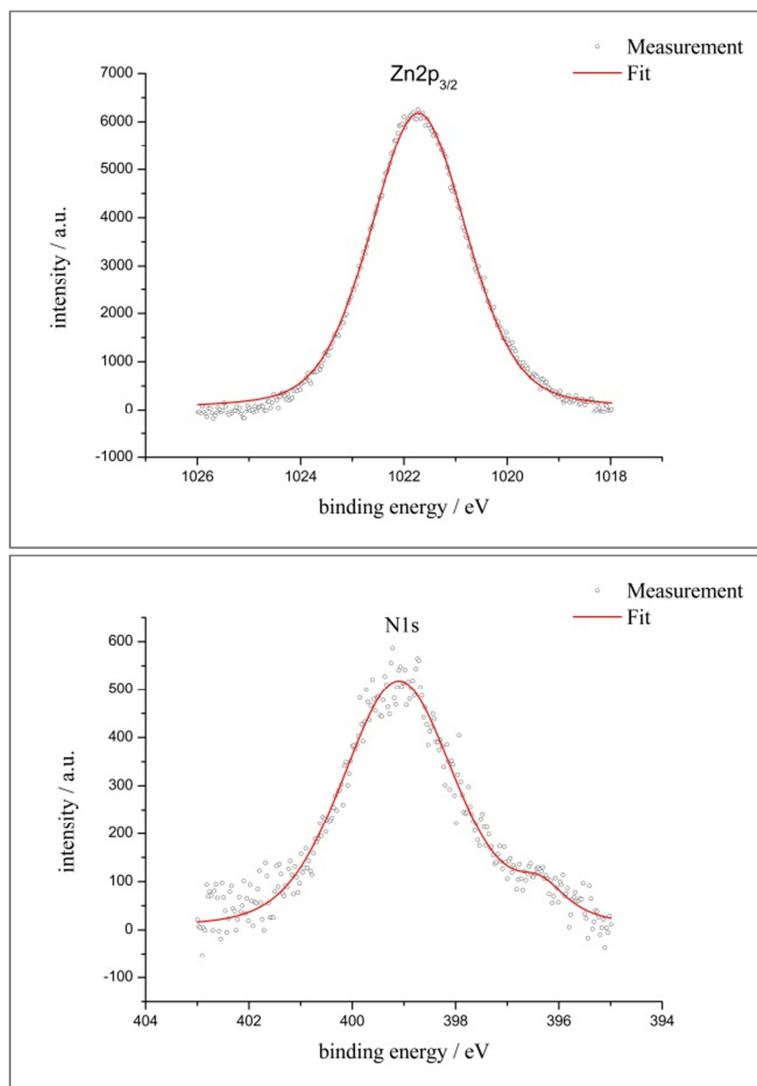


**Figure 8.4.4** XPS spectrum of the Zn2p<sub>3/2</sub> (top) and N1s peak (bottom) of SP-O@MOF-5 (**19**) with experimental data (dots) and fit (red).

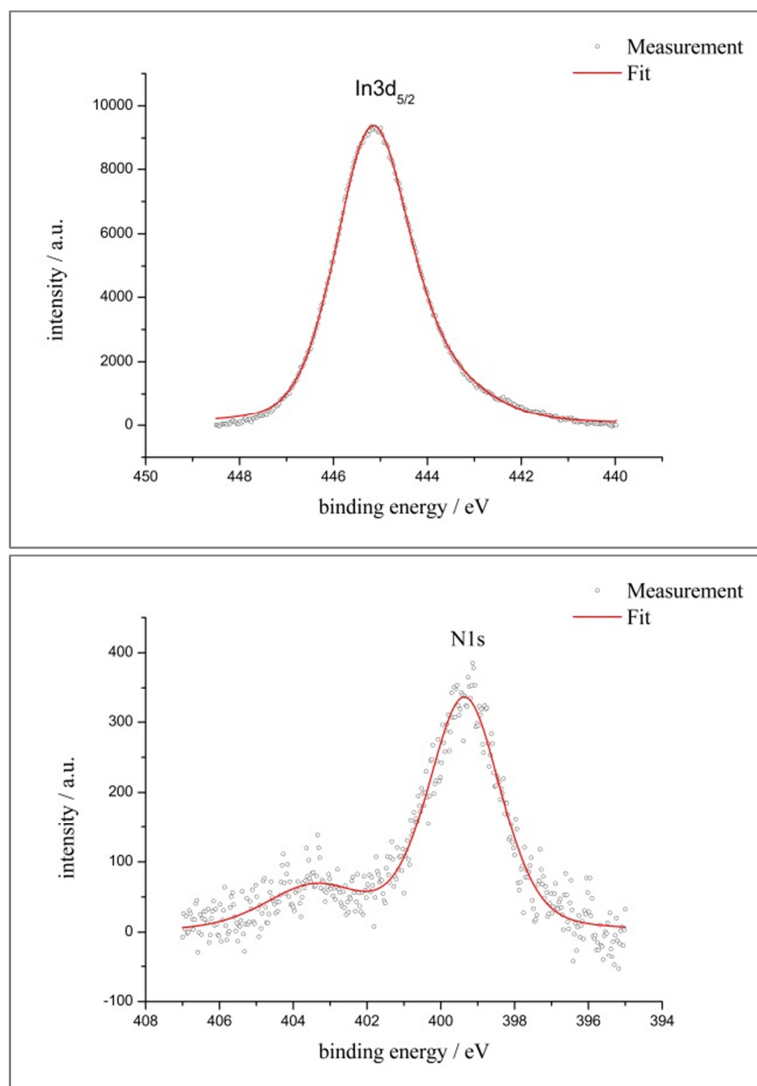


**Figure 8.4.5** XPS spectrum of the In<sub>3d<sub>5/2</sub></sub> (top) and N<sub>1s</sub> peak (bottom) of SP-O@MIL-68(In) (20) with experimental data (dots) and fit (red).

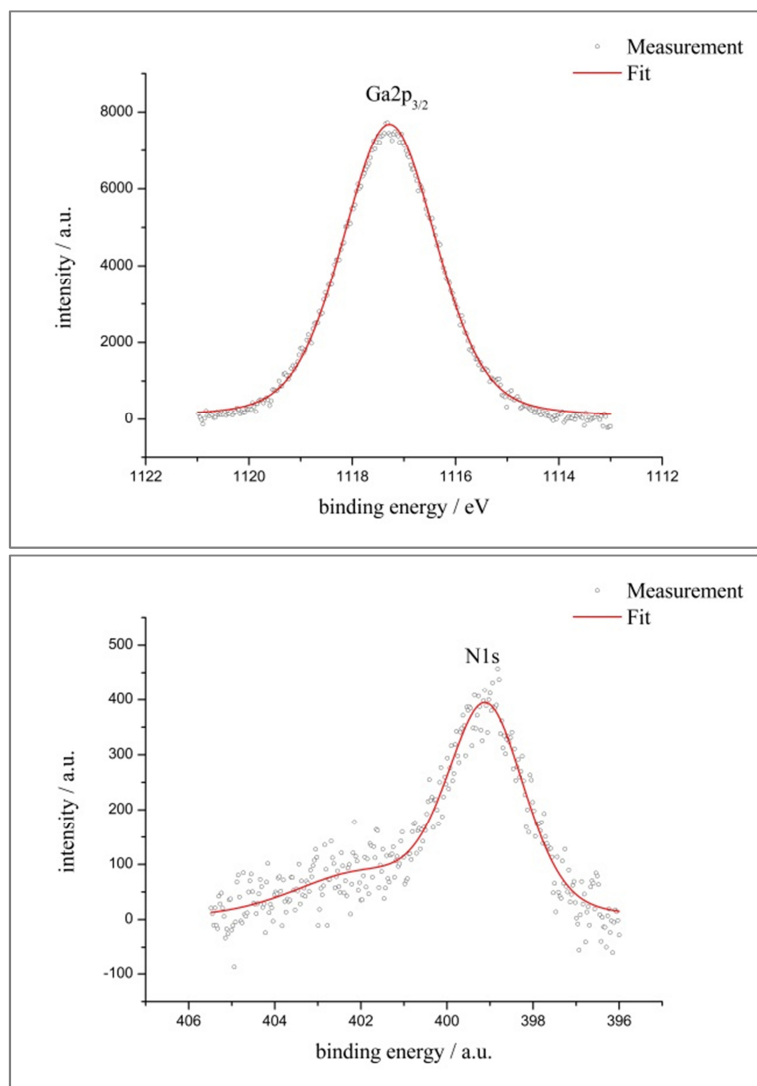


**Figure 8.4.6** XPS spectrum of the Ga<sub>2p<sub>3/2</sub></sub> and N1s peak of SP-O@MIL-68(Ga) (**21**) with experimental data (dots) and fit (red).

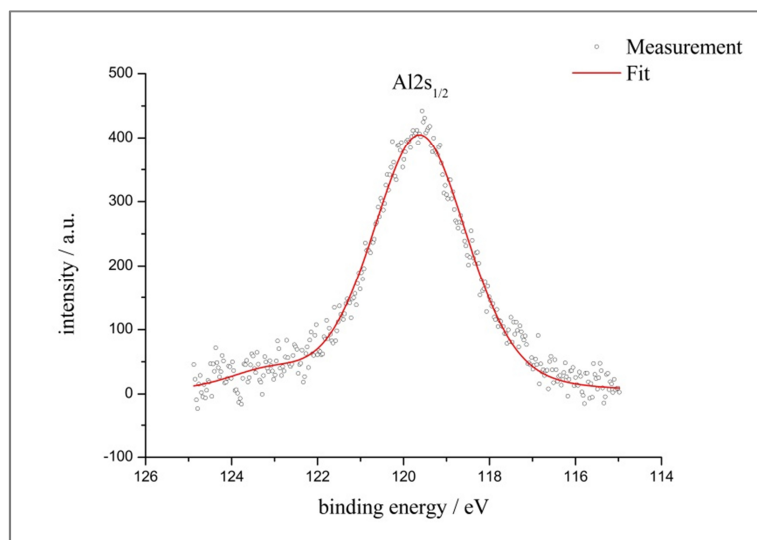


**Figure 8.4.7** XPS spectrum of the Al<sub>2s<sub>1/2</sub></sub> of SP-O@MIL-53(Al) (**22**) with experimental data (dots) and fit (red).

**Table 8.4.1** Calculation of the composition of compounds **19** to **22** via XPS.

	<b>19</b>	<b>20</b>	<b>21</b>	<b>22</b>
Nitrogen atoms per formula unit of SP-O	2	2	2	2
Metal atoms per formula unit of the respective MOF	4 [Zn <sub>4</sub> O(bdc) <sub>3</sub> ]	1 [In(OH)(bdc)]	1 [Ga(OH)(bdc)]	1 [Al(OH)(bdc)]
RSF factor for nitrogen	1.77 N1s	1.77 N1s	1.77 N1s	1.77 N1s
RSF factor for the respective metal	18.01 (Zn 2p <sub>3/2</sub> )	13.23 (In 3d <sub>5/2</sub> )	20.47 (Ga 2p <sub>3/2</sub> )	0.681 (Al 2s <sub>1/2</sub> )
Peak area for nitrogen	1743	1183	1036	944
Peak area for the respective metal	16537	23288	20127	1366
SP-O : MOF	2.15: 1	0.19 : 1	0.29: 1	0.13 : 1

## 8.5 Phth@MOF/PM systems

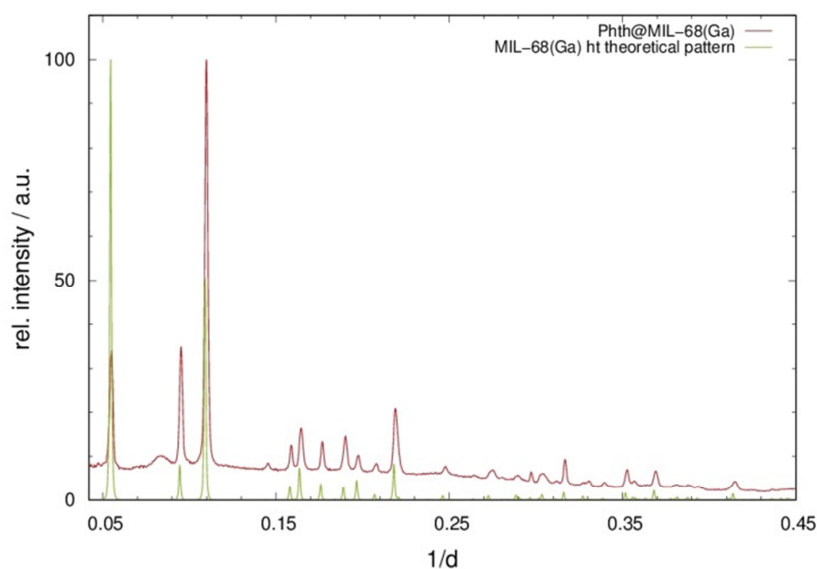


**Figure 8.5.1** XRPD pattern of **(25)** (red), measured at 298 K (BL9/DELTA:  $\lambda = 0.49594 \text{ \AA}$ ), in comparison to theoretical data of MIL-68(Ga) (green).

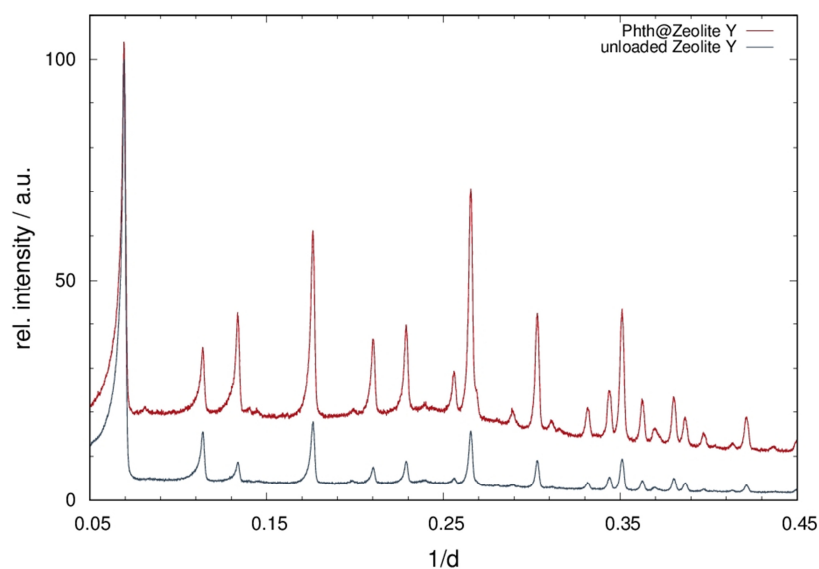


**Figure 8.5.2** XRPD pattern of **(27)** (red) in comparison to unloaded Zeolite Y (blue-grey), measured at 298 K (*Huber G670*:  $\lambda = 1.54 \text{ \AA}$ ).

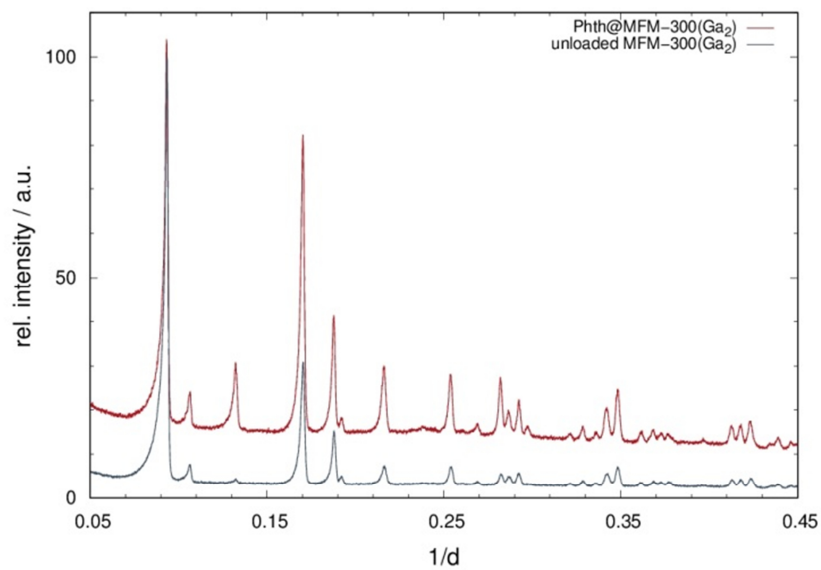


**Figure 8.5.3** XRPD pattern of **(28)** (red) in comparison to unloaded MFM-300(Ga<sub>2</sub>) (blue-grey), measured at 298 K (*Huber G670*:  $\lambda = 1.54 \text{ \AA}$ ).

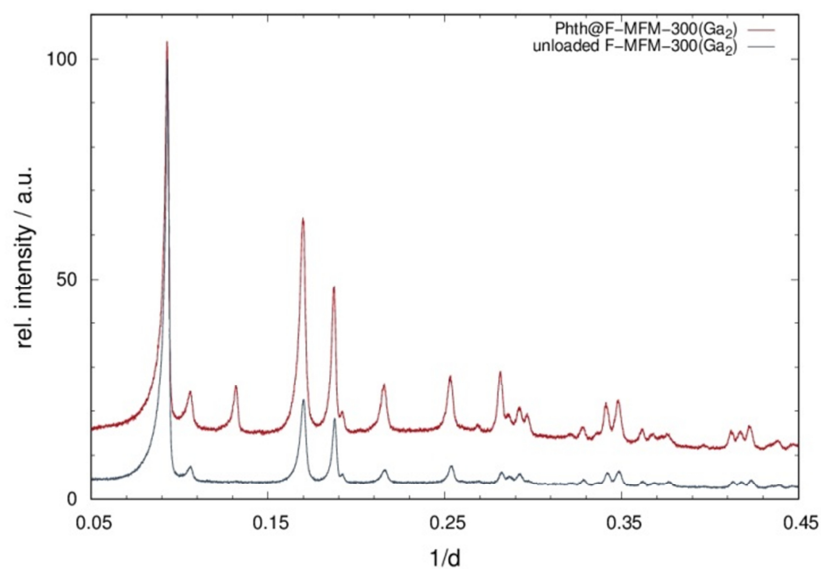


**Figure 8.5.4** XRPD pattern of **(29)** (red) in comparison to unloaded F-MFM-300(Ga<sub>2</sub>) (blue-grey), measured at 298 K (*Huber G670*:  $\lambda = 1.54 \text{ \AA}$ ).

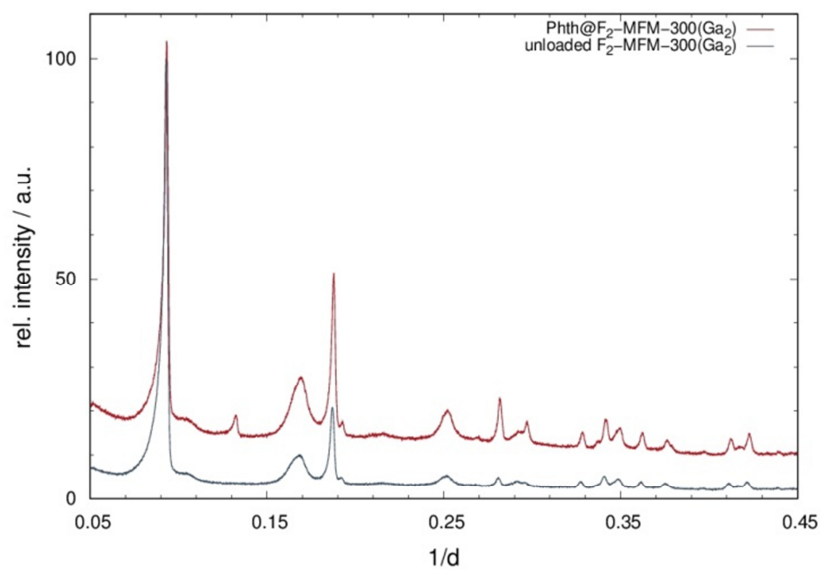


**Figure 8.5.5** XRPD pattern of **(30)** (red) in comparison to unloaded  $F_2$ -MFM-300( $Ga_2$ ) (blue-grey), measured at 298 K (*Huber G670*:  $\lambda = 1.54 \text{ \AA}$ ).

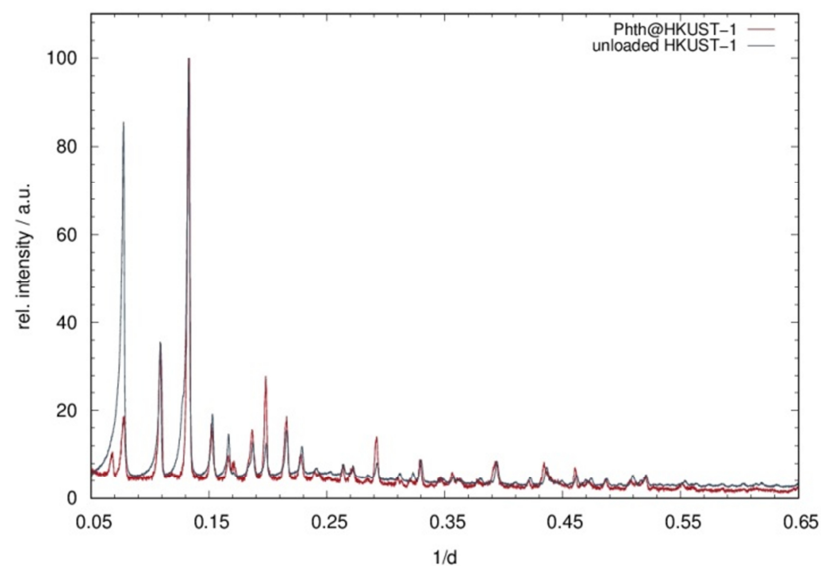


**Figure 8.5.6** XRPD pattern of **(31)** (red) in comparison to unloaded HKUST-1 (blue-grey), measured at 298 K (*Stoe Stadi P*:  $\lambda = 1.54 \text{ \AA}$ ).

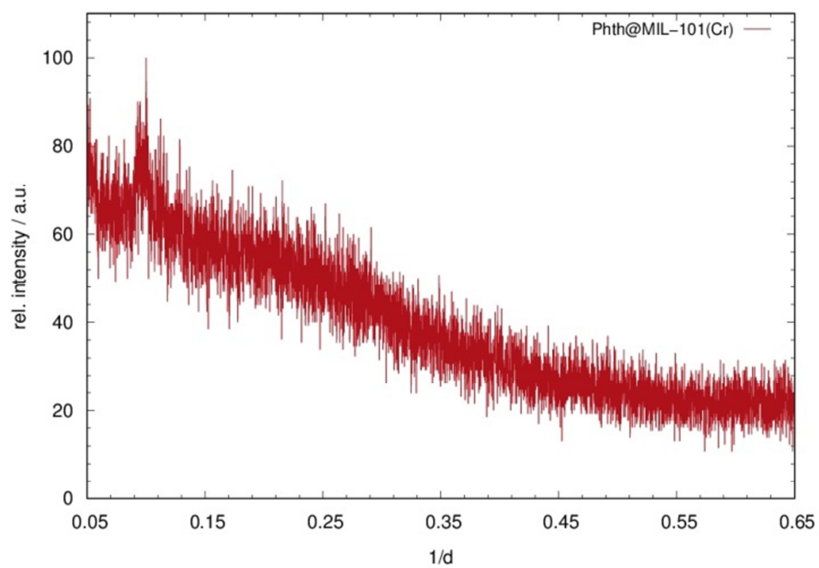


**Figure 8.5.7** XRPD pattern of (32) (red) measured at 298 K (*Stoe Stadi P*:  $\lambda = 1.54 \text{ \AA}$ ).

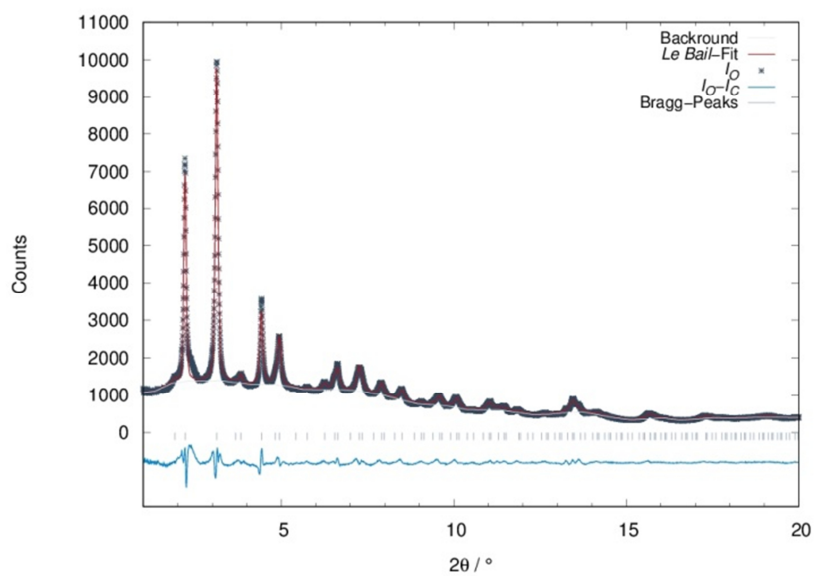


**Figure 8.5.8** *Le Bail* fit of Phth@MOF-5 (23) (298 K, BL9/DELTA:  $\lambda = 0.49594 \text{ \AA}$ ).

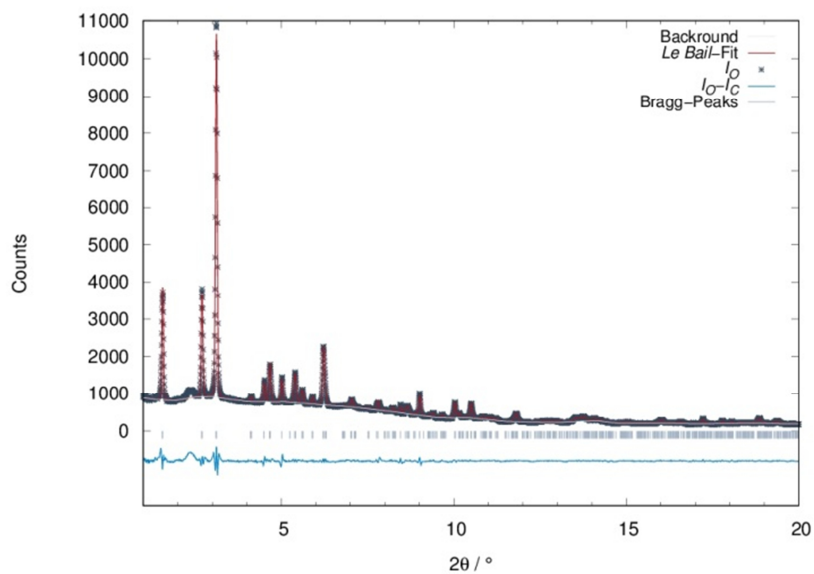


**Figure 8.5.9** *Le Bail* fit of Phth@MIL-68(Ga) (**25**) (298 K, BL9/DELTA:  $\lambda = 0.49594 \text{ \AA}$ ) with measured intensities (grey, crosses), calculated intensities (red), differential curve (turquoise), *Bragg* peaks (light blue, ticks) and background of refinement (white).

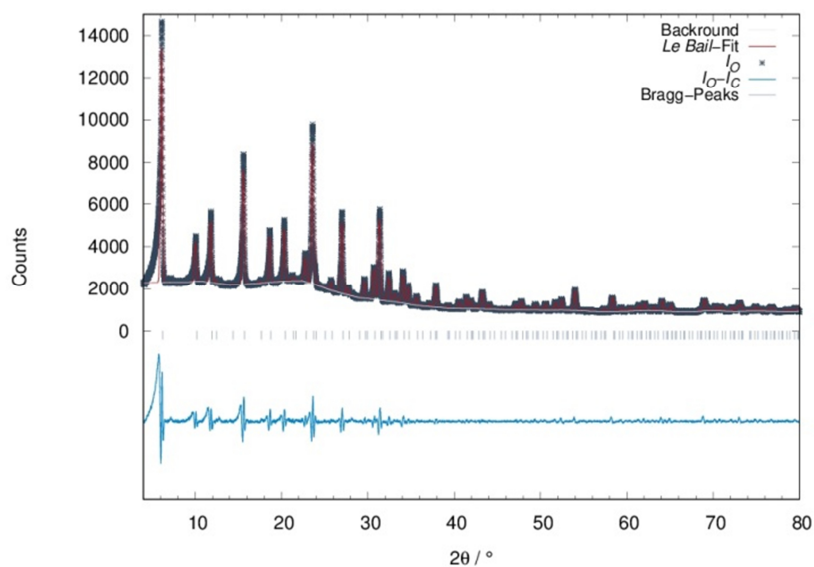


**Figure 8.5.10** *Le Bail* fit of Phth@Zeolite Y (**27**) (298 K, Huber G670,  $\lambda = 1.54 \text{ \AA}$ ) with measured intensities (grey, crosses), calculated intensities (red), differential curve (turquoise), *Bragg* peaks (light blue, ticks) and background of refinement (white).

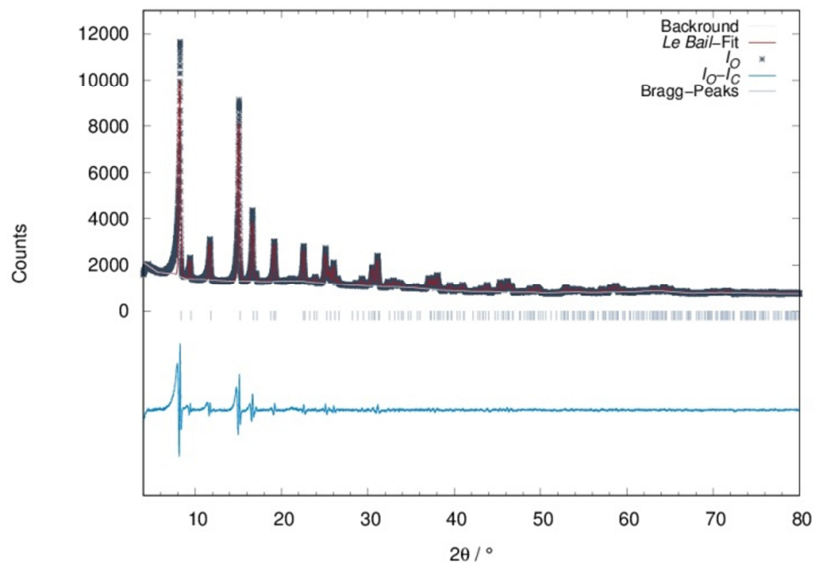


**Figure 8.5.11** *Le Bail* fit of Phth@MFM-300(Ga<sub>2</sub>) (**28**) (298 K, *Huber G670*,  $\lambda = 1.54 \text{ \AA}$ ) with measured intensities (grey, crosses), calculated intensities (red), differential curve (turquoise), *Bragg* peaks (light blue, ticks) and background of refinement (white).

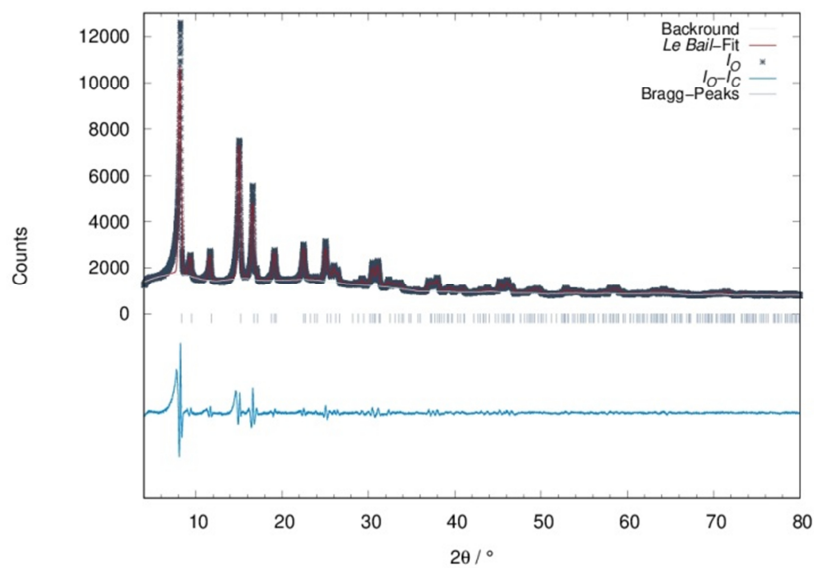


**Figure 8.5.12** *Le Bail* fit of Phth@F-MFM-300(Ga<sub>2</sub>) (**29**) (298 K, *Huber G670*,  $\lambda = 1.54 \text{ \AA}$ ) with measured intensities (grey, crosses), calculated intensities (red), differential curve (turquoise), *Bragg* peaks (light blue, ticks) and background of refinement (white).

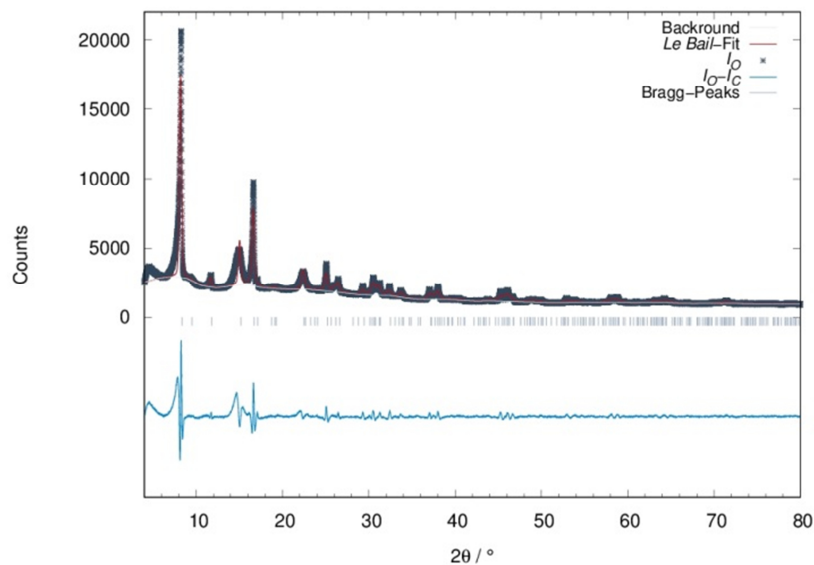


**Figure 8.5.13** *Le Bail* fit of Phth@F<sub>2</sub>-MFM-300(Ga<sub>2</sub>) (**30**) (298 K, *Huber G670*,  $\lambda = 1.54 \text{ \AA}$ ) with measured intensities (grey, crosses), calculated intensities (red), differential curve (turquoise), *Bragg* peaks (light blue, ticks) and background of refinement (white).

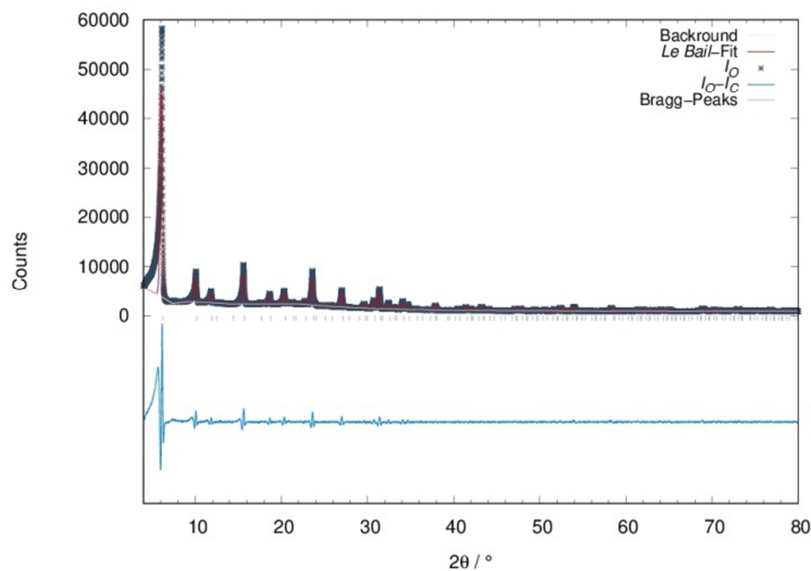


**Figure 8.5.14** *Le Bail* fit of Zeolite Y (298 K, *Huber G670*,  $\lambda = 1.54 \text{ \AA}$ ) with measured intensities (grey, crosses), calculated intensities (red), differential curve (turquoise), *Bragg* peaks (light blue, ticks) and background of refinement (white).

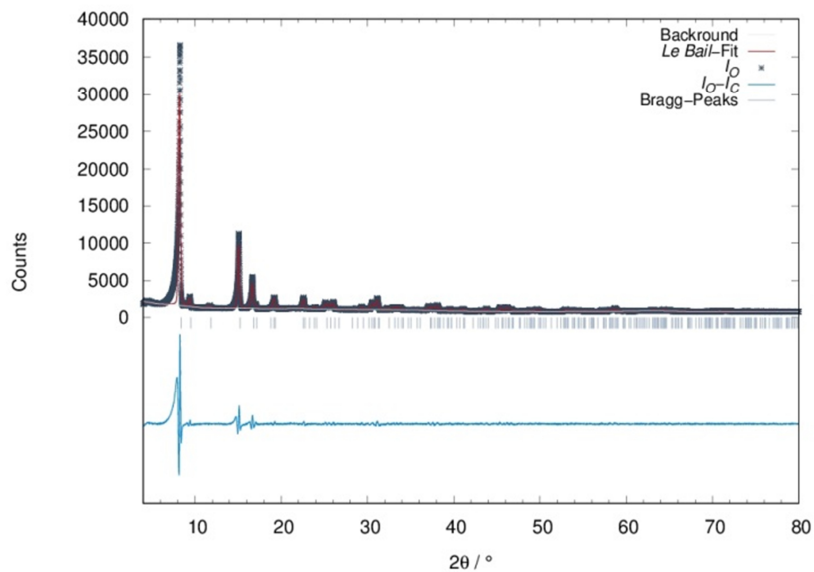


**Figure 8.5.15** *Le Bail* fit of MFM-300(Ga<sub>2</sub>) (298 K, *Huber G670*,  $\lambda = 1.54 \text{ \AA}$ ) with measured intensities (grey, crosses), calculated intensities (red), differential curve (turquoise), *Bragg* peaks (light blue, ticks) and background of refinement (white).

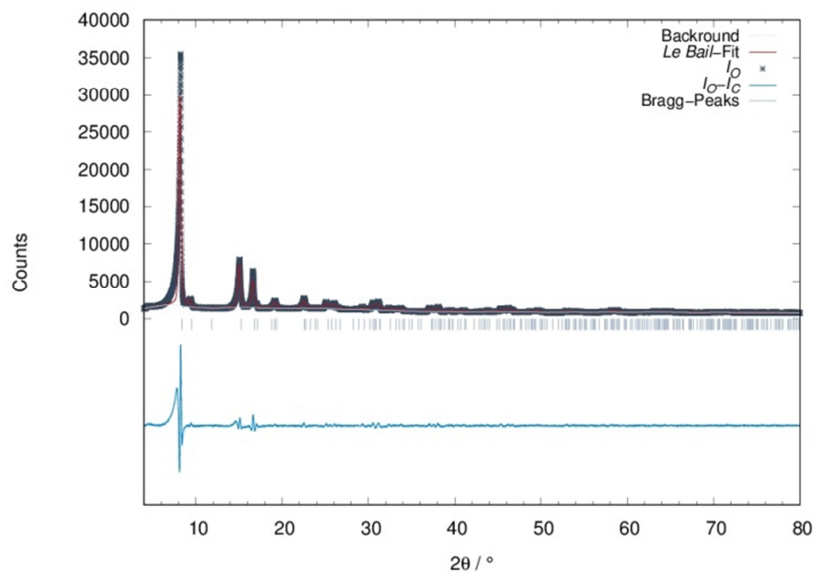


**Figure 8.5.16** *Le Bail* fit of F-MFM-300(Ga<sub>2</sub>) (298 K, *Huber G670*,  $\lambda = 1.54 \text{ \AA}$ ) with measured intensities (grey, crosses), calculated intensities (red), differential curve (turquoise), *Bragg* peaks (light blue, ticks) and background of refinement (white).

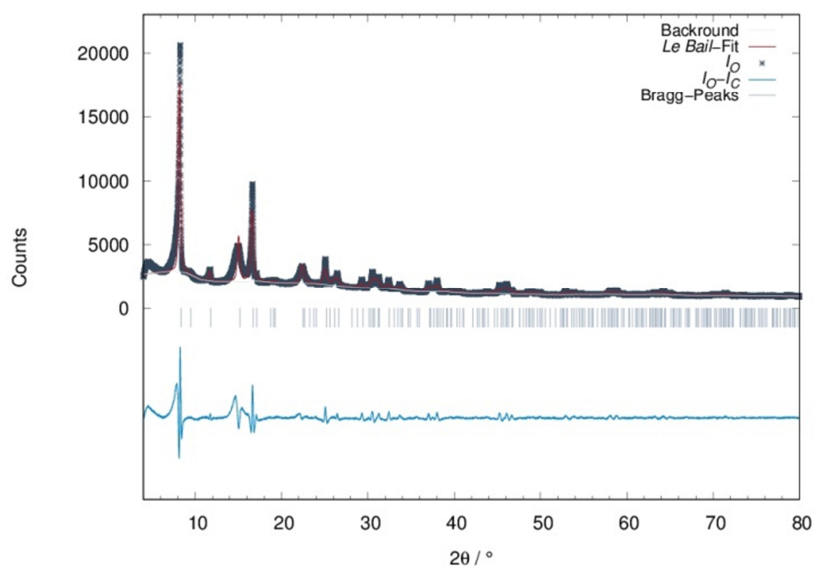


**Figure 8.5.17** *Le Bail* fit of  $F_2$ -MFM-300( $Ga_2$ ) (298 K, *Huber G670*,  $\lambda = 1.54 \text{ \AA}$ ) with measured intensities (grey, crosses), calculated intensities (red), differential curve (turquoise), *Bragg* peaks (light blue, ticks) and background of refinement (white).

**Table 8.5.1** Results of *Le Bail* fits of powder diffraction data of Zeolite Y, MFM-300( $Ga_2$ ), F-MFM-300( $Ga_2$ ) and  $F_2$ -MFM-300( $Ga_2$ ).

	Zeolite Y	MFM-300( $Ga_2$ )	F-MFM-300( $Ga_2$ )	$F_2$ -MFM-300( $Ga_2$ )
T/K	298	298	298	298
Space Group / No.	$Fd\bar{3}m / 227$	$I4_122 / 98$	$I4_122 / 98$	$I4_122 / 98$
GOF	8.9	6.02	5.54	4.58
$R_p$	0.1211	0.0902	0.0881	0.0736
$wR_p$	0.2006	0.1702	0.1506	0.1114
$V/\text{\AA}^3$	14796(1)	2636.2(6)	2632(1)	2658(1)
a	24.55(0)	14.918(2)	14.910(3)	14.976(3)
b	-	14.918(2)	14.910(3)	14.976(3)
b	-	11.846(2)	11.841(4)	11.851(4)

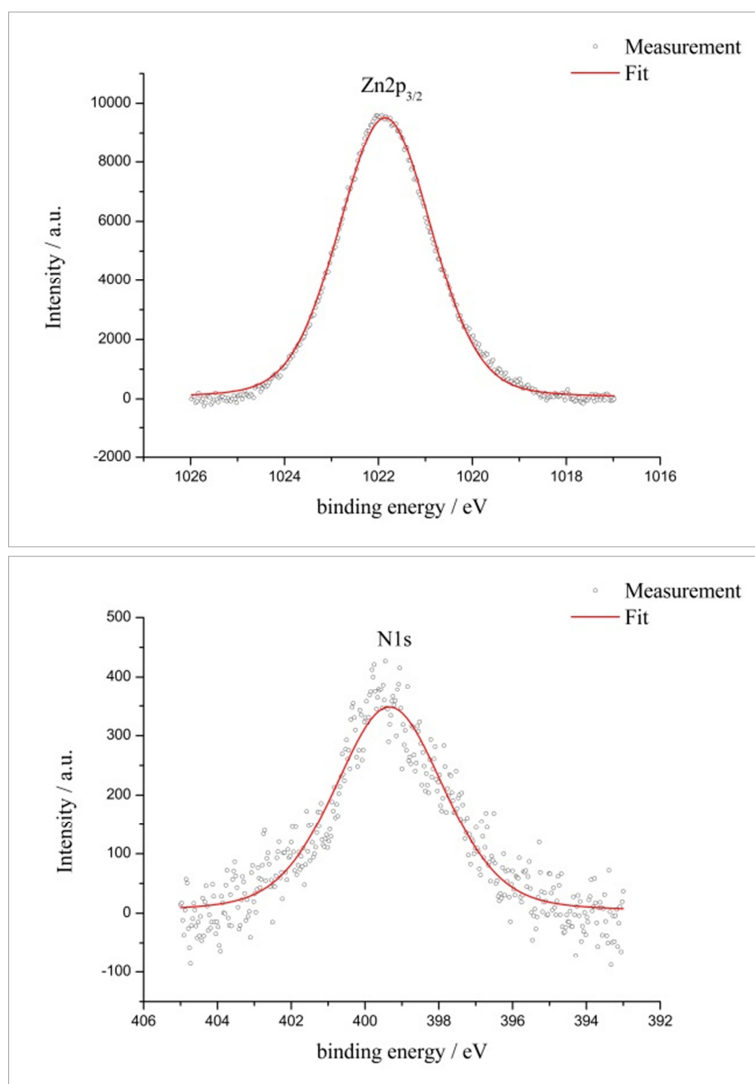


**Figure 8.5.18** XPS spectrum of the Zn2p<sub>3/2</sub> (top) and N1s peak (bottom) of Phth@MOF-5 (23) with experimental data (dots) and fit (red).

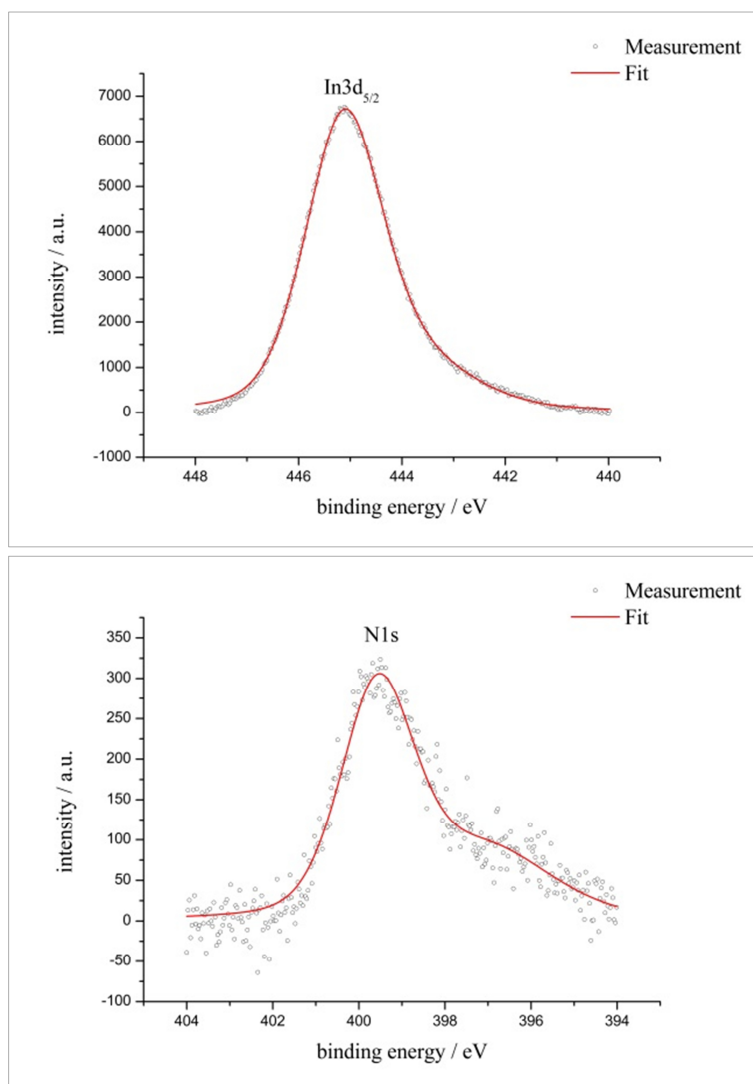


**Figure 8.5.19** XPS spectrum of the In<sub>3d<sub>5/2</sub></sub> (top) and N<sub>1s</sub> peak (bottom) of Phth@MIL-68(In) (24) with experimental data (dots) and fit (red).

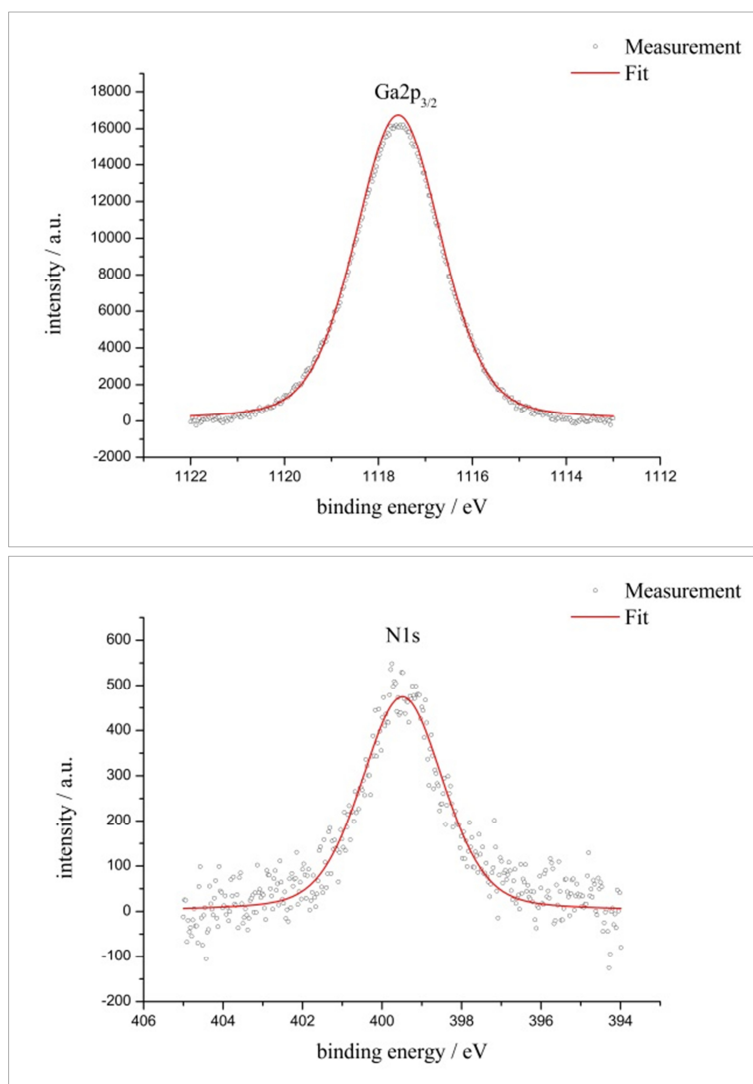


**Figure 8.5.20** XPS spectrum of the Ga<sub>2p</sub><sub>3/2</sub> (top) and N<sub>1s</sub> peak (bottom) of Phth@MIL-68(Ga) (**25**) with experimental data (dots) and fit (red).

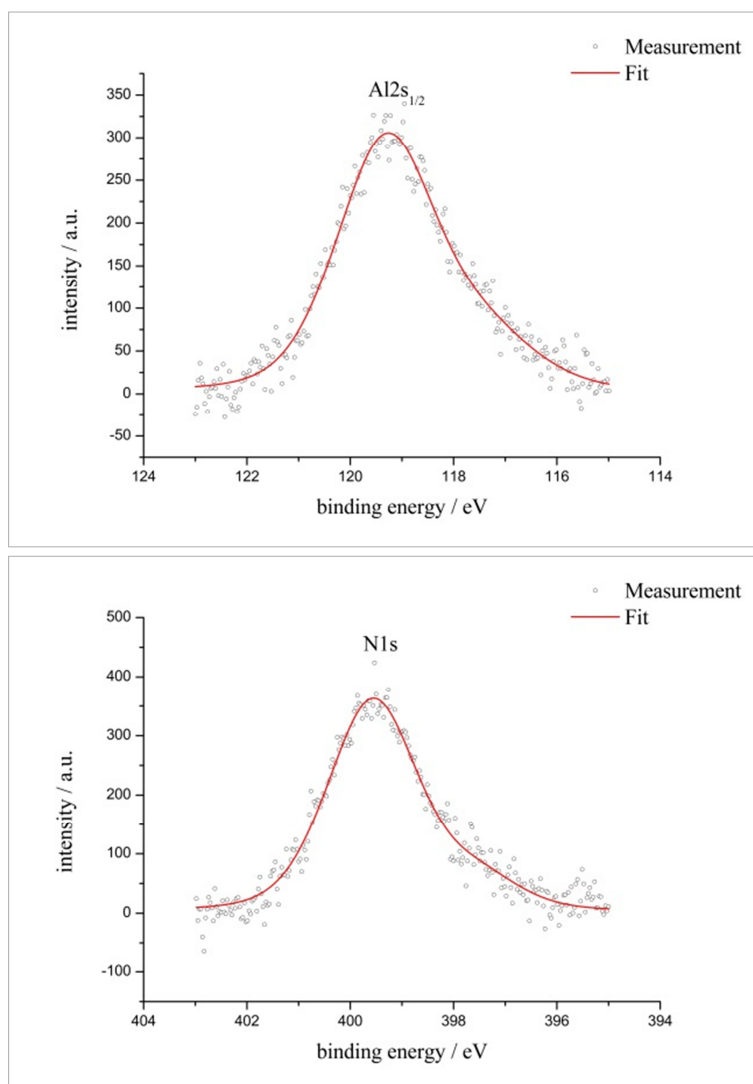


**Figure 8.5.21** XPS spectrum of the Al<sub>2s</sub><sub>1/2</sub> (top) and N1s peak (bottom) of Phth@MIL-53(Al) (26) with experimental data (dots) and fit (red).

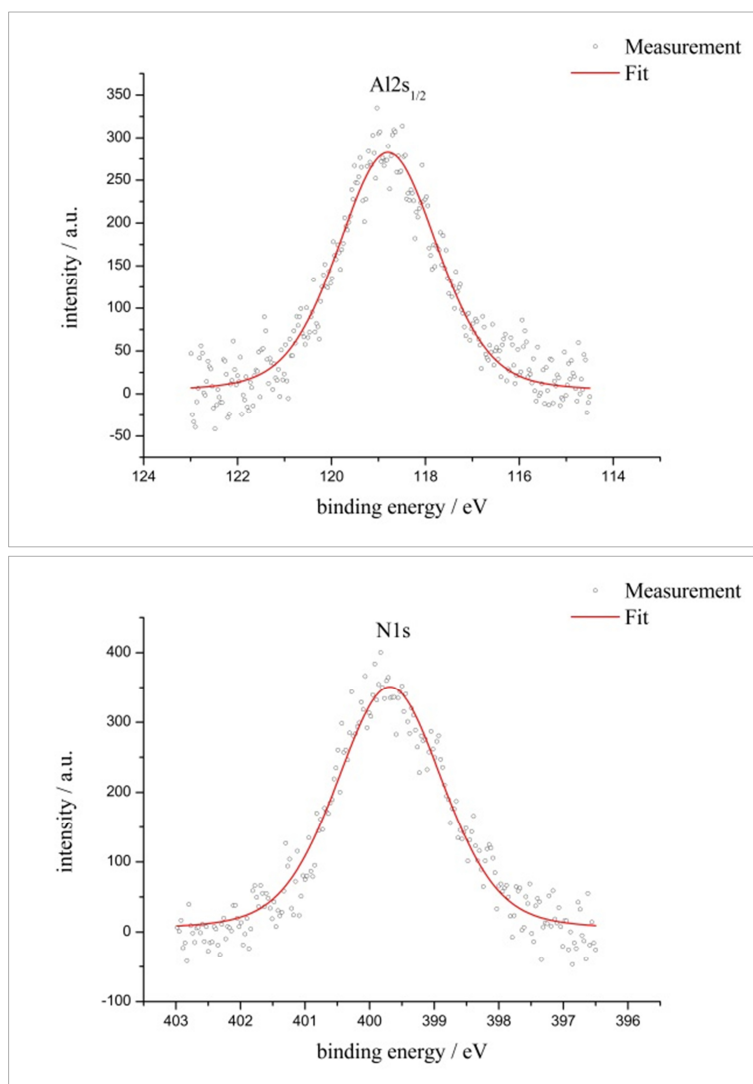


**Figure 8.5.22** XPS spectrum of the  $Al2s_{1/2}$  (top) and  $N1s$  peak (bottom) of Phth@Zeolite Y (27) with experimental data (dots) and fit (red).

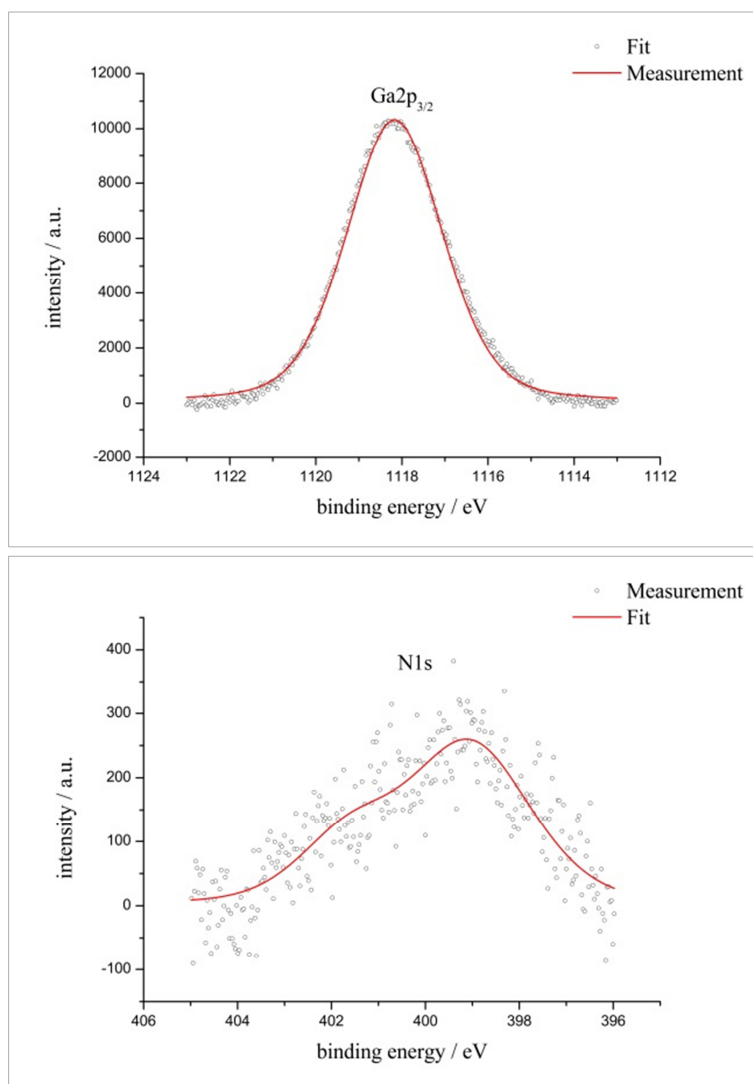


**Figure 8.5.23** XPS spectrum of the Ga<sub>2p<sub>3/2</sub></sub> (top) and N<sub>1s</sub> peak (bottom) of Phth@MFM-300(Ga<sub>2</sub>) (**28**) with experimental data (dots) and fit (red).

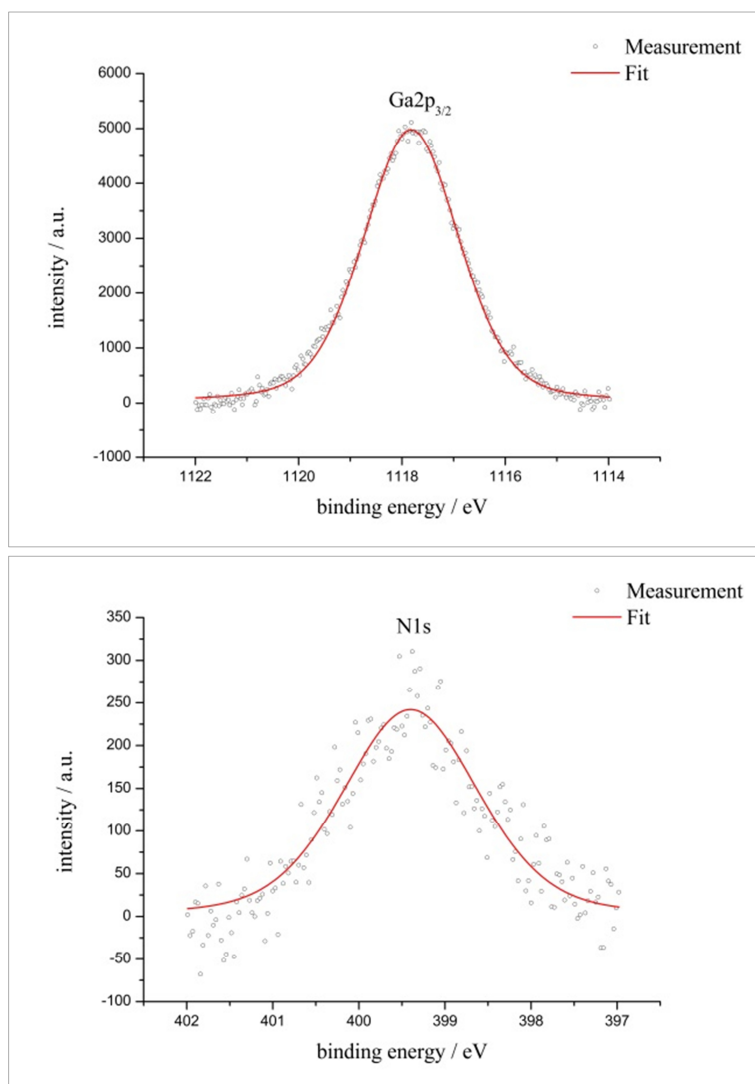


**Figure 8.5.24** XPS spectrum of the Ga<sub>2p<sub>3/2</sub></sub> (top) and N1s peak (bottom) of Phth@F-MFM-300(Ga<sub>2</sub>) (**29**) with experimental data (dots) and fit (red).

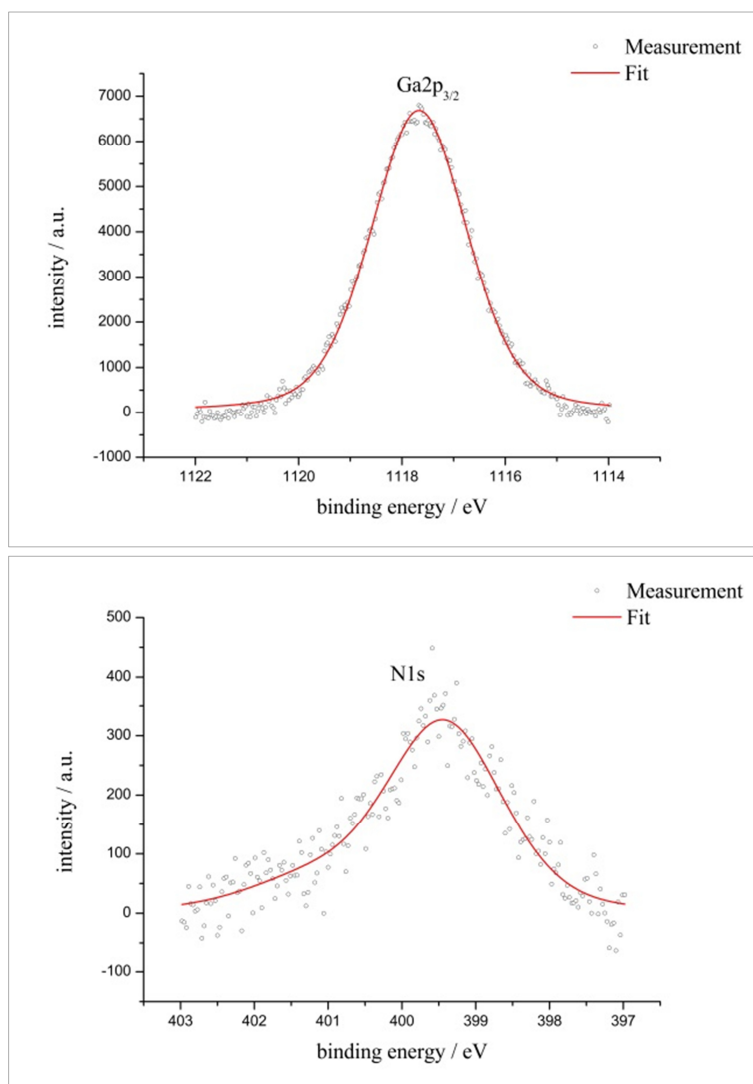


**Figure 8.5.25** XPS spectrum of the Ga<sub>2p<sub>3/2</sub></sub> (top) and N1s peak (bottom) of Phth@F<sub>2</sub>-MFM-300(Ga<sub>2</sub>) (**30**) with experimental data (dots) and fit (red).

**Table 8.5.2** Calculation of the composition of compounds **23** to **26** via XPS.

	<b>23</b>	<b>24</b>	<b>25</b>	<b>26</b>
Nitrogen atoms per formula unit of Phth	1	1	1	1
Metal atoms per formula unit of the respective porous host	4 [Zn <sub>4</sub> O(bdc) <sub>3</sub> ]	1 [In(OH)(bdc)]	1 [Ga(OH)(bdc)]	1 [Al(OH)(bdc)]
RSF factor for nitrogen	1.77 N1s	1.77 N1s	1.77 N1s	1.77 N1s
RSF factor for the respective metal	18.01 (Zn 2p <sub>3/2</sub> )	13.23 (In 3d <sub>5/2</sub> )	20.47 (Ga 2p <sub>3/2</sub> )	0.681 (Al 2s <sub>1/2</sub> )
Peak area for nitrogen	1494	1074	1411	1026
Peak area for the respective metal	25888	16452	44027	979
Phth : MOF/PM	2.35 : 1	0.48 : 1	0.37 : 1	0.40 : 1

**Table 8.5.3** Calculation of the composition of compounds **27** to **30** via XPS.

	<b>27</b>	<b>28</b>	<b>29</b>	<b>30</b>
Nitrogen atoms per formula unit of Phth	1	1	1	1
Metal atoms per formula unit of the respective porous host	2 (Al) (SiO <sub>2</sub> ) <sub>5.1</sub> :Al <sub>2</sub> O <sub>3</sub>	2 Ga <sub>2</sub> (OH) <sub>2</sub> (bptc)	2 Ga <sub>2</sub> (OH) <sub>2</sub> (F-bptc)	2 Ga <sub>2</sub> (OH) <sub>2</sub> (F <sub>2</sub> -bptc)
RSF factor for nitrogen	1.77 N1s	1.77 N1s	1.77 N1s	1.77 N1s
RSF factor for the respective metal	0.681 (Al 2s <sub>1/2</sub> )	20.47 (Ga 2p <sub>3/2</sub> )	20.47 (Ga 2p <sub>3/2</sub> )	20.47 (Ga 2p <sub>3/2</sub> )
Peak area for nitrogen	838	1238	550	854
Peak area for the respective metal	867	33026	13273	17943
Phth : MOF/PM	0.74 : 1	0.86 : 1	0.95 : 1	1.1 : 1

### 8.5.1 Dilution of Phth in MOF-5 and MIL-68(Ga)

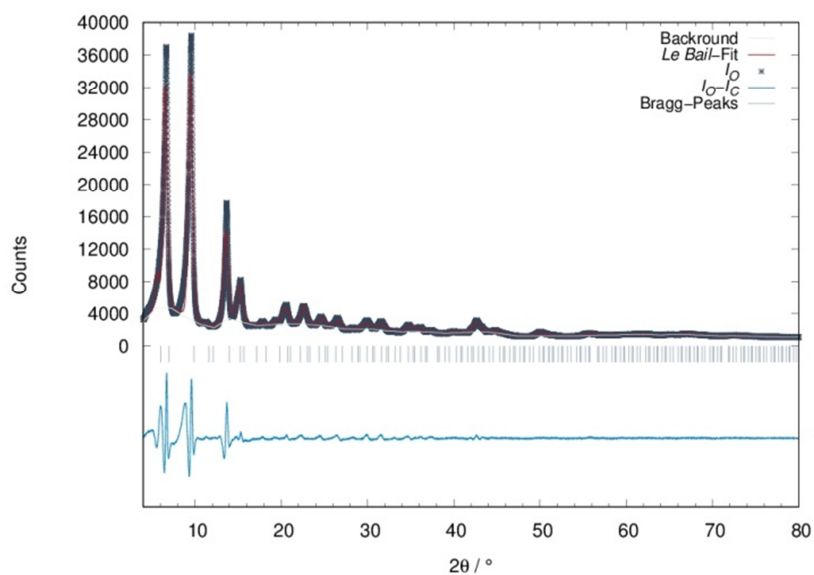


**Figure 8.5.26** *Le Bail* fit of Phth<sub>0.1</sub>@MOF-5 (298 K, *Huber G670*,  $\lambda = 1.54 \text{ \AA}$ ) with measured intensities (grey, crosses), calculated intensities (red), differential curve (turquoise), *Bragg* peaks (light blue, ticks) and background of refinement (white).

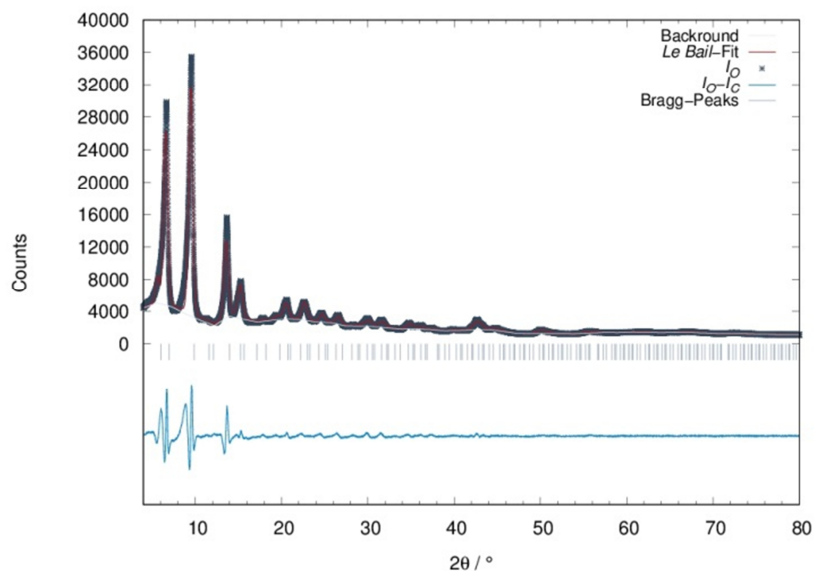


**Figure 8.5.27** *Le Bail* fit of Phth<sub>0.25</sub>@MOF-5 (298 K, *Huber G670*,  $\lambda = 1.54 \text{ \AA}$ ) with measured intensities (grey, crosses), calculated intensities (red), differential curve (turquoise), *Bragg* peaks (light blue, ticks) and background of refinement (white).

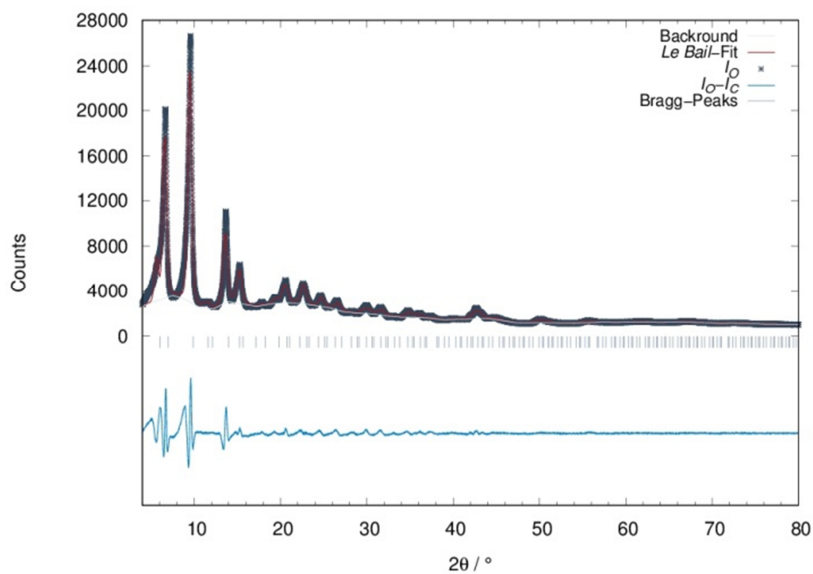


**Figure 8.5.28** *Le Bail* fit of Phth<sub>0.5</sub>@MOF-5 (298 K, Huber G670,  $\lambda = 1.54 \text{ \AA}$ ) with measured intensities (grey, crosses), calculated intensities (red), differential curve (turquoise), *Bragg* peaks (light blue, ticks) and background of refinement (white).

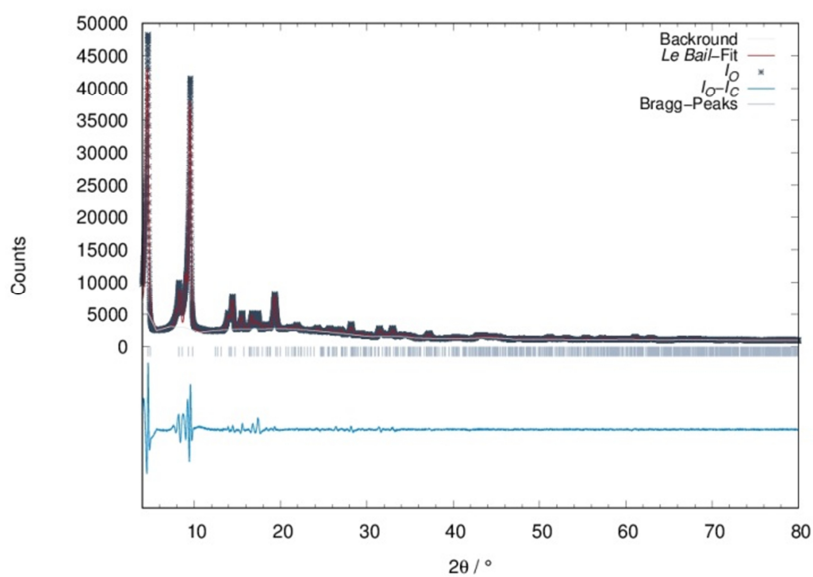


**Figure 8.5.29** *Le Bail* fit of Phth<sub>0.1</sub>@MIL-68(Ga) (298 K, Huber G670,  $\lambda = 1.54 \text{ \AA}$ ) with measured intensities (grey, crosses), calculated intensities (red), differential curve (turquoise), *Bragg* peaks (light blue, ticks) and background of refinement (white).

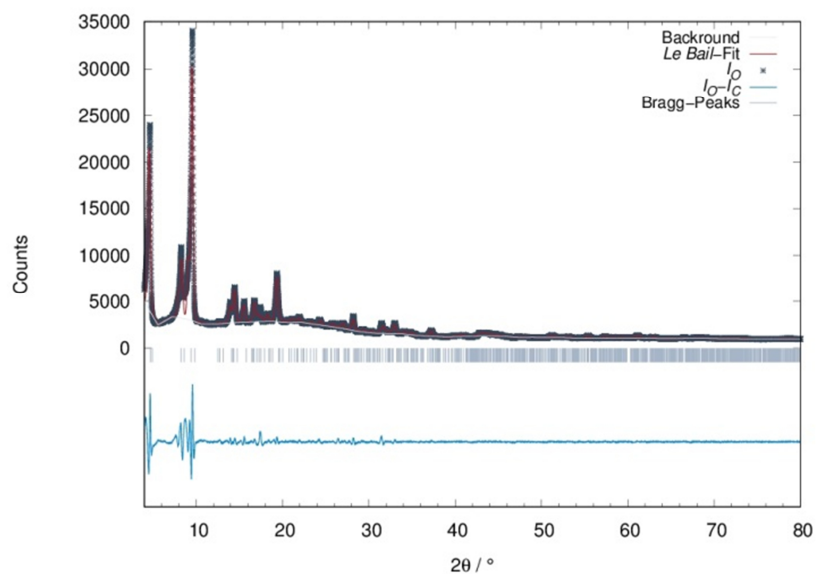


**Figure 8.5.30** *Le Bail* fit of Phth<sub>0.25</sub>@MIL-68(Ga) (298 K, *Huber G670*,  $\lambda = 1.54 \text{ \AA}$ ) with measured intensities (grey, crosses), calculated intensities (red), differential curve (turquoise), *Bragg* peaks (light blue, ticks) and background of refinement (white).

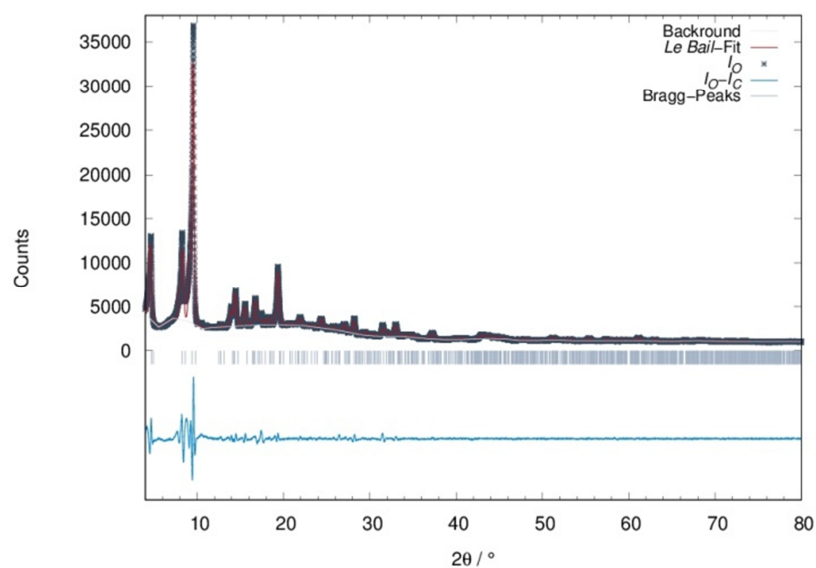


**Figure 8.5.31** *Le Bail* fit of Phth<sub>0.5</sub>@MIL-68(Ga) (298 K, *Huber G670*,  $\lambda = 1.54 \text{ \AA}$ ) with measured intensities (grey, crosses), calculated intensities (red), differential curve (turquoise), *Bragg* peaks (light blue, ticks) and background of refinement (white).

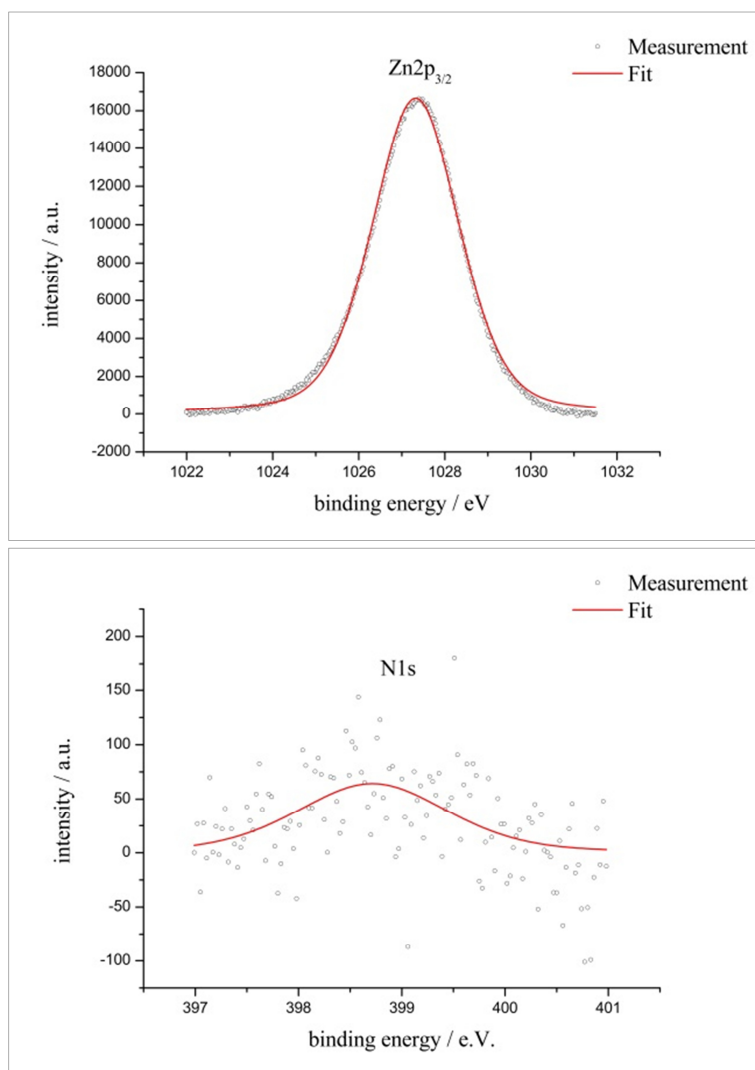


**Figure 8.5.32** XPS spectrum of the Zn2p<sub>3/2</sub> (top) and N1s peak (bottom) of Phth<sub>0.1</sub>@MOF-5 with experimental data (dots) and fit (red).

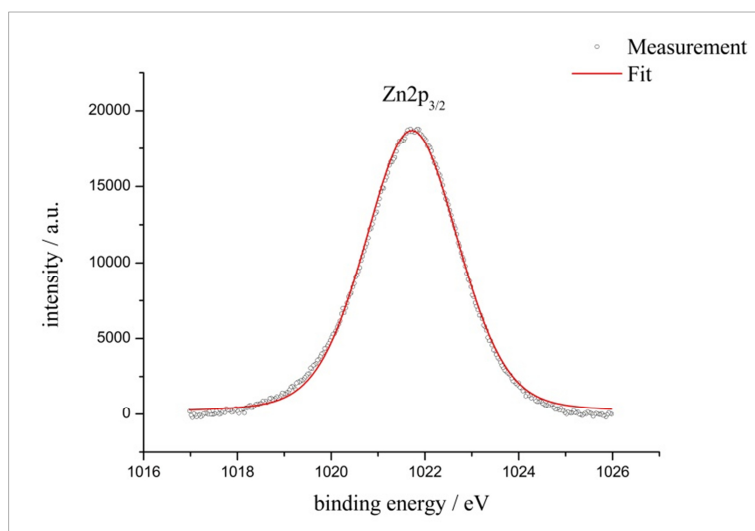


**Figure 8.5.33** XPS spectrum of the Zn2p<sub>3/2</sub> peak of Phth<sub>0.25</sub>@MOF-5 with experimental data (dots) and fit (red).

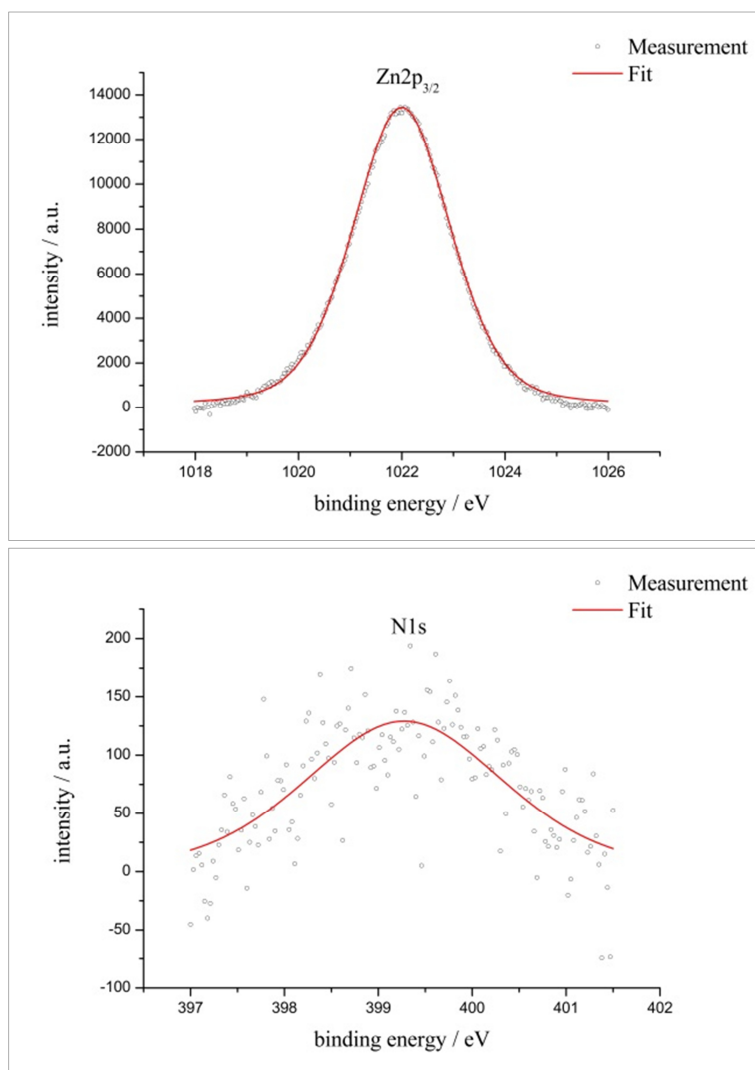


**Figure 8.5.34** XPS spectrum of the Zn2p<sub>3/2</sub> (top) and N1s peak (bottom) of Phth<sub>0.5</sub>@MOF-5 with experimental data (dots) and fit (red).

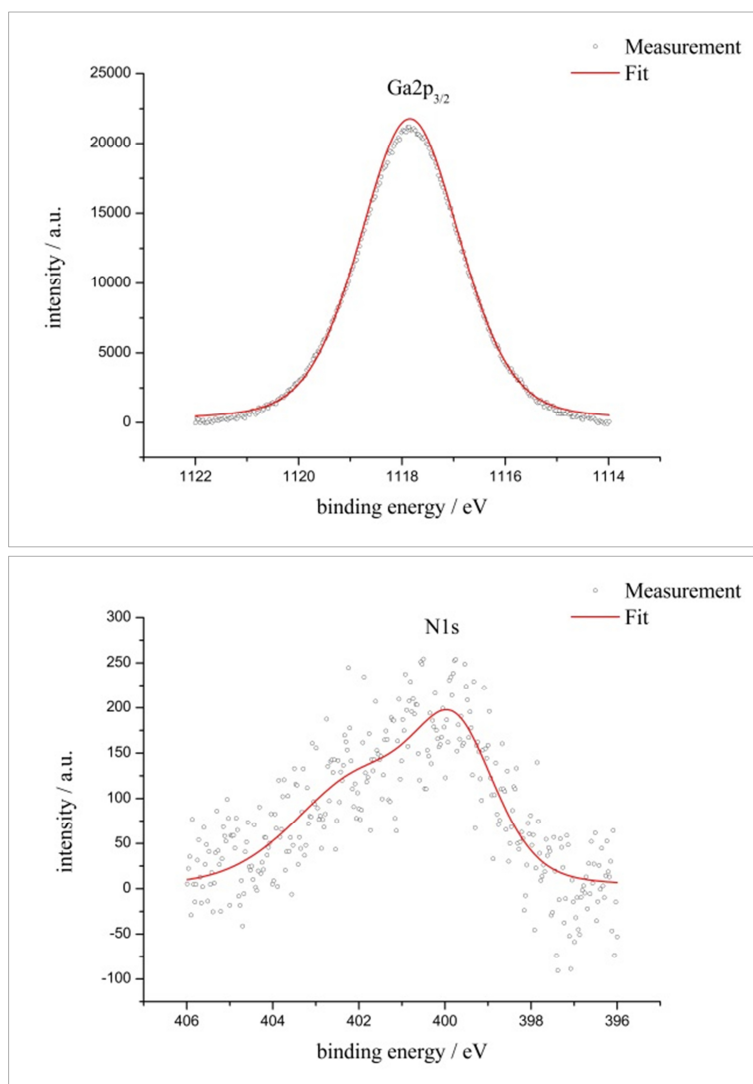


**Figure 8.5.35** XPS spectrum of the Ga<sub>2p<sub>3/2</sub></sub> (top) and N<sub>1s</sub> peak (bottom) of Phth<sub>0.1</sub>@MIL-68(Ga) with experimental data (dots) and fit (red).

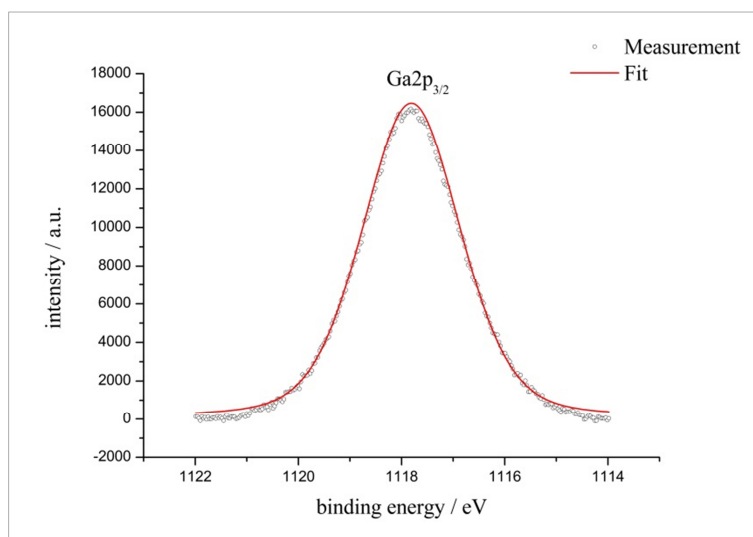


**Figure 8.5.36** XPS spectrum of the Ga2p<sub>3/2</sub> peak of Phth<sub>0.25</sub>@MIL-68(Ga) with experimental data (dots) and fit (red).

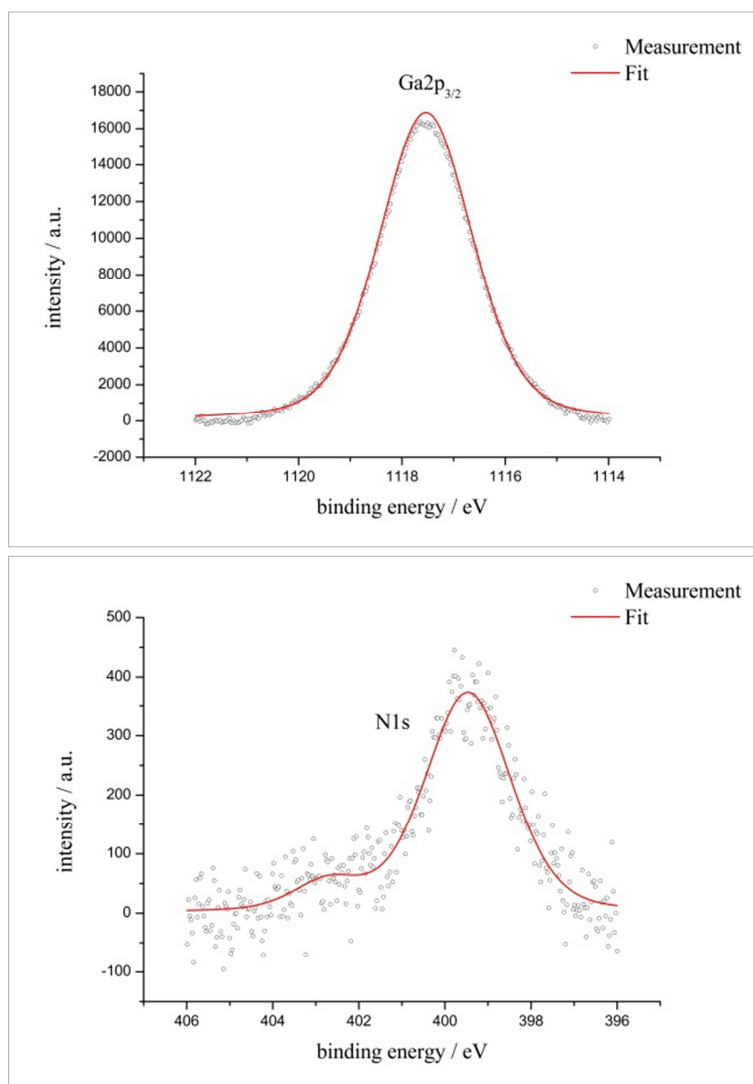


**Figure 8.5.37** XPS spectrum of the Ga2p<sub>3/2</sub> (top) and N1s peak (bottom) of Phth<sub>0.5</sub>@MIL-68(Ga) with experimental data (dots) and fit (red).

**Table 8.5.4** Calculation of the composition of the serial dilution of Phth in MOF-5 via XPS.

	<b>0.1</b>	<b>0.25</b>	<b>0.5</b>
Nitrogen atoms per formula unit of Phth	1	1	1
Metal atoms per formula unit of the respective MOF	4 [Zn <sub>4</sub> O(bdc) <sub>3</sub> ]	4 [Zn <sub>4</sub> O(bdc) <sub>3</sub> ]	4 [Zn <sub>4</sub> O(bdc) <sub>3</sub> ]
RSF factor for nitrogen	1.77 N1s	1.77 N1s	1.77 N1s
RSF factor for the respective metal	18.01 (Zn 2p <sub>3/2</sub> )	18.01 (Zn 2p <sub>3/2</sub> )	18.01 (Zn 2p <sub>3/2</sub> )
Peak area for nitrogen	135	266	394
Peak area for the respective metal	48294	52653	36545
SP-O : MOF	0.11: 1	0.2 : 1	0.43 : 1

**Table 8.5.5** Calculation of the composition of the serial dilution of Phth in MIL-68(Ga) via XPS.

	<b>0.1</b>	<b>0.25</b>	<b>0.5</b>
Nitrogen atoms per formula unit of Phth	1	1	1
Metal atoms per formula unit of the respective MOF	1 [Ga(OH)(bdc)]	1 [Ga(OH)(bdc)]	1 [Ga(OH)(bdc)]
RSF factor for nitrogen	1.77 N1s	1.77 N1s	1.77 N1s
RSF factor for the respective metal	20.47 (Ga 2p <sub>3/2</sub> )	20.47 (Ga 2p <sub>3/2</sub> )	20.47 (Ga 2p <sub>3/2</sub> )
Peak area for nitrogen	930	1008	1190
Peak area for the respective metal	60926	45081	43736
Phth : MOF	0.22 : 1	0.25 : 1	0.32 : 1

## Dank

Am Ende dieser Arbeit möchte ich all denjenigen meinen Dank aussprechen, die zum Gelingen dieser Dissertation beigetragen haben. Dabei möchte ich mich als Erstes bei meinem Doktorvater *Prof. Dr. Uwe Ruschewitz* dafür bedanken, dass ich mit einem sehr interessanten Thema in seinem Arbeitskreis meine Dissertation anfertigen durfte. Weiterhin danke ich ihm nicht nur für seine fachliche Unterstützung und die angeregten Diskussionen, sondern vor allem auch für das stets nette menschliche Miteinander, Danke! Herrn *Prof. Dr. Dominik Schaniel* danke ich zum einen für die Übernahme des Zweitgutachtens, zum anderen dafür, dass ich bei ihm in Nancy optische Experimente durchführen und in Fachgesprächen mit ihm einen Menge lernen konnte. Herrn *Prof. Dr. Klaus Meerholz* danke ich für die Übernahme des Prüfungsvorsitzes. Bei *Dr. Selina Olthof* möchte ich mich für die Übernahme der Schriftführung bedanken. Zudem danke ich ihr für die vielen Stunden im ESCA-Labor, wo sie zahlreiche Fragen von mir beantwortet und mir bei den XPS-Messungen und deren Auswertung geholfen hat sowie für das Vertrauen dafür die Messungen selbstständig durchzuführen. Mein Dank gilt weiterhin *Prof. Dr. Axel Griesbeck* sowie seinen Mitarbeitern *Dr. Murat Atar* und *Moritz Vollmer* für das gemeinsame Projekt zu den Fluoreszenzfarbstoffen. Ich möchte mich bei *Dr. Lars Heinke* bedanken, dafür, dass er zunächst als Kooperationspartner und dann auch als mein Mentor mir mit jeglichem Rat zur Seite stand. Bei der Frauenförderung der Universität zu Köln sowie der IPAK-Förderung bedanke ich mich für die finanzielle Unterstützung bei Konferenzen und Forschungsaufenthalten.

Beim jetzigen Arbeitskreis *Ruschewitz, Daniel, Markus, Melanie, Carina, Christian* und *Marc* und auch bei den ehemaligen Mitgliedern *Daniela, Steffi, Verena, Miriam, Irek* und *John*, möchte ich mich für die vielen netten und lustigen Arbeitstage, Ausflüge, die Freundschaft,..., und das Korrekturlesen bedanken und vor allem dafür, dass ihr es mit mir, vor allem in der letzten Phase, so gut ausgehalten habt ;) Bei den Nachbararbeitskreisen *Klein* sowie *Wickleder* möchte ich mich ebenfalls für die tolle Zeit bedanken. Für die helfenden Hände und das „Praktikum“ in unserer Werkstatt sowie das immer nette und lustige Abholen von Edukten aus dem Chemikalienmanagement bedanke ich mich sehr. Bei *Silke Kremer* bedanke ich für die elementaranalytischen Untersuchungen.

Mein Dank gilt insbesondere meinen Freunden neben und auf der Laufstrecke, die mich auf ganz andere Gedanken gebracht und damit sehr unterstützt haben. Dabei möchte ich *Arndt*

*Fontes* erwähnen, der mir als Trainer und Freund sowohl bei sportlichen als auch bei beruflichen Höhen und Tiefen immer zur Seite stand und steht. Weiterhin möchte ich mich bei *Verena Gramm* und *Miriam Sobieray* bedanken, für die schönen Zeiten im Büro bis spät abends, für die Freundschaft, Matcha Latte und noch vieles mehr.

Am Ende möchte ich mich bei denjenigen bedanken, ohne die es diese Danksagung und Arbeit nicht gäbe: meiner Familie Mama, Papa und *Lena* und meinem Freund *Max*, die in dieser Zeit auf verschiedenste Weise für mich da waren. Meiner Mama, *Monika Schwartz*, danke ich aus tiefstem Herzen dafür, dass sie immer für mich da ist, bei den täglichen Telefonaten, bei persönlichen Höhen und Tiefen und vor allem dafür, dass sie meine beste Freundin ist. Ich danke ihr für den steten und auch kritischen Rat. Danke, meine Mama. Meinem Papa, *Dr. Herbert Schwartz*, danke ich ebenfalls aus tiefstem Herzen dafür, dass er als mein bester Freund immer an meiner Seite steht, immer für mich da ist und mich in allen Belangen unterstützt. Ich danke ihm, dass er mir mit kritischem Auge und ehrlichem Rat in jeglichen Fragen (insbesondere bei der kritischen Durchsicht dieser Arbeit!) immer geholfen hat und hilft, dafür schätze ich dich sehr, Papa, ich danke dir dafür.

Meinem Freund *Max Kreitner* danke ich dafür, dass er in der gesamten Promotionszeit für mich da war, mir in schwierigen Phasen immer Mut gibt und mich ohne Vorbehalte unterstützt. Ich danke ihm ebenfalls für die kritische Durchsicht dieser Arbeit und der Hilfe bei sprachlichen Schwierigkeiten. Ich danke ihm dafür, dass er immer an meiner Seite steht, danke Max.

## Erklärung

Ich versichere, dass ich die von mir vorgelegte Dissertation selbstständig angefertigt, die benutzten Quellen und Hilfsmittel vollständig angegeben und die Stellen der Arbeit – einschließlich Tabellen, Karten und Abbildungen –, die anderen Werken im Wortlaut oder dem Sinn nach entnommen sind, in jedem Einzelfall als Entlehnung kenntlich gemacht habe; dass diese Dissertation noch keiner anderen Fakultät oder Universität zur Prüfung vorgelegen hat; dass sie – abgesehen von den unten angegebenen Teilpublikationen noch nicht veröffentlicht worden ist sowie, dass ich eine solche Veröffentlichung vor Abschluss des Promotionsverfahrens nicht vornehmen werde.

Die Bestimmungen dieser Promotionsordnung sind mir bekannt.

Die von mir dargelegte Dissertation ist von Herrn Prof. Dr. Uwe Ruschewitz betreut worden.

Köln, den 28. Mai 2018, Heidi Annemarie Schwartz

Zur Wahrung der Priorität wurden Teile dieser Arbeit bereits publiziert:

H. A. Schwartz, S. Olthof, D. Schaniel, K. Meerholz and U. Ruschewitz, *Inorg. Chem.*, **2017**, *56*, 13100–13110; DOI: 10.1021/acs.inorgchem.7b01908

Teilergebnisse dieser Arbeit gingen in den folgenden Tagungsbeitrag ein:

D. Hermann, H. Schwartz, U. Ruschewitz, *Z. Anorg. Allg. Chem.* **2016**, *642*, 1005; DOI: 10.1002/zaac.201604005

H. Schwartz, U. Ruschewitz, *Z. Anorg. Allg. Chem.* **2016**, *642*, 1059; DOI: 10.1002/zaac.201605072



# Curriculum Vitae

Gustavstraße 4  
50937 Cologne  
Germany

**Heidi Annemarie Schwartz**

email: heidi-annemarie@gmx.de

---

## Education

- approx. 07/2018                      PhD thesis with the Topic “Metal-Organic Frameworks as Crystalline Porous Hosts for Photoactive Molecules“ under the supervision of Prof. Dr. Uwe Ruschewitz at the Institute of Inorganic Chemistry (University of Cologne)
- 05/2015                                  First state examination in Biology and Chemistry (mark: 1.3); Thesis with the Topic: „Metallorganische Gerüstverbindungen als Wirtsmaterialien für photochrome Moleküle (Metal-Organic Frameworks as host materials for Photochromic Molecules)“ (mark: 1.0)
- 07/2009                                  „Allgemeine Hochschulreife“(Gymnasium Syke, mark 1.7) - Grade 7-10 bilingual lessons (lessons in geography (grade 7, 8, 10), history (grade 8, 9, 10), music (grade 9, 10) and biology (grade 9, 10) were taught in English)
- 

## Work Experience

- since 07/2015                      **Scientific Assistant** (Organization and Supervision of Laboratory Courses (basic and advanced) and Supervision of Bachelor and Master Theses for B.Sc. and M.Sc. as well as B.A. and M.A. in the Institute of Inorganic Chemistry, University of Cologne)
- 10/2012 – 06/2015                **Student Assistant** (Organization and Supervision of Laboratory Courses (basic and advanced) for B.Sc. and M.Sc. as well as B.A. and M.A. in the Institute of Inorganic Chemistry, University of Cologne)
- 

## Languages

- German (first language)
- English (fluently spoken and written)
- Latin

### Conferences (selection)

07/2017	Participation at the ICP 2017 in Strasbourg with the lecture <i>MOFs as "solid solvents" for Spiropyrans?</i>
09/2016	Participation at the "25 <sup>th</sup> Lecture Conference on Photochemistry" in Jena with a poster presentation
04/2016	Participation at the "Multiresponsive Photochromes – Conference" in Nantes with a poster presentation
10/2015	Participation at the "1 <sup>st</sup> European Conference on Metal Organic Frameworks and Porous Polymers" in Potsdam with a poster presentation
10/2015	Participation at the "MOF Young Investigator Symposium" in Berlin
07/2015	Presentation of the research project for the DFG SPP "Coornets" in Reisenburg
09/2014	Participation at the "24 <sup>th</sup> Lecture Conference on Photochemistry" in Cologne with a poster presentation

---

### Research stays

12/2017	Research stay at the Faculté de Sciences et Technologies/ Université de Lorraine (FRA) for <i>in situ</i> UV/vis spectroscopic measurements
08/2017	Research stay at the University of Siegen for fluorescence measurements
01/2017	Research stay at the DELTA in Dortmund
12/2016	Research stay at the Faculté de Sciences et Technologies/ Université de Lorraine (FRA) for <i>in situ</i> IR spectroscopic measurements. A lecture with the Topic <i>Metal-Organic Frameworks hosting Spiropyrans</i> was given
04/2016	Research stay at the ESRF in Grenoble (FRA) as main applicant
06/2015	Research stay at the ESRF in Grenoble (FRA) as main applicant

---

### Personal Interests/Hobbies

athletics, long distance running, reading

